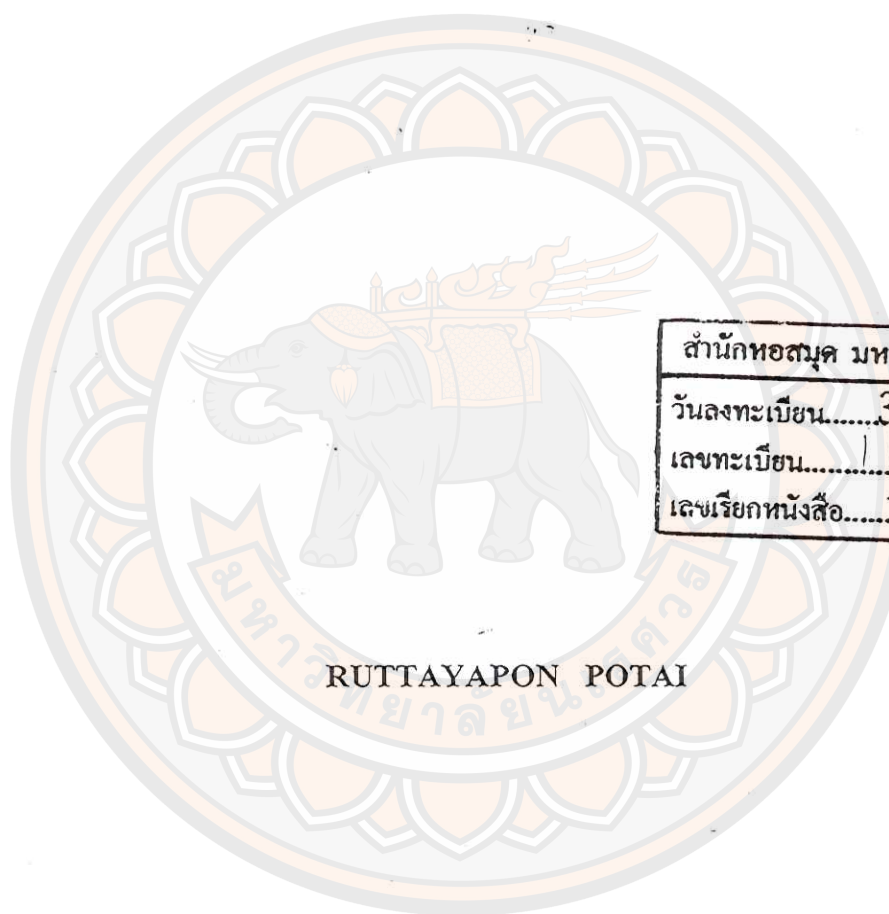อภินันทนาการ

CONTROL OVER PHOTOPHYSICAL PROPERTIES OF CONJUGATED POLYMERS IN DIFFERENT STATES: STUDIES OF REGIOREGULAR POLY(3-OCTYLTHIOPHENE) AND POLY[2-METHOXY-5-(2'-ETHYLHEXYLOXY)-1,4-PHENYLENEVINYLENE]
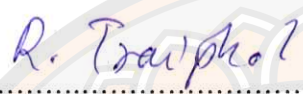
RUTTAYAPON POTAI

A Thesis Submitted to the Graduate School of Naresuan University

in Partial Fulfillment of the Requirements

for the Doctor of Philosophy Degree in Chemistry

July 2014

This dissertation entitled "Control over photophysical properties of conjugated polymer in different states: studies of regioregular poly(3-octylthiophene) and poly[2-methoxy-5-(2'-ethylhexyloxy)-1,4-phenylenevinylene]" submitted by Ruttayapon Potai in partial fulfillment of the requirements for the Doctor of Philosophy Degree in Chemistry is hereby approved.
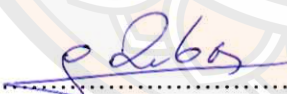
....Chair
(Assistant Professor Toemsak Srikhirin, Ph.D.)

....Committee
(Assistant Professor Rakchart Traiphol, Ph.D.)

....Committee
(Assistant Professor Nipaphat Charoenthai, Ph.D.)

....Committee
(Associate Professor Metha Rutnakornpituk, Ph.D.)

....Committee
(Assistant Professor Yuthapong Udnan, Ph.D.)

....Committee
(Stephan Dubas, Ph.D.)

Approved
....
(Professor Rattana Buosonte, Ph.D.)
Dean of Graduate School
23 July 2014

ACKNOWLEDGEMENT

Title	CONTROL OVER PHOTOPHYSICAL PROPERTIES OF CONJUGATED POLYMERS IN DIFFERENT STATES: STUDIES OF REGIOREGULAR POLY(3-OCTYL THIOPHENE) AND POLY[2-METHOXY-5-(2'-ETHYLHEXYLOXY)-1,4-PHENYLENEVINYLENE]
Author	Ruttayapon Potai
Advisor	Assistant Professor Rakchart Traiphol, Ph.D.
Co - Advisor	Assistant Professor Nipaphat Charoenthai, Ph.D.
	Associate Professor Metha Rutnakornpituk, Ph.D.
Academic Paper	Thesis Ph.D. in Chemistry, Naresuan University, 2013
Keywords	conjugated polymer, chain organization, photophysics, solvent effect

ABSTRACT

This study focuses on detailed investigation of solvent effects on controlling over the aggregation of conjugated polymers in different states and their photophysical properties. Regioregular poly(3-octylthiophene) (*rr*-P3OT) and poly[2-methoxy,5-(2'-ethylhexyloxy)-1,4-phenylenevinylene] (MEH-PPV) have been extensively studied in this work due to their excellent electro-optical properties. The various types of poor solvent are utilized to tune the solubility of polymer and the solvent-solute interaction of polymer solutions. The conjugated polymers in good solvent adopt an extended conformation, allowing long conjugation length of π-electrons. The selective segmental interactions of *rr*-P3OT with poor solvent induce conformational change of the polymer. Addition of cyclohexane, a good solvent for octyl side chain but a poor solvent for the thiophene backbone, into the polymer solution leads to chain coiling, which in turn causes significant decrease of the conjugation length. Absorption and PL spectra of the *rr*-P3OT in cyclohexane exhibit a blue-shift compared to those of the polymer in good solvents. The change of chain conformation is also detectable by the drop of variation of quantum yield when the extended *rr*-P3OT chain transforms into coiled conformation upon increasing cyclohexane ratio. Decrease the solubility parameter forces dense packing of thiophene rings within the coiled chain.

An intrachain aggregation occurs in this system, leading to the appearance of three distinct redshift peaks in absorption spectra and the drastic drop of quantum yield. Correlation between the growth of redshift peaks and the decrease of quantum yield is clearly observed. The use of poor solvent, ethanol, which is non-solvent for polymer backbone and side chain, forces the polymer chains to densely pack indicated by the growth of redshift peaks in absorption spectra. The measurements of site selective photoluminescent (PL) and photoluminescent excitation spectra (PLE) spectra detect the existence of two types of aggregates, non-emissive and emissive species. An early stage of the interchain association results in the non-emissive species. When the chain segments are forced to densely pack within the aggregates, emissive species are formed. A series of linear alcohols is used to control the properties of aggregates. The increase of polarity of alcohol results in a large fraction of emissive aggregate. The use of long chain alcohol leads to the formation of non-emissive aggregate. Therefore, the change of solvents is an important role to control the chain conformation, the aggregate of conjugated polymer and its photophysical properties.

In conjugated polymer nanoparticles (CPNs) system, the change of initial solvents also affects the aggregation within the CPNs and its photophysical properties. The CPNs of MEH-PPV and rr-P3OT are prepared by reprecipitation method. This method involves the injection of polymer solution into an excess amount of water. The water solubility of the initial solvent is a major factor dictating mechanism of the CPN formation. The CPNs exhibit different sizes and photophysical properties. The low water solubility of initial solvent provides a large size of CPNs. Their absorption and PL spectra shift to higher energy region compared to those of the isolated chain. When the solvent is miscible in water, opposite results are observed. Average size of the nanoparticles decreases and significant redshift of their absorption and PL spectra is detected. Detailed data analysis indicates that the individual chain conformation and degree of segmental aggregation within the CPNs are quite different. This leads to drastic discrepancies of their photophysical properties.

LIST OF CONTENTS

LIST OF CONTENTS (CONT.)

LIST OF CONTENTS (CONT.)

LIST OF CONTENTS (CONT.)

LIST OF TABLES

LIST OF FIGURES

LIST OF FIGURES (CONT.)

LIST OF FIGURES (CONT.)

LIST OF FIGURES (CONT.)

LIST OF FIGURES (CONT.)

LIST OF FIGURES (CONT.)

LIST OF FIGURES (CONT.)

CHAPTER I

INTRODUCTION

Conjugated polymer

Conjugated polymer is material that combines the optoelectronic properties of semiconductors with the mechanical properties and processing advantages of plastics. Conjugated polymer has a base structure of alternating single and double/triple bonds of which parent structures. The polymer structures may be the linear structures or the connecting aromatic rings. The arrangement of the π-orbital in the planar allows the π-electrons to delocalize from one position to another position within the molecule, as shown in Figure 1. The distance that electron can move along the polymer chains is called "conjugation length". The electron delocalization along the polymer backbone permits the polymer to exhibit the semiconductor and the electroluminescence properties. From these properties, the conjugated polymer can be used in organic electronic technology such as plastic solar cell (PSC) [1, 2, 3, 4, 5], organic light emitting diode (OLED) [5, 6, 7, 8, 9], and organic field-effect transistors (OFET) [10, 11, 12], as shown in Figure 2.
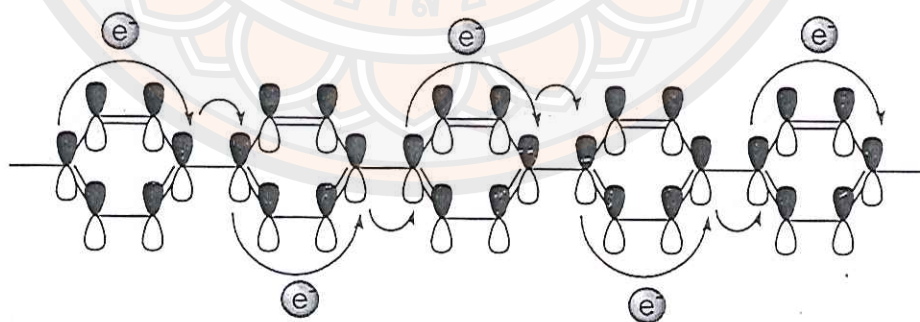
Figure 1 Conjugation of π-orbital in polymer chain

The organic electronic technology has several advantages for example the low-cost technology, lightweight and flexible plastic substrates and environment friendly. In this technology, the polymer can fabricate on the flexible plastic substrates leading to the flexible device technology. The conjugated polymer is usually used in the active layer within the devices. The fabrication of polymer thin film easy manufactures of thin film devices by vacuum evaporation/sublimation or solution cast or printing onto any suitable substrate by an inkjet printer.

The organic light emitting diode (OLED) technology is well-known as a future technology for display. In this device, the light is emitted by applying electric voltage. When the voltage is applied into the device, electrical current can flow from the cathode to the anode through the organic layer. The electron and hole are injected from electrode. After that, the hole jumps to the emissive layer and recombine with the electrons. The recombination releases their extra energy as light. The main advantages of OLED include thinner and lighter than liquid crystal display LCD display. The emission color can tune by modifying the chemical structures.

In plastic solar cell (PSC) technology, the principle of PSC is the reverse process of the OLED. In PSC technology, the conjugated polymers are used to absorb light and then convert to electricity. The PSC function is based on a transfer of electrons that is initiated by sunlight. The absorption of sunlight causes the excitation of electron in conjugated polymer which can generate the charge carrier. The charge separation between hole and electron generates electrical current. The development of plastic solar cell receives widespread interest because it has many advantages, including its flexibility, lightweight, disposable and inexpensive to fabricate.
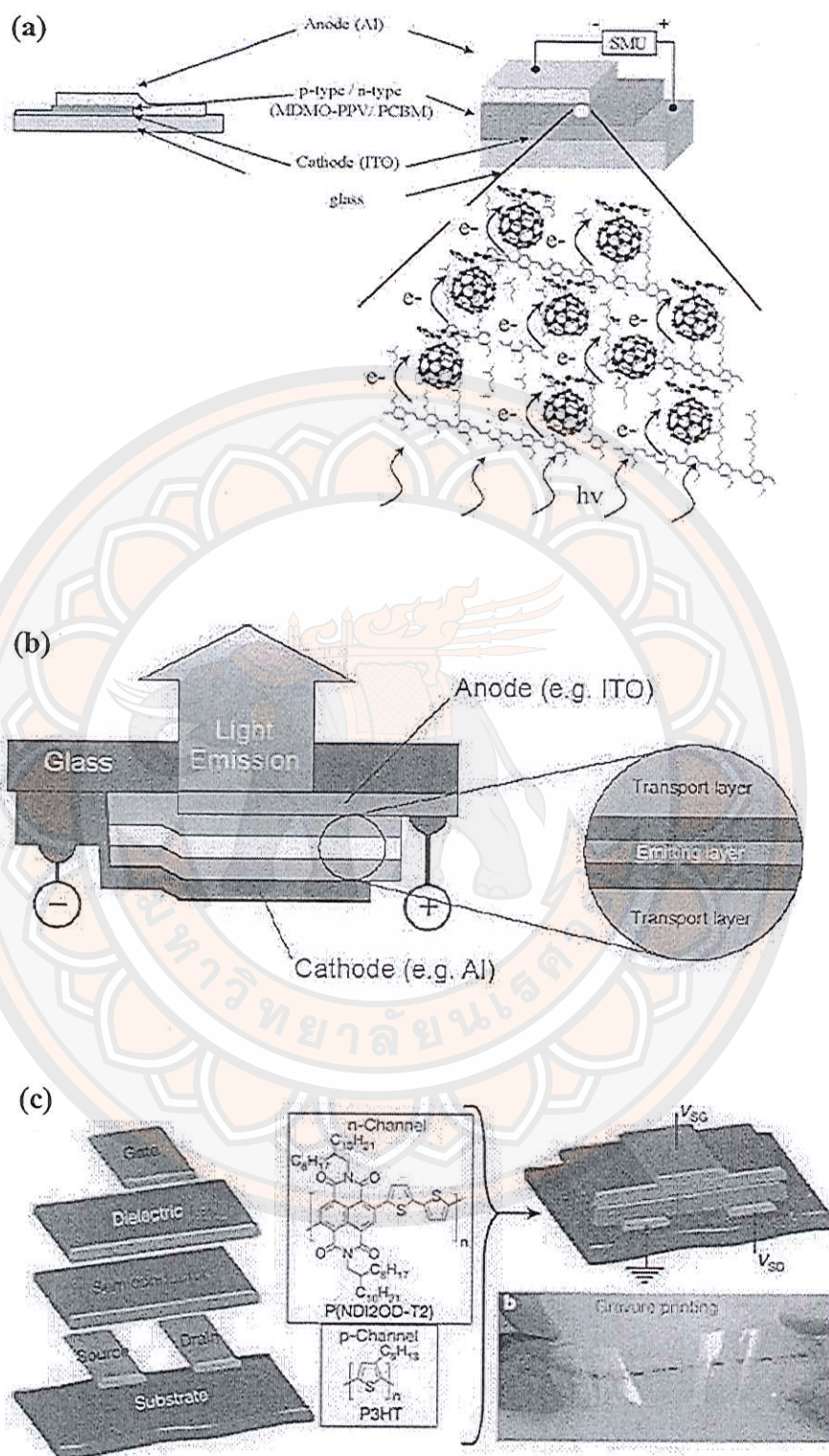
Figure 2 Applications of conjugated polymer. (a) plastic solar cell [2], (b) organic light emitting diode [9] and (c) organic field-effect transistor [12]

Figure 3 explains the concept of the conjugation length of conjugated polymer. The electrons can continually migrate along the polymer backbone which overlaps the π-orbital in the same plane. If the π-orbitals twist out of plane, the conjugation is disturbed. Therefore, the modification of the polymer planarity and the degree of π-orbital overlap, will alter energy gap (E_g) and as a sequence the relative position of the highest occupied molecular orbital (HOMO) and the lowest unoccupied molecular orbital (LUMO) levels. There are several parameters that affect the band gap involving molecular weight, bond length alternation (E_{BLA}), planarity (E_θ), aromatic resonance energy (E_{Res}), substituents (E_{sub}) and intermolecular interactions (E_{inter}) [13]. Although conjugated polymer chain shows a very long chain, maybe consisting of thousands monomers, conjugation length is very short. It may be only 7-15 units in length [14, 15]. The conjugation length also depends on the chemical structure of polymer. For example, the modifications of side chain result in the easier or more difficult of backbone twisting as shown in Figure 3b and Figure 4. The side chain engineering can tune a polymer's physical properties, including absorption, emission, energy level, molecular packing, and charge transport [16, 17, 18]. Polyphenylenevinylene (PPV) has no side chain group. The aromatic backbone can easily twist out of plane causing the conjugated perturbation, so the conjugation length is short. For poly(2,5-dimethoxyphenylene-vinylene) (DMOPPV), the methoxyl side chain can force the polymer to be more rigid structure. The conjugation length is longer than that of PPV. Moreover, the modification of side chain on polymer backbone shows different emission color. PPV molecule can emit green color, while DMOPPV molecules with methoxyl side chain can emit red color [18].
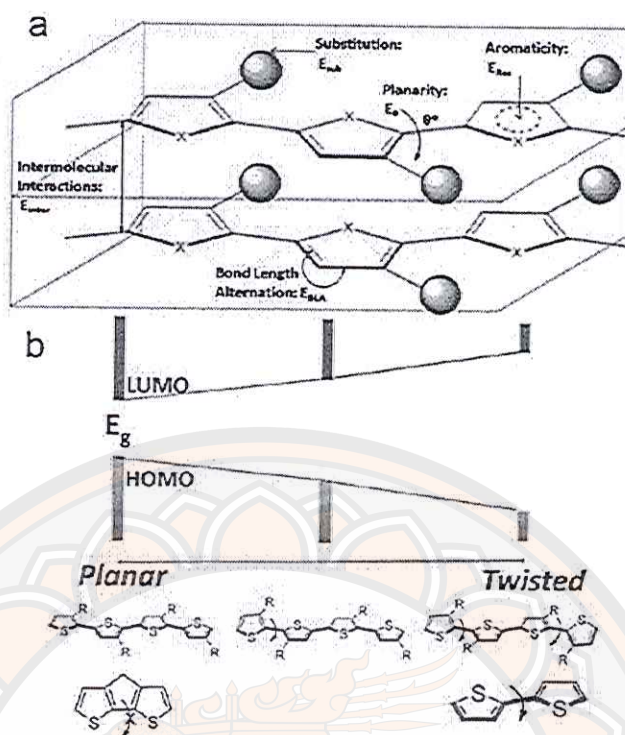
Figure 3 Structural factors affecting the band gap of π-conjugated polymers [13]
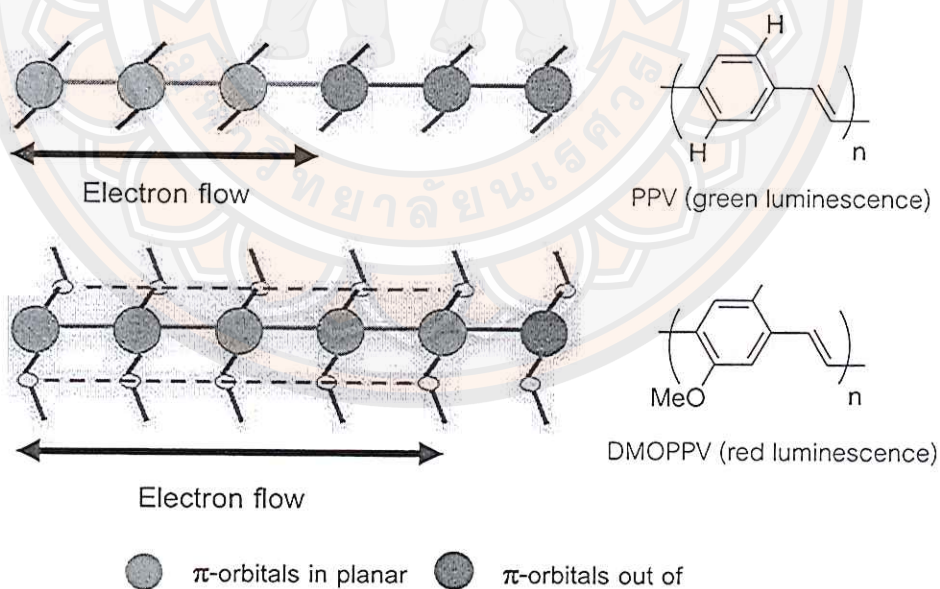
Figure 4 Influence of the side chain on electrons delocalization along the π-conjugation of polyphenylenevinylene derivatives [18]

In addition to organic electronic technology, conjugated polymers are potential materials for biotechnology such as biological fluorescence imaging [19, 20, 21, 22], biological label [23, 24] and fluorescent sensor [25, 26] as shown in Figure 5. In order to apply the polymer in these technologies, the conjugated polymer is mostly used as the nanoparticle form. Compared with other nanoparticle system such as liposomes and micelles, conjugated polymer nanoparticle possesses an increased colloidal stability, and a better chemical resistance. The formation is also usually easier [27]. In addition, the biocompatibility and non-toxicity properties make these materials highly attractive for the technology [28]. Their fluorescent properties of nanoparticle can be tuned by varying their size and composition. Figure 6 shows the molecular structures of the well-known conjugated polymers that have been widely interested in both organic electronic technology and biotechnology applications.
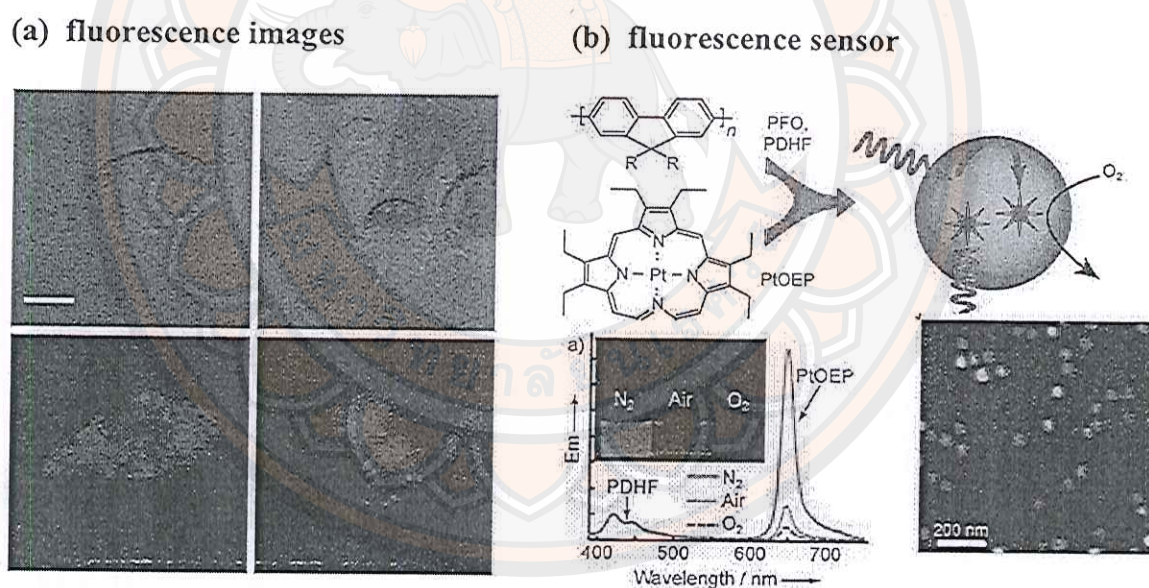
Figure 5 Applications of conjugated polymer nanoparticle. (a) differential inter-
ference contrast images and fluorescence images of macrophage cells
labeled with nanoparticle [19] and (b) Schematic illustration of the
formation of conjugated polymer dots for oxygen sensing and oxygen
dependent emission spectra of the 10% PtOEP doped PDHF dots [25]
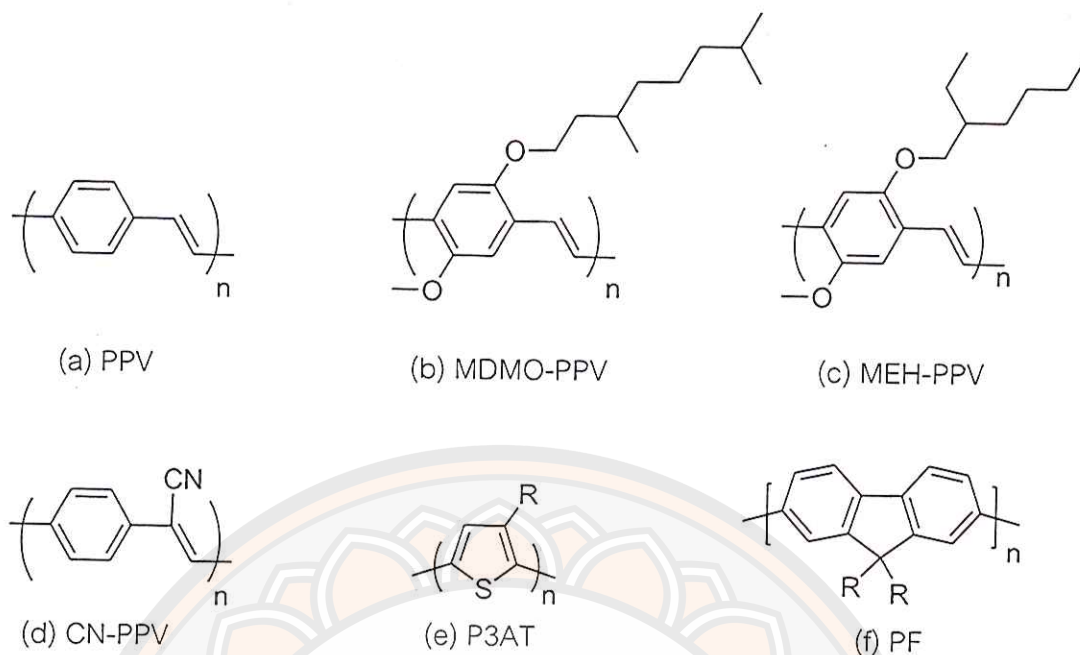
Figure 6 **The structure of typical conjugated polymers. (a) poly(*p*-phenyleneviny-**
lene) (PPV), (b) poly(2-methoxy-5-(3',7'-dimethyl-octyloxy))-*p*-pheny-
lenevinylene) (MDMO-PPV), (c) poly(2-methoxy-5-(2'-ethylhexyloxy)-
1,4-phenylvinylene) (MEH–PPV), (d) cyanopolyphenylenevinylene (CN-
PPV), (e) poly (3-alkylthiophene) (P3AT), and (f) polyfluorene (PF)

Among conjugated polymers, polyphenylenevinylene (PPV) and poly-
thiophene (PT) derivatives have been intensively studied. PPV derivatives have been
major candidates for the active layer in the electroluminescent display, while PT
derivatives are promising for plastic solar cell because of high charge carrier. Within
the class of PPV derivatives, poly[2-methoxy-5-(2'-ethylhexyloxy)-1,4-phenylene-
vinylene] (MEH-PPV) (see Figure 6) has attracted much attention because of its high
quantum yield of fluorescence with a bright orange color, resulting of a π-π transition
centered near 500 nm. The polymer is good solubility in common organic solvents.
This allows easy fabrication of devices by utilizing spin-coating process. MEH-PPV
also exhibits favorable charge injection properties in devices.

In order to apply the conjugated polymer in the application, it is necessary to
fully understand the optical and electronic properties of polymer. Moreover, we need
to optimize properties of the polymer which are appropriate for each technology. It is
well-known that the performance of optoelectronic devices is strongly influenced by

polymer morphology of the conjugated polymer layer, including the polymer chain packing, and polymer chain conformation with respect to the film morphology [29, 30, 31, 32, 33]. For example, controlling conformational disorder or conjugation length of polymer chain can profoundly affect the fluorescence quantum yield and charge transport efficiency and therefore the overall efficiency of OLED devices. To control the conformation of the polymer, study of the properties of conjugate polymer in the solution is required. Real conjugated polymer chains in solutions and films, however, do not have the ideal structure because they tend to twist and coil. Each conjugated segment is roughly planar with its extent of conjugation limited by twisting of the polymer backbone.

Conjugated polymer in solution

Polymer molecule can take many different shapes or conformations due to its degree of freedom for rotation around the σ bonds. Unperturbed chain exhibits a random chain conformation or Gaussian chain (see Figure 7). The polymer random chains are found in polymer solution, in polymer melts and in glassy amorphous polymers. The random chain can be characterized by either of the two dimensions, the average end-to-end distance (r) or the radius of gyration (s).
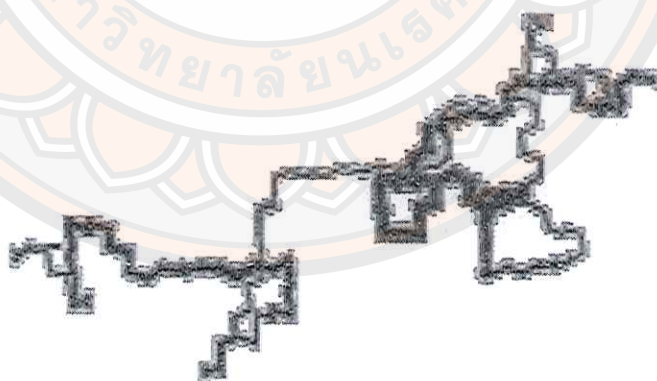
Figure 7 Gaussian chain [34]

Consider a flexible polymer chain consists of n segments (main-chain bonds), each bond have a length l. The end-to-end vector $(\overline{r})$ is the sum of the individual bond vectors according to:

$$\overline{r} = \sum_{i=1}^{n} \overline{r_i} \tag{1}$$

The average end-to-end vector of an isotropic collection of chain of n backbone atom is zero $(\overline{r} = 0)$. The simplest no-zero average is the mean-square end-to-end distance (r^2) as follows:

$$r^2 = \sum_{i=1}^{n} \overline{r_i} \sum_{j=1}^{n} \overline{r_j} = \sum_{i=1}^{n} \overline{r_i}^2 + 2 \sum_{i=1}^{n-1} \sum_{j=i+1}^{n} \overline{r_i} \overline{r_j} \tag{2}$$

The end-to-end distance is a useful parameter for describing an ideal chain for calculation of the radius of gyration and hydrodynamic radius of chains. Instead of the end-to-end distance, the radius of gyration (s) is more meaningful parameter to determine the size of the polymer coil. The value of radius of gyration can get from several experimental techniques such as static light scattering, x-ray scattering and neutron scattering.

The radius of gyration (s) is defined as the root-mean-square distance of any point in the object (polymer coil) from their common center of gravity as follow:

$$s^2 = \frac{\sum_{i=1}^{n} m_i \overline{r_i}^2}{\sum_{i=1}^{n} m_i} \tag{3}$$

where $\overline{r_i}$ is the vector from the center of gravity to atom i.

For large values of n, i.e. for polymer, the radius of gyration can be given by the relationship holds between the second moment of the mean values, as follow:

$$\langle s^2 \rangle = \frac{\langle r^2 \rangle}{6} \tag{4}$$

From equation (4), it indicates that the radius of gyration is smaller than the root mean square end-to-end distance a factor of $\sqrt{6}$.

There are several advantages to using the radius of gyration rather than the end-to-end distance. For branched, ring or star chains the end-to-end distance has no meaning while the radius of gyration retains its meaning. The radius of gyration easily measures in the scattering experiments. The radius of gyration can be defined for any object.

The size of random coil of polymer in solution can be determined by several experimental techniques. The size of the molecular coil of polymer is dependent on the solvent (see Figure 8). A good solvent expands the coil. A poor solvent, on the other hand, causes shrinkage. In between these two solvents, so-called theta solvents are found. Typical of these is that intermolecular and intramolecular interactions are similar in magnitude. In good solvent, polymer-polymer interaction is less than polymer-solvent interaction. The polymer-polymer interaction in theta solvent is equal to the polymer-solvent interaction. For poor solvent, the polymer-polymer interaction is more that polymer-solvent interaction.

Good solvent:
$\alpha > 1$

Theta solvent:
$\alpha = 1$

Poor solvent:
$\alpha < 1$
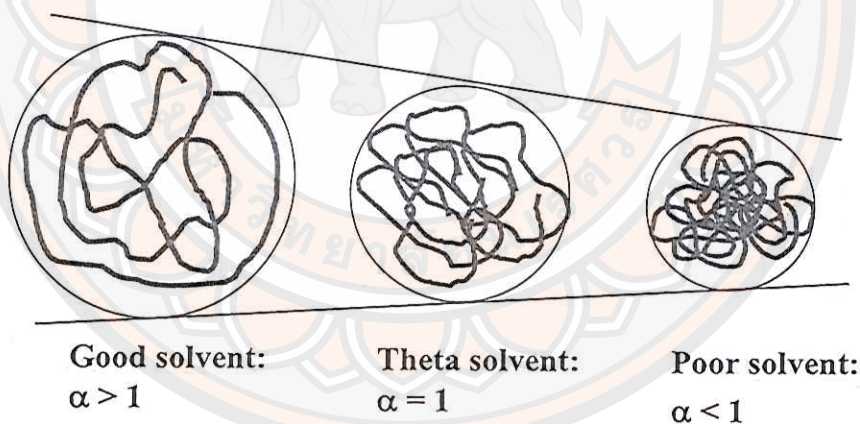
Figure 8 Polymer random coils in solvents of different power. α is the linear coil expansion factor which according to the definition is equal to 1 in the theta solvent. The picture is adapted from [34].

The unperturbed polymer chain dissolved in theta solvent adapt to the following equation:

$$\langle r^2 \rangle_0 = Cnl^2 \tag{5}$$

where the subscript signifies theta conditions, and C is a constant which depend on the nature of the polymer. In good solvent, the long-range intramolecular interaction causes the expansion of coil, which can be express by a linear factor α:

$$\langle r^2 \rangle = \alpha^2 \langle r^2 \rangle_0 \tag{6}$$

The expansion factor (α) is affected by temperature and type of solvent. It has been shown both theoretically and experimentally that α is a faction of the molar mass in good solvents:

$$\alpha^5 - \alpha^3 = C\psi\sqrt{n}\left(1 - \frac{\theta}{T}\right) \tag{7}$$

where C is a polymer-related constant, ψ is the interaction entropy and θ is the theta temperature or Flory temperature. At theta conditions (T = θ), α becomes 1, whereas in a good solvent (T > θ), α is proportional to $n^{1/10}$.

It has been known that the conjugated polymers in solution adopt the different chain conformations, depending on local polymer-solvent interaction [14, 15, 33, 34, 35]. Sumpter, et al. [14, 15] used the molecular dynamic (MD) simulation to show the MD snapshots of polymer chain in solution. In a good solvent, the polymer chains have expanded structures with longer conjugation length, as shown in Figure 9. Conversely, in a poor solvent, the polymer chains have compact structures confining in the short chain (see Figure 10) to minimize polymer-solvent interaction. Hu, et al. [35] used the Monte Carlo simulation to propose six types of polymer chain conformations interaction, including random coil, molten globule, toroid, rod, defect coil, and defect cylinder, to show how the polymer chain form to minimize polymer-solvent (see Figure 11). Moreover, the solution concentration has an effect on the structure of conjugated polymer [14, 15].
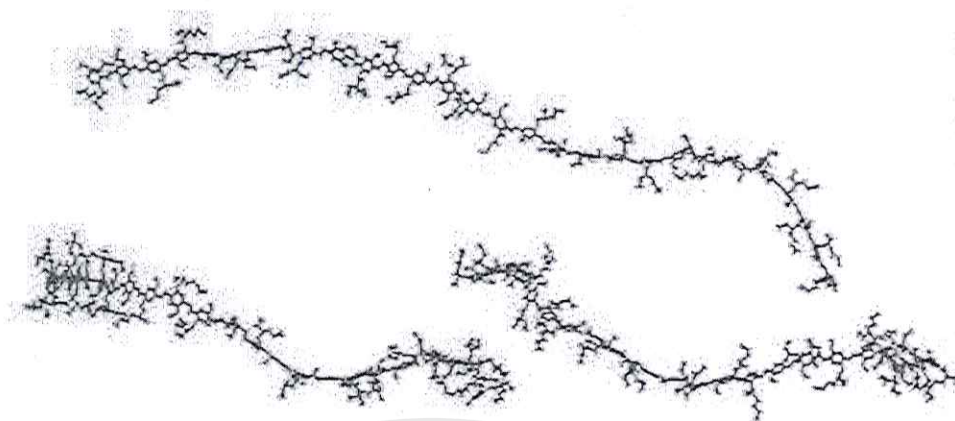
Figure 9 The different chain conformations of polymer in good solvent [14]
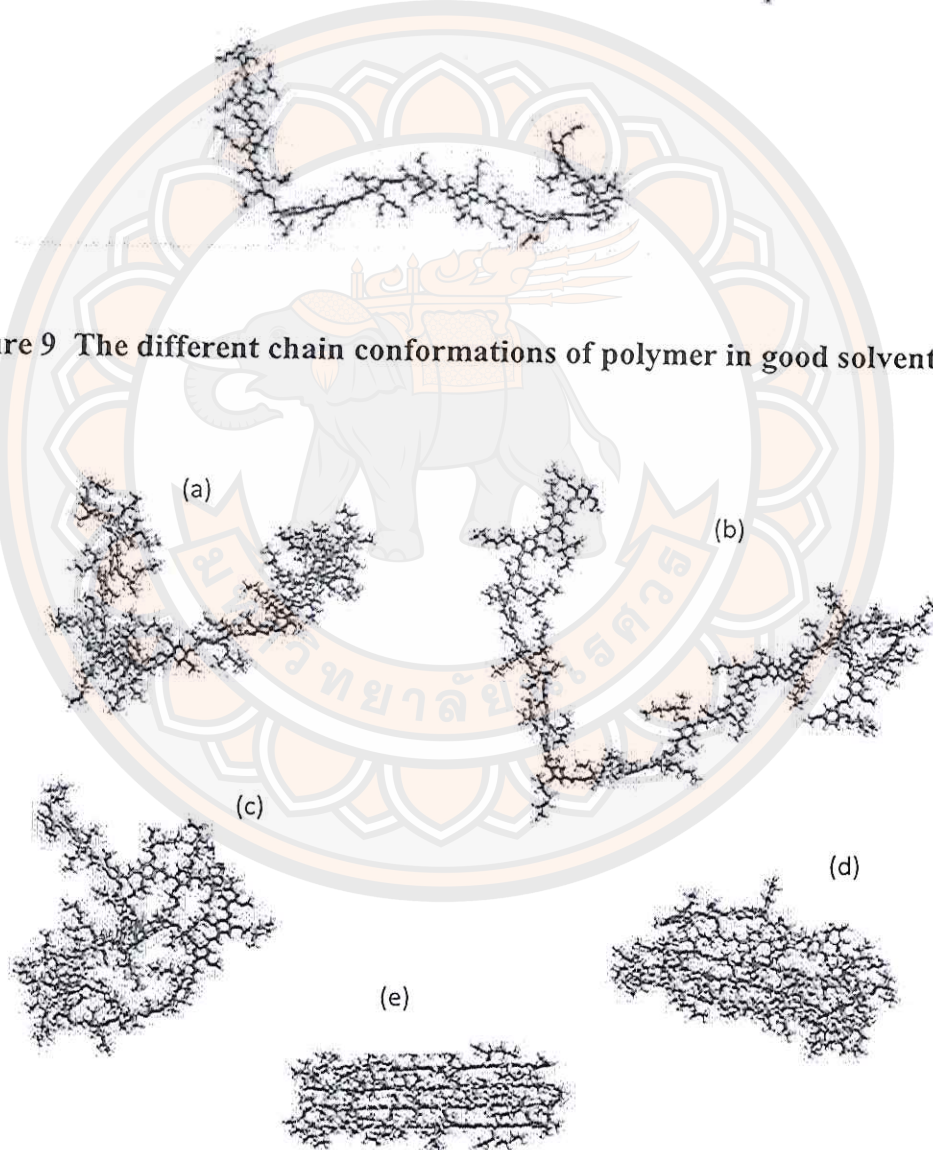
Figure 10 The progression of chain conformations of polymer when the solvent
quality is decreased. The conformations are (a,b) initial conformations,
(c,d) chain fold propagation and (d) collapsed chain in final step. [14]

Figure 11 The conformations of conjugated polymer generated by Monte Carlo
simulations. They are denoted as (I) random coil, (II) molten globule,
(III) toroid, (IV) rod, (V) defect-coil and (VI) defect-cylinder. [35]

Solubility parameter

The solubility parameter (δ) is a numerical value that indicates a relative
solvency behavior of a specific solvent [36, 37, 38]. To achieve a solubility of a
polymer in solvent, the solubility parameter of two substances should be close enough.
It is frequently found that the mixture of two components can be dissolved when
difference of solubility parameter between solute and solvent is less than 1 cal$^{1/2}$cm$^{-3/2}$.
The solubility parameter is derived from the cohesive energy density of the solvent,
which in turn is derived from the heat of vaporization. The heat of vaporization is the
energy required to vaporization the liquid. From the heat of vaporization, in unit of
calories per cubic centimeter of liquid, the cohesive energy density (c) can be derived
by the following expression

$$c = \frac{\Delta H - RT}{V_m}$$

(8)

where ΔH is the heat of vaporization, R is gas constant, T is temperature and V_m is molar volume.

The cohesive energy density can be used to indicate the degree of van der Waals force holding the molecules of the liquid together. The relation between vaporization and van der Waals force also translates into a correlation between vaporization and solubility behavior.

The square root of the cohesive energy density is known as the solubility parameter.

$$\delta = \sqrt{c} = \left(\frac{\Delta H - RT}{V_m}\right)^{1/2} \tag{9}$$

The solubility parameter in equation (9) proposed by Joel H. Hildebrand, called *Hildebrand solubility parameter*. It is usually used in term of the total solubility parameter. The solubility of two materials is possible when their intermolecular attractive forces are similar, one might also expect that materials with similar cohesive energy density values would be miscible.

Three modes of interactions between molecules are most used in solubility theory: dispersion forces, polar forces and hydrogen bonding forces. The dispersion force or London force arise from the fluctuating atomic dipole which results from a positive nucleus and an electron cloud. The polar force can be divided into dipole-dipole and dipole-induced dipole interactions which results from nonuniform charge distribution. The hydrogen bonding is specific interaction where a hydrogen atom is attached to an extremely electron-hungry atom such as oxygen, nitrogen or fluorine.

The concept of Hildebrand parameter is used for only one or two of these forces (i.e. Hildebrand value and hydrogen bonding value). The development of Hildebrand parameter can be applied into all three forces or derivatives of them.

Charles Hansen proposed the concept of the three component solubility parameter, which is the most widely accepted as *Hansen solubility parameter*. This solubility parameter divides the total Hildebrand parameter into three parts including dispersion force component, polar component and hydrogen bonding component. Therefore, the total solubility can be express as follow:

$$\delta_t^2 = \delta_d^2 + \delta_p^2 + \delta_h^2 \tag{10}$$

where δ_t^2 is total Hildebrand parameter, δ_d^2 is dispersion component, δ_p^2 is polar component and δ_h^2 is hydrogen bonding component.

The three-dimensional model is used to plot polymer solubility. If the δ_d scale is expand by a factor of 2, a spherical solubility volume for a solute may be formed. This volume can be described in Figure 12. The coordinates at the center of the solubility sphere are located by means of three component parameters (δ_d, δ_p, δ_h). The radius of the sphere is the interaction radius (R).
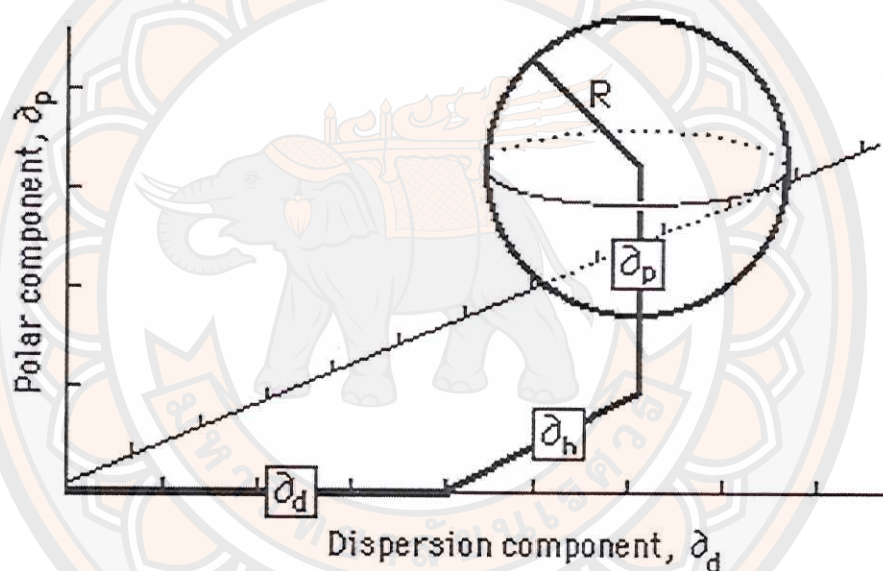
Figure 12 The schematic of the Hansen volume of solubility [37]

Hansen's three dimensional volumes can be presented in two dimensions by plotting a cross-section through the center of the solubility sphere by using only two of the three parameters. The most commonly used parameters are δ_p and δ_h as the X and Y axis, respectively. Figures 13 illustrate this approach by plotting the volumes of solubility of polymethyl methacrylate (small circle) and polyethyl methacrylate (large circle). The circles are generated by the radius of interaction for each polymer. The symbols indicate the respective locations of solvents. A small circle at the center indicates the center of solubility spheres. Liquids outside the solubility area of polymer are nonsolvents. The graph indicates that polymethyl methacrylate will

tolerate a greater proportion of ethanol than that of polyethyl methacrylate. Accordingly, polymethyl methacrylate should be soluble in toluene/acetone 3:1 but not in 100% toluene.
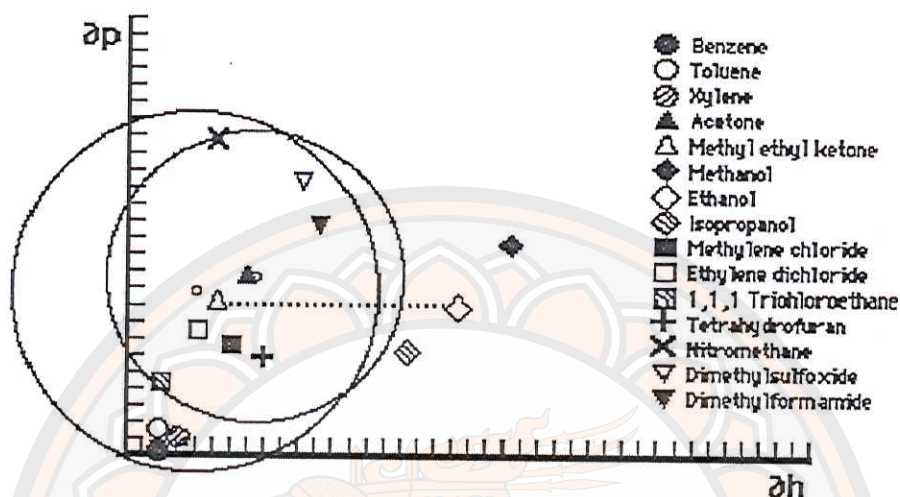
Figure 13 Hansen graph of solubility areas for polymethyl methacrylate (smaller circle) and polyethyl methacrylate (larger circle) [37]

Hansen parameters are reasonably accurate in predicting solubility behavior because the precise values for all three components parameter are used. Hansen graphs are easy to use because solvent positions are constant and polymer solubility areas may be drawn with a compass. The accuracy of predicting solubility behavior is about 90%, with solvent locations nearest the edge of a solubility area being the least predictable. This is due to the three-dimensional nature of the actual solubility sphere. When reduced to two dimensions, solvents that appear near the edge inside the solubility area may in fact be outside it, in front or behind, in three dimensions.

Units of measurement

Since the solubility parameter is derived from cohesive energy density, the unit usually present in energy unit, calories/cc. The SI unit is used for the convenience. The SI unit present in mega Pascal, MPa. However, the most appropriate and convenient unit for the solubility parameter is the $MPa^{1/2}$, which is numerically to the $J^{1/2}cm^{-3/2}$. The solubility parameter units and their conversion factors are shown in Table 1.

Table 1 Solubility parameter units and conversion factors [36]

	$cal^{1/2}\ cm^{-3/2}$	$J^{1/2}\ cm^{-3/2} = MPa^{1/2}$	$atm^{1/2}$
1 $cal^{1/2}\ cm^{-3/2}$	1	2.0455	6.4260
1 $J^{1/2}\ cm^{-3/2} = 1\ MPa^{1/2}$	0.48888	1	3.1415
$atm^{1/2}$	0.15562	0.31832	1

The solubility parameter of polymer can be determined by several methods i.e. swelling experiment, solvent-nonsolvent titration, inverse gas chromatography, calculate from chemical structure data of the polymer. Neher, et al. [39] used the solvent-nonsolvent titration method for determining the solubility parameter of poly(3-alkylthiophene)s. They used the equation that proposed by Suh and Clarke in 1967 for calculating the solubility parameter of the polymer as followed:

$$\delta_p = \frac{\sqrt{V_{12}}\delta_{12} + \sqrt{V_{13}}\delta_{13}}{\sqrt{V_{12}} + \sqrt{V_{13}}} \tag{11}$$

Where

$$V_{1i} = \frac{V_1 V_i}{\emptyset_1 V_i + \emptyset_i V_1} ; i = 2,3 \tag{12}$$

$$\delta_{1i} = \emptyset_1 \delta_1 + \emptyset_i \delta_i ; i = 2,3 \tag{13}$$

with

$$\emptyset_i = 1 - \emptyset_1 = \frac{v_i}{v_1 + v_i} ; i = 2,3 \tag{14}$$

In this case, δ_p is the solubility parameter of polymer, V_i is the molar volume, ϕ_i is the volume fraction, and v_i is the volume of the nonsolvent that is added to the polymer solution to induce polymer aggregation. The subscript 1 refers to the solvent and subscripts 2 and 3 refer to the nonsolvent with the lower and higher solubility parameter, respectively. By using this method, they found that solubility parameter of rr-P3OT is 8.9 ± 0.02 $cal^{1/2}cm^{3/2}$.

Poly(3-alkylthiophene)

Poly(3-alkylthiophene)s (P3ATs) is one class of conjugated polymer that receives tremendous attention. Polythiophenes are an important representative class of conjugated polymers that form some of the most environmentally and thermally stable materials and well-ordered semicrystalline structure. The close packing of conjugated backbone in their crystalline domains allows the overlap of π-orbitals, promoting charge carrier mobility [40, 41, 42, 43]. This characteristic is particularly important for plastic solar cell application where high degree of charge separation upon photoirradiation is desired [3, 4, 5, 43, 44]. The addition of the alkyl side chains enhances its solubility in various organic solvents [17, 40, 41, 43]. This is desirable for fabrication P3AT thin film in active layer of devices via wet processes such as spin coating and dip coating.

In polythiophene, there are three relative orientations available when two thiophenes are coupled between the 2- and 5-positions. The first of these is 2,5' or head-to-tail (HT) coupling, the second is 2,2' or head-to-head (HH) coupling and the third is 5,5' or tail-to-tail (TT) coupling [40, 41] (see Figure 14). All of the above methods afford products with three possible regiochemical coupling: HH, TT, and HT. This leads to a mixture of regioisomers when 3-substituted thiophenes are introduced. The substituted polythiophene with most of unfavorable HH and/or TT are denoted as regiorandom (*rra-*) or regioirregular polythiophene. The regiorandom consist of only 50-80% head-to-tail (HT) couplings. This causes a sterically driven twist of thiophene rings resulting in a loss of conjugation. On the other hand, introduction of head-to-tail (HT) poly(3-sub-stituted)thiophene is defined as regioregular (*rr-*) polythiophene. This structure easily accesses a low energy planar conformation, leading to highly conjugation. Steric twisting of backbones leads to destruction of high conductivity and other desirable properties [40, 41, 45, 46, 47, 48].
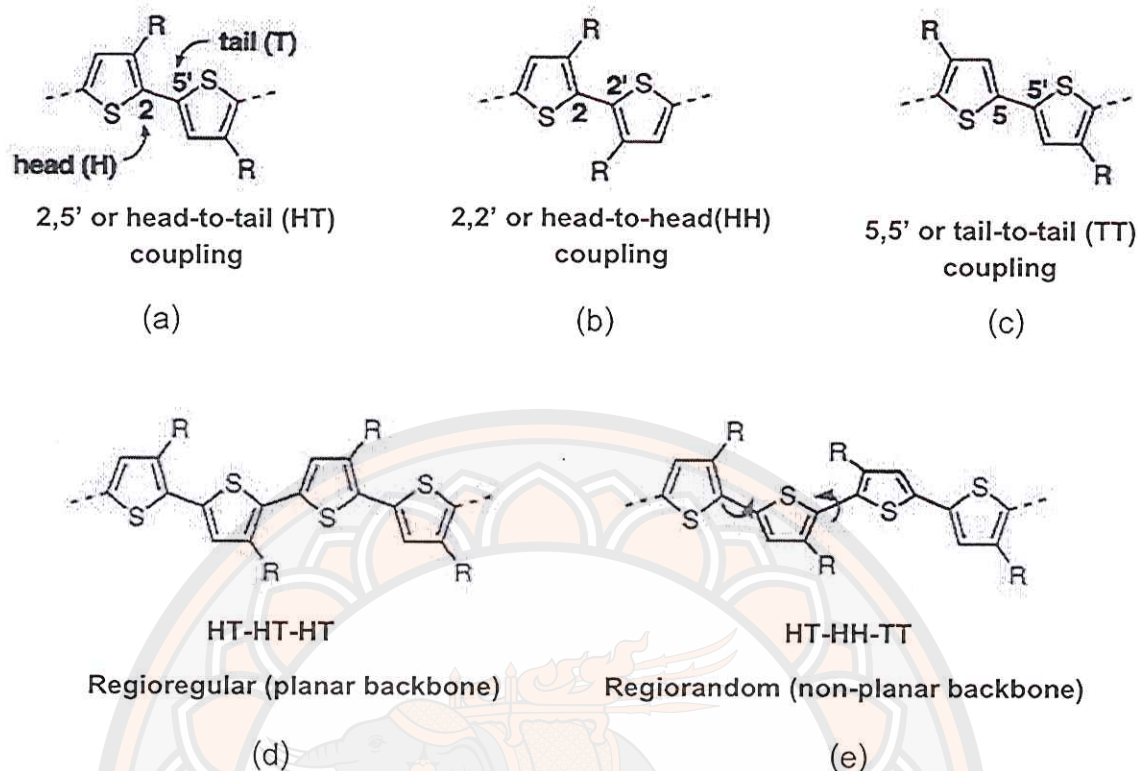
Figure 14 (a)-(c) Regioisomeric couplings of 3-alkylthiophenes, (d) and (e) regio-
regular and regiorandom [41]

The experimental data of the P3AT in solution are shown in Figure 15. The absorption spectra show absorption peak at about 454 nm for regioregular poly(3-hexylthiophene) (rr-P3HT) and blue shifted with a peak at 430 nm for regiorandom poly(3-hexylthiophene) (rra-P3HT). The photoluminescence (PL) spectra show that the emission peaks of rr-P3HT and rra-P3HT occur at 577 and 572 nm, respectively. The blue-shift of regiorandom polymers was attributed the twisting of polymer chains lead to the decrease of the effective conjugation length that causes the increase of HOMO-LUMO energy gap. In addition, the variation of thiophene backbone, such as molecular weight controls the variable degree of planarization which influences the π-electron delocalization along polymer backbones limited by the torsional disorder [49, 50, 51]. Increasing the torsion angles between thiophene rings leads to greater energy band gap, with consequent destruction of high conductivity and other desirable properties [52, 53, 54]. An alkyl side chain attaching to each thiophene unit also exerts its influence on carrier mobility through tuning the steric hindrance effect or rotational

angles. The additions of alkyl side chains with head-to-tail coupling have no steric hindrance between alkyl chains, results the longer effective conjugation length that provides the better electronic and optical properties. The alkyl side chain also enhances its solubility in various organic solvents [17, 40, 41, 55].
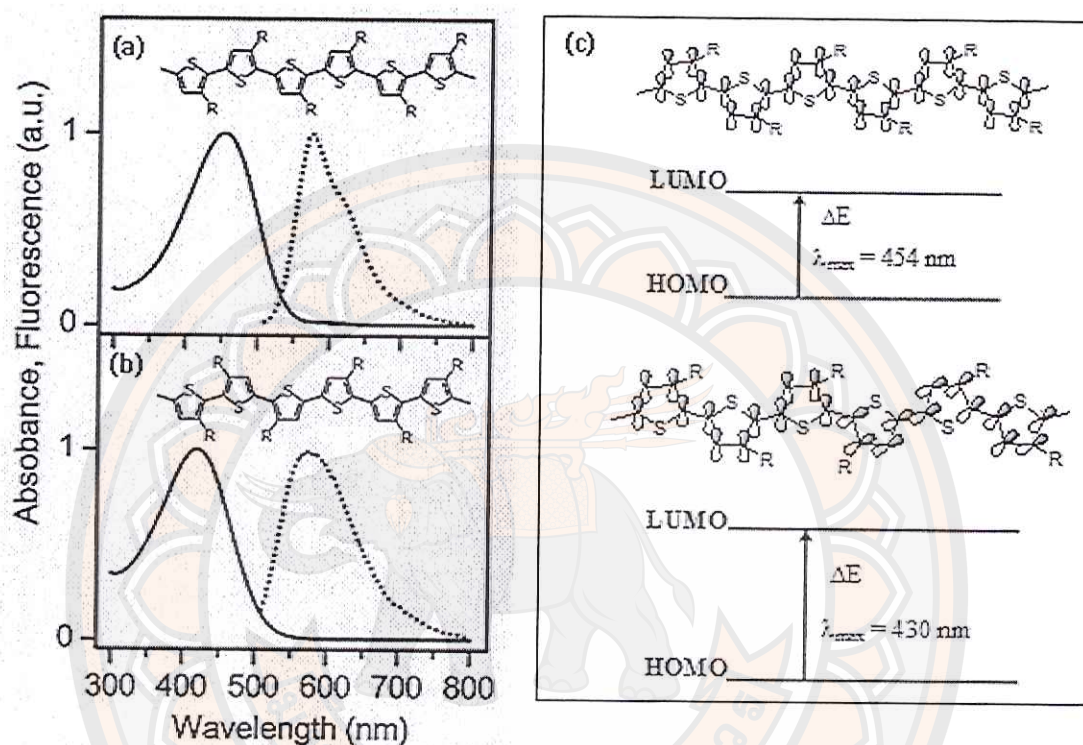
Figure 15 Absorption (solid) and PL (dotted) spectra of (a) regioregular (*rr*) (97% HT-HT) and (b) regiorandom (*rra*) (64% HT-HT) P3HT in chloroform. (c) Representative of electronic transition of *rr*-P3AT (top) and *rra*-P3AT (bottom). Spectra are adapted from [46].

Studying the basic factors affecting the optical properties of the conjugated polymer is not only important in the creation of new knowledge, but also important benefits to the application. Therefore, in this research, we want to investigate the photophysical properties of conjugated polymers in different states to provide more basic knowledge for the future application. The main techniques used to measure the photophysical data are UV-vis absorption and photoluminescence (PL) spectroscopy. In this work, we study the photophysical properties of conjugated polymers in different environments, including polymer solution and nanoparticle dispersion.

In addition, study of polymer thin films is used to detect the different in chain organization of conjugated polymer. Conformation change of isolated chain *rr*-P3OT is induced by adding cyclohexane, good solvent for side chain but poor solvent for thiophene backbone. The twist of thiophene backbone to minimize the unfavorable interaction between polymer backbone and solvent leads to the coil conformation. The photophysical properties show the blue-shift of the spectra and the quantum yield is decreased. The aggregate of conjugated polymer is induced by using poor solvent which is nonsolvent for all parts of polymer. Two types of aggregates are observed in the system. The non-emissive aggregate type occurs in the early state. Then, the emissive aggregate type can be found by adding more amount of poor solvent. The change of polarity of poor solvent can control the properties of aggregate. Decrease of polarity of poor solvent by using long chain alcohol as a poor solvent provide the formation of non-emissive in the system. The properties of conjugated polymer nanoparticle can be controlled by changing the initial solvents of polymer solution. The solvent which is miscible in water show the nanoparticle with small size and redshift of their absorption and PL spectra. On the other hand, the low water solubility of initial solvent provides a large size of nanoparticles. Their absorption and PL spectra shift to higher energy region compared to those of the isolated chain. Therefore, the study indicates that the type of solvents is an important factor, affecting the chain conformation and aggregation in the system. A careful choice of the solvent can control the aggregate segment with desired the photophysical, which is suitable for particular application.

CHAPTER II

LITERATURE REVIEWS

Single chain conjugated polymer in solution

The study of conjugated polymer in solution is very important issue because the chain conformation of polymer in solution has an influence on the photophysical and electronic properties of conjugated polymer. Studies have shown that the initial chain conformation of polymer in solution play an important role on the aggregation behavior of the polymer in solution and the structure in film and subsequent properties of devices [14, 15, 33, 56, 57]. The polymer in solution adopts different chain conformations depending on polymer-solvent interaction. In good solvent, polymer-polymer interaction is less than polymer-solvent interaction. The polymer-polymer interaction in theta solvent is equal to the polymer-solvent interaction. For poor solvent, the polymer-polymer interaction is more that polymer-solvent interaction. The various chain conformations of polymer solution show in Figure 9, 10 and 11. The variations of polymer conformation result in different optical and electrical properties of polymer which are based on the π-π communication of the intrachain and interchain and the conjugation length of polymers. Therefore, the study of photophysical properties of isolated chain polymer in solutions is useful to understand the optical and electronic properties of the conjugated polymer. In addition, the study of polymer in solution system is easy to control the conformation of polymer and to control subsequent properties of films. The quantitative fluorescent quantum yield is straightforwardly measured.

Study of conformation change of polymer in solution has been explored by several experimental techniques. Light scattering is the most commonly used methods for determining the polymer random coil size. The scattering of light is caused by the difference in refractive index between solvent and polymer. The particle coil size information is determined by the intensity characteristics of the scattering pattern at various angles. By using dynamic light scattering, the particle size is determined by correlating variations in light intensity to the Brownian movement of the particle [34].

Small-angle neutron scattering (SANS) can be also use to investigate the arrangements of polymer in concentrated solution and in the solid state. In this method, the conformation structure obtained of polymer in solution i.e. end-to-end distance or radius of gyration is determined by deuterium labeling [34, 58, 59]. Nguyen, et al. [56] used dynamic light scattering experiments to determine the polymer conformation of MEH-PPV conjugated polymer. The measurement of diffusion coefficient of the individual polymer chain and the Stokes-Einstein relation provide the size distribution (hydrodynamic radius, R_H) of the polymer chains from light scattering data. The R_H of MEH-PPV in different solvents, chlorobenzene (CRB) and tetrahydrofuran (THF) is 21.5 nm and 12.5 nm, respectively. The absorption of polymer in CRB is more red-shift than that of in THF. The shift can be explained by the extended chain of polymer in CRB allowing the longer conjugation length. In the system of THF, on the other hand, the polymer is expected to coil to minimize the interaction between polymer and solvent. Kumar, et al. [15] also examined the effect of solvent on the structure of MEH-PPV conjugated polymer. They demonstrated that the final structure of chain progression of polymer when decreasing solvent quality depend on the initial solvents. The interchain distance of MEH-PPV final structure is 4 Å in THF, 4.1 Å in dichloromethane and 3.4 Å in toluene.

For poly(3-alkylthiophene) derivatives (P3ATs), studies have shown that the regioregularity in P3ATs can control their optical properties, conductivity, and physical properties such as solid-state packing mode. The simulation of conformation of polythiophene with different regioregularity has been shown that the regioregular chain exhibits the well-aligned folded structures due to the packing of alkyl side-chains. In contrast, the regiorandom chain forms a similar folded hairpin structure, due to the steric interactions between the randomly located side-chain units. The backbone of regiorandom is twisted and is unable to form structures with the level of ordering [46] (see Figure 16). These results demonstrate that regioregularity govern the morphology of P3HT, even at the single chain level. Single molecule spectroscopy has shown that the chromophores in *rra*-P3AT are more disordered than *rr*-P3AT. This suggests that the polymer chain conformation may be more flexible for regiorandom P3AT. In addition, the alkyl side chain play importance role on the single P3AT conformation. If the percentage of regioregularity decreases, side-chain interactions

perturb polymer chain conformations, resulting in the wider distribution of chain conformations [46, 47, 48].

(a)

(b)
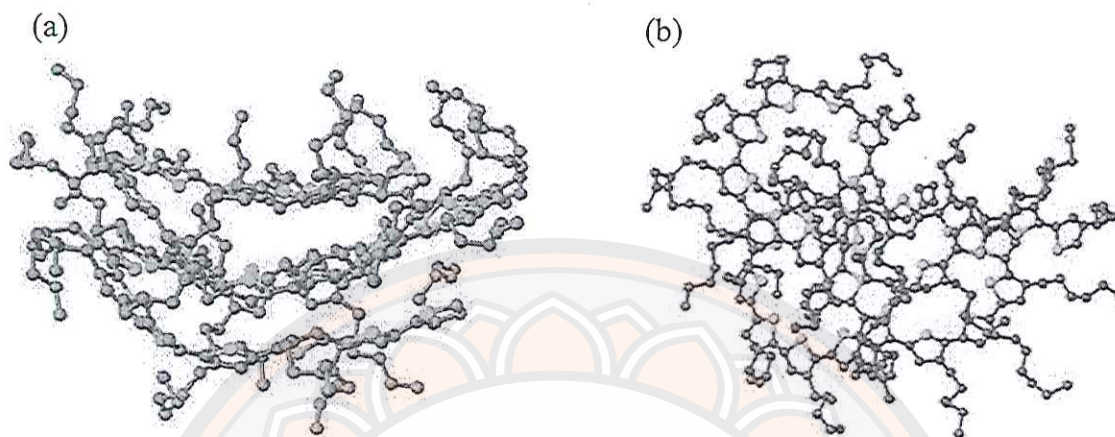
Figure 16 (a) Side view of *rr*-P3HT chain conformation and (b) top view of *rra*-P3HT chain conformation. [46]

Shibaev, et al. [53] studied effect of alkyl side chain with short propyl and long hexadecyl substituents. The observed conformational changes of PT molecules in good solvent are not completely rigid. They prefer to stay in coiled conformation. The rigidity of the molecule increases by increasing the length of the alkyl chains attached to the backbone. The end-to-end distances are achieved at 40 Å and 80 Å for stretched structure at initial state for propyl and hexadecyl substituents, respectively. Figure 17 illustrates the stable conformers of the single polypropyl-3-thiophene and polyhexadecyl-16-thiophene molecule in poor solvent.
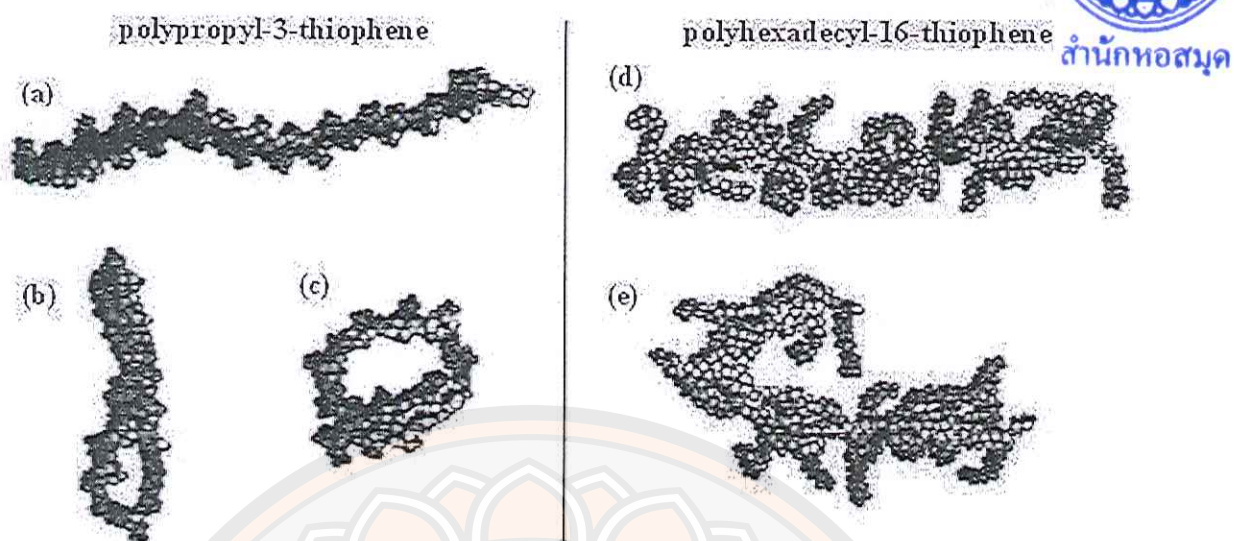
Figure 17 The chain conformations of polypropyl-3-thiophene and polyhexa-decyl-16-thiophene in a poor solvent. The conformations are (a,d) stretch chain, (b) folded structure, (c) ring structure and (e) bended structure. [53]

Small angle neutron scattering (SANS) study can be used to investigate the chain conformation change of conjugated polymer in solution as well. SANS study of polythiophene derivatives with the different alkyl side chains in solutions indicated that the polymer chain adopt a random coil chain with a semiflexible backbone [58, 59]. The first study into the chain shape of P3AT by using SANS was carried out by Aim, et al. [58]. The found that the persistence length of poly(3-butylthiophene) in nitrobenzene was around 5.5 nm. Recently, McCulloch, et al. [59] have reported that persistence length of rr-P3AT is about 3 nm at room temperature and decrease at higher temperature. The polymer adopts random coil geometry by fitting with the wormlike chain model. The model represents the persistence length of conjugated polymer shown in Figure 18.
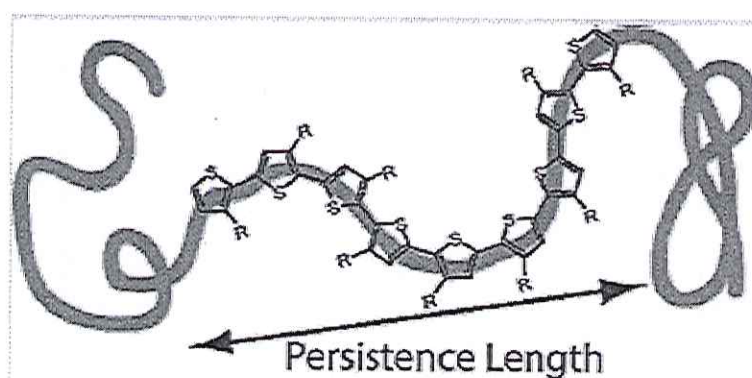
Figure 18 The persistence length of conjugated polymer polythiophene [59]

The change of polymer chain conformations alters the photophysical properties of polymer. Generally, the optical properties of MEH-PPV in good solvent exhibits the absorption peak at about 500 nm and emission peak at about 560 nm, respectively. Nguyen, et al. [58] has observed the red shift of absorption and PL spectra of MEH-PPV in CB when compared to in THF. The red shifts can be explained by the increase of conjugation length of the polymer chain. The change of local solvent environment also affects the fluorescent quantum yield. The luminescence efficiency of MEH-PPV is 0.39 ± 0.01 in CRB and 0.27 ± 0.01 in THF. Traiphol, et al. [60] also reported that the polymer conformation is a dominant factor in controlling the photophysical change. They suggested that the solvent quality can affect the conformation of polymer chain. The quality of solvent was sensitive to three parameters including polarity, aromaticity and structure of solvents. The results obtained from toluene, pyridine, and chloroform do not show the relationship between the polarity. It is dominated by the structure of solvent. The polarity of hexane, cyclohexane, and toluene are similar, but the optical properties of MEH-PPV solution are very different. This is due to the influence of aromaticity of solvent. Moreover, they varied a series of linear alcohol. This allowed solvent polarity to gradually increase with decreasing alkyl length. The results showed the red-shifted peak in absorption and PL spectra with increasing the length of alcohol. The absorption spectra of MEH-PPV in various solvents are shown in Figure 19. Photoluminescence properties are consistent with absorption spectra.

The measurement of photoluminescence excitation (PLE) and photo-luminescence emission (PL) spectra at different emission and excitation wavelengths polymer provide more details about the multiple chromophores within single chain polymer [60, 61]. The independent pattern of PL and PLE spectra detected at different excitation and emission wavelength of MEH-PPV in toluene indicate the presence of only one type of emitter in the conjugated chains although the conjugated polymer consists of multiple emitters (see Figure 20a). This implies that the shorter conjugation length can transfer energy to the neighboring longer conjugated segments before it emits the light (see Figure 21b). In cyclohexane system, on the other hand, the PL spectra show different patterns varying with the excitation wavelength (see Figure 20b). The PLE profiles also show different patterns. This confirms that nature of the conjugated chain consists of multiple emitters with various conjugation lengths. The energy transfer of conjugated polymer in cyclohexane is more difficult than that in toluene system. The observation is consistent with study by Barbara's group [47, 62, 63, 64] and Chen, et al. [48]. They presented clear evidence for the multiple chromophores in the single molecule of polymer by utilizing low-temperature single molecule fluorescent spectroscopy. Two types of low-temperature spectra are observed. Single-chromophore type fluorescence and multi-chromophore type fluorescence show in the spectra b and c in Figure 21a, respectively. Figure 21b show the energy transfer of emitter in polymer chain. The shorter chromophore with higher energy (blue color) can transfer energy to the neighboring longer chromophore with lower energy (red color). The lower energy species consequently emits the light.
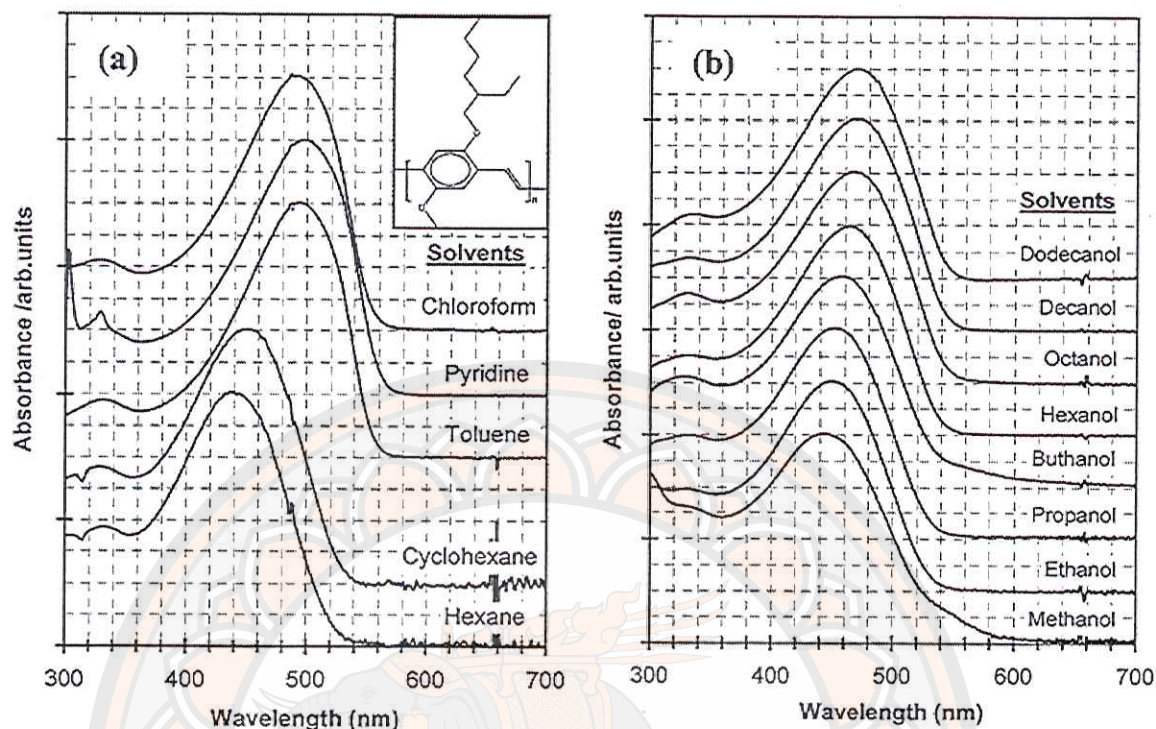
Figure 19 Absorption spectra of MEH-PPV in various solvents shown on the right side of each spectrum [60]
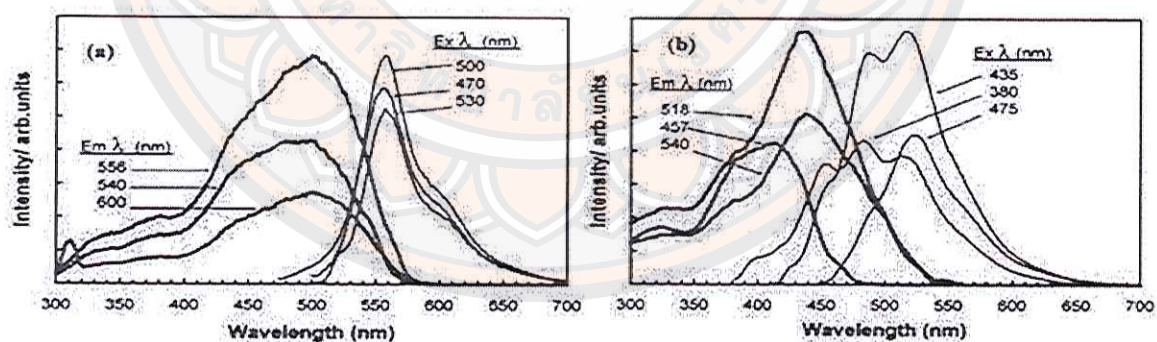
Figure 20 PLE spectra (bold lines) and PL spectra (thin lines) of MEH-PPV in (a) toluene and (b) cyclohexane measured at different emission wavelengths (Emλ) and excitation wavelengths (Exλ), respectively. [60]
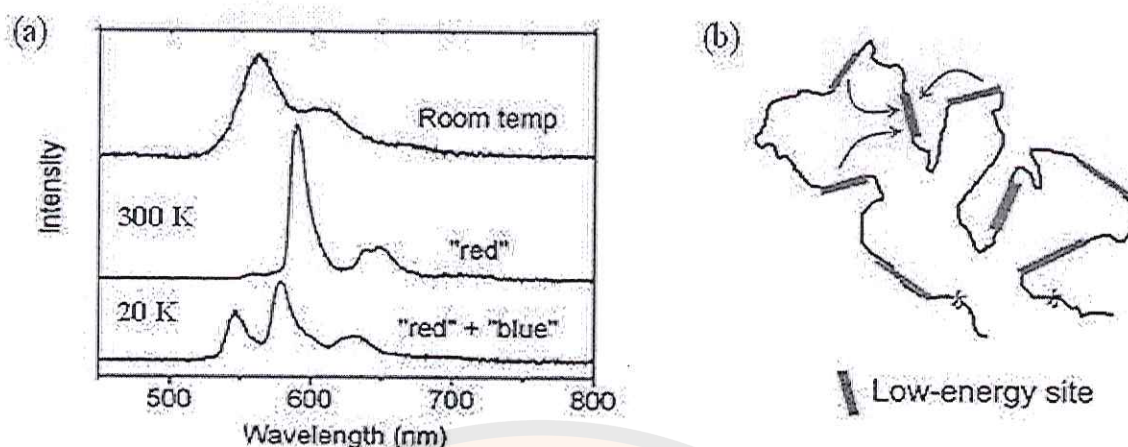
Figure 21 (a) Single molecule spectra of MEH-PPV in an inert polymer film measured at room temperature, 300 K and 20 K and (b) representation of energy transfers of emitter in polymer chain [63]

Photophysical properties of aggregated conjugated polymer in solution

The molecular structure of the conjugated polymer comprises a lot of π-bonds which results in strong attraction between polymer chains, the so called "π-π interaction". The π-π interaction between polymer backbones is the major driving force for the assembling. When the polymer chains are in close proximity, the local π-π interaction enables the formation of interchain species known as aggregates. The aggregate of conjugated polymer is defined by stacking of conjugated segments on the top of each other. The aggregate allows the delocalization of π-electrons over multiple segments. The extent of π-electron delocalization is significant enough to form novel electronic species exhibiting lower HOMO-LUMO energy gap relative to that of an isolated chain. The aggregation has been known to cause a red-shift peak in absorption and emission spectra (see Figure 22) and decrease of the quantum yield. Theoretical studies suggest that interchain distance of the stacked chain required for altering the electronic properties of the individual chains is about 3.5-4 Å [14, 15, 29, 65, 66].
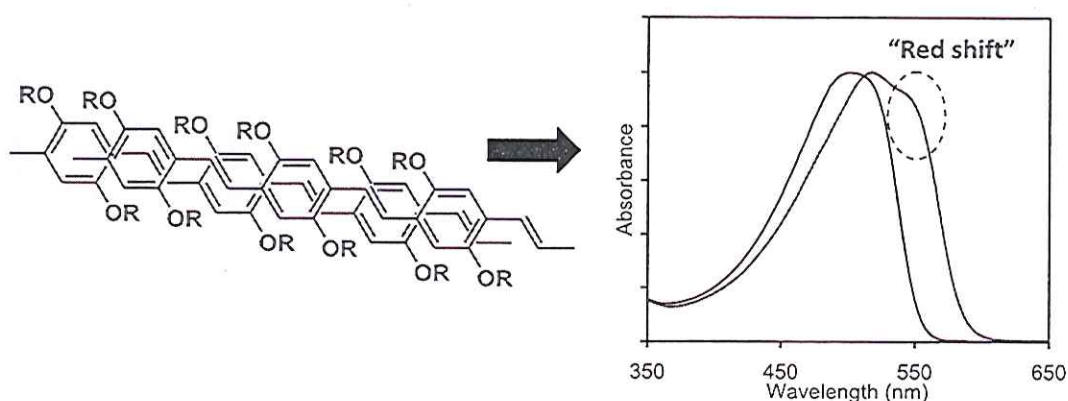
Figure 22 Model of aggregated segments and red-shifted peak in absorption spectra of aggregated segments

The aggregate behavior of conjugated polymer is importance issue that needs to be considered when applying the polymer in device applications. When the polymer chains form the aggregate, the emission efficiency is decreased. This is the problem for OLED technology. However, controlling the crystallite within the aggregate can improve the charge transport properties [5, 7, 43, 67]. This phenomenon is desirable for their utilization in plastic solar cell. Therefore, the careful control of the amount of aggregates as well as an optimized chain conformation can improve the performance of polymer devices (see Figure 23).

The aggregation can be promoted in solvents. Aggregate fractions increase with increasing polymer concentration. In addition, polymer aggregation in solution can be achieved by adding a poor solvent into a solution of polymer in good solvents. The decrease of solvent quality and the π-π interaction between neighboring conjugated polymers is major parameter that leads to the binding of polymer chains into assembled particles. There are many ways that conjugated polymer chromophores can interact together (see Figure 24). Aggregate is one type of assembled chain when the segments of the conjugated chain stack efficiently. This results in a red-shift of the spectra. The emission intensity is also reduced. Other types of interchain association where chromophores do not interact electronically are called agglomeration. Moreover, some of polymer chains can collapse, which results in a blue shift of spectra. Therefore, the degree of aggregation depends on both the choice of solvent and the polymer concentration.
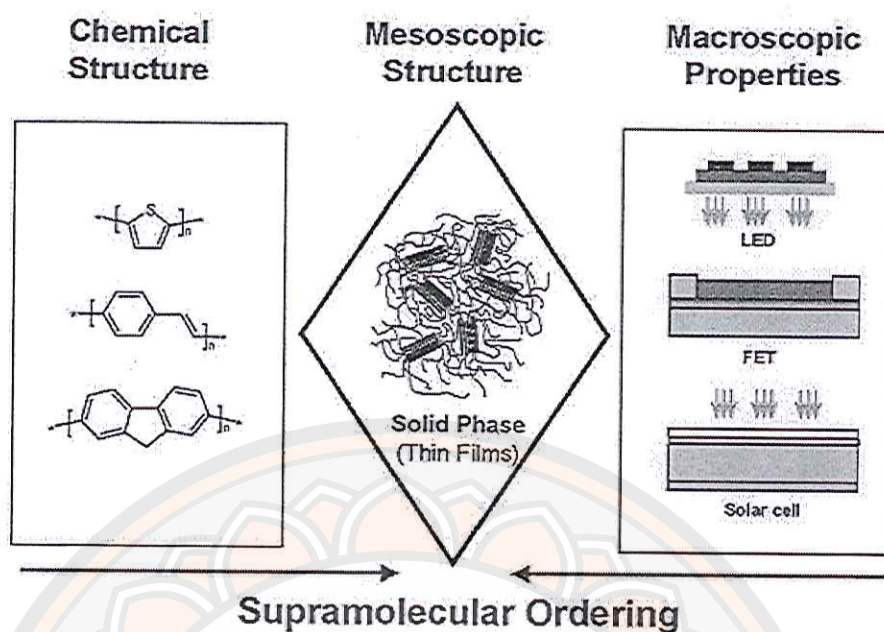
Figure 23 Schematic representations on how the properties of organic devices are related to chemical structure and supramolecular organization. [43]
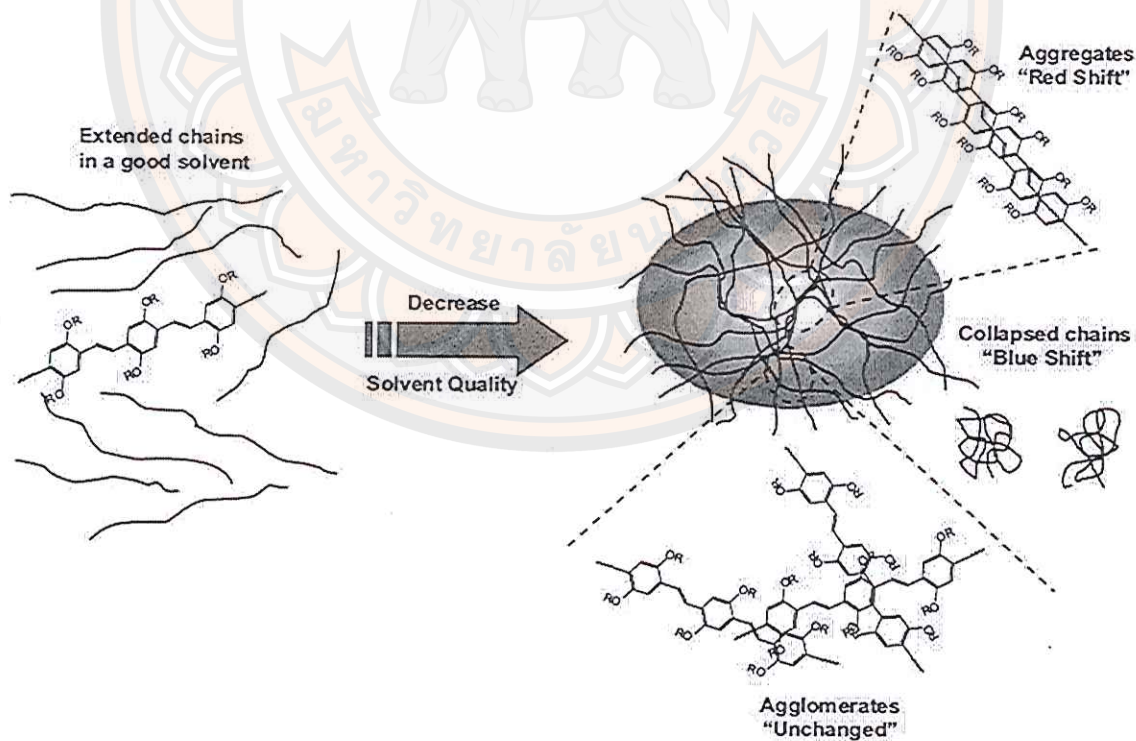
Figure 24 Schematic representations of the association and the collapse of isolated chains in poor solvents [61]

The most two common ways to produce the aggregated polymer are the mixed-solvent method and the whisker method. The polymer chains generally organize the crystalline into one-dimensional structure which is well-known as nanowires, nanofibers or nanowhiskers [42, 44]. In the mixed-solvent method, the polymer chains are forced into self-assembly by using a combination of good and poor solvent. In the whisker method, the conjugated polymer is dissolved in marginal solvent which is a poor solvent for polymer at room temperature and a good solvent at elevated temperature. The polymer solution is heated and then cooled down to room temperature. The crystalline structures can form. In almost all reports, the study of aggregated polymer is utilized by solvent-nonsolvent method. The polymer molecules are first dissolved in good solvent. Then a small amount of poor solvent is added to the main solution. The idea is to tune the interaction between polymer chains and poor solvent molecules to induce self-assembly and aggregation of polymer chains. Since the interaction energy between the poor solvent and the polymer provides the driving force for self-assembly, the degree of crystallization within aggregation is dependent on the amount of poor solvent in the system. The aggregated species show the red-shift peak in absorption and PL spectra when the amount of poor solvent is increased. The aggregation behavior of MEH-PPV in solution has been studied by many research groups [58, 60, 61, 68, 69, 70]. Figure 25 shows the growth of red-shift peak at 550 nm in absorption spectra and 585 nm in PL spectra upon increasing the amount of methanol corresponds to the aggregation of MEH-PPV in tetrahydrofuran (THF)/methanol mixture [68]. The emission intensity also gradually decreases upon the addition of methanol. Other mixed solvent systems such as toluene/hexane [69], toluene/cyclohexane [70] are also studied, which provide similar results. Traiphol, et al. [51] has reported effect of chain conformation and chain length on degree of aggregation. They have found that, in early stage of the aggregation, the amount of aggregates is controlled by the solubility of polymer. The aggregate fraction is highest in the system of THF with less ability to dissolve the polymer than dichloromethane and chloroform. When the polymer chains are forced to densely pack within assembled particles by increasing ratio of poor solvent, cyclohexane, to 99 v/v %, the conformation of individual chain plays important role. The aggregation is more

favorable when the extended chains are induced to assemble. Increasing chain length of polymer promotes the aggregation in early stage and densely packed particles.
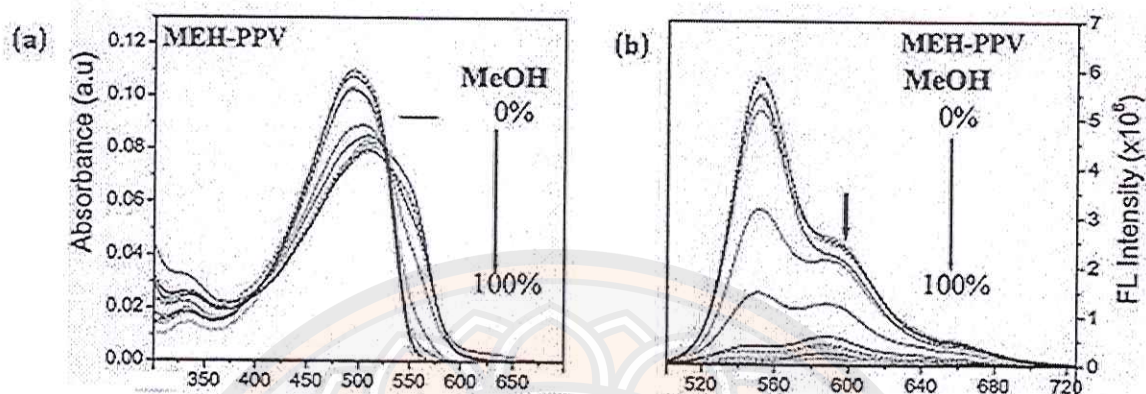
Figure 25 (a) Absorption and (b) PL spectra of MEH-PPV in THF/methanol [68]

The aggregation of regioregular poly(3-alkylthiophene) (*rr*-P3AT) lead to the growth of three distinct red-shift peaks in absorption spectrum which was first reported by Rughooputh, et al. [71]. The aggregated *rr*-P3AT show the solvatochromism and thermochromism properties by dramatically change the solution color from yellow to purple when adding the amount of poor solvent (solvatochromism) or cooling to low temperatures. The following reports have been studied by Rumbles group [72, 73]. They observed similar results in the system of regioregular poly(3-dodecylthiophene) (*rr*-P3DDT) where the aggregation is induced by varying ratio of toluene/methanol mixture. They also found that the length of alkyl side chain can affect the photophysical properties of aggregated *rr*-P3AT. Long alkyl chain, *rr*-P3DDT, presented the low energy of aggregate by showing more redshift in absorption spectra than that of the system of regioregular poly(3-hexylthiophene) (*rr*-P3HT) which have shorter alkyl side chain. Figure 26 present the absorption spectra of aggregated *rr*-P3HT in chloroform/hexane mixture. The spectra clearly exhibit red-shift peaks at about 520, 560 and 605 nm, respectively [74, 75]. These red-shift peaks increase when the ratio of hexane is increased. Lanzi, et al. [76] studied the effect of main chain regioregularity of P3AT on the degree of aggregation, as shown in Figure 27. The red-shift peaks in absorption spectra of *rr*-P3AT are clearly observed when the quality of solvent is decreased by adding methanol. On the other hand, the

regiorandom P3AT (*rra*-P3AT) exhibited small change in the spectra, indicating less quantity of aggregated segment in the system. These results indicate that the main chain regioregularity play an important role on the aggregation behavior of polythiophene conjugated polymer.
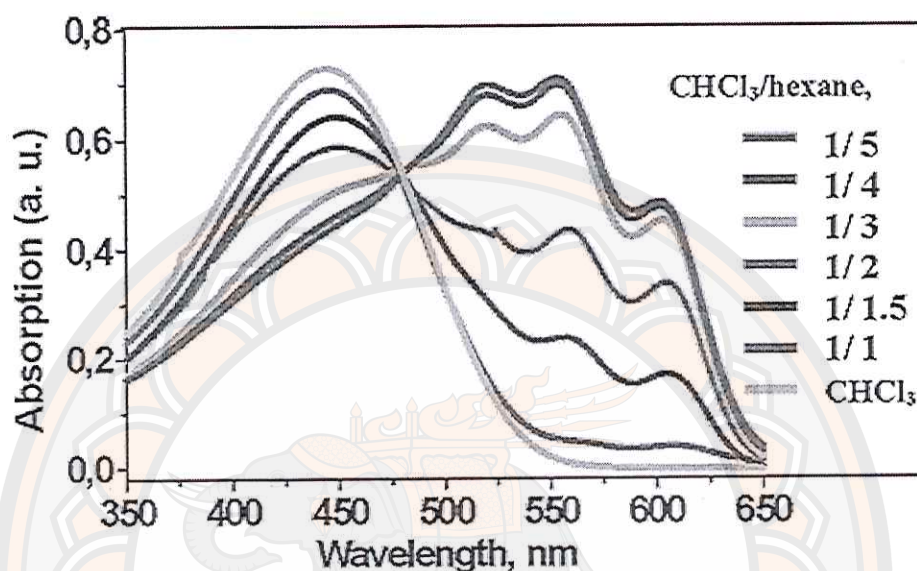
Figure 26 Absorption spectra of *rr*-P3HT in mixed chloroform/hexane [74]
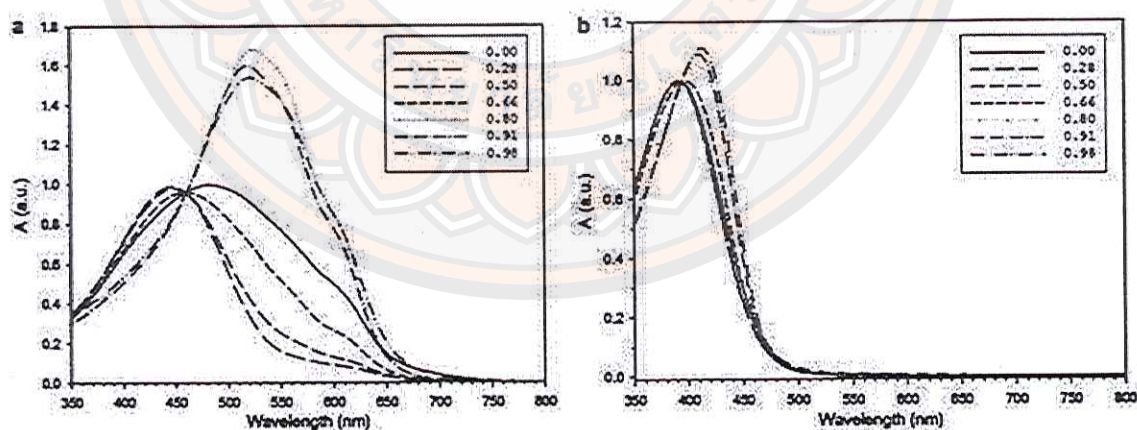
Figure 27 Absorption spectra of (a) regioregular and (b) regiorandom of polyalthiophene in chloroform/methanol mixtures. Inset is methanol molar fractions. [76]

The characteristic layer of P3AT exists in two different crystal structures, called Form I and II [77, 78, 79, 80, 81, 82], which differ mainly by the side chain conformation as shown in Figure 28. Interdigitation of the *n*-alkyl side chains is observed in the structure of Form II, whereas in the structure of Form I, the *n*-alkyl side chains are not interdigitated. Form I and Form II differ also by the stacking of the thiophene backbones. In Form I, the polythiophene backbones are separated by 0.38 nm along the b axis when compared with 0.47 nm along the c axis in Form II. The chain packing shows the different in the shift of polymer chain along the c axis. In Form I, two polymer chains along the π-stacking direction (b axis) are shifted by 0.15 nm parallel to the chain axis direction. In Form II, the thiophene backbones almost overlap along the c axis.
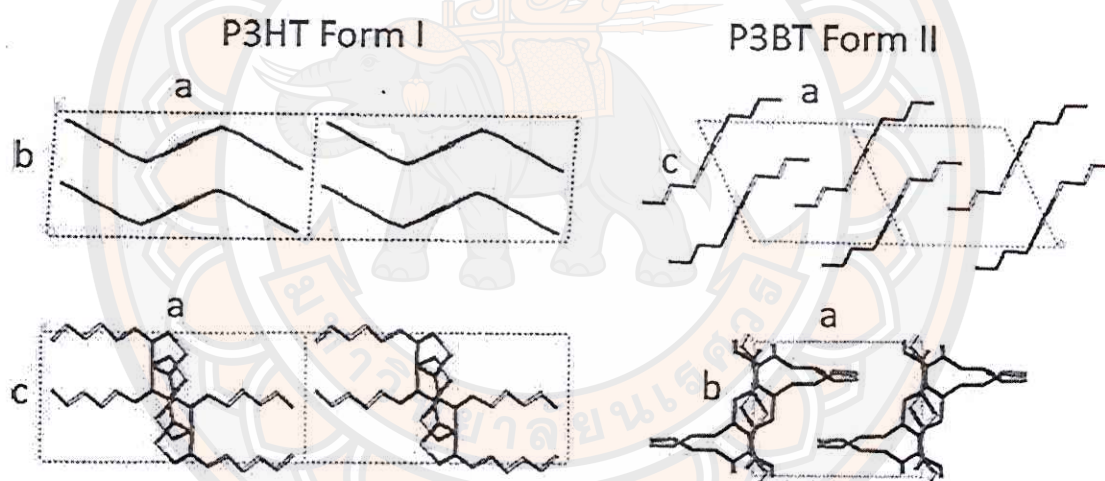
Figure 28 Crystal structures of Form I P3HT and Form II P3BT [79, 80, 81]

Several research groups have been demonstrated the aggregation behavior of P3AT in solvent-nonsolvent system. Kiriy, et al. [74, 75] study the conformational transition of P3HT chain into aggregate state by adding different types of poor solvents, hexane and methanol, into polymer in chloroform solution. The main chain collapsed in one-direction aggregate is observed in hexane system due to the selective solvent for alkyl side chain. A helical conformation has been proposed in this system (See Figure 29). The unfavorable interaction for both alkyl side chain and thiophene backbone in methanol provide the P3HT chain fold into compact poorly ordered

structure and three-direction aggregate at high concentration. They have shown that the absorption spectra of P3HT in hexane system exhibit a formation of red-shift of highly ordered structure than that of in methanol system.

Other group reported the formation of nanofiber of P3AT in mixed solvent system. Samitsu, et al. [83, 84] prepared P3AT nanofiber by using anisole solvent. The formation of nanofiber originate from one dimensional crystallization of P3AT resulted from the π-π interaction between thiophene backbone and the crystallization of alkyl side chains. Park, et al. [85] showed the similar demonstration of P3HT aggregation. The organization of P3HT in solution is transformed from random coil conformation in chloroform solution to order aggregated by adding poor solvent acetonitrile. The formation of one-direction or two-direction aggregation of P3HT depends on the concentration. Sun, et al. [86] controls P3HT nanofiber growth by using a mixed solvent system. They have found that the addition of a small amount of good solvent, chlorobenzene, in anisole solvent provide a higher degree of crystallization and thinner nanofiber as compared to pure anisole system. In addition to the formation of nanofiber, the assembly of P3AT can provide the nanowhiskers. Xu, et al. [87] controlled the solvent composition and aging time to induce the P3DDT nanowhiskers. The coil-to-rod transition and π-π stacking of the rods have been accepted for the processes of P3AT crystallization from solution. Scharsich, et al. [88] studied the effect of molecular weights, 5 kDa, 11 kDa and 19 kDa, on the controlling of P3HT aggregate. The growth of low energy absorption peak increases with the molecular weight of P3HT. The fraction of aggregate chain is about 55% although the poor solvent, ethyl acetate, is increased to 90%. The difference of molecular weight also provides the variation of polymer chain packing in aggregate.

All *anti*-conformation
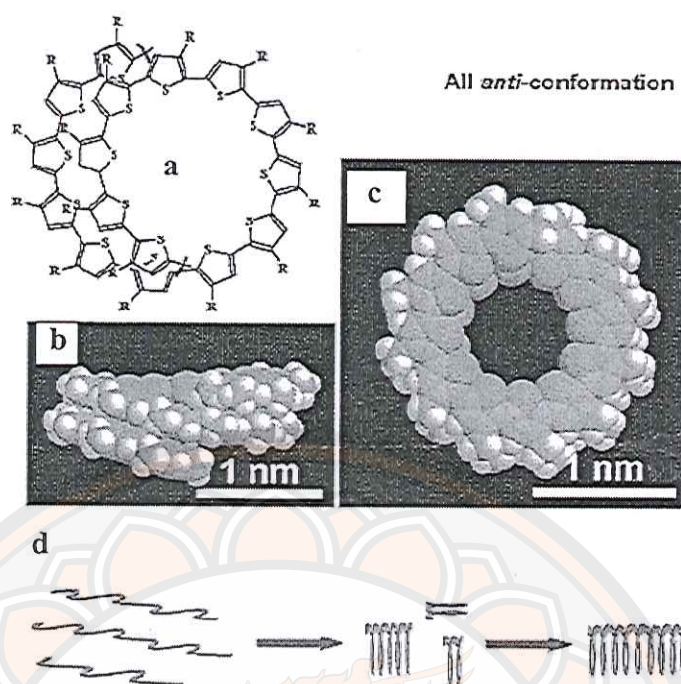
Figure 29 (a) The helical conformation of P3ATs molecules and the model of P3AT in the helical conformation showed in (b) side view and (c) top view. (d) Model shows 1D aggregation into helical nanotubes. [74]

Photophysical properties of conjugated polymer nanoparticles

Conjugated polymer nanoparticles (CPNs) are highly versatile nanostructured materials that have received attention in various applications such as optoelectronics, photonics [89], bioimaging, biosensing and nanomedicine [19, 20, 21, 22, 23, 24, 25, 26, 90]. The CPNs are desirable for a number of reasons. The advantage of CPNs for optoelectronic device is that the domain of electron and hole transporting polymer can be conducted by tuning size and aggregates structure within the particle. For biological applications in particular, the biocompatibility is an important consideration for fluorescent nanoparticles. CPNs have less toxic and more biocompatible compared to the inorganic nanoparticles. CPNs also exhibit excellent characteristics as fluorescent probes, including their extraordinary fluorescence brightness, fast emission rate, excellent photostability and nonblinking. Additionally, their photoluminescent properties can be tuned by varying particle size, composition, type of conjugated polymers and surface modification. Pras, et al. [91] prepared nanoparticles of 2,7-poly(9,9-dialkylfluorene-co-fluorenone) (PFFO) with particle sizes ranging between

5 and 500 nm. The PL spectra of these nanoparticles shifted from blue luminescence to yellow luminescence when the particle size increased.

CNPs can be easily prepared. Two main preparation techniques are the miniemulsion and the reprecipitation methods [27, 28]. Using miniemulsion method, the conjugated polymer in mixture of organic solvent and aqueous solution of surfactant is ultrasonicated to form the small droplets miniemulsions of polymers. The organic solvent is removed to obtain the dispersion of polymer nanoparticles in water, as shown in Figure 30. The size of nanoparticles could vary from 30 nm to 500 nm depending on the type and amount of the surfactant [28] and the concentration of the polymer solution [27]. Using this method to prepare MEH-PPV nanoparticles provided the particle size of about 100 nm [24]. Nanoparticles of poly(arylene diethynylenes) with molecular weights (M_n) in the range of 10^4 to 10^5 g/mol provided the particle size of $\leq$ 30 nm [92].

Figure 30 Process of miniemulsion polymerization [28]

For reprecipitation method, the conjugated polymer in a good solvent is rapidly injected into an excess volume of nonsolvent, usually water, without the use of surfactant. Mixing of the solvent with the nonsolvent causes sudden decrease of solvent quality, which induces precipitation of the polymer. The resulting mixture is stirred rapidly using a sonicator to assist the formation of nanoparticles. The organic solvent is removed to obtain the dispersion of polymer nanoparticles in water (see Figure 31). The average size of nanoparticles is in range of 5-50 nm [93, 94]. It is possible to prepare nanoparticles in desired sizes by adjusting the polymer concentration. Moreover, the preparation does not involve the use of any additives such as surfactants. Thus, the method can be applied to a wide variety of conjugated polymers that are soluble in organic solvents.
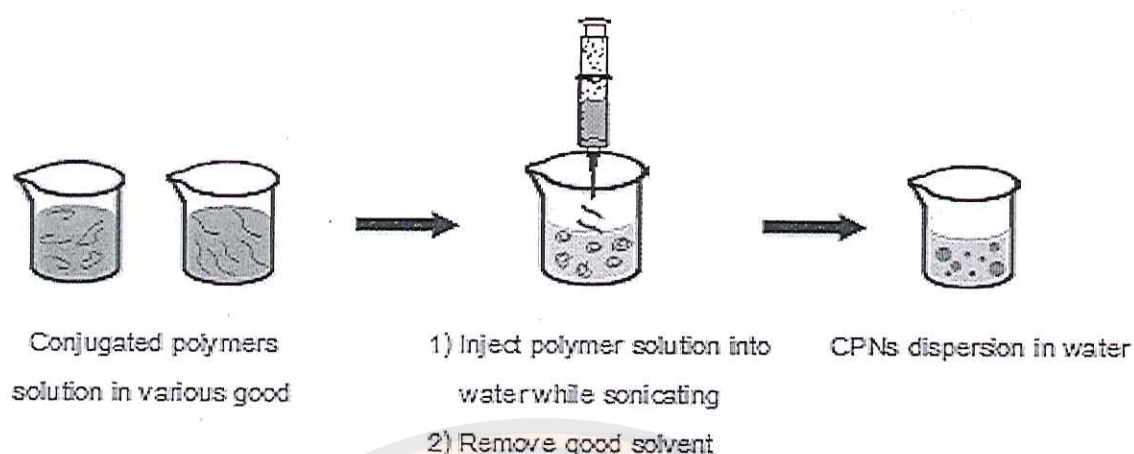
Figure 31 Process of reprecipitation method

McNeill and co-worker [19, 20, 94, 95, 96] have prepared the conjugated polymer nanoparticles by using reprecipitation technique. They varied the types of conjugated polymers to receive different emission colors of nanoparticles (see Figure 33c), as shown in Figure 32. The nanoparticle diameters are in the range of 5-10 nm. The particles dispersed in water exhibits blue-shifted absorption as compared to those of the polymer in good solvent. Figure 33 shows absorption and PL spectra of these CPNs. The observed blue-shift of the absorption peaks has been attributed to an overall decrease in the conjugation length, due to the bending or kinking of the polymer backbone in densely packed structure of particles. A red tail is also observed in the absorption spectra of polymer nanoparticles, indicating the presence of aggregate states due to interactions between segments of the polymer chain. The PL spectra of nanoparticles exhibit a redshift and a long red tail. This could be ascribed to increased interactions between segments of the polymer chain due to chain collapse, resulting in a fraction of red-shifted aggregate species.
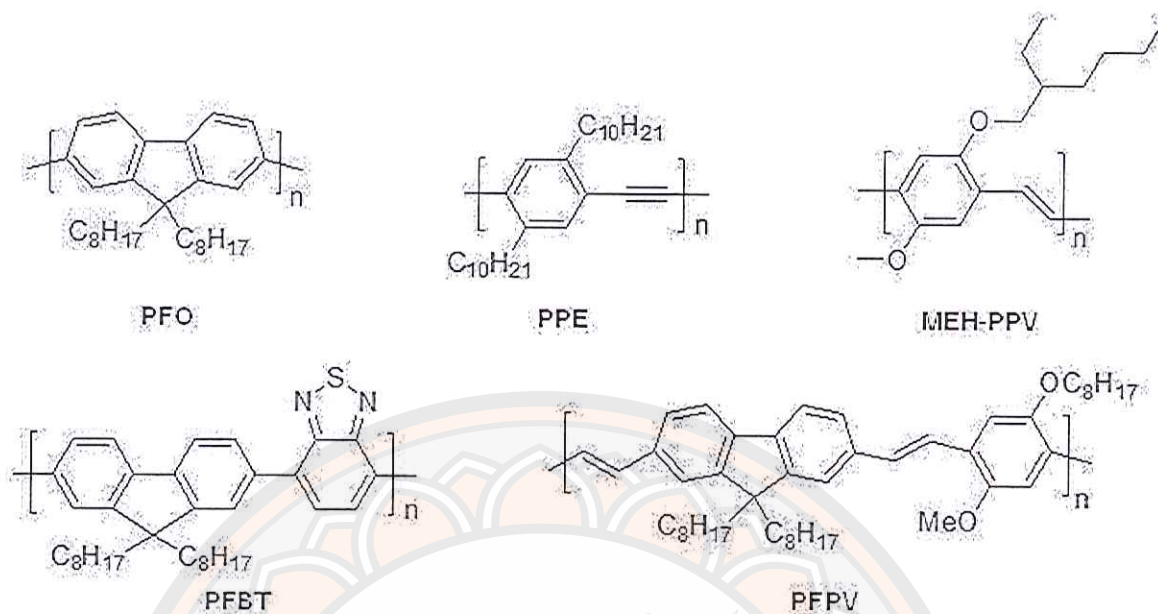
Figure 32 Chemical structures of conjugated polymers used in the formation of nanoparticles by McNeill group [19, 94, 95, 96]
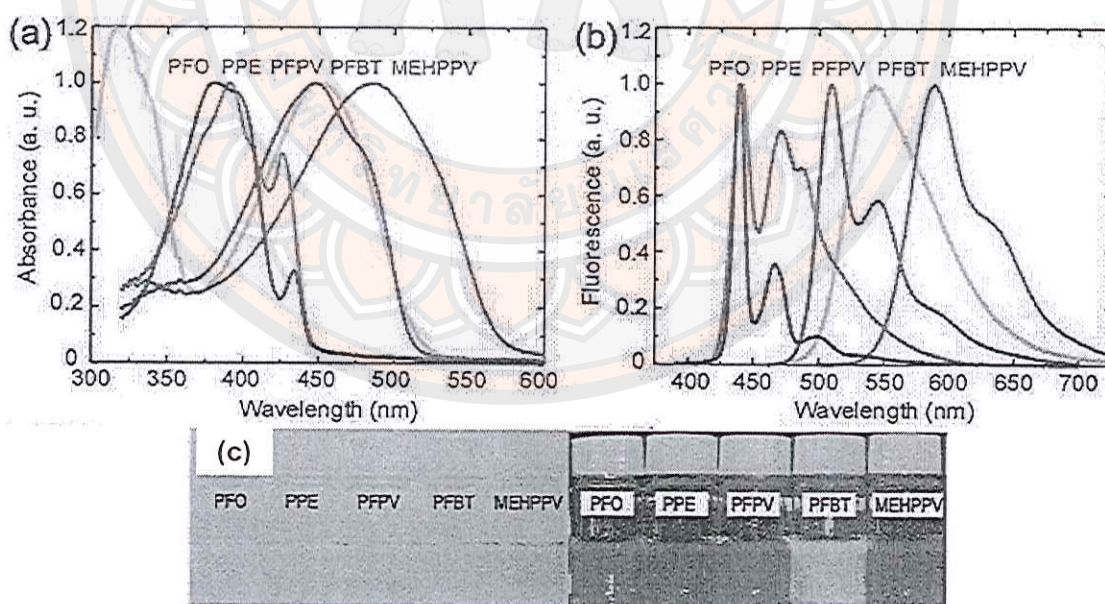
Figure 33 (a) Absorption and (b) PL spectra of the conjugated polymer nanoparticles. (c) Photograph of conjugated polymer nanoparticles under room light (left) and UV light (right). [19]

CPNs can be also prepared by using oxidative polymerization especially for preparing polythiophene nanoparticle. The properties of nanoparticles have been optimized by varying the surfactant/metal ion (oxidant)/thiophene monomer ratio, thiophene concentration, polymerized temperature, and reaction time [97]. Lee, et al. [98, 99] has prepared PT nanoparticles in $FeCl_3/H_2O_2$ system. They found the decrease of particle size from 51 to 12 nm with increasing H_2O_2 molar concentration. The PL spectra show the red-shift of λ_{max} when the particles size increase, as shown in Figure 34. The emission color changes from blue color to red color.
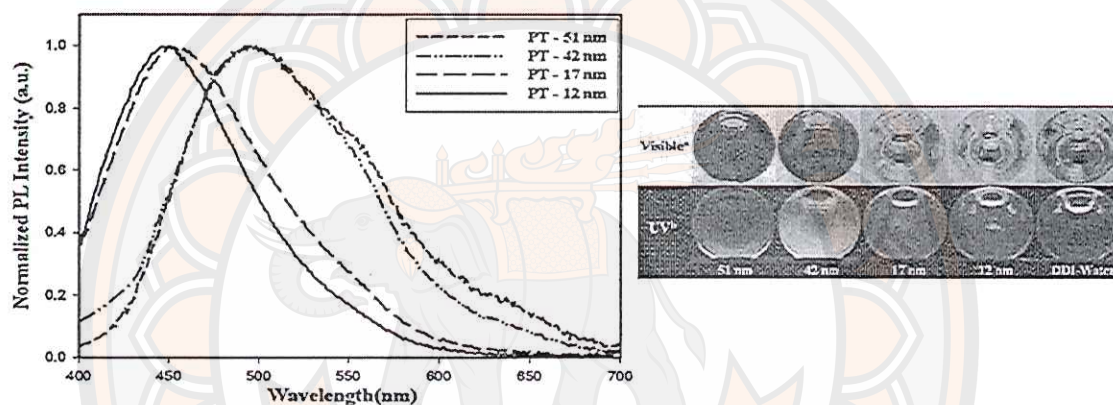
Figure 34 (a) Normalized PL spectra of polythiophene nanoparticle with various particle sizes and (b) the emission color tuning of polythiophene nanoparticle under visible and 365 nm UV region [99]

The different aggregate behaviors within nanoparticle can affect the photophysical properties. Ko, et al. [100] controlled the aggregation behavior of primary amine-containing poly(phenylene ethynylene) (PPE-NH$_2$) nanoparticles via organic acid treatments, acetic acid (AA) and tartaric acid (TA). They found the change in absorption spectra when the aggregated polymer within the particle is different. The loose aggregation with minimal π-π stacking within nanoparticle was found when the nanoparticle was treated by acetic acid, while nanoparticle formed by tartaric acid treatment exhibit a high degree of π-π stacking among chains, as shown in Figure 35. The loose aggregation within nanoparticle exhibits blueshift in absorption and comparable to that of polymer in an organic solvent. Nanoparticle with dense

aggregation shows redshift and broadening in both absorption and emission spectra due to the formation of better planarization of the conjugated backbone and extended conjugation through space (see Figure 36). Dense aggregation causes lower quantum yields than weak aggregation because of the high degree of π-π stacking.
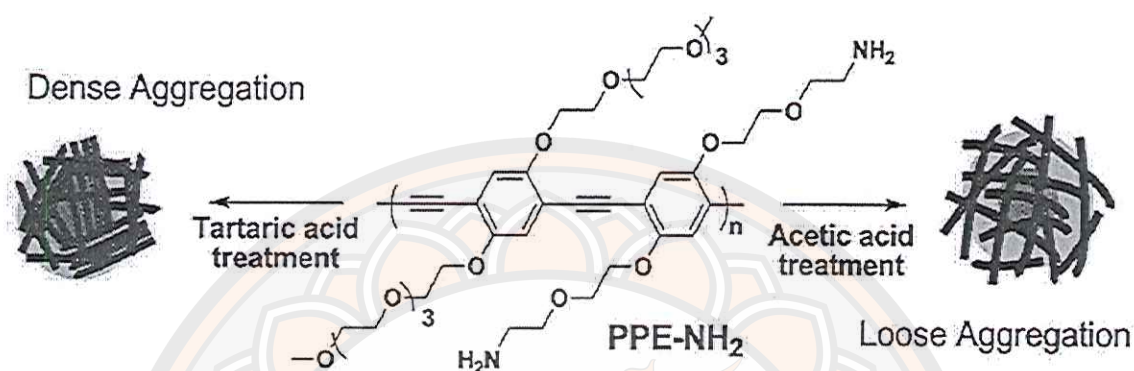
Figure 35 Schematic of PPE-NH$_2$ nanoparticle produces different aggregation structures depending on the organic acid treatment [100]
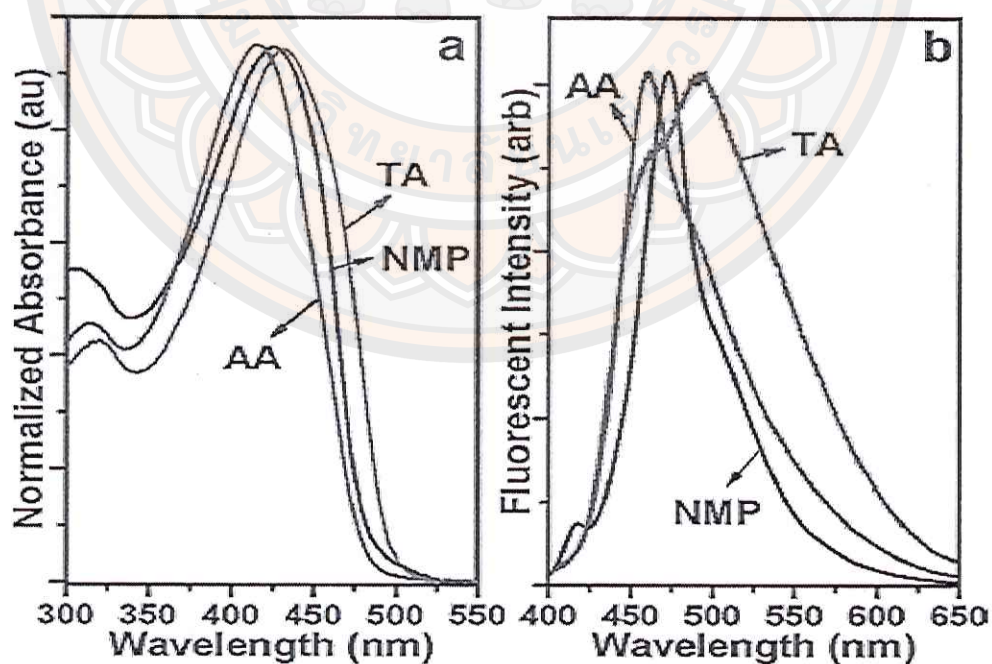
Figure 36 (a) Absorbance and (b) emission spectra of the PPE-NH$_2$ in solution, CPN-AA and CPN-TA [100]

Nagarjuna, et al. [101] studied the aggregate structure of P3HT within nanoparticles by tuning the solvent composition during nanoparticle fabrication under miniemulsion. The polymer solutions as the oil phase were varied by using three different solvents for fabricating P3HT nanoparticles: chloroform, toluene, and a mixture of toluene/chloroform (1:4). The solvents have an impact of P3HT aggregation within the nanoparticles. The solubility of solvent and the boiling point of solvent is key role in the final aggregate structures. They found that the CPNs from chloroform, good solvent for P3HT, have the largest degree of the internal structural disorder. The rapid evaporation of chloroform leads fast polymer aggregation due to the kinetically trapped causing a higher degree of dispersity in polymer aggregated. Toluene is marginal solvent for P3HT and the evaporation rate of toluene is much slower than that of chloroform. Therefore, the concentration of the polymer within the droplet is high. The polymer chain has time to a tighter packing, leading to small particle size compared to that of chloroform. In mixed solvent system, the solubility of the polymer is lower but the presence of good solvent enhanced the chain mobility thereby allowing the aggregated to solvent-anneal resulting in a higher degree of uniformity and structural order. The measurement of absorption strum also shows that the CPNs comprise with the amorphous and the aggregate structure. The decrease of solvent quality does not affect the formation of the amorphous component to the absorption spectra, but does appear to affect the aggregate absorption spectra, as shown in Figure 37.
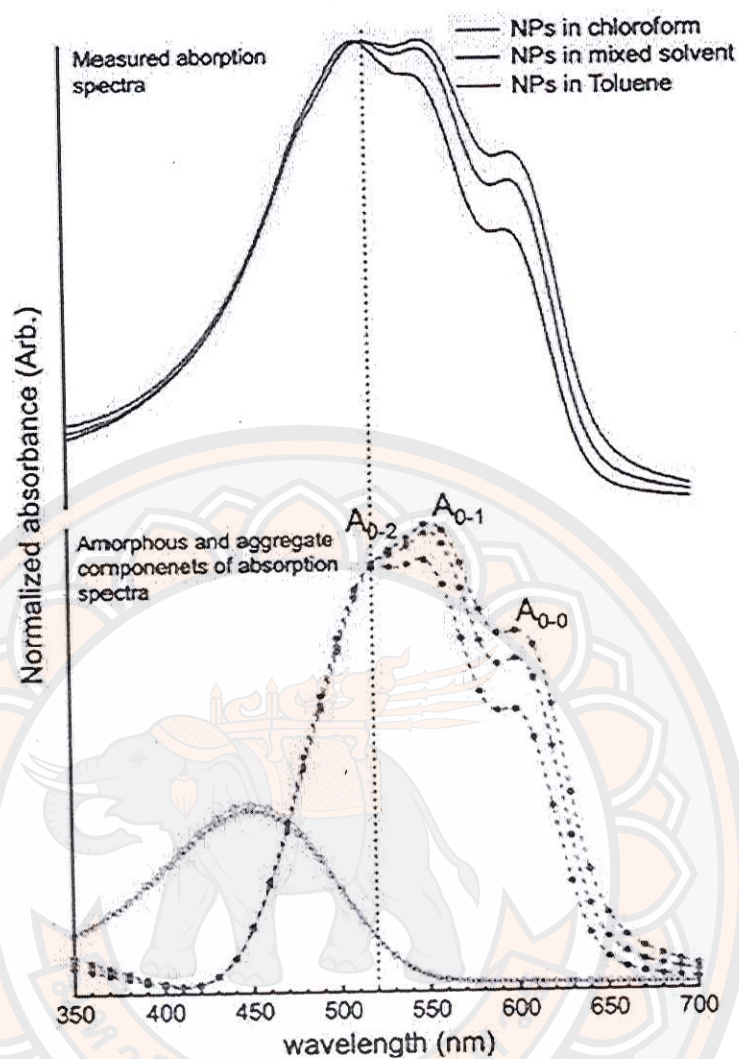
Figure 37 (top) Normalized absorption spectra of P3HT nanoparticles prepared from solution in chloroform, toluene, and mixture of chloroform and toluene and (bottom) amorphous absorption (open-circled line) and aggregate absorption (close-circled line) P3HT nanoparticles. [101]

Morphology and photophysical properties of conjugated polymer film

A successful application of organic electronic devices such as organic light-emitting and organic solar cell depends on the control of electronic and optical properties of polymer film. The efficient charge transport and strong luminescence are two major issues that need to be considered for the device applications. The morphology and the chain orientation in thin film play important role on the optimization of the device performances. There are two differences of polymer chain orientations on the substrates affect the properties of devices [11, 82, 102] as shown in Figure 38. The edge-on orientation of polymer chain on substrate is suitable for the OFETs application while the face-on orientation is appropriated to plastic solar cell. For tuning properties of materials in devices, it is therefore necessary to understand the behaviors of conjugated polymers in thin films such as molecular packing and the formation of various nanostructures. The film morphology and their properties are controlled by many parameters such as molecular parameter, substrate condition, solvents properties, processing condition, and post-annealing treatments. Previous study has shown that the morphology of MEH-PPV film depends on the molecular weight [103]. MEH-PPV chains with high molecular weight tend to orient parallel to the film plane. In contrast, thin films of low molecular weight MEH-PPV have random orientation of the chain segments.
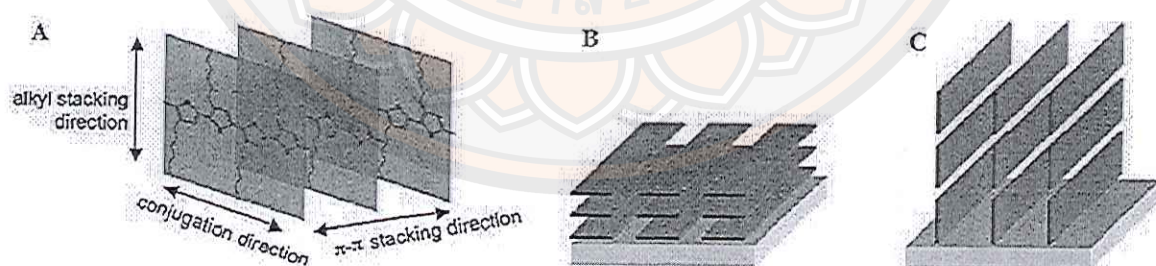
Figure 38 Schematic representations of (A) the molecular packing of P3AT, (B) face-on and (C) edge-on orientation of the polymer chains on the substrates. [11]

The chain packing or morphology of P3AT thin film depend on many parameters such as molecular weight [51], degree of regularity [104, 105], and length of alkyl side chain [106]. The higher molecular weight of P3AT yields the increase of the total crystalline region as compared to low molecular weight. This behavior results in the increase of charge carrier mobility [51]. Previous study has shown that P3AT film with high head-to-tail (HT) coupling exhibits the morphology consisting of crystalline, quasi-ordered, and disordered phases [105]. P3AT film with moderate HT regularity is normally amorphous with a quasi-ordered phase dispersed in continuous disordered domains, as shown in Figure 39.

(a) Crystaline Phase

(b) Quasi-Ordered Phase
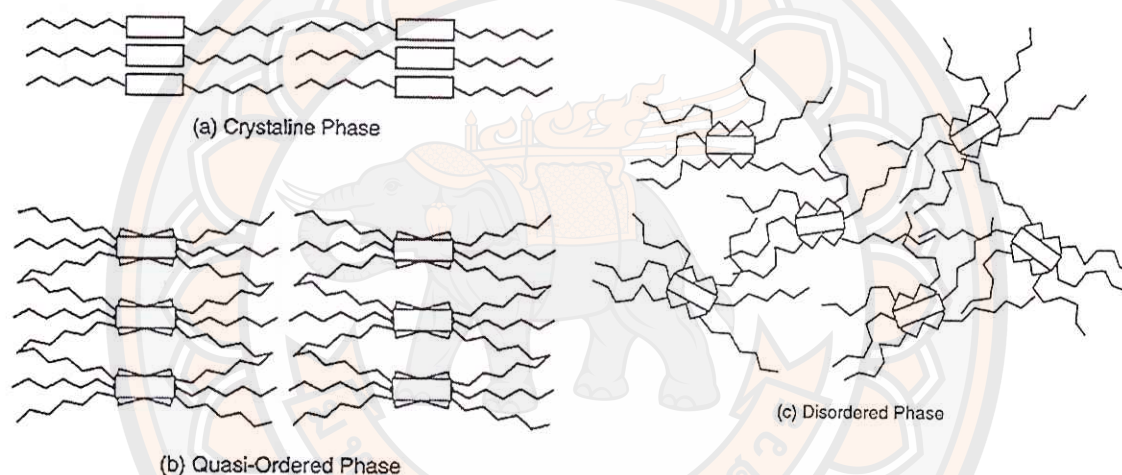
(c) Disordered Phase

Figure 39 Schematic representations of (a) crystalline, (b) quasi-ordered and (c) disordered phases of P3ATs (viewing along the thiophene chain) [105]

The different length of alkyl side chain causes great difference in the molecular chain packing [106]. The degree of order chain packing of rr-P3AT thin films has been investigated by using uv-visible absorption spectroscopy. The alkyl side-chain lengths include butyl, hexyl, octyl, and decyl. The absorption spectra showed that the rr-P3HT had the strongest red-shift peak, indicating a significantly higher degree of order in P3AT films (see Figure 40). In contrast, P3BT with the shortest side-chain length shows weak vibronic features and the maximum absorption is highly blue shifted. This indicates the less of order chain packing.
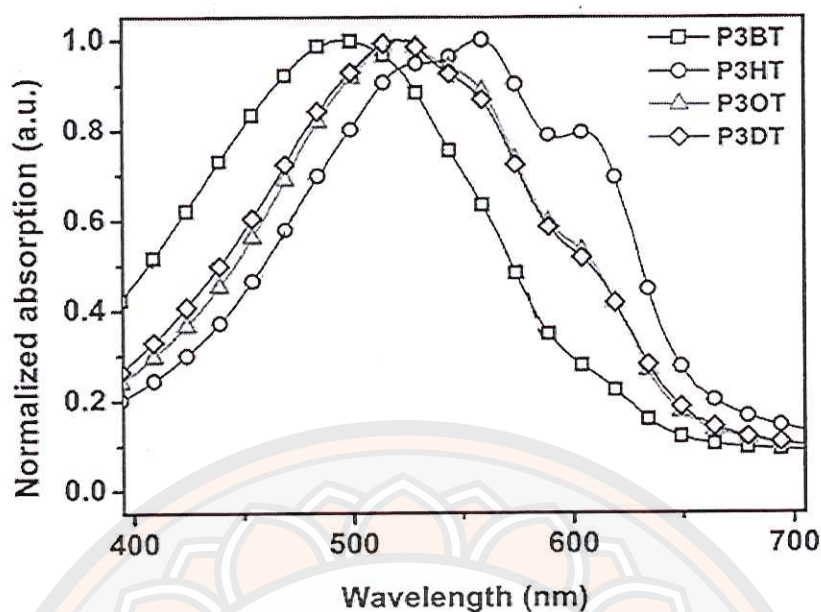
Figure 40 Normalized absorption spectra of P3AT thin films [106]

The solvents also affect the morphology and crystallization of P3AT film. Xue, et al. [107] reported that solvent solubility greatly affects the film morphology. P3HT film prepared from good solvent, chlorobenzene, showed a dot-like structure (Figure 41a) since no crystalline aggregates formed in solution. A thin layer of P3HT fibrillar crystals was obtained when the polymer solution in chloroform was used (Figure 41b). The films prepared from toluene and xylene solutions, however, showed densely stacked network structures (Figure 41c and d). They explain that the halogenated solvents (chlorobenzene, chloroform) have high dielectric constants, so it possesses better solubility properties. For alkane solvents (toluene, xylene), they interact with conjugated chains via π-π interactions which promotes the formation of the fibrillar crystals. Figure 42a illustrates the absorption spectra of the polymer solution aged for 7 days. No change can be found in the chlorobenzene solution, which indicated that P3HT chains maintain the coiled conformation. The additional low-energy absorptions at $\lambda = 562$, and 614 nm was found in the system of toluene and xylene which indicate the existent of low-energy specie. Studied have reported that the absorption band at around 610 nm comes from the interchain π-π^* transition of P3HT. Thus, the intensity of this absorption is correlated to the degree of interchain order. In addition, compared with the absorption spectra of the solutions, the main absorptions

of thin films were significantly red-shifted to 556 nm (Figure 41b), which means that the conjugated length of P3HT molecules increased when deposited onto the substrate. The absorption at 607 nm increased gradually following the aging time similar to the phenomenon in the solution. The crystallinity of the film increased gradually. The increase of crystallinity of P3HT films should be the result of increasing amount of preexisted crystalline aggregates in the solution.
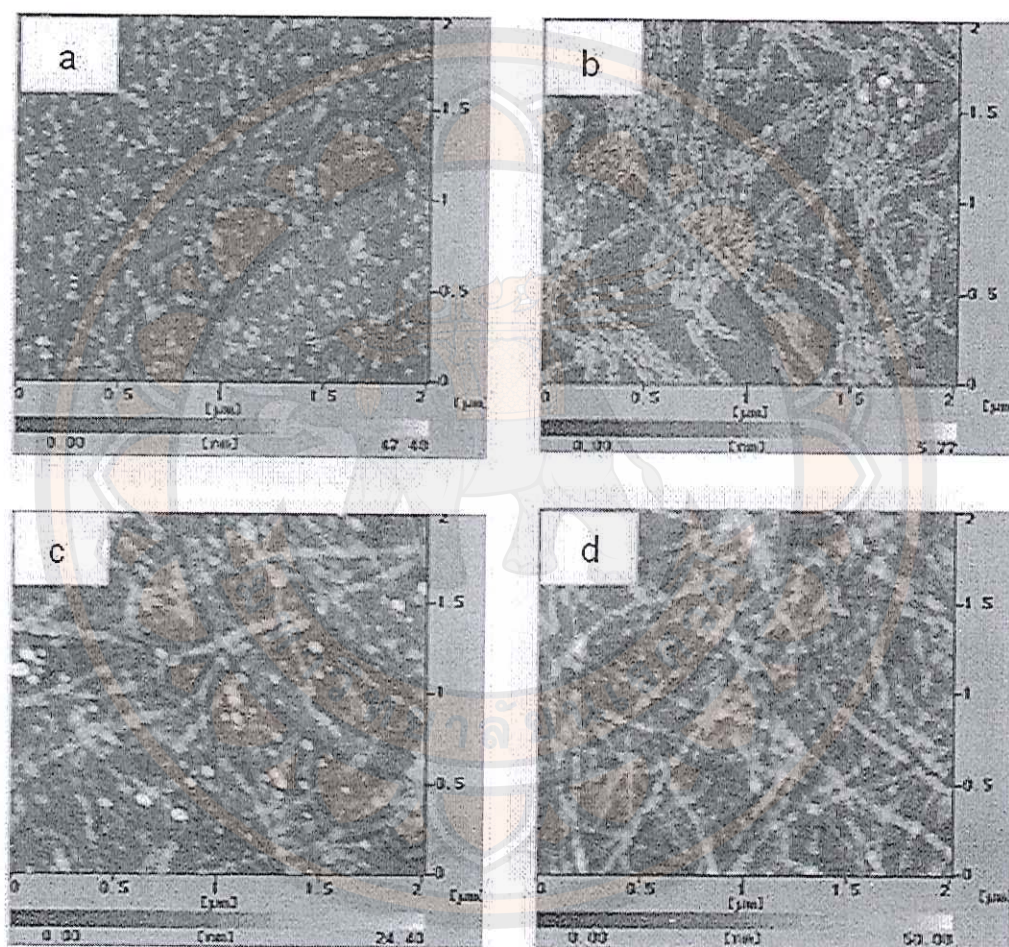
Figure 41 AFM height images of P3HT films prepared from 2-days-aged 0.4 mg/mL solutions with solvents of (a) chlorobenzene, (b) chloroform, (c) xylene, and (d) toluene by spin-coating process, respectively. [107]
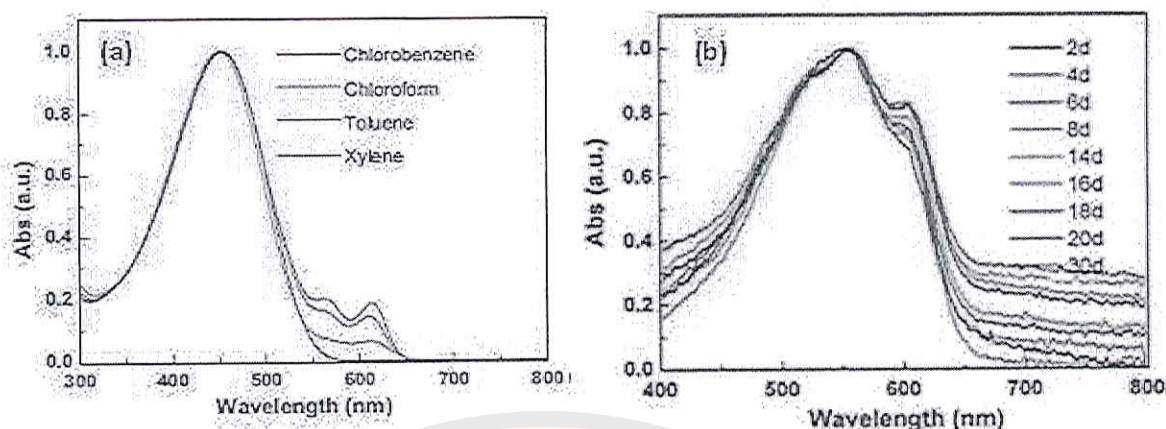
Figure 42 Normalized absorption spectra of (a) 7-days aged solution of 0.4 mg/mL P3HT in chlorobenzene, chloroform, toluene, and xylene solution and (b) the spectra of corresponding P3HT thin films prepared from toluene solution [107]

In addition, the morphology of thin film can be controlled by adjusting the solvent composition and aging time. Xu and coworkers [87] observed the transformation of poly(3-dodecylthiophene) (P3DDT) morphology from one-dimensional nanowhiskers to two-dimensional nanoribbons and foliated agglomerates when increasing anisole content in the mixed carbon disulfide/anisole solvent and aging time, as shown in Figure 43. The differences of morphologies result from the role of π-π interaction and the alkyl interaction. At the early stage of solution crystallization, π-π interaction is dominance, which leads to the growth of nanowhiskers. After crystallization for a period of time, the growth of P3DDT nanowhiskers reaches its equilibrium. Then van der Waals force becomes the dominating interaction among nanowhiskers and leads to formation of nanoribbons and foliated agglomerates via side chain packing.
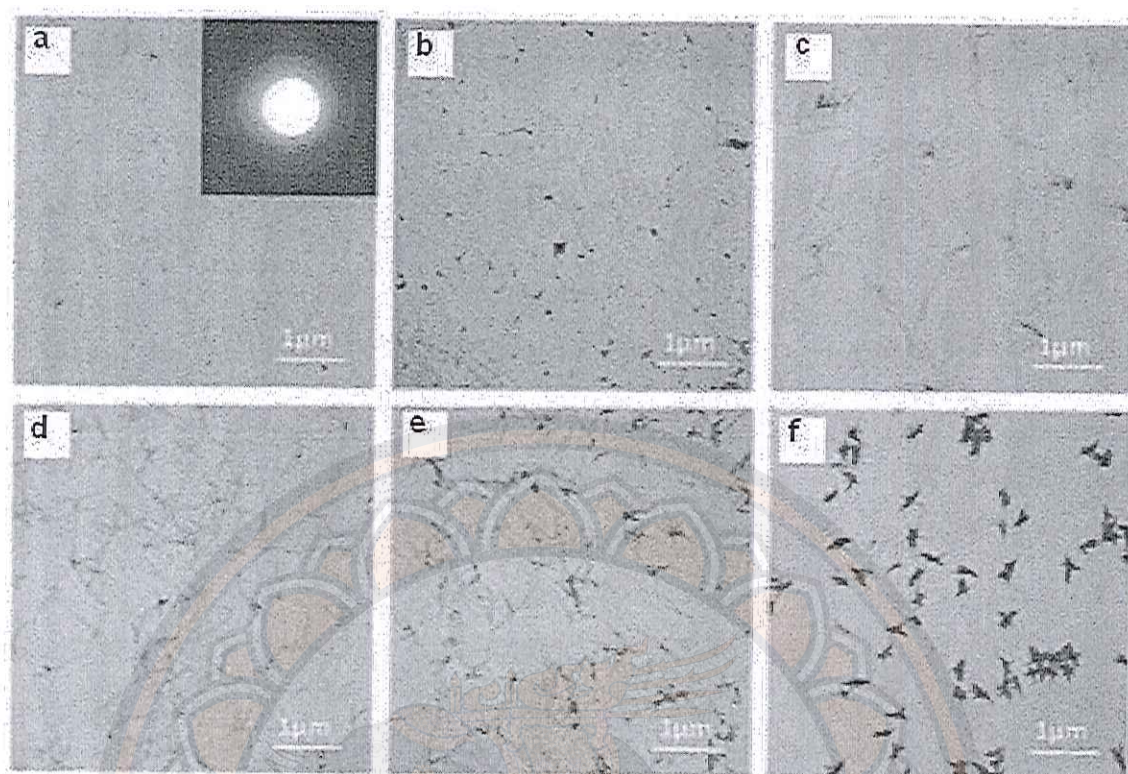
Figure 43 TEM images of P3DDT nanowhiskers and nanoribbons drop-cast from 0.25 mg/mL P3DDT in mixture of carbon disulfide (CS_2)/anisole solutions with different solvent ratios and aging times. (a) 1:5, 12 h; (b) 1:7, 12 h; (c) 1:9, 12 h; (d) 1:11, 12 h; (e) 1:7, 24 h and (f) 1:7, 2 months [87]

CHAPTER III

METHODOLOGY

UV-visible absorption spectroscopy

The UV-visible absorption spectroscopy uses electromagnetic radiations between 190 nm to 800 nm and is divided into the ultraviolet (UV, 190-400 nm) and visible (VIS, 400-800 nm) regions. Since the absorption of ultraviolet or visible radiation by a molecule leads transition among electronic energy levels of the molecule, it is also often called as electronic spectroscopy. The technique is usually applied to molecules or inorganic complexes.

The fundamental process in absorption spectroscopy is the absorption of a discrete amount of energy. The energy required for the transition from a state of lower energy (E_1) to state of higher energy (E_2) is exactly equivalent to the energy of electromagnetic radiation that causes transition (see Figure 44)

$$E_2$$

$$E_2 - E_1 = E = h\nu$$

$$E_1$$
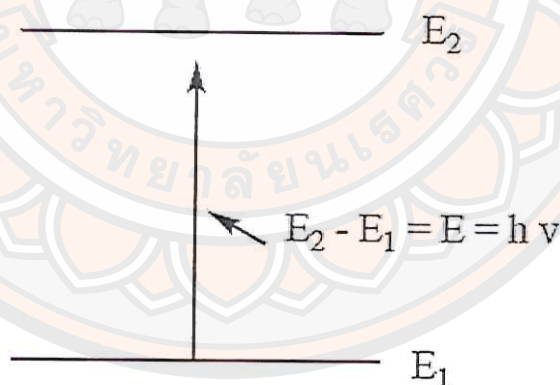
Figure 44 Energy transition for the absorption of any electromagnetic radiation

When light is absorbed by a molecule, the total energy of a molecule is the sum of its electronic, its vibrational energy and its rotational energy.

$$E_{total} = E_{electronic} + E_{vibrational} + E_{rotational} \qquad (15)$$

The amount of energy a molecule possesses in each form is not a continuum but a series of discrete levels or states. The differences in energy among the different states are in the order:

$$E_{electronic} > E_{vibrational} > E_{rotational}$$

These transitions should result in very narrow absorbance bands at wavelengths highly characteristic of the difference in energy levels of the absorbing species. However, for molecules, vibrational and rotational energy levels are superimposed on the electronic energy levels. Therefore, the absorption bands are broadened as shown in Figure 45.
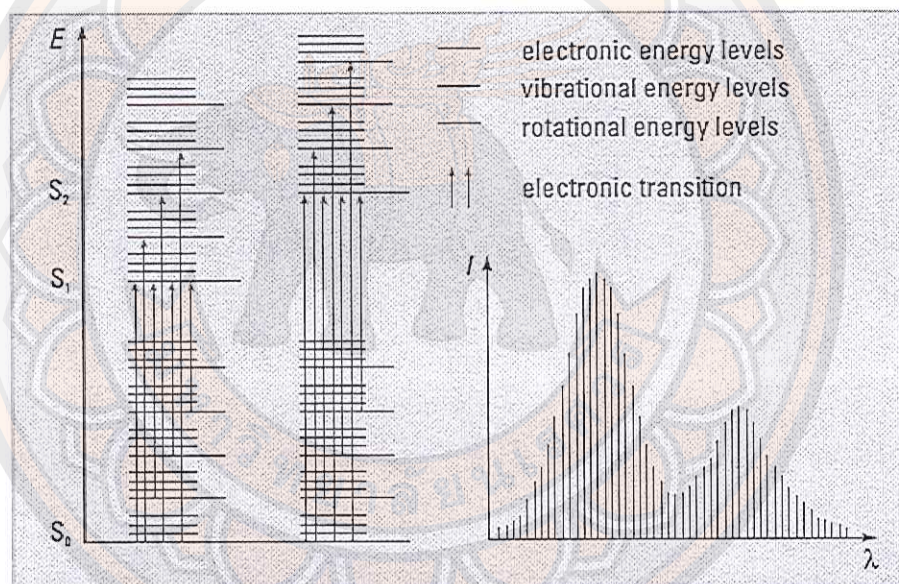
Figure 45 Electronic transitions and UV-visible spectra in molecules [108]

UV-visible absorption spectroscopy studies the changes in electronic energy levels within the molecule arising due to transfer of electrons from π- or non-bonding orbitals. It commonly provides the knowledge about π-electron systems, conjugated unsaturation, aromatic compounds and conjugated non-bonding electron systems etc.

As a molecule absorbs energy, an electron is promoted from an occupied molecular orbital (usually a non-bonding n or bonding π orbital) to an unoccupied molecular orbital (an antibonding π^* or σ^* orbital) of greater potential energy. For most

organic molecules, the lowest-energy occupied molecular orbitals are σ orbitals, which correspond to σ bonds. The π orbitals lie at relatively higher energy levels than σ orbitals and the non-bonding orbitals that hold unshared pairs of electrons lie even at higher energies. The antibonding orbitals (π^* and σ^*) are orbitals of highest energy. The relative potential energies of these orbitals and various possible transitions have been depicted in Figure 46.

The most probable transition would appear to involve the promotion of one electron from the highest occupied molecular orbital (HOMO) to the lowest unoccupied molecular orbital (LUMO). For instance, in formaldehyde, the HOMO is the n orbital and the LUMO is the π^* orbital (see Figure 46). In conjugated dienes system, the $\pi \rightarrow \pi^*$ orbitals of the two alkene groups combine to form new orbitals. It is apparent that a new $\pi \rightarrow \pi^*$ transition of low energy is available as a result of conjugation. The presence of conjugate double bond decreases the energy difference between HOMO and LUMO of resulting diene. Figure 47 shows the change in energy of molecular orbital on conjugation. As the number of conjugated double bonds is increased, the gap between HOMO and LUMO is progressively lowered. Therefore, the increase in size of the conjugated system gradually shifts the absorption maximum (λ_{max}) to longer wavelength (bathochromic shift or red shift) and also increases the intensity of absorption.
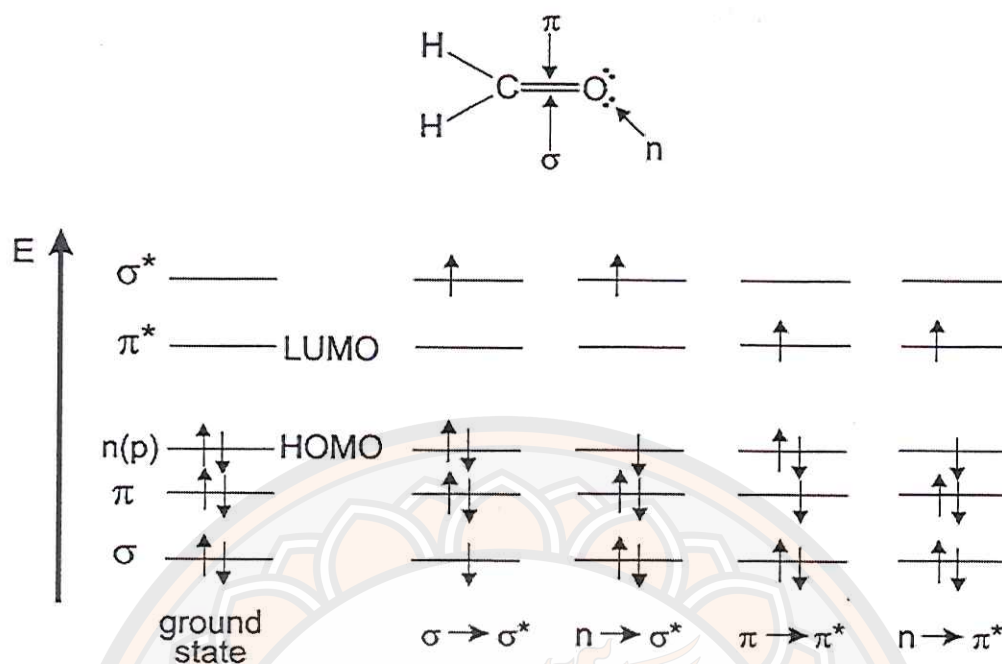
Figure 46 Energy levels of molecular orbitals in formaldehyde and possible electronic transitions [109]
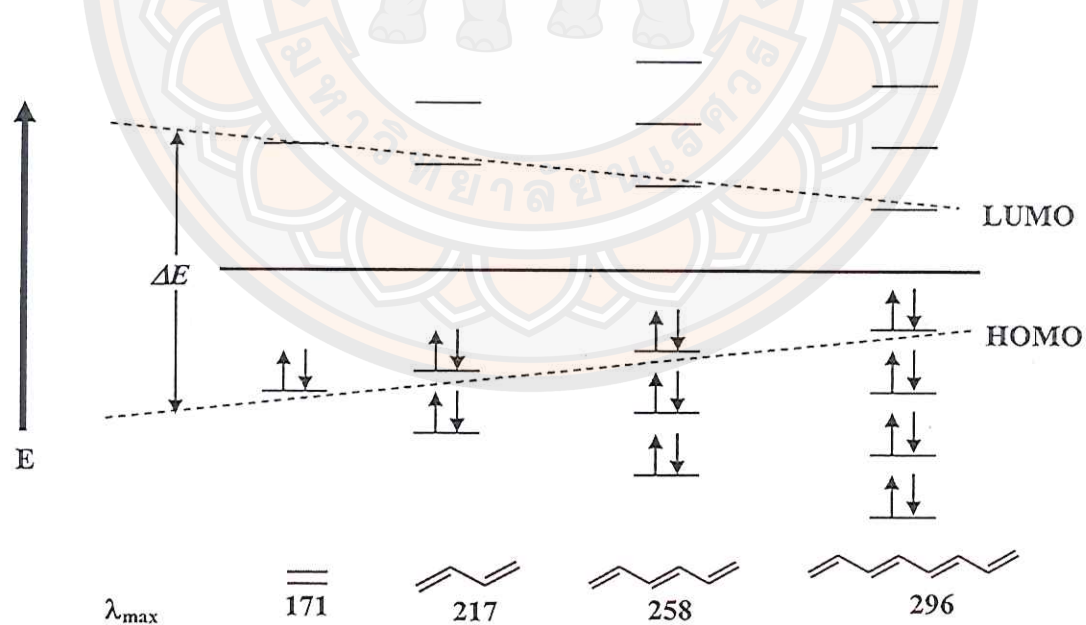
Figure 47 Effect of conjugation and the level of HOMO-LUMO energy gap

Principles of absorption spectroscopy: Beer's and Lambert's Law

When the radiation passes through a solution, the amount of light absorbed is the difference between the incident radiation (I_o) and the transmitted radiation (I). The amount of light absorbed is expressed as either transmittance or absorbance. Therefore, the absorbance (A) and the transmittance (T) are defined as:

$$T = I/I_o \text{ or } \%T = (I/I_o) \times 100 \tag{16}$$

$$A = \log I_o / I = -\log T \tag{17}$$

The Beer-Lambert Law states that the absorbance is proportional to the molecular concentration of the solute and also a function of length of the path of radiation through the sample. The Beer-Lambert law is defined by the following equation:

$$A = \varepsilon bc \tag{18}$$

where c is the concentration (in mol L^{-1}) of absorbing species and b is the absorption path length (thickness of the absorbing medium) (in cm), ε is the molar absorptivity or the molar extinction coefficient of the substance (commonly expressed in L mol^{-1} cm^{-1}). ε is a constant value and is the characteristic of molecule or ion to absorb light in a given at a particular wavelength.

This rule is limited in that it requires a low concentration solution and a homogeneous solution. The light that is through the solution needs to be a monochromatic light.

Deviations from the Beer–Lambert Law

Beer's law describes the absorption behavior of media containing relatively low analyte concentrations. It is a limiting law. At high concentration usually is more than 0.01 M, the extent of solute-solvent interactions, solute-solute interactions, or hydrogen bonding can affect the analyte environment and its absorptivity. Beer's law strictly applies only when measurements are made with monochromatic source radiation.

The diagram of UV/vis spectroscopy is shown in Figure 48. The basic parts of a spectrophotometer are made up of the following components, light source (UV and visible), holder for the sample, diffraction grating in monochromator or prism to separate the different wavelengths of light, detector, signal processor and readout. A spectrophoto- meter can be either single beam or double beam. In a single beam instrument all of the light passes through the sample cell. I_o must be measured by removing the sample. This was the earliest design and is still in common use in both teaching and industrial labs. For double-beam instrument, the light is split into two beams before it reaches the sample. One beam is used as the reference; the other beam passes through the sample. The reference beam intensity is taken as 100% Transmission (or 0 Absorbance) and the measurement displayed is the ratio of the two beam intensities.
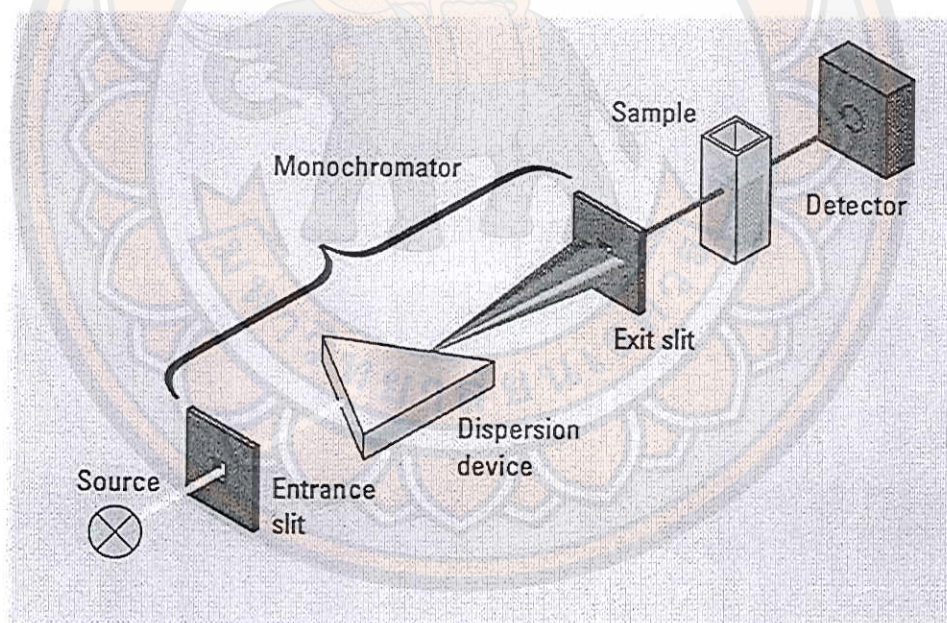
Figure 48 Diagram of single beam UV-visible spectrometry [108]

Fluorescence spectroscopy

Fluorescence spectroscopy is a very sensitive analytical tool that has wide ranges of application in various disciplines of scientific and medical research. Fluorescence is now a dominant methodology because there is no longer the need for the expense and difficulties of handling radioactive tracers for most biochemical measurements.

Luminescence is the emission of light from any substance, and occurs from electronically excited species. Luminescence is formally divided into two types of light emissions including fluorescence and phosphorescence. The emission of photons accompanying de-excitation is then called photoluminescence (fluorescence, phosphorescence or delayed fluorescence), which is one of the possible physical effects resulting from interaction of light with matter. The emission of fluorescence or phosphorescence depends on the nature of the excited state. For fluorescence, the emission of photon came from the electron in excited singled state, which the electron in the excited orbital is paired (by opposite spin). This process occurs rapidly. The emission rates of fluorescence are about $10^8 \, s^{-1}$. The fluorescence lifetime is near 10 ns (10×10^{-9} s). Phosphorescence is emission of light from triplet excited states, in which the electron in the excited orbital has the same spin orientation as the ground-state electron. Transitions to the ground state are forbidden. The emission rates are slow (10^3 to $100 \, s^{-1}$). Therefore, phosphorescence lifetimes are typically milliseconds to seconds. Even longer lifetimes are possible, as is seen from "glow-in-the-dark" toys.

Fluorescence typically occurs from aromatic molecules. Some typical fluorescent substances (fluorophores) are shown in Figure 49.
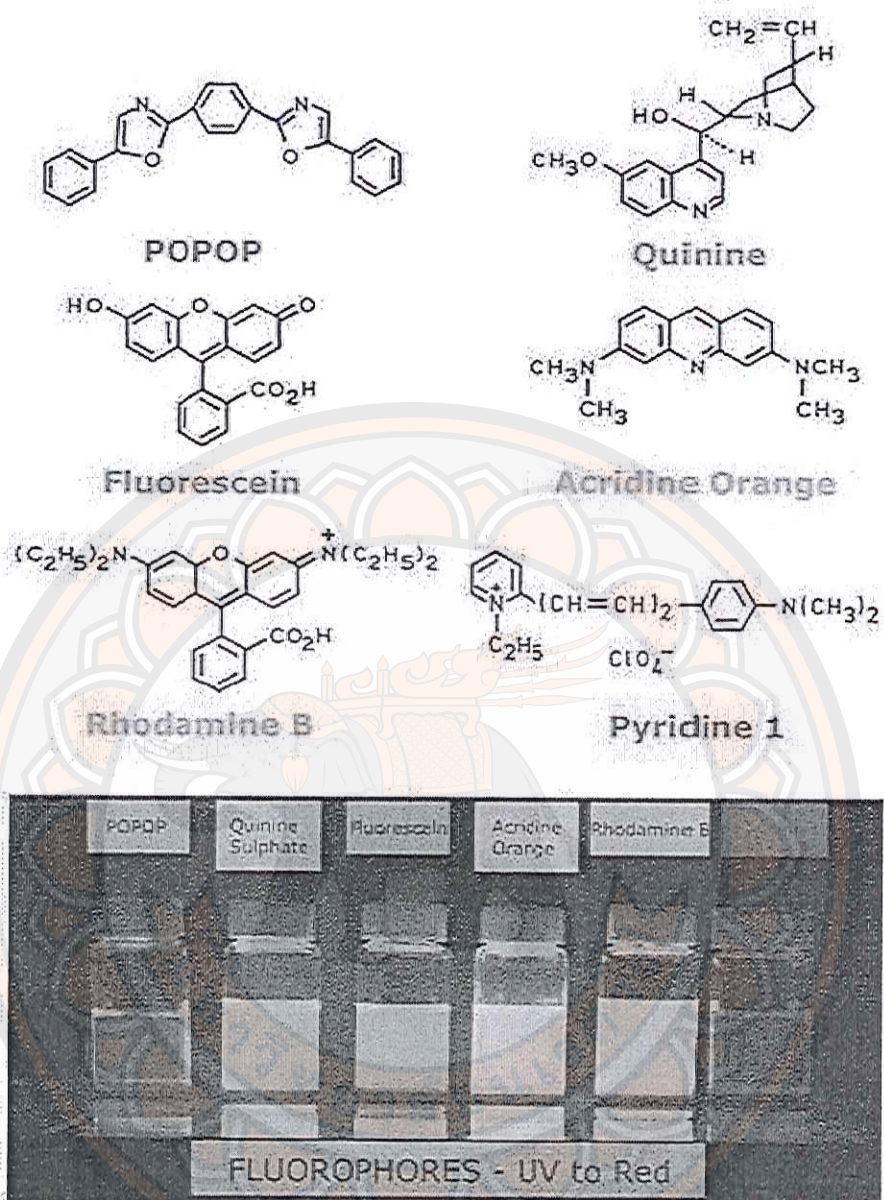
Figure 49 Structures of typical fluorescent substances [110]

Jablonski diagram

Jablonski diagrams (Figure 50) are often used for discussing light absorption and emission. The diagrams are used in a variety of forms, to illustrate various molecular processes that can occur in excited states.

When molecules absorb the light, several processes usually occur. The molecule is usually excited to higher vibrational level of either S_1 or S_2. The excited molecules try to de-excite to lower energy, which is more stable state. The molecules rapidly relax to the lower vibrational level. For example, if the excited molecules are in S_2, the molecule can return to the lower vibrational energy level, S_1, without change the electronic spin. This process is called *internal conversion* (IC) and generally occurs within 10^{-12} s or less. Since fluorescence lifetimes are typically near 10^{-8} s, internal conversion is generally complete prior to emission. In solution, this process is followed by a vibrational relaxation towards the lowest vibrational level of the final electronic state. The excess vibrational energy can be indeed transferred to the solvent during collisions of the excited molecule with the surrounding solvent molecules.

From S_1, internal conversion to S_0 is possible but is less efficient than conversion from S_2 to S_1, because of the much larger energy gap between S_1 and S_0. Therefore, internal conversion from S_1 to S_0 can compete with emission of photons. Emission of photons accompanying the $S_1 \rightarrow S_0$ relaxation is called *fluorescence*. An interesting consequence of emission to higher vibrational ground states is that the emission spectrum is typically a mirror image of the absorption spectrum of the $S_0 \rightarrow S_1$ transition. This similarity occurs because electronic excitation does not greatly alter the nuclear geometry. Hence the spacing of the vibrational energy levels of the excited states is similar to that of the ground state. As a result, the vibrational structures seen in the absorption and the emission spectra are similar.

In addition, molecules in the S_1 state can undergo a spin conversion to the first triplet state T_1. Emission from T_1 is termed *phosphorescence*, and is generally shifted to longer wavelengths (lower energy) relative to the fluorescence. Conversion of S_1 to T_1 is called *intersystem crossing* (ISC). Intersystem crossing may be fast enough (10^{-7}-10^{-9} s) to compete with other pathways of de-excitation from S_1 (fluorescence and internal conversion $S_1 \rightarrow S_0$). In fact, the transition $T_1 \rightarrow S_0$ is forbidden. However, if the spin-orbit coupling is large, the transition is possible.

The probability of intersystem crossing depends on the singlet and triplet states involved. If the transition $S_0 \rightarrow S_1$ is of $n \rightarrow p$ type for instance, intersystem crossing is often efficient. It should also be noted that the presence of heavy atoms (i.e. whose atomic number is large, for example Br, Pb) increases spin–orbit coupling and thus favors intersystem crossing and thus enhance phosphorescence quantum yields.
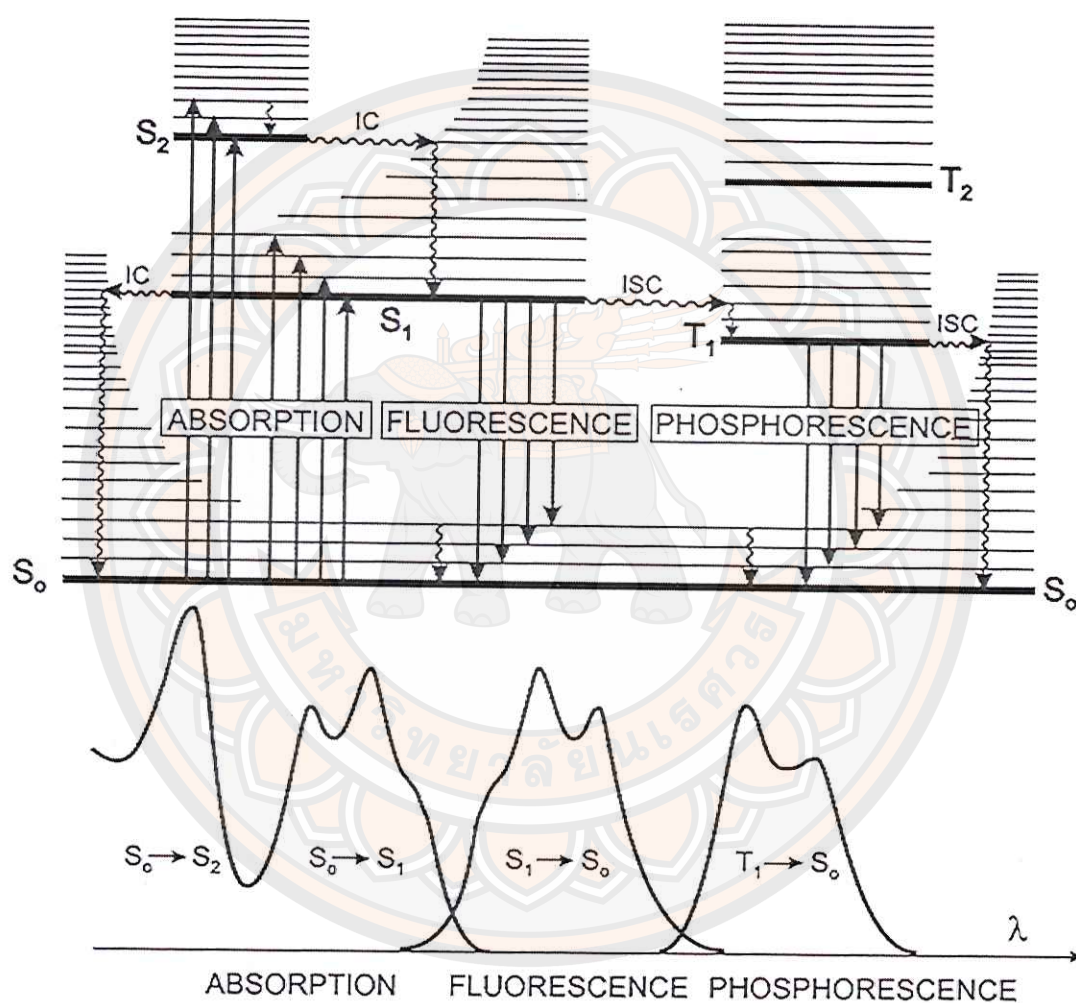
Figure 50 Jablonski diagram and illustration of the relative positions of absorption, fluorescence and phosphorescence spectra [109]

Fluorescence quantum yield

The fluorescence quantum yield (Φ_F) is the fraction of excited molecules that return to the ground state S_0 with emission of fluorescence photons.

$$\Phi_F \frac{k_r^S}{k_r^S + k_{nr}^S} = k_r^S \tau_S \tag{19}$$

where the rate constants for the various processes will be denoted as follows:

k_r^S : rate constant for radiative deactivation $S_1 \rightarrow S_0$ with emission of fluorescence.

k_{ic}^S : rate constant for internal conversion $S_1 \rightarrow S_0$.

k_{isc} : rate constant for intersystem crossing.

k_{nr}^S : non-radiative rate constant such that $k_{nr}^S = k_{ic}^S + k_{isc}$

τ_S : lifetime of excited state S_1 given by $\tau_S = \frac{1}{k_r^S + k_{nr}^S}$

In other word the, fluorescence quantum yield is the ratio of the number of photons emitted to the number absorbed (see equation 20). The quantum yield also gives the probability of the excited state being deactivated by fluorescence rather than by another, non-radiative mechanism.

$$\Phi_F = \frac{Emitted\ photon}{Absorbed\ photon} \tag{20}$$

The reliable method for measuring Φ_F is the comparative method. The method involves the comparison of the emission intensity of fluorescence standard material which is known Φ_F values and the test sample. Importantly, the fluorescence standard and the test sample must have the absorbance at excitation wavelength in the same range, which can be assumed to be absorbing the same number of photons. Hence, a simple ratio of the integrated fluorescence intensities of the two solutions (recorded under identical conditions) will yield the ratio of the quantum yield values. Since Φ_F for the standard sample is known, it is trivial to calculate the Φ_F for the test sample. The quantum yield of fluorescence standard materials is shown in Table 2.

Table 2 Lists of standard materials and their quantum yield [111]

Compounds	Solvents	Literature Quantum yield	Emission range (nm)
Cresyl violet	Methanol	0.54	600-650
Rhodamine 101	Ethanol + 0.01% HCL	1.00	600-650
Quinine sulfate	0.1M H_2SO_4	0.54	400-600
Fluorescein	0.1M NaOH	0.79	500-600
Norharmane	0.1M H_2SO_4	0.58	400-550
Harmane	0.1M H_2SO_4	0.83	400-550
Harmine	0.1M H_2SO_4	0.45	400-550
2-methylharmane	0.1M H_2SO_4	0.45	400-550
Chlorophyll A	Ether	0.32	600-750
Zinc phthalocyanine	1% pyridine in toluene	0.30	660-750
Benzene	Cyclohexane	0.05	270-300
Tryptophan	Water, pH 7.2, 25°C	0.14	300-380
2-Aminopyridine	0.1M H_2SO_4	0.60	315-480
Anthracene	Ethanol	0.27	360-480
9,10-diphenyl anthracene	Cyclohexane	0.90	400-500

To measurement the fluorescence quantum yield, the standard samples should be chosen to ensure they absorb at the excitation wavelength of choice for the test sample, and, if possible, emit in a similar region to the test sample. For preparing the solution concentration, the absorbance of solution should never exceed 0.1 for the 10 mm fluorescence cuvette. All solutions were measured the fluorescence intensity after that the spectra of both standard material and sample were integrated the spectra area. The plot of integrated area and the absorbance (see Figure 51) is useful for calculating the fluorescence quantum yield as following equation:

$$\Phi_X = \Phi_{ST} \left(\frac{Grad_X}{Grad_{ST}} \right) \left(\frac{\eta_X^2}{\eta_{ST}^2} \right) \tag{21}$$

Where the subscripts ST and X are denoted as standard and sample, respectively. Φ is the fluorescence quantum yield. Grad is the slope from the plot of integrated fluorescence intensity vs absorbance. η is the refractive index of the solvent.
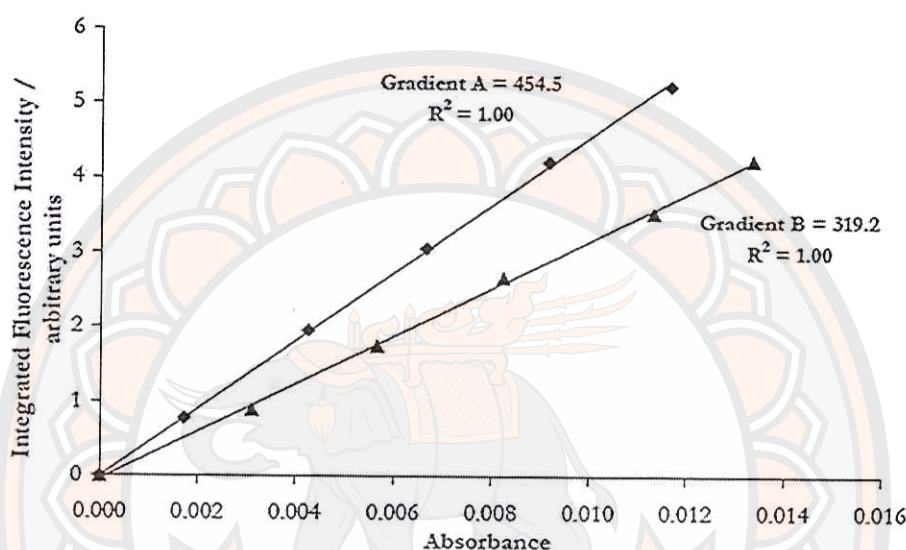
Figure 51 Plot of integrated fluorescence intensity and the absorbance [111]

Generally fluorescence spectrometers consist of light sources, filter and monochromators, and detector. Most fluorescence spectrometers can record both excitation and emission spectra. A schematic representation of a fluorescence spectrometer is shown in Figure 52. The light source produces high intensity light sources to bombard a sample with as many photons as possible. Because this technique is very sensitivity and the sensitivity of the analysis depends on the intensity of light, this technique requires light with high intensity. The light sources usually made from xenon-arc lamp or mercury-arc lamp, which provides higher intensity than tungsten or hydrogen. The light is either passed through a filter, selecting a fixed wavelength, or excitation monochromator, which allows you to select a wavelength of interest to use as the exciting light. The filtered light passes into the sample cell causing fluorescent emission by fluorphors within the sample. Emitted light enters the emission monochromator, which is positioned at a 90° angle from the excitation light path to

eliminate background signal and minimize noise due to stray light. Again, emitted light is passed through a filter of emission monochromater and finally enter to the photomultiplier tube. The signal is amplified and creates a voltage that is proportional to the measured emitted intensity.
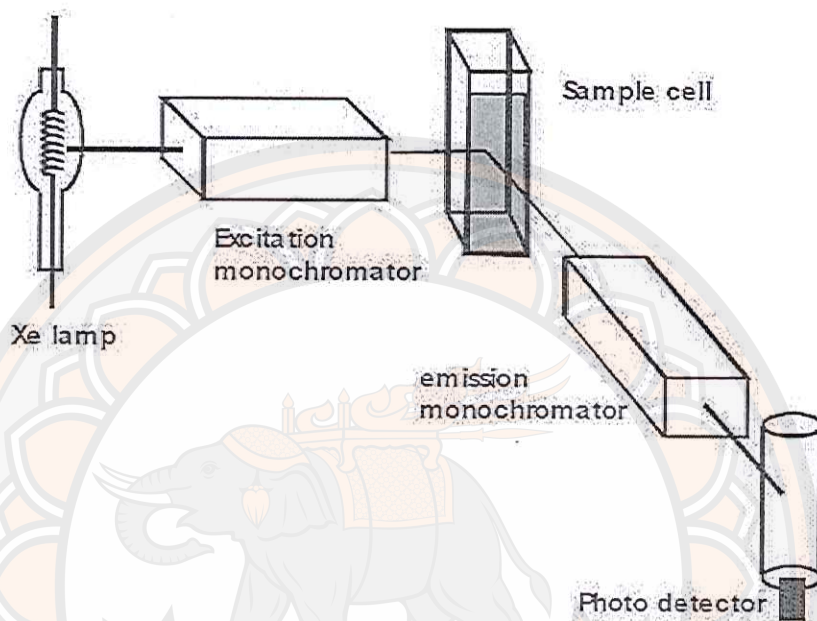
Figure 52 Schematic representation of a fluorescence spectrometer

Source: http://www.thefullwiki.org/Spectrofluorometer

The fluorescence intensity is proportional to the concentration only for low absorbance. Deviation from a linear variation increases with increasing absorbance (Table 3). Moreover, when the concentration of fluorescent compound is high, inner filter effects reduce the fluorescence intensity as a result of quenching. In particular, the photons emitted at wavelengths corresponding to the overlap between the absorption and emission spectra can be reabsorbed (radiative transfer). Consequently, when fluorometry is used for a quantitative evaluation of the concentration of a species, it should be kept in mind that the fluorescence intensity is proportional to the concentration only for diluted solutions. Other parameters that can cause quenching include presence of impurities, increased temperature, or reduced viscosity of the solution media.

Table 3 Deviation from linearity in the relation between fluorescence intensity and concentration for various absorbances [109]

Absorbance	Deviation (%)
10^{-3}	0.1
10^{-2}	1.1
0.05	5.5
0.10	10.6
0.20	19.9

Electron microscopy

An electron microscope is a type of microscope that uses a beam of electrons to illuminate a specimen and create a highly-magnified image. The electron microscope uses electromagnetic lenses to focus onto a specimen a beam of electrons traveling through an evacuated tube. The electron microscope has higher magnification of up to 2 million times and resolution reaches the order of 0.1 nm than that of normal light microscopes. The short wavelength of the electrons results in the greater resolving power of the electron microscope, the wavelengths being about 10,000 times shorter than that of normal light.

There are two types of electron microscopes are available:

1. Transmission electron microscope (TEM): the TEM use the electron beam that is transmitted through an ultrathin specimen. An image is formed from the interaction of the electrons transmitted through the specimen. TEM has higher resolution as compare to other microscope techniques. The magnification is approximately 0.1 nm.

2. Scanning electron microscope (SEM): SEM is generally used to study the detailed morphology and surface characteristics of the samples by scanning the electron on the sample's surface. The images obtained from the SEM would be the appearance of a 3D image. The magnification of the SEM is not as high as that of the TEM.

The comparison between optical microscopy and electron microscopy is summarized in Table 4.

Table 4 Comparison between optical microscopy and electron microscopy [112]

	Optical microscopy	Electron microscopy	
		TEM	SEM
Source	Light rays	Electrons	Electrons
Lens	Glass	Electromagnetic lens	Electromagnetic lens
Size of studied objects	0.2-200 mm	0.2 nm -20 mm	4 nm – 4000 mm
Magnification	5-2000X	1000X-500,000X	10X-100,000X
Objects	Surface or bulk structure	Bulk structure, surface structure (replicate)	Surface structure
Specimen environment	Ambient	High vacuum	High vacuum
Image visibility	By eye	Fluorescent screen	Cathode Ray Tube
Image type	2D	2D	3D

Image formation in the electron microscope is dependent on the acquisition of signals produced from the electron beam and specimen interactions. When the electron beam interaction with the specimen, the interactions are responsible for a multitude of signal types including backscattered electrons, secondary electrons, X-Rays, Auger electron and cathadoluminescence (see Figure 53). Some of them are used in TEM. For example, elastic scatter is the dominant component of the total scatter occurring in the TEM. It is also the principle source of contrast in TEM images and intensity distributions in diffraction patterns. The backscattered and secondary electrons are useful for SEM.
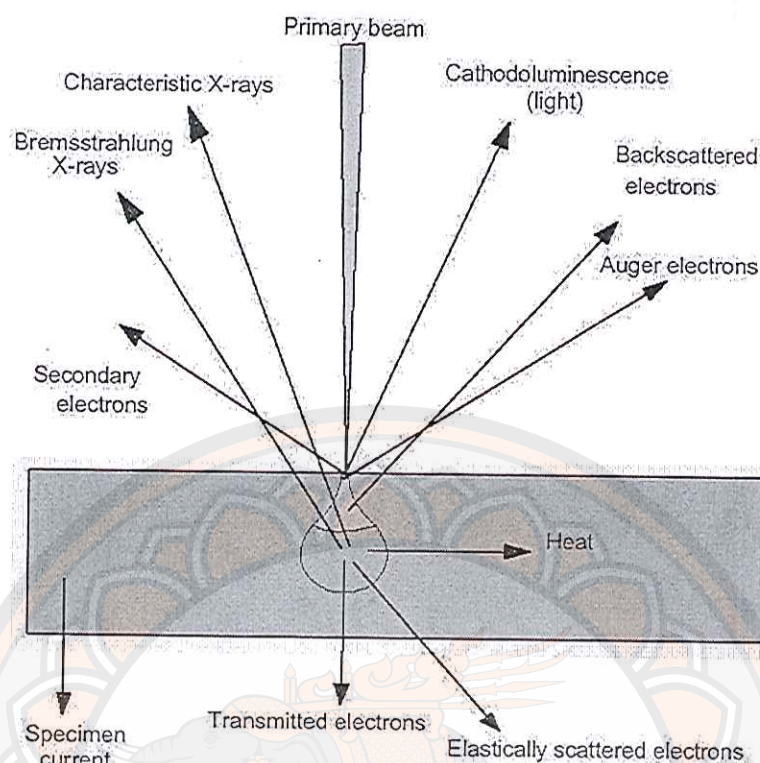
Figure 53 Signals from electron-sample interaction [112]

Transmission electron microscopy

Transmission electron microscopy (TEM) was the first type of electron microscope to be developed by Max Knoll and Ernst Ruska in Germany in 1931. Its pattern is exactly same as the light transmission microscope except that a focused beam of electrons is used instead of light to see through the specimen. TEM use the electron beam that is transmitted through an ultrathin specimen. An image is formed from the interaction of the electrons transmitted through the specimen. The image is magnified and focused onto an imaging device, such as a fluorescent screen, on a layer of photographic film, or to be detected by a sensor such as a CCD camera.

The TEM contains four main parts including an illumination system, a specimen stage, an imaging system and an image recording system as shown in Figure 54. The illumination consists of electrons source (electron gun) and a condenser lens. The electron source is the heart of the illumination system which typically uses LaB_6 thermio emission source or a field emission source. The electron gun generates the electrons then the condenser lenses will focus the electron to the illuminating beam on

the specimen. The specimen must be thin enough to transmit the electrons, typically 0.5 μm or less. The specimen stage locates between the illumination and imaging systems. The imaging system consists of an objective lens, an eye piece/intermediate and projector lenses. The objective lens will focus the beam after it passes through the specimen and forms an intermediate image of the specimen. The objective lens is the heart of the TEM, which determines the limit of image resolution. The intermediate lens and the projection lens magnify portions of the intermediate image to form the final image onto the viewing device at the bottom of the column. The magnification is up to 1.5 million. The image recording system including fluorescent screen, which emitted light when impacted by the transmitted electrons, or CCD camera converts the electron signal to an image. In TEM, all of the process must maintain at high vacuum level.

Images in TEM are usually dominated by three types of contrast, diffraction contrast, phrase contrast and mass-thickness contrast. The diffraction contrast determines a specimen which has a crystalline nature. The diffraction contrast is produced due to a local distortion in the orientation of the crystal. Thus, the diffracted intensity of the incident electron beam is perturbed, leading to contrast observed in the bright-field image. For phase contrast, the differences in intensity arise from interference effects between scattered and unscattered electrons which pass through the objective aperture. This type of contrast is sensitive to the atom distribution in the specimen. Mass-thickness or atomic number produced contrast. This type is enhanced by atomic number, density and specimen thickness. Atomic with different atomic numbers exhibits different powers of scattering. This type of image is usually performed for non-crystals specimen such as amorphous polymer and biology sample. [112, 113]
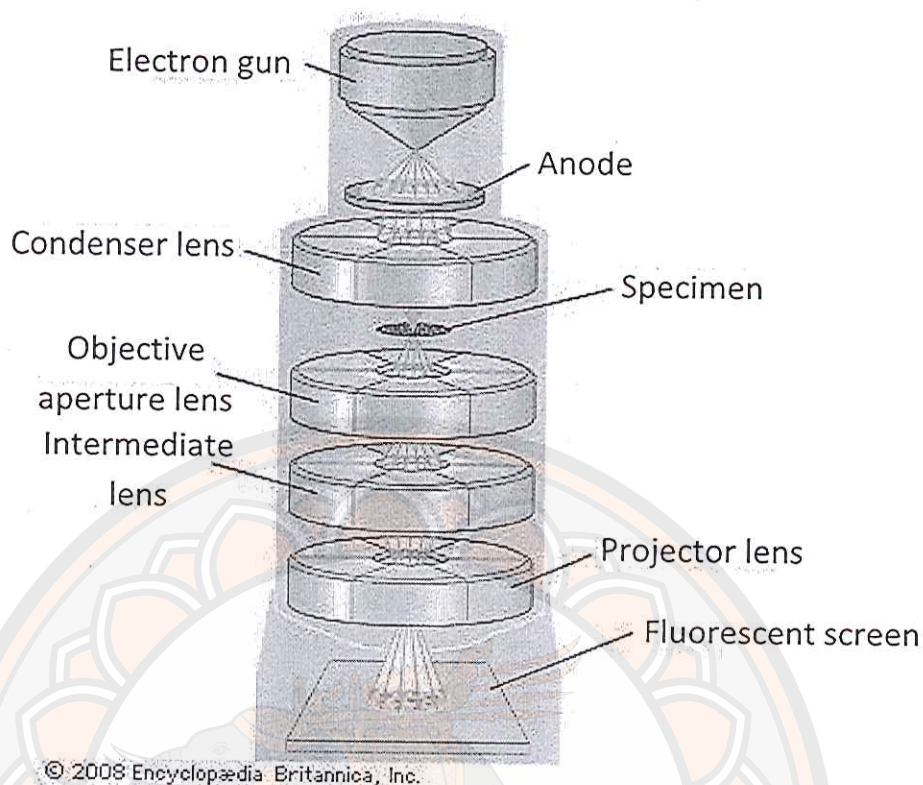
Figure 54 Schematic representation of a TEM

Source: http://global.britannica.com/EBchecked/topic/602949/transmission-electron-microscope-TEM

Scanning electron microscopy

Scanning electron microscope (SEM) is a type of electron microscope that images the sample surface by scanning it with a high-energy beam of electrons in a raster scan pattern. The electrons interact with the atoms that make up the sample producing signals that contain information about the sample's surface topography, composition and other properties such as electrical conductivity.

The components of SEM are shown in Figure 55. The *electron source or electron gun*, which is available for either thermionic or field emission, produces the electrons to enter the system. The electron produced from field emission has more intensity than that of thermionic. The electrons will be accelerated to pass thought the column by the accelerating voltage in the range of 1-40 kV. The movement direction of electron is controlled by two series of electromagnetic lens. The amount of

electrons is controlled by the aperture which has different sizes depending on the usages. The electrons that enter to column are collected by *condenser lens*. This lens is the most important part in term of the control the optical properties of electron. The condenser lens help to adapt the size of electron beam in which small or large. For high contrast image, the electron beam should be small. The *objective lens* serves to focus the electron beam to fall on the surface of the sample. The *scan coils* help to scan electrons on the surface. After the scanning electron beam onto the specimen will produce secondary electron. The signal is recorded by *detector* and then converted to electronic signals. After process the signal, the image will be created on the screen. [112, 114]
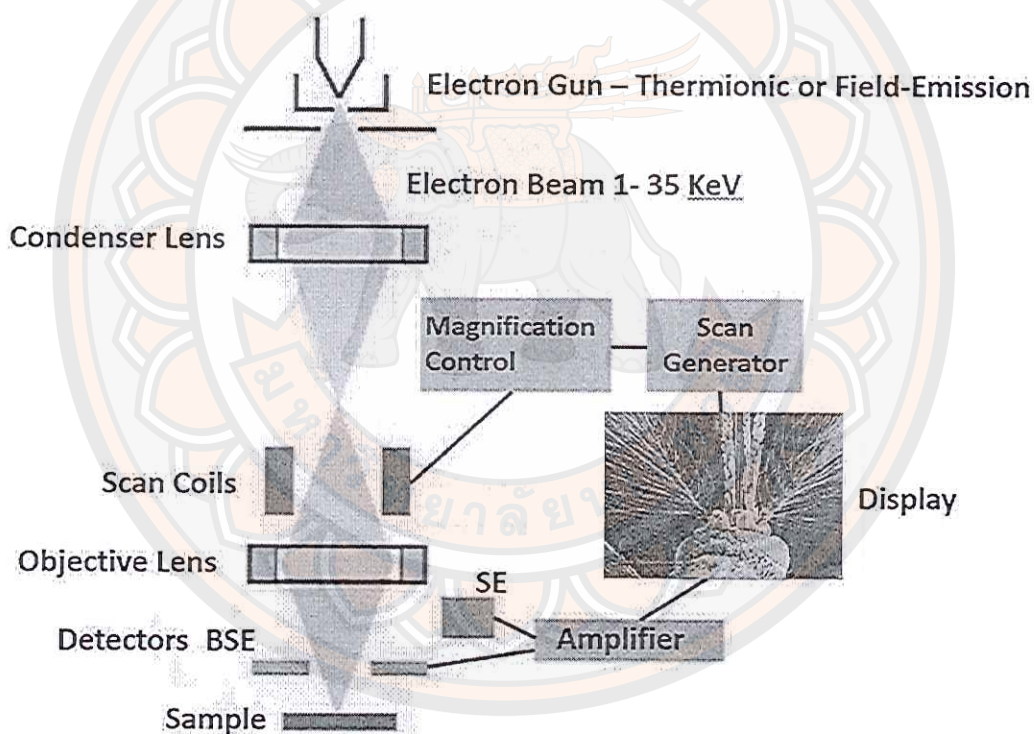
Figure 55 Schematic representation of a SEM

Source: http://zenofstem.com/project/using-the-sem/

The scanning electron microscope has many advantages over optical microscopes. The SEM has a large depth of field, which allows more of a specimen to be in focus at one time. The SEM also has much higher resolution, so closely spaced specimens can be magnified at much higher levels. Because the SEM uses electromagnets rather than lenses, the researcher has much more control in the degree of magnification. All of these advantages, as well as the actual strikingly clear images, make the scanning electron microscope one of the most useful instruments in research today.

Atomic force microscopy

Atomic force microscopy (AFM) is the most widely used form of scanning probe microscopy (SPM), which provides nanometer-scale mapping of numerous sample properties in essentially any environment. This technique measures the interaction between tip and sample. Piezoelectric tube scanner allow accurate, sub-angstrom positioning of the tip or sample in three dimensions. Optical deflection systems and microfabricated cantilevers can detect forces in AFM down to the picoNewton range.

The AFM measures ultrasmall force (less than 1 nN) present between the AFM tip surface and the sample surface. This technique relies on a scanning technique to produce very high resolution, 3-D image of sample surface. The small forces between tip and sample are measured by measuring the motion of a very flexible cantilever beam with an ultrasmall mass. AFM is capable of investigating the surface of both conductors and insulators on an atomic scale. The instruments can be used in any environment, such as ambient air, various gas, liquids, vacuum, at low temperatures (lower than about 100K) and at high temperature. The AFM has become a popular surface profiler for topographic and normal force measurement on the micro- to nanoscale.

There are the basic components of AFM.

1. The AFM probe consists of a sharp tip mounted on a soft cantilever.

2. The optical lever measures the cantilever deflections.

3. The feedback loop allows for monitoring the interaction forces between the molecules on the tip with the ones on the cell surface.

4.   The piezoelectric scanner moves the tip relative to the sample in a 3-D pattern.

5.   The conversion system from raw data acquired by the instrument into an image or other useful display.

In the principle of operation of the AFM (see Figure 56), sample mounted on a piezoelectric scanner is scanned against a short tip. The cantilever deflection is usually measured using a laser deflection technique. The force (in contact mode) or the force gradient (in noncontact mode) is measured during scanning. The sample is mounted on a PZT tube scanner, which consists of separate electrodes used to precisely scan the sample in the x-y plane in a raster pattern and to move the sample in the vertical (z) direction. A sharp tip at the free end of a flexible cantilever is brought into contact with the sample. The feature on the sample surface causes the cantilever to deflect in the vertical and lateral directions as the sample moves under the tip. A laser beam from a diode laser is directed by a prism onto the back of a cantilever near its free end, tilted downward at about 10° with respect to the horizontal plane. The reflected beam from the vertex of the cantilever is directed through a mirror onto a quad photodetector. The difference in signal between the top and bottom photodiodes provides the AFM signal, which is a sensitive measure of the cantilever vertical deflection. The topographic feature of the sample causes the tip to deflect in the vertical direction as the sample is scanned under the tip. This tip deflection will change the direction of the reflected laser beam, changing the intensity difference between the top and bottom sets of photodetectors (AFM signal).
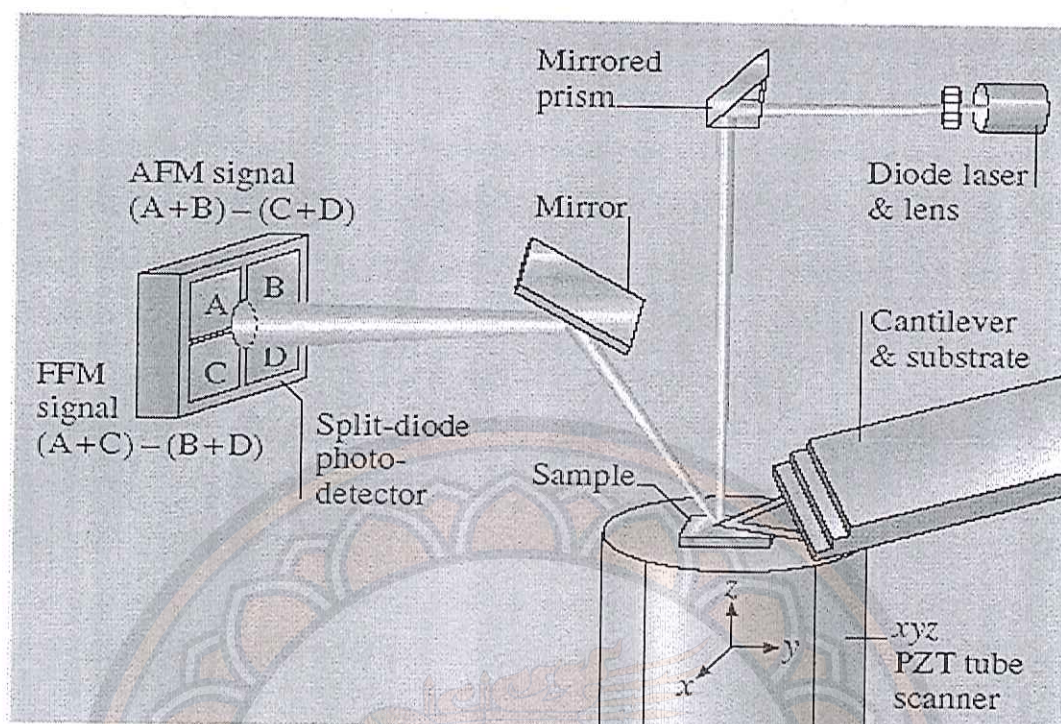
Figure 56 Principle operation of AFM [115]

AFM can operate in contact mode, noncontact mode and tapping mode. In *contact mode* or static mode, a shape tip is brought into contact with the surface of the sample. During initial contact with the surface, the atoms at the end of the tip experience a very weak repulsive force due to electronic orbital overlap with the atoms in the surface of the sample. The force acting on the tip causes the cantilever to deflect, which is measured by tunneling, capacitive, or optical detectors. The deflection can be measured to within 0.02 nm, so a force as low as 0.2 nm can be detected for typical cantilever spring constant of 10 N/m. In *noncontact mode* or dynamic mode, the tip is brought into close enough to the sample (within a few nanometers), but not contact with the sample. The cantilever is oscillated at a frequency slightly above its resonant frequency where the amplitude of oscillation is typically a few nanometers (<10 nm). Decrease in resonant frequency caused by van der Waals force combined with the feedback loop system maintains a constant oscillation amplitude or frequency by adjusting the average tip-to-sample distance to construct a topographic image of the sample surface. The *tapping mode* is the most AFM operation used for topography measurement. In the tapping mode, the oscillating

tip slightly taps the surface during scanning at the resonant frequency of the cantilever (70-400 kHz) with constant (20-100 nm) amplitude of vertical oscillation and a feedback loop keeps the average normal force constant. The electrostatic forces increase when tip gets close to the sample surface, therefore the amplitude of the oscillation decreases. The amplitude of cantilever oscillation is sensed and feedback loop maintains constant oscillation amplitude by moving the scanner vertically at every x, y data point.

The key component in an AFM is the measurement of force on the AFM tip due to its interaction with the sample. A cantilever (with a sharp tip) with an extremely low spring constant is required for high vertical and lateral resolutions at small force (0.1 nN or lower), but a high resonant frequency is desirable (about 10 to 100 kHz) to minimize the sensitivity to building vibrations, which occur at around 100 Hz. This requires a spring with an extremely low vertical spring constant (typically 0.05 to 1 N/m) as well as a low mass (on the order of 1 ng). Silicon nitride (Si_3N_4), Si and diamond cantilevers are the most common as shown in Figure 57. The Young's modulus and the density are the material parameters that determine the resonant frequency, aside from the geometry as summarized in Table 5. Hardness is an important indicator of the durability of the cantilever. Si_3N_4 cantilever less expensive than those made of the other materials. They are very rugged and well suited to imaging in almost all environments. The most commonly used cantilever beam is the 115 μm-long, wide-legged cantilever (vertical spring constant = 0.58 N/m). Cantilever with smaller spring constant should be used on softer samples.

To obtain atomic resolution with the AFM, the spring constant of the cantilever should be weaker than the equivalent spring between atoms. The cantilever beam with a spring constant of about 1 N/m or lower is desirable. Tips must be as sharp as possible, and tip radii of 5 to 50 nm are commonly available.

Table 5 Properties of materials used for fabricating cantilever [115]

Property	Young's Modulus (E) (GPa)	Density (ρg) (kg/m^3)	Microhardness (GPa)	Speed of sound (m/s)
Diamond	900-1050	3515	78.4-102	17000
Si$_3$N$_4$	310	3180	19.6	9900
Si	130-188	2330	9-10	8200
W	350	19310	3.2	4250
Ir	530	-	≈3	5300
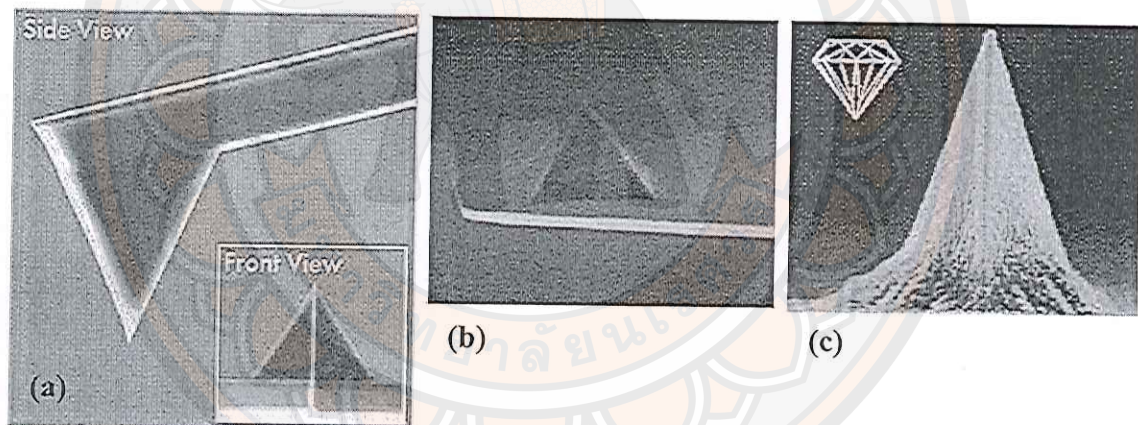
Figure 57 Cantilevers made of (a) Si, (b) Si$_3$N$_4$ and (c) diamond [115]

CHAPTER IV

EXPERIMENTALS PROCEDURES

Materials

The conjugated polymers, MEH-PPV and rr-P3OT, were purchased from Sigma–Aldrich. Number average molecular weight (M_n) and polydispersity (M_w/M_n) of the polymers determined by gel permeation chromatography (GPC) with polystyrene standard are 120,000 g/mol (M_w/M_n = 4.3) for MEH-PPV and 58,300 g/mol (M_w/M_n = 2.3) for rr-P3OT. Tetrahydrofuran (THF) was used as a solvent in the GPC measurement. It has been known that the GPC measurement of rigid rod polymer usually overestimates the absolute molecular weight by a factor of about 2–2.3 [116, 117]. By comparing the M_n of GPC with MALDI-TOF data, the M_n of rr-P3OT in this study is approximately 26,900 g/mol [117] and the contour length of rr-P3OT in this study is ~51 nm [116]. The regioregularity of rr-P3OT provided by the supplier is about 98%. The solvents used in this study are analytical grade. The properties of solvents and the polymer used in this study are shown in Table 6.

Instruments

Absorption spectra of conjugated polymer solutions were recorded by using Analytica Specord 100 UV/vis spectrometer with 4 and 10 cm thick quartz cuvettes, depending on the polymer concentration. The measurements of PL emission spectra were carried out on Perkin-Elmer LS55 spectrometer.

Morphology of the polymer films were measured by using atomic force microscopy (AFM) (SPI3800N Nanoscope II, Seiko Instrument Inc., Japan). The transmission electron microscopy (TEM, Tecnai 12, D291) and scanning electron microscopy (SEM, LEO 1455 VP) were used to study the morphology and size distribution of the conjugated polymer nanoparticle and polymer film as well.

Table 6   Properties of solvents and polymers used in study [36, 39, 118, 119, 120]

Sample	Boiling point (°C)	Density (g cm⁻³)	Reflective index	Dielectric constant	Solubility parameter (δ, $J^{1/2}$ cm⁻³ᐟ²)
rr-P3OT	-	-	-	-	18.2
Thiophene	84.0	1.0649	1.5289	2.7	20.2
Chlorobenzene	131.7	1.1058	1.5241	5.7	19.6
Pyridine	115.2	0.9819	1.5059	13.3	21.8
Toluene	110.6	0.8668	1.4961	2.4	18.2
Cyclohexane	80.7	0.7739	1.4235	2.0	16.8
n-Hexane	68.7	0.6606	1.3727	1.8	14.9
n-Octane	125.7	0.6986	1.3944	1.9	15.5
Ethanol	78.3	0.7893	1.3611	25.3	26.5
n-Butanol	117.7	0.8095	1.3988	17.8	23.1
n-Hexanol	157.6	0.8136	1.4178	13.0	21.5
n-Octanol	195.2	0.8262	1.4295	10.3	21.0
n-Decanol	231.1	0.8297	1.4372	7.9	20.3

Study of conformational change, intrachain aggregation and photophysical properties of *rr*-P3OT

rr-P3OT solutions were prepared by dissolving powder sample in good solvents, chlorobenzene (CRB) and pyridine (PRD), assisted by mechanical stirring and ultrasonication. In PRD solvent, the polymer solution was stirred for several days to achieve complete dissolution. The solution appears clear to naked eyes. To vary local polymer–solvent interactions, poor solvents were added into the systems. In this study, the dissolved polymer solutions in solvents were injected into a mixture of solvent-nonsolvent under stirring. Concentration of the polymer was kept constant at 0.001 mg/mL. An inner-filtered effect is negligible at this concentration. When cyclohexane was used as a poor solvent, the ratio of the cyclohexane was varied from 0 to 100 %v/v. In this system, the properties of solution are independent of aging time.

To induce larger extent of chain coiling, a nonsolvent, hexane, was added into the *rr*-P3OT solution in cyclohexane. Ratio of hexane was increased up to 90% v/v. When the hexane ratio was above 50% v/v, it was important to use freshly prepared solutions to avoid the polymer precipitation. Absorption spectra of polymer solutions were recorded by using Analytica Specord 100 UV/vis spectrometer with 4 and 10 cm thick quartz cuvettes, depending on the polymer concentration. The measurements of PL emission spectra were carried out on Perkin-Elmer LS55 spectrometer.

Study of aggregation of *rr*-P3OT in different local environments

Formation of non-emissive and emissive aggregates

The solutions of *rr*-P3OT in CRB and PRD were injected into a mixture of solvent–nonsolvent under stirring. In this study, ethanol (EtOH) is used as a poor solvent. Ratio of the EtOH was increased to 99 %v/v. Concentration of the *rr*-P3OT was kept constant at 0.001 mg/mL. An inner-filtered effect is negligible at this concentration. In these systems, freshly prepared solutions were used to avoid the polymer precipitation. Absorption spectra of the solutions were recorded by using Analytica Specord 100 UV/vis spectrometer with a 4 cm thick quartz cuvette. The measurements of PL and PLE spectra were carried out on Perkin-Elmer LS55 spectrometer.

Control over the photophysical properties of aggregates

The solution of *rr*-P3OT was prepared by dissolving *rr*-P3OT powder in toluene (TOL) assisted by ultrasonication. The alternation of polymer-solvent interactions is performed by varying types of poor solvents. The poor solvents are divided into two groups, alkane group and alcohol group. Hexane is a representative for alkane group. A series of linear alcohols, ethanol, butanol, hexanol, octanol and decanol, are used to tune the solubility parameter. The solubility parameter of solvents is shown in Table 6. Ratio of the poor solvent was increased to 99% v/v. Concentration of the *rr*-P3OT was kept constant at 0.001 mg/mL to avoid the inner-filtered effect. The freshly prepared solutions were used to measure the absorption, PL and PLE spectra.

Fluorescence quantum yield measurement

The quantum yield of rr-P3OT (Φ_X) was measured by using 0.1 M NaOH aqueous solution of fluorescien ($\Phi_{ST} = 0.79$) as a standard. A series of solution exhibiting absorbance less than 0.1 was used. The calculation was performed by using the following equation (25).

$$\Phi_X = \Phi_{ST}\left(\frac{slope_X}{slope_{ST}}\right)\left(\frac{\eta_X^2}{\eta_{ST}^2}\right) \tag{25}$$

The slopes ($slope_X$ and $slope_{ST}$) were obtained from the plots between integrated area of PL spectra and absorbance at the excitation wavelength. The refractive indices of solvent (η_X) and standard (η_{ST}) were taken into account in the calculation. In the system of mixtures, refractive indices were estimated by interpolation from those of the pure solvents.

Morphology of rr-P3OT film

Morphology of the self-assembled rr-P3OT films was explored by atomic force microscopy (AFM) (SPI3800N Nanoscope II, Seiko Instrument Inc., Japan) operating in a dynamic contact mode. The cantilever was fabricated from Si_3N_4 with a spring constant of about 15 N/m. At least three areas were scanned for each sample. To minimize the line broadening effect due to a finite shape of AFM tip, the width of nanostructures was measured as full width at half height.

Samples for AFM measurement were prepared by drop casting from 0.05 mg/mL solutions. The solution droplet was allowed to dry in a clean atmosphere under ambient condition. Three samples were prepared for each condition. Polished silicon wafer, used as a substrate, was freshly cleaned before the deposition. The substrate was soaked in a piranha solution (7:3 v/v of conc. H_2SO_4 and 30% H_2O_2) at 80 °C for 1 h. It was rinsed by using deionized water and dried with nitrogen gas.

For scanning electron microscopy (SEM) measurement, the SEM images were recorded by using LEO 1455 VP microscope model. The rr-P3OT sample films were prepared by one drop of polymer solution in a polished silicon substrate. The concentration of polymer solution in mixture of toluene and 80 %v/v of series of alcohols including ethanol, butanol, hexanol and octanol keep constant at 0.001

mg/mL. The droplet of polymer solution was allowed to dry in a clean atmosphere under ambient condition. After the evaporation of solvents, the samples were coated with gold.

Study of conjugated polymer nanoparticles

Nanoparticles of conjugated polymers MEH-PPV and *rr*-P3OT were prepared by using reprecipitation method. The conjugated polymers were dissolved in tetrahydrofuran (THF) and dichloromethane (DCM) solvents and then diluted to concentration of 0.001 mg/mL. To prepare CPNs, each of 0.2 mL polymer solution was injected in a step-wise process into 32 mL of deionized water, while the mixtures were under continuous ultrasonication at 60 °C. The 0.2 mL addition of solution is equivalence to 8.3 g/L concentration of the organic solvents in water. This concentration is still lower than their water solubility (see Table 8). The mixtures appeared clear to naked eyes indicating complete miscibility. The time interval between each step was about 2 min, allowing the evaporation of organic solvents. The sum volume of polymer solution was 8 mL requiring the addition time of about 1.5 h. The ultrasonication process was continued for 30 min to ensure complete evaporation of the organic solvents. The resultant aqueous suspensions were filtered through 0.45 μm pore size cellulose acetate membrane. The CPN aqueous suspensions were clear and stable for months with no sign of agglomeration. The photophysical properties of thin films of conjugated polymer is use to compare the properties of CPNs. Thin films were prepared by drop-casting from 1 mg/mL solution onto quartz slide. The solution droplet was allowed to dry in a clean atmosphere under ambient condition. The AFM images reveal that the films exhibit rough surface with thickness ranging from about 30 to 400 nm. Absorbance of all films is less than 0.1.

The UV-vis absorption spectra of CPNs were recorded by employing Analytic Specord 100 spectrometer with 10 cm thick quartz cuvette, while the PL spectra were measured by using Perkin–Elmer LS55 spectrometer. Absorbance of the CPN aqueous suspensions is less than 0.4 (equivalence to 0.04 for 1 cm thick cuvette). Since the absorbance of conjugated polymer is very low, an inner-filtered effect in the PL measurement is negligible in all systems [109].

Morphology and size distribution of the CPNs were characterized by transmission electron microscopy (TEM, Tecnai 12, D291) and SEM (LEO 1455 VP). The samples for TEM were prepared by drop-casting from CPN aqueous suspensions onto copper grids coated with carbon film. For SEM samples, one drop of CPN aqueous suspensions was deposited on a polished silicon substrate. After the evaporation of water, the samples were coated with gold.

CHAPTER V

CONFORMATIONAL CHANGE, INTRACHAIN AGGREGATION AND PHOTOPHYSICAL PROPERTIES OF *rr*-P3OT

Introduction

Structural-property relationship of conjugated polymers has been a subject of interest in the past few decades. This is mainly due to their potential applications in various advanced technologies such as plastic solar cell [1, 2, 3, 4, 5], organic light emitting diode (OLED) [5, 6, 7, 8, 9], and organic field-effect transistors (OFET) [10, 11, 12]. Poly(3-alkylthiophene)s (P3ATs) is one class of conjugated polymer that receives tremendous attention. Advantages of the P3AT include high environmental stability and well-ordered semicrystalline structure [40, 41]. The close packing of conjugated backbone in their crystalline domains allows the overlap of π-orbitals, promoting charge carrier mobility [40, 41, 42, 43]. This characteristic is particularly important for plastic solar cell application where high degree of charge separation upon photoirradiation is desired [3, 4, 5]. The presence of alkyl side chains also allows high solubility in common organic solvents, which facilitates the fabrication of P3AT thin films in the devices via wet processes [40, 41].

It has been demonstrated that properties of conjugated polymers can be controlled by structural modification of main chain and/or side chains [5, 13, 16, 17, 41, 43, 55]. To optimize efficiency of the aforementioned devices, tremendous effort has been dedicated for synthesizing new classes of conjugated polymers. However, other molecular parameters such as interchain/intrachain aggregation and individual chain conformation also affect their properties significantly [33, 43, 121]. The stacking of conjugated backbone within aggregates promotes the overlap of π-orbitals, which in turn facilitates intersegmental delocalization of π electrons. The aggregation of conjugated polymers normally leads to the formation of new electronic species with lower HOMO–LUMO energy gap compared to that of the isolated chain. As the existence of aggregates strongly affects important properties of conjugated polymers such as charge carrier mobility, photo/electroluminescence intensity and color [7, 11,

29, 30, 31, 43], it is essential to understand molecular and experimental parameters dictating the aggregate formation. Previous studies reported by different groups have shown that the aggregation of P3AT leads to the growth of three distinct redshift peaks in absorption spectrum [45, 71, 72, 73, 74, 75, 76, 80, 83, 85, 86, 87]. The quantum yield also decreases significantly [73, 74].

The change of individual chain conformation affects π-electron delocalization along conjugated backbone. Roles of chain conformation on photophysical properties have been extensively investigated in the system of well-known MEH-PPV [14, 15, 56, 57, 60, 61]. In good solvent, the conjugated polymer normally prefers extended conformation owning to its rigid backbone [14, 15]. The conjugated chain folds or collapses in poor solvent to minimize local interactions. The presence of physical defects or kinks along the conjugated backbone of collapsed chain interrupts the delocalization of π-electrons [60, 61]. In other words, the conjugation length decreases when conjugated chain adopts folded or collapsed conformation, causing a blueshift in absorption and PL spectra. In previous studies by one of the authors, the blueshift of absorption spectrum as much as 60 nm is detected when the extended MEH-PPV chain is forced to collapse in very poor solvent [60]. In the system of P3AT, however, the blueshift of absorption and PL spectra is never detected in poor solvent. The decrease of solvent quality normally leads to the growth of new redshift peaks, arising from interchain and/or intrachain aggregation [71, 72, 85, 86, 88]. Some authors also suggest the planarization of each individual chain in poor solvent [74, 83, 87].

In this study, we systematically induce conformational change of regioregular poly(3-octylthiophene) (rr-P3OT) using cyclohexane and hexane as poor solvents. The solubility parameters (δ) of these solvents are much lower than that of rr-P3OT (see Table 6). However, the δ values are close to that of the octyl side chain, providing selective local polymer–solvent interactions. The hexane can only dissolve a trace amount of the polymer. The solubility of rr-P3OT increases significantly in cyclohexane, attributed to its higher δ value. Therefore, cyclohexane can be used to induce chain coiling without intrachain aggregation. AFM is used to follow conformational change in each system. In our study, we detect a significant blueshift in absorption and PL spectra.

Results and discussions

Conformational change in cyclohexane

Solubility parameters (δ) and dielectric constant of all solvents and rr-P3OT are listed in Table 6. The comparison of these δ values can provide an insight about local interactions between the solvent and each segment of rr-P3OT [36, 39, 83, 107]. The difference between solubility parameters of CRB and rr-P3OT is relatively small. This suggests strong polymer–solvent interactions, resulting in high solubility. PRD is a more polar solvent with higher δ value. Therefore, the PRD is a poorer solvent compared to the CRB. The weaker polymer–solvent interaction in PRD system is indicated by the decrease of polymer solubility. Cyclohexane is a nonpolar solvent. It is a poor solvent for thiophene group due to the large difference of their δ values. However, the octyl side chain of rr-P3OT has strong dispersion interaction with this solvent. The disparity of these segmental interactions leads to the change of chain conformation.

Absorption and PL spectra of rr-P3OT in pure CRB and their mixtures with cyclohexane are shown in Figure 58a,b. In good solvent CRB, the rr-P3OT chain adopts an extended conformation where dihedral angles between thiophene rings are relatively small [53, 59, 122, 123]. This allows large extent of π orbital overlapping along conjugated backbone, resulting in relatively long conjugation length. Absorption spectrum of rr-P3OT in this solvent exhibits a broad pattern with λ_{max} at 454 nm, assigned to π–π transition within conjugated backbone of the isolated chain. The PL spectrum exhibits a peak at 574 nm accompanied with vibronic shoulder at about 615 nm [46, 47]. When the cyclohexane is added into this system, local environment around rr-P3OT chain is altered. The absorption and PL spectra systematically shift to high-energy region upon increasing the cyclohexane ratio. The change takes place in a continuous fashion while the shape of spectra remains the same. The blueshift of about 16 nm is detected when the cyclohexane ratio reaches 100%.
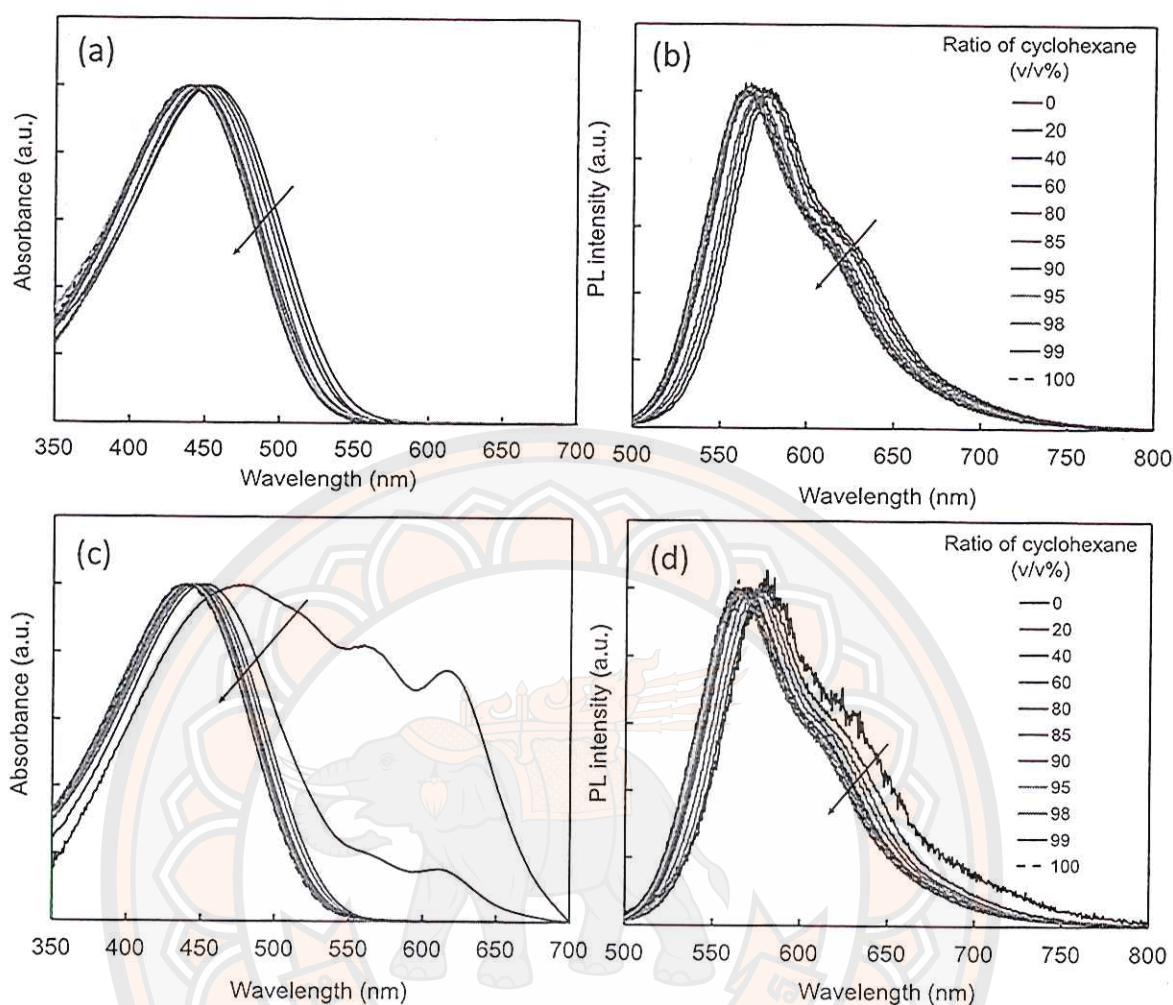
Figure 58 (Left) Absorption and (right) PL spectra of 0.001 mg/mL *rr*-P3OT in (a,b) mixture of chlorobenzene and cyclohexane and (c,d) mixture of pyridine and cyclohexane. Arrows indicate the change of spectra upon increasing ratio of cyclohexane. All spectra are normalized for clarity.

The position of maximum absorption and PL emission are at 438 and 558 nm, respectively. The variation of λ_{max} value as a function of cyclohexane ratio is shown in Figure 59. It is important to note that the blueshift of absorption and PL spectra in cyclohexane is not due to the change of dielectric constant of solvent. The use of nonpolar toluene as a solvent for *rr*-P3OT does not provide the same result.
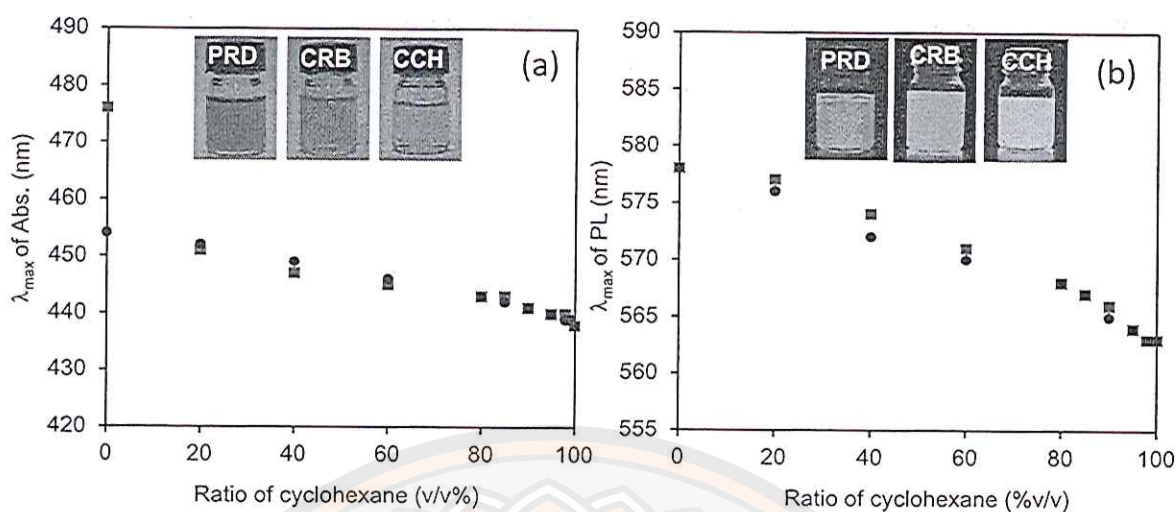
Figure 59 Variation of (a) λ_{max} of absorption and (b) PL spectra upon increasing ratio of cyclohexane (CCH) in *rr*-P3OT solutions. The initial solvents are (circle) chlorobenzene (CRB) and (square) pyridine (PRD). Insets show photographs of *rr*-P3OT in the pure solvents taken in (a) ambient condition and (b) under UV light irradiation.

The blueshift of absorption and PL spectra is attributed to the conformational change of *rr*-P3OT in cyclohexane. Previous studies by Kiriy, et al. [74, 75] suggest that *rr*-P3OT can form helical conformation in the system of mixed chloroform and hexane. In this structure, the octyl side chain extends toward the nonpolar medium due to favorable dispersion interaction. The helical conformation also minimizes contact between the polar thiophene backbone and nonpolar hexane. In contrast to our result, the authors observed the growth of three distinct redshift peaks in absorption spectra upon increasing the hexane concentration. As the redshift peaks were still observed at extremely low polymer concentration, it was concluded that the planarization of *rr*-P3OT backbone occurred at a single-molecule level, resulting in the increase of conjugation length. However, the possibility of intrachain aggregation was not considered in their discussion. We believe that the *rr*-P3OT chain also forms helical conformation in cyclohexane. The twisting of thiophene group in the helix interrupts π-electron delocalization, causing the decrease of conjugation length. As the solubility of *rr*-P3OT in cyclohexane is higher than that of the hexane, the magnitude of chain coiling and segmental packing along helical axis are expected to be lesser. Therefore,

the intrachain aggregation along helical axis and/or planarization does not occur in this system.

Conjugated polymer in solution is a semiflexible chain. The chain can twist and fold causing physical defects or kinks along the conjugated backbone. Small angle neutron scattering measurements reveal that poly(3-butylthiophene) in nitrobenzene is a semiflexible chain with persistence length of about 14 thiophene units [58, 124]. Study of poly(2,5-dinonyl-p-phenyleneethynylene) in toluene also observes the chain bending in dilute concentration [124]. As the presence of physical defects interrupts π electron delocalization, an effective conjugation length (ECL) of conjugated polymer is normally much shorter than the contour length. To further analyze our result, the ECL of rr-P3OT in each solvent is estimated by utilizing optical properties of its oligomers [125, 126, 127, 128]. Bidan, et al. [125] demonstrate that the absorption energy of regioregular oligo(3-octylthiophene)s ($n = 1$–6) varies linearly with reciprocal of the number of thiophene rings (n). The obtained linear relationship is shown in equation (26).

$$E_{(eV)} = 2.54 + \frac{3.15}{n} \tag{26}$$

The ECL of rr-P3OT in CRB and cyclohexane is estimated by substituting the absorption energy (in eV unit) into (1). This calculation yields ECL of rr-P3OT in CRB and cyclohexane equivalent to about 17 and 11 thiophene units. However, several studies have shown that deviation from linear equation (26) occurs when the size of oligomers becomes relatively long [127, 128]. Meier, et al. [127] suggests an exponential relationship between absorption energy and n as shown in equation (27), which takes into account the convergent behavior of λ_{max} of the long oligomers.

$$\lambda_{max}(n) = \lambda_{\infty} - (\lambda_{\infty} - \lambda_1)e^{-b(n-1)} \tag{27}$$

The λ_1, $\lambda_{max}(n)$, and λ_∞ are the maximum absorption wavelength of monomer, oligomers, and polymer, respectively. The convergent factor b can be obtained by fitting optical properties of oligomers [125] and rr-P3OT (λ_∞ = 454 nm), which provides the b value of 0.308 (regression coefficient = 0.99). The ECL is estimated by substituting b value into equation (28).

$$n_{ECL} = \frac{\ln(\lambda_\infty - \lambda_1)}{b} + 1 \tag{28}$$

The ECL of rr-P3OT in CRB is equivalent to 18 thiophene units. For cyclohexane system, the ECL is estimated by substituting $\lambda_{max}(n)$ = 438 nm into eq (27), which yields n = 9 thiophene units. These data analysis demonstrates significant decrease of ECL in cyclohexane due to the conformational change of rr-P3OT.

In the system of PRD, the polymer–solvent interactions are relatively weak. The rr-P3OT chains are forced to assemble into aggregates, indicated by the presence of three redshift peaks at about 515, 560, and 616 nm in absorption spectrum [see Figure 58(c)]. Previous studies suggest that the improved π–π stacking causes the increase of conjugated length within aggregates [15, 29, 43, 44, 56, 61, 87]. The PL intensity also drops significantly compared to that of the CRB system. However, the shape and peak position of PL spectrum still resemble those of the isolated chain. This result suggests that the aggregates of rr-P3OT in PRD are the nonemissive species. This type of aggregates was also observed in the system of poly(9,9-di(2-ethyl-hexyl)fluorene) [129]. When a small amount of cyclohexane is added into the system, the redshift peaks in absorption spectrum significantly decrease. The λ_{max} also shifts from 476 to 452 nm. This observation indicates that the enhanced dispersion interaction between octyl side chain of rr-P3OT and cyclohexane leads to the dissociation of aggregates. At 40% v/v of cyclohexane, the redshift peaks disappear and the shape of absorption spectrum is similar to that of the CRB system. At this stage, the rr-P3OT chains separate from each other. The systematic blueshift of absorption and PL spectra occurs upon increasing cyclohexane ratio to 99% v/v, indicating the conformational change. The decrease of λ_{max} is comparable to the system of CRB (see Figure 59). Therefore, the polarity of initial solvent hardly affects the magnitude of conformational change of rr-P3OT.

The change of chain conformation significantly affects the quantum yield of *rr*-P3OT. The extended chain in CRB exhibits a quantum yield of about 0.17±0.01. The addition of cyclohexane ratio up to 60% v/v leads to continuous increase of quantum yield to 0.21 ±0.01 (see Figure 60). This is probably due to the change of local polymer–solvent interactions and conformational change of *rr*-P3OT, affecting the radiative de-excitation pathways of excited π electrons [109, 118]. However, it is not trivial to separate these two effects because they are closely related. Interestingly, significant drop of quantum yield to 0.11±0.01 occurs upon increasing the cyclohexane ratio to 80% v/v. The discontinuous change of quantum yield indicates an abrupt increase of nonradiative de-excitation processes within the system. This behavior cannot be attributed to the change of solvent composition because the quantum yield remains roughly constant at higher cyclohexane ratio. We believe that the magnitude of chain coiling or shrinking at this stage is relatively large, causing intrachain segmental interactions. This leads to the drop of quantum yield similar to the effect of interchain/intrachain aggregation. However, the strength of segmental interactions within aggregates is much stronger, leading to the growth of new absorption peaks and further drop of quantum yield. The presence of aggregates in PRD system causes the decrease of quantum yield to about 0.02±0.01. The aggregates dissociate upon increasing cyclohexane ratio, leading to systematic increase of quantum yield as shown in Figure 60. At 40% v/v of cyclohexane, the chains are in isolated conformation. Therefore, the quantum yield of *rr*-P3OT at this stage is comparable to that of the CRB system. The significant drop of quantum yield is detected at higher cyclohexane ratio.
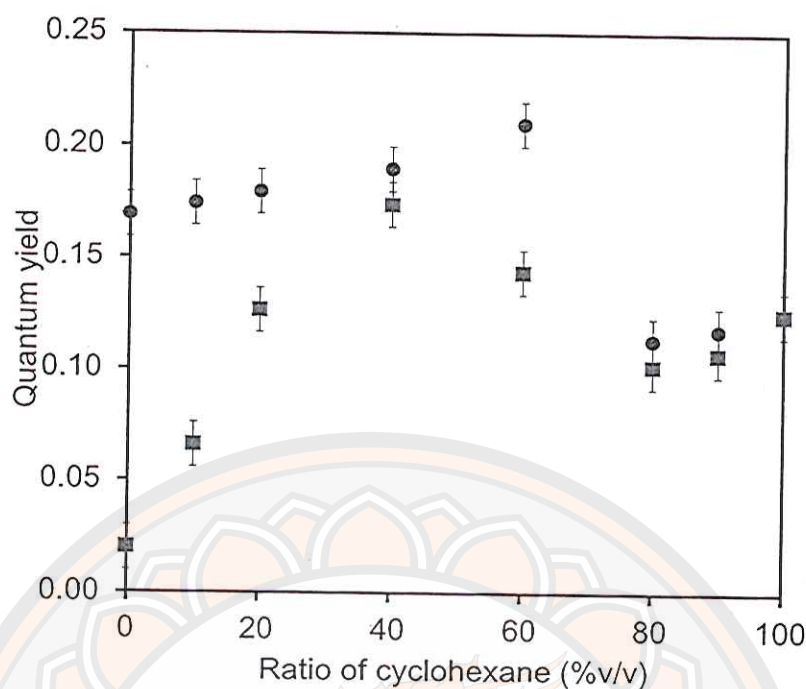
Figure 60   Variation of quantum yield of *rr*-P3OT in mixed solvents, chlorobenzene/cyclohexane (circle) and pyridine/cyclohexane (square)

AFM is utilized to investigate the conformational change of *rr*-P3OT. Samples are prepared by drop casting from different solutions onto flat SiO_x/Si substrate where the isolated chains assemble into large domains. Although the AFM does not directly reveal the conformation of isolated chain, morphology of the assembled domains can reflect the conformation of individual chains. The self-assembling from pure CRB leads to the formation of nanoribbons and clusters [see Figure 61(a)]. It has been observed in different types of conjugated polymers that their rigid rod nature drives the formation of nanoribbons [83, 130, 131, 132]. In this structure, the main chains arrange parallel to each other perpendicular to the nanoribbon axis [51, 78, 81, 82, 133]. The width of nanoribbons is defined by contour length of conjugated backbone. The nanoribbons of *rr*-P3OT in this study exhibit a width of about 60.2±7.5 nm, consistent with its contour length. When the sample is prepared from PRD solution, spherical nanoparticles with large size distribution are observed as shown in Figure 61(b). We believe that these nanoparticles form in solution due to relatively weak polymer–solvent interactions. The segmental aggregation occurs within these nanoparticles. We note that micron-size particles are

also detected in some areas of the sample. The addition of 50% v/v cyclohexane into CRB solution leads to the formation of flat sheet-like structure with homogeneous thickness of about 11.7±1.8 nm [see Figure 61d)]. Width of the nanosheets is in a micron range. We suggest that the *rr*-P3OT chains are still extended at this condition. These extended chains arrange into the nanosheets where their thickness depends on number of the stacked *rr*-P3OT layers. This hypothesis is parallel with molecular packing model suggested by previous works [51, 78, 81, 82]. The width of nanosheets is much larger than that of the nanoribbons, attributed to the decrease of polymer solubility. In the system of PRD and 50% v/v cyclohexane, we also observe the formation of nanosheets [see Figure 61(e)]. The sheet thickness, however, increases to about 17.7±2.2 nm. Some nanoparticles are still detected. This result indicates that the addition of 50% v/v cyclohexane causes the dissociation of aggregates. The chains also become extended before the assembling into nanosheets.

The preparation of thin films from *rr*-P3OT solution in pure cyclohexane provides rather different morphology. We observe the formation of dot-like and rod-like structures [see Figure 61(c)]. The width and thickness of these structures are quite uniform, about 135±6.8 and 21.8±3.3 nm, respectively. Some of the dots also arrange into nanorods. Previous studies by Kiriy, et al. [74, 75] observe one-dimensional (1D) aggregation of *rr*-P3OT and *rr*-P3HT in the mixtures of chloroform and hexane, yielding micron-long nanorods. Based on the width of nanorods, the authors suggest that helical coils of the polymers aggregate in one dimensional direction. The width of nanorods in this study is much larger than that of the previous studies. It cannot be attributed to the diameter of single helical coil. However, we still observe the aggregation of nanodots in 1D direction. We suggest that multiple helical coils assemble to form the nanodots and nanorods in this study. The formation of helical coil aggregates has been observed in the systems of polythiophene derivatives [134, 135]. It is important to note that the self-assembling of *rr*-P3OT in a random fashion will lead to the formation of nanoparticles as detected in the system of pure PRD.
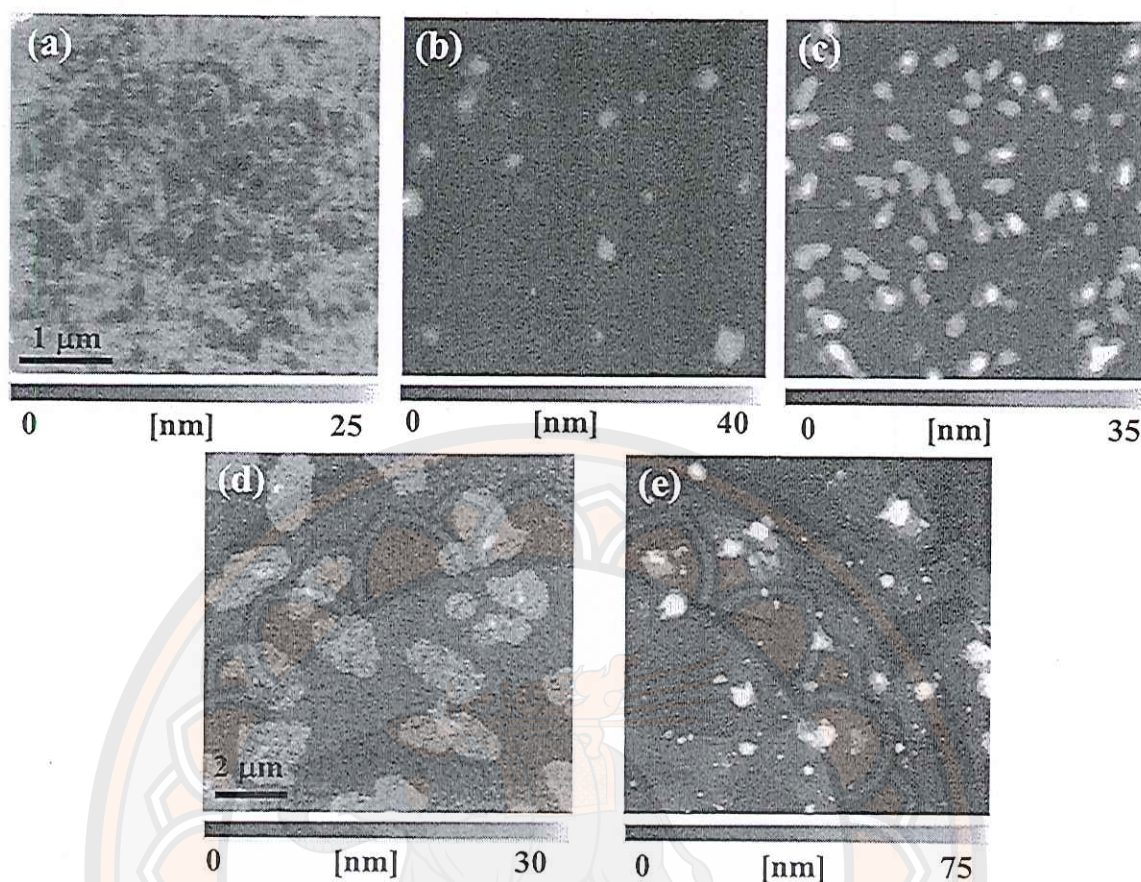
Figure 61 AFM topography images of *rr*-P3OT on silicon wafer prepared by drop casting from 0.05 mg/mL solution in (a) chlorobenzene, (b) pyridine, (c) cyclohexane, (d) mixed chlorobenzene/cyclohexane (50:50 v/v %), and (e) mixed pyridine/cyclohexane (50:50 v/v %). Scale bars are 1 mm for (a,b,c) and 2 mm for (d,e).

Intrachain aggregation in hexane/cyclohexane

In this section, the conformational change of *rr*-P3OT is further induced by addition of hexane into the cyclohexane solution. From Table 6, the solubility parameters (δ) of *rr*-P3OT, cyclohexane and hexane are 18.2, 16.8, and 14.9 $J^{1/2}$ $cm^{-3/2}$, respectively. In general, the solubility of polymer in solvent is reduced when the difference between their δ values is large [36, 37, 39]. The δ value of hexane is 1.9 $J^{1/2}$ $cm^{-3/2}$ lower than that of the cyclohexane, which leads to the reduction of *rr*-P3OT solubility. Therefore, the magnitude of helical coiling is expected to increase upon increasing the hexane ratio. Absorption and PL spectra of *rr*-P3OT in cyclohexane and

hexane mixtures are shown in Figure 62. The addition of 30% v/v hexane does not cause the blueshift of absorption and PL spectra, indicating that the conjugation length of *rr*-P3OT still remains the same. An increase of hexane ratio to 40% v/v leads to the growth of redshift peaks. The absorbance of these new peaks increases systematically upon increasing the hexane ratio. At 90% v/v hexane, the redshift peaks are at about 525, 558, and 605 nm. As the redshift peaks are still detected at extremely low concentration of the polymer (see Figure 63), this phenomenon is likely to occur at a single molecule level. Kiriy, et al. [74, 75] suggests that the formation of helical coil causes planarization of the conjugated backbone, which in turn results in the increase of conjugation length. Their computational study shows that the dense packing of thiophene rings along helical axis limits the dihedral SCCS angle to about 1–6 °. They also observe that it takes about 12 thiophene units to complete one turn of the helix. However, our calculation by utilizing equation (26) indicates that the fully extended *rr*-P3OT chain (n = 1) yields λ_{max} of about 488 nm. This number is much lower than the detected λ_{max} values in mixed cyclohexane/hexane. Therefore, the backbone planarization is not a sole factor causing the growth of redshift peaks in absorption spectra. We suggest that the intrachain aggregation also contributes to the increase of conjugation length. The decrease of solvent quality forces the packing of main chain along helical axis, allowing the overlap of π orbitals. The enhanced π electron delocalization leads to the formation of new electronic species with lower HOMO–LUMO gap [66, 136, 137]. The transition between two distinct electronic species is indicated by the observation of isosbestic point in Figure 62. However, it is not trivial to separate the effects from those two phenomena. This is mainly because the conjugated backbones become planar when they stack on top of each other to form aggregates [82, 83].
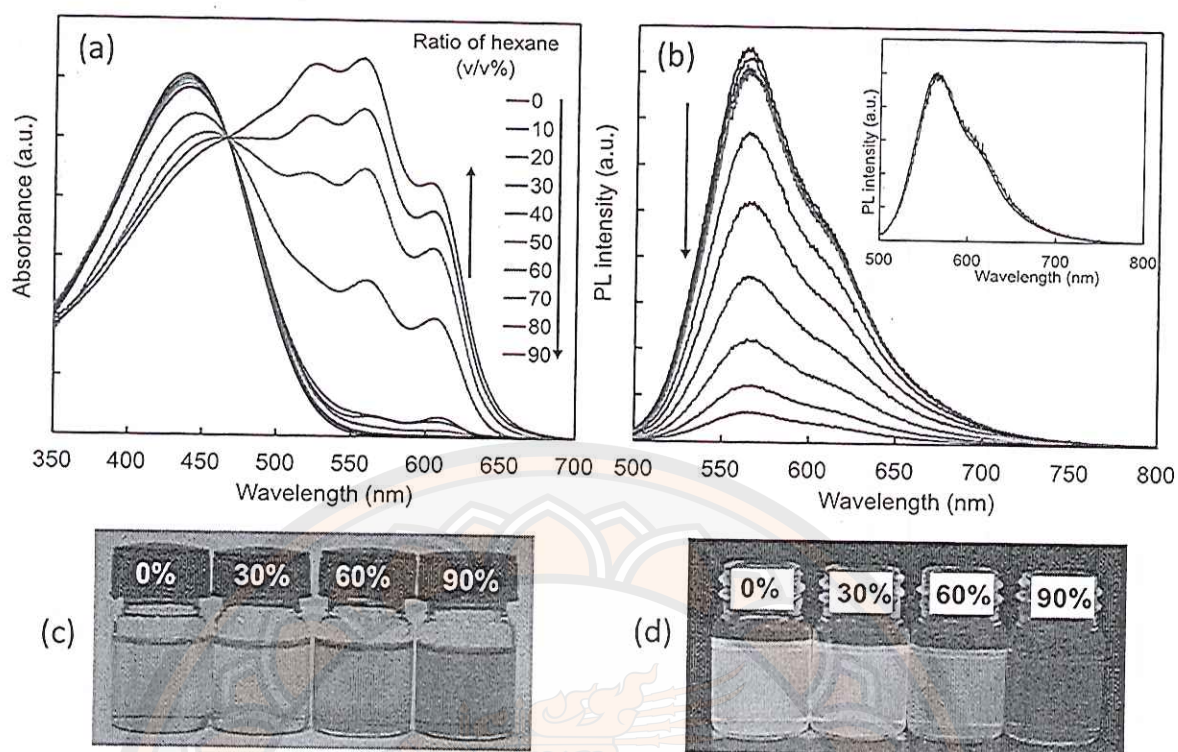
Figure 62 (a) Absorption and (b) PL spectra of 0.001 mg/mL *rr*-P3OT in mixtures of cyclohexane and hexane. The inset compares PL spectra of *rr*-P3OT in pure cyclohexane and mixture with 90% v/v hexane. Photographs of *rr*-P3OT in mixtures of cyclohexane and hexane in (c) ambient condition and (d) under UV light irradiation.
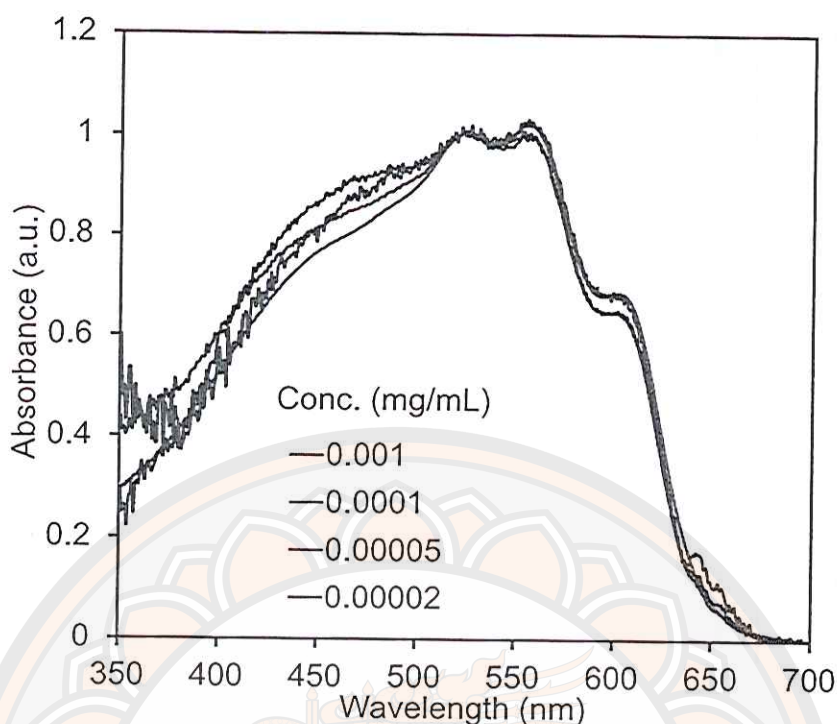
Figure 63 Normalized absorption spectra of *rr*-P3OT in mixture of cyclohexane and 90% v/v hexane. Polymer concentrations ranges from 1×10^{-3} to 2×10^{-5} mg/mL.

The intrachain aggregation is also indicated by the decrease of quantum yield. Figure 62(b) shows systematic decrease of PL intensity upon increasing the hexane ratio. Correlation between the growth of redshift peaks and quantum yield of *rr*-P3OT is illustrated in Figure 64. The ratio of absorbance at 550/435 nm reflects the aggregate fraction within the system. An increase of hexane ratio to 30% v/v hardly affects the absorption spectra and quantum yield of *rr*-P3OT. The appearance of small redshift peaks at 50% v/v hexane causes slight decrease of the quantum yield. The aggregate fraction increases abruptly at higher hexane ratio, which in turn causes a sharp drop of quantum yield. At 90% v/v hexane, the quantum yield of *rr*-P3OT is comparable to the system of pure PRD, also containing large aggregate fraction. AFM measurements also show supporting results (see Figure 65). When the sample is prepared from the solution containing 40%v/v hexane, we observe sheet-like structure with thickness of about 8.1±1.0 nm. Some nanoparticles are also detected. At 60% v/v hexane, the amount of these nanoparticles increases significantly. They assemble into

large clusters in the thin film. We believe that the intrachain aggregation takes place within these nanoparticles. The formation of large cluster is an indication of sudden decrease of the polymer solubility. It is worthwhile to note that 1D aggregation is not observed in our system. This is probably due to the difference of solvent used in the previous study.
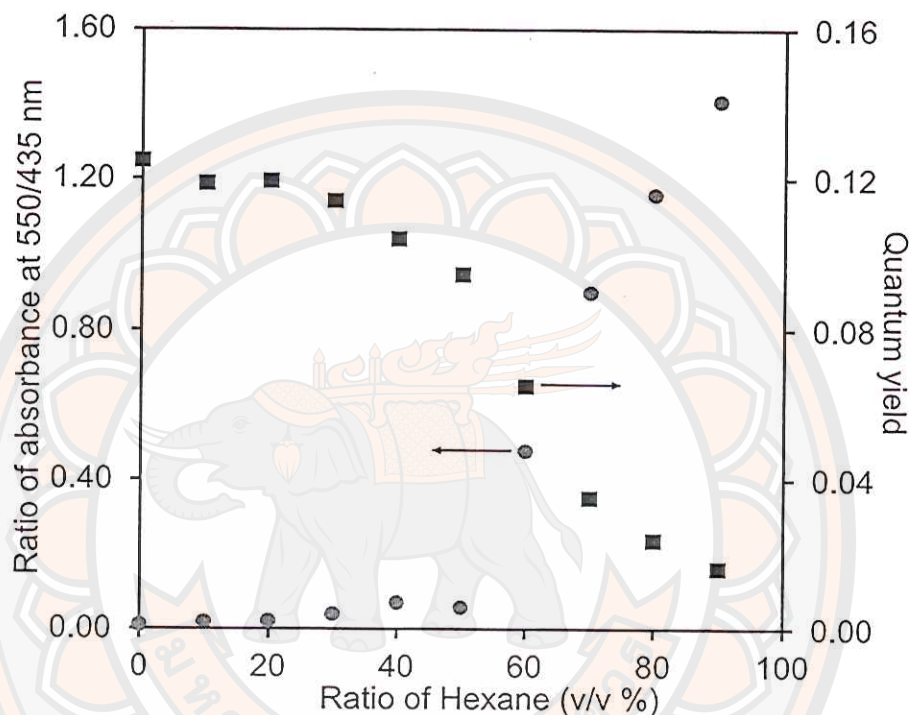
Figure 64 Variation of absorbance at 550/435 nm and quantum yield upon increasing hexane ratio. The error bars of quantum yield are omitted for clarity of presentation.

The PL pattern hardly changes upon increasing the hexane ratio (see inset of Figure 62(b)]. This is in contrast to the results from absorption spectra, which detect a significant redshift. The PL spectrum of rr-P3OT solution containing 90%v/v hexane still exhibits λ_{max} at about 558 nm, which is the same as that of the pure cyclohexane system. This observation indicates that the aggregates in this system are the non-emissive species. The observed PL intensity arises from the photoemission of non-aggregated segments within the system. We also observe that PL spectrum of rr-P3OT in PRD is detected at lower energy region compared to the system of mixed

cyclohexane/hexane. The λ_{max} is detected at 574 nm. This λ_{max} value is equal to that of the extended *rr*-P3OT chain is pure CRB. Therefore, the conformation of non-aggregated chain does not change in the PRD. In system of cyclohexane/hexane, the chain form helical coil, resulting in the decrease of conjugation length, before the intrachain aggregation takes place.
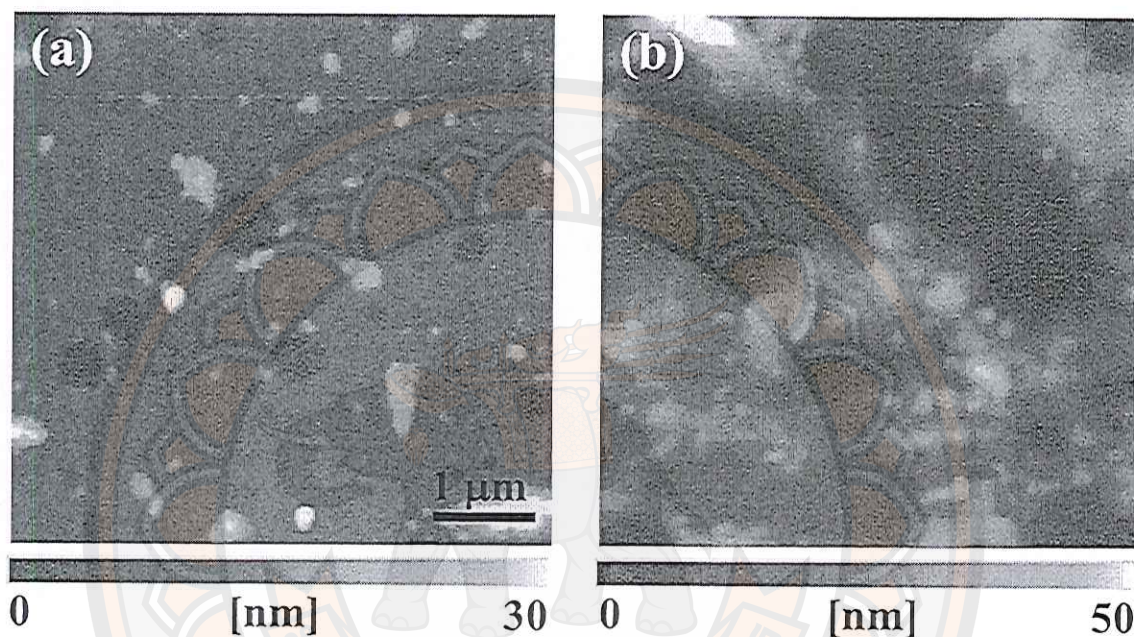
Figure 65 AFM topography images of *rr*-P3OT on silicon wafer prepared by drop casting from 0.05 mg/mL solutions in mixture of cyclohexane and hexane at different ratios (a) 60:40 v/v % and (b) 40:60 v/v %.

Conclusions

In this study, we have shown that conformational change of *rr*-P3OT chain occurs in cyclohexane solution. The unfavorable interaction between thiophene conjugated backbone and the nonpolar solvent induces chain coiling, which in turn causes the decrease of ECL. When the extended *rr*-P3OT chain in CRB transforms into coiled conformation in cyclohexane, the decrease of ECL is comparable to the shortening of about 6–9 thiophene units. The chain coiling in cyclohexane also causes the drop of quantum yield. The extent of chain coiling is further induced by addition of a nonsolvent hexane. The dense packing of thiophene units within the coiled chain

allows intrachain aggregation, which is responsible to appearance of three redshift peaks in absorption spectrum and the drastic drop of quantum yield. We also observe that the intrachain aggregates are the nonemissive species. Our study clearly distinguishes the effects of individual chain conformation and segmental aggregation on photophysical properties of polythiophene derivative.

CHAPTER VI

FORMATION OF NON-EMISSIVE AND EMISSIVE AGGREGATES OF *rr*-P3OT

Introduction

Poly(3-alkylthiophene) (P3AT) is a class of conjugated polymer that is known to exhibit interesting opto-electronic properties and high charge transport. These characteristics are suitable for the utilization in advanced organic-electronic technologies such as organic solar cells (OSC) [1, 2, 3, 4], organic field-effect transistors(OFET) [11, 12] and organic light emitting diode (OLED) [5, 6, 7, 8]. It has been known that segmental aggregation of conjugated polymer strongly affect their electroluminescence and photoconductivity, which in turn dictates the performance of aforementioned devices [29, 43]. Therefore, it is important to get a full understanding about molecular and experimental parameters that control the chain organization of conjugated polymers in different states. For example, the aggregation of conjugated polymers leads to the increase of charge carrier mobility while photoluminescence intensity is reduced [5, 7, 11]. These properties are desirable in OSC application. The OLED device, on the other hand, prefers less amount of aggregate to maximize its brightness. In the past few decades, aggregation behaviors of various conjugated polymers have been extensively investigated. It has been observed that the change of experimental parameters such as concentration, temperature, or quality of solvent can lead to the formation of aggregates [45, 71, 72, 73, 74, 75, 76, 83, 85, 86, 87, 88].

An early work by Rughooputh, et al. [71] shows that the aggregation of regioregular poly(3-hexylthiophene) (*rr*-P3HT) in mixtures of methyltetrahydrofuran/ acetonitrile leads to the growth of three distinct redshift peaks in absorption spectrum. Rumbles, et al. [72] observe similar results in the system of regioregular poly(3-dodecylthiophene) (*rr*-P3DDT) where the aggregation is induced by varying ratio of toluene/methanol mixtures. The aggregation also causes redshift peaks in photo-luminescence (PL) spectrum and the drop of quantum yield. Many research groups have investigated molecular parameters that influence the aggregation behaviors of

P3AT. The main chain of regioregular P3AT possesses a more planar-like structure compared to that of the regiorandom one. Therefore, it is more favorable for *rr*-P3AT to form aggregates where appropriate interchain stacking is required [45, 46, 76]. The increase of chain length also promotes the aggregation. Recent study by Scharsich, et al. [88], investigating *rr*-P3HT with molecular weights of 5 kDa, 11 kDa and 19 kDa, observes the increase of aggregate fraction upon increasing molecular weight. The change of side chain length also affects photophysical properties of the aggregates. Magnani, et al. [73] observe that the absorption and PL peaks of *rr*-P3DDT aggregates occur at lower energy region compared to those of *rr*-P3HTwith shorter side chain length.

In recent studies by several research groups, the aggregation of *rr*-P3AT in solvent–nonsolvent has been utilized to grow various types of nanostructures. The self-assembling of *rr*-P3AT in this system often leads to the formation of nanofibers [83, 84, 86, 117], nanowires [42, 44, 138] and nanowhiskers [87, 139, 140]. For example, Samitsu, et al. [83] prepare P3AT nanofiber by adding anisole into the polymer solution in a good solvent. The formation of nanofiber originates from one dimensional packing of P3AT, driven by strong π-π interaction between thiophene backbone and the crystallization of alkyl side chains. Xu, et al. [87] control solvent composition and aging time to induce the formation of *rr*-P3DDT nanowhiskers with different dimensions. They suggest that conformational change from coil to rod occurs prior to the assembling process. Park, et al. [85] observe similar results in the system of *rr*-P3HT. The random coils of *rr*-P3HT in chloroform assemble into order aggregates upon adding poor solvent acetonitrile. The dimension of aggregation also depends on local polymer-solvent interactions. Kiriy, et al. [74, 75] investigate different types of poor solvents used to induce the aggregation of *rr*-P3AT. They observe the variation of aggregation behaviors depending on properties of the poor solvent. The use of methanol, a non-solvent for both alkyl side group and aromatic backbone, provides 3 dimensional (3D) aggregates. The P3AT chain in hexane, which is a good solvent for the alkyl side chain but poor solvent for the thiophene backbone, undergoes helical coil formation followed by 1D aggregation.

In these previous works, the authors have noticed the variation of aggregation behaviors as well as photophysical properties in different systems. However, detailed

study exploring the origins of these discrepancies is rather limited. Therefore, we look closely into nature and photophysical properties of regioregular poly(3-octylthiophene) (*rr*-P3OT) aggregates in this study. We systematically induce the aggregation by varying properties of solvents. Mixed solvents are also used for fine tuning the strength of local polymer-solvent interactions. The photophysical change of *rr*-P3OT in different states is followed by utilizing uv/vis absorption, steady state PL, photoluminescence excitation (PLE) and site selective PL spectroscopy. Atomic force microscopy (AFM) is also used to probe the nanostructure of assembled *rr*-P3OT chains. We have observed the formation non-emissive and emissive aggregates depending on the extent of local segmental packing. The properties of aggregates can also be controlled by varying type of the solvents.

Results and discussions

Photophysical properties of aggregates

In this section, we focus on the nature and photophysical properties *rr*-P3OT aggregates in mixtures of CRB/EtOH and PRD/EtOH. The small difference between solubility parameter (δ) of CRB (19.6 $J^{1/2}cm^{-3/2}$) [36] and *rr*-P3OT (18.2 $J^{1/2}cm^{-3/2}$) [39] suggests that CRB is a good solvent for the *rr*-P3OT chain. Studies have shown that polymer can dissolve in a solvent at relatively high concentration when the difference of their solubility parameters is less than 2 $J^{1/2}cm^{-3/2}$ [36, 107]. Absorption and PL spectra of *rr*-P3OT in CRB exhibit λ_{max} at 454 nm and 574 nm, respectively (see Figure 66). The addition of EtOH ($\delta = 26.5$ $J^{1/2}cm^{-3/2}$), a poor solvent for both thiophene backbone and alkyl side chain, results in systematic change of the absorption and PL spectra. The presence of 40% v/v EtOH in the system hardly affects the pattern of absorption and PL spectra, indicating that the *rr*-P3OT chains remain well-dissolved and isolated. The absorption spectrum change significantly when the EtOH ratio is increased to 60% v/v. A growth of three redshift peaks at about 515, 555 and 605 nm is clearly observed. The pattern and absorbance of these redshift peaks hardly change upon increasing the EtOH ratio to 99% v/v. These redshift peaks are attributed to the aggregation of *rr*-P3OT chains to minimize unfavorable polymer-solvent interactions. The stacking of conjugated backbone within aggregates allows the overlap of π orbitals and also induces planarization of thiophene rings, which in

turn results in the increase of conjugation length [83, 85, 86, 87, 88, 107, 138, 139, 140]. The redshift peak at 605 nm corresponds to pure electronic transition (0-0) while the bands at 555 nm and 515 nm are assigned to vibronic transition (0-1) and (0-2), respectively. The photophysical change of *rr*-P3OT in mixed CRB/EtOH can be observed via naked eyes as shown in Figure 66c where the solution color changes from bright orange to pink-purple.

The PL pattern of *rr*-P3OT in mixed CRB/EtOH changes accordingly (see Figure 66b). The addition of 60% v/v EtOH causes the growth of redshift peak at about 638 nm, indicating the formation of new emissive species with lower HOMO–LUMO energy gap. The quantum yield also decreases significantly at this condition due to the aggregation of *rr*-P3OT chains (see Figure 66d). When the EtOH ratio is increased to 80% v/v, PL peak of the non-aggregated chains at 574 nm disappears. The PL spectrum of *rr*-P3OT at this state constitutes peak and shoulder at about 658 nm and 720 nm, respectively. Further increase of the EtOH ratio to 99% v/v does not affect the PL pattern. This observation indicates that the dense packing of *rr*-P3OT chains within the aggregates results in new type of emissive species. Our result is consistent with previous studies of *rr*-P3HT, *rr*-P3DDT where the new emissive species also form upon increasing the alcohol ratio [72, 73]. The PL spectra of *rr*-P3OT aggregates in condensed phases such as thin film and nanoparticles also exhibit a redshift pattern similar to this study [101]. However, our recent study in the system of cyclohexane/hexane does not detect the formation of new emissive species. Although an increase of the poor solvent ratio, hexane, causes the growth of three redshift peaks in absorption spectra, the PL pattern remains the same. Therefore, the aggregates detected in the cyclohexane/hexane system are designated as non-emissive aggregates. It is worthwhile to note that the absorption pattern of aggregates in this study is quite different from that of the cyclohexane/hexane system. Our results indicate that the photophysical properties of *rr*-P3OT aggregates depend significantly on local chain arrangement.
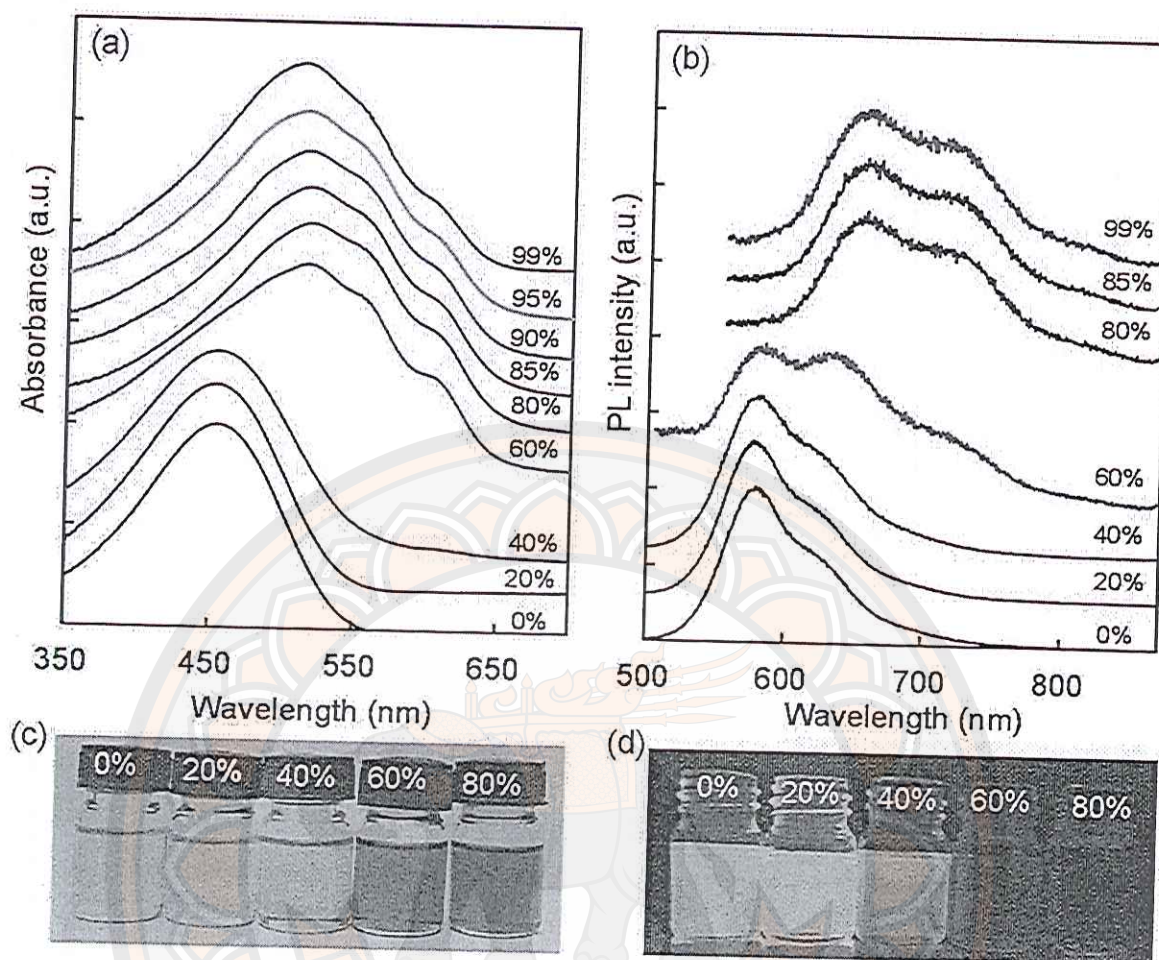
Figure 66 (a) Absorption and (b) PL spectra of 0.001 mg/mL *rr*-P3OT in mixtures of chlorobenzene and ethanol. Photographs of *rr*-P3OT in mixtures of chlorobenzene and ethanol in (c) ambient conditions and (d) under UV light irradiation. Ratios of ethanol in % v/v are shown on the right side of each spectrum and on top of each vial.
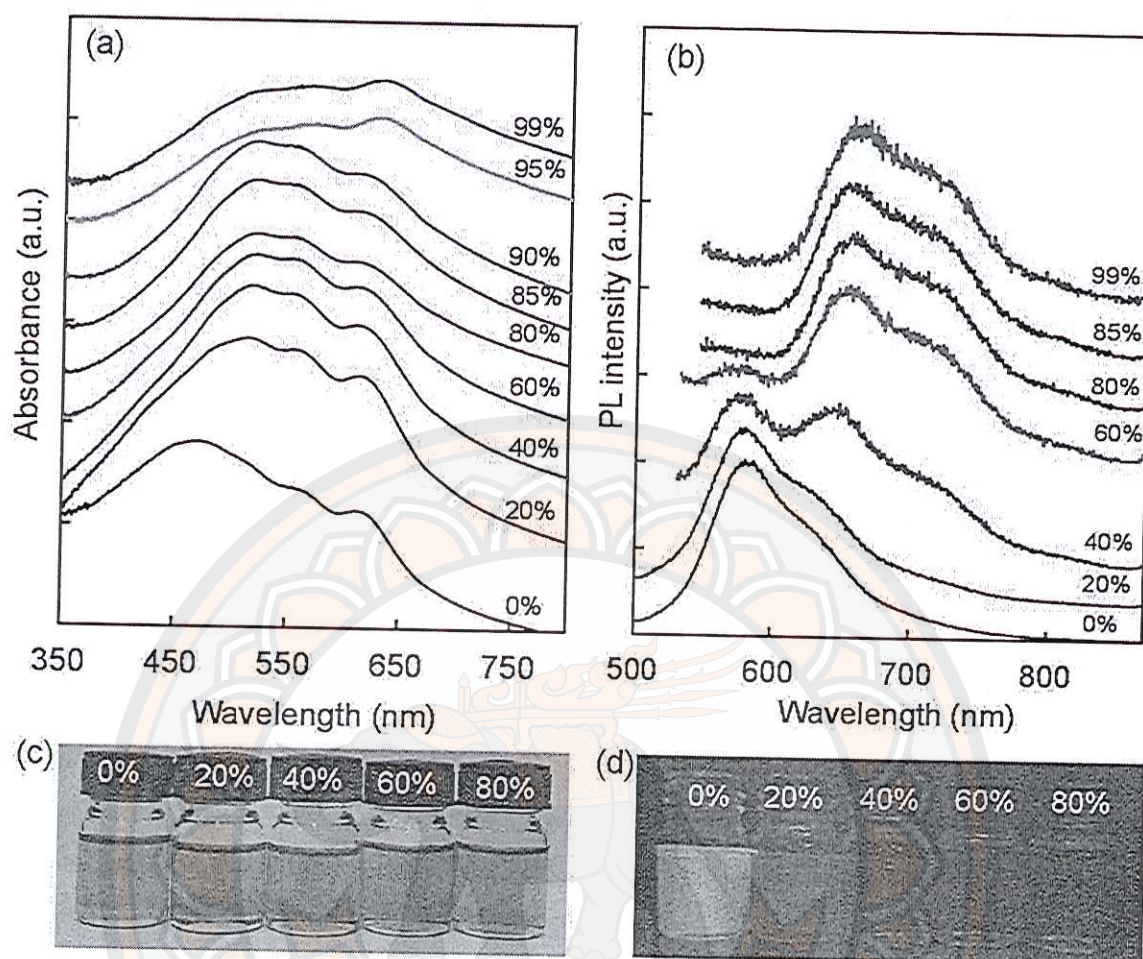
Figure 67 (a) Absorption and (b) PL spectra of 0.001 mg/mL *rr*-P3OT in mixture
of pyridine and ethanol. Photographs of *rr*-P3OT in mixture of
pyridine and ethanol in (c) ambient conditions and (d) under UV light
irradiation. Ratios of ethanol in % v/v are shown on the right side of
each spectrum and on top of each vial.

We further investigate the nature of non-emissive and emissive aggregates by using PRD as an initial solvent. PRD is a more polar solvent with higher solubility parameter ($\delta = 21.8$ J$^{1/2}$cm$^{-3/2}$) compared to those of the CRB and rr-P3OT. Therefore, the rr-P3OT chains aggregate in this solvent. Absorption spectrum of rr-P3OT in PRD solution shows λ_{max} at about 470 nm, accompanied with three redshift peaks at about 515 nm, 560 nm and 616 nm (see Figure 67a). The pattern of these redshift peaks is similar to that of the CRB/EtOH system. The absorbance of redshift peaks in the PRD solution is rather strong, indicating the existence of large aggregated fraction. However, we do not detect any drastic change in the photoemission pattern. The PL spectrum of rr-P3OT in PRD shown in Figure 67b is still very similar to that of the isolated chain in pure CRB solution. While the color of PRD solution is pink-purple in ambient condition, the PL emission shows relatively bright orange color (see Figure 67c and d). This result indicates that the rr-P3OT aggregates in PRD solution are the non-emissive species. We suggest that the observed PL spectrum arises from the non-aggregated segments, which may exist as isolated chain and/or associated particles. The PLE and site selective PL spectra in the following section provide supportive results. Since the association of rr-P3OT chains in this system occurs in a random fashion, some conjugated segments or chromophores may not stack on top of each other, a requirement for aggregate formation [78, 79, 80, 81, 82]. Therefore, the photophysical properties of these non-aggregated segments remain unaltered. Detail discussion of this topic is given in our previous reports, investigating the well-known poly[2-methoxy-5-(2'-ethylhexyloxy)-1,4-phenylenevinylene] (MEH-PPV) [57, 61, 70].

The addition of 20% v/v EtOH causes significant growth of the redshift peaks in absorption spectrum, corresponding to the increase of aggregated fraction. The PL pattern, however, still remains the same. At this state, the polymer forms loose aggregates, which do not emit light upon photoexcitation. The further increase of EtOH ratio to 40 and 60% v/v hardly affects the absorption pattern. Interestingly, we detect drastic growth of redshift peaks in PL spectra. The absorption and PL pattern are not affected upon increasing EtOH ratio to 90% v/v. At these conditions, the PL spectra constitute a peak and shoulder at about 658 nm and 720 nm, respectively. In this system, the increase of EtOH ratio causes the decrease of solvent quality, which in

turn forces dense packing of *rr*-P3OT chains within aggregates. Our observation indicates that the dense packing of *rr*-P3OT segments leads to the formation of new emissive species with lower HOMO-LUMO energy gap. Similar behavior is observed in the system of poly(9,9-di(2-ethylhexyl)fluorene) in mixtures of chloroform and methanol [129]. Previous studies have shown that the crystalline *rr*-P3OT in solid state can exist in the so called Form I and Form II [78, 79, 80, 81, 82]. The interlayer distance is slightly larger in the Form II crystal. Thermal annealing of the Form II causes the decrease of interlayer distance, resulting in the formation of Form I crystal. We suggest that segmental rearrangement probably occurs upon increasing EtOH ratio in our system. The shift of segment along chain axis, affecting the overlap of π orbitals, may occur [78, 82]. The dense packing of P3OT chains within aggregates may also induce the conjugated backbone to become more planar, resulting in the increase of conjugation length (i.e. red shift of absorption and PL spectra).We note that this emissive species may belong to aggregates or excimers. The discussion of this topic is presented in following section.

The segmental rearrangement is still detected upon increasing EtOH ratio to 95 and 99% v/v, indicated by the growth of a red-shift peak at about 625 nm in absorption spectra. Since the growth of this peak is independent from the other peaks at 515 and 560 nm, we suggest that this band belongs to different type of aggregates. The formation of this electronic species probably requires different packing parameters of the conjugated backbone. This result is in contrast to the CRB/EtOH system where the absorption pattern remains the same at EtOH ratio ranging from 80 to 99% v/v. The drastic discrepancy of absorption pattern in the two systems is illustrated in Figure 68a. At 99% v/v of EtOH ratio, local environments in the PRD/EtOH and CRB/EtOH systems is roughly the same but the absorption spectra of aggregates are quite different. Our results demonstrate that the segmental arrangements within the aggregates vary with the preparation conditions and largely dictate its photophysical properties. This observation is consistent with our previous reports on the systems of MEH-PPV in solvent/nonsolvent [57] and *rr*-P3OT nanoparticles where the amount of aggregates also depends on type of the initial solvent. However, the PL spectra of *rr*-P3OT at 99% v/v EtOH of the two systems still show similar pattern indicating the presence of same emissive species (Figure 68b).

Therefore, segmental rearrangements in the PRD/EtOH system only affect the amount and nature of non-emissive aggregates.
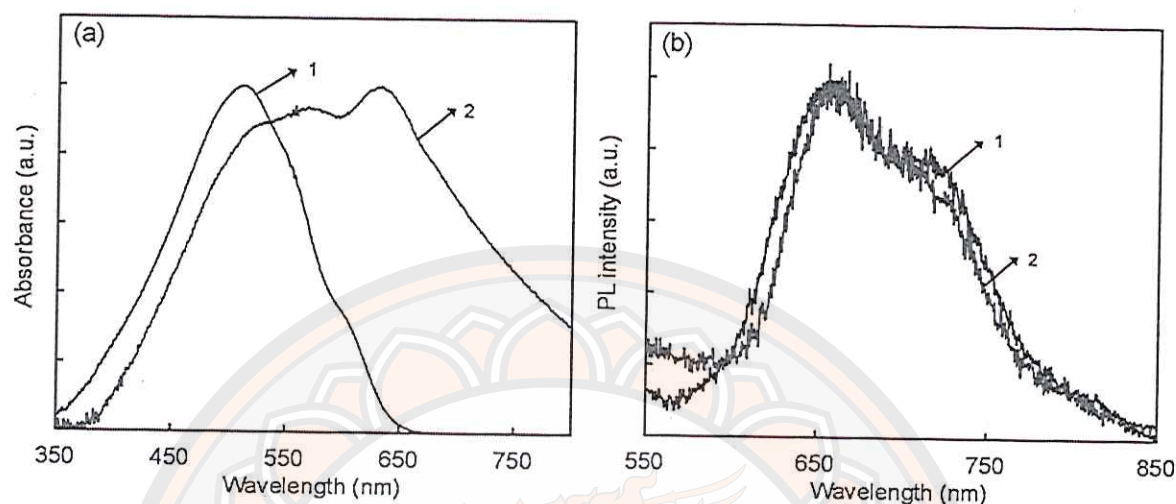
Figure 68 (a) Absorption and (b) PL spectra of 0.001 mg/mL *rr*-P3OT in mixtures of (1) chlorobenzene and 99% v/v ethanol and (2) pyridine and 99% v/v ethanol

AFM is utilized to explore the aggregation behaviors of *rr*-P3OTchains in the mixed CRB/EtOH and PRD/EtOH systems. Samples are prepared by drop casting from solutions onto flat surface of silicon wafer. Although the AFM cannot directly reveal the molecular packing within the aggregates, morphologies of the samples still provide an insight into the assembling behaviors of individual chains. The AFM topography images of *rr*-P3OT films in Figure 69 show that the addition of EtOH causes the formation of large domains. In CRB/EtOH system, the addition of 50% v/v EtOH yields flat sheet-like structure with thickness of about 12.7 ± 2.1 nm. Some polymeric particles also randomly disperse on the surface. Previous studies have shown that the sheet-like structure forms by parallel stacking of conjugated backbone, where its dimensions correspond to chain length and number of the stacked layers [82, 87, 130, 132].We suggest that large fraction of *rr*-P3OT chains is still isolated and extended in the mixed CRB/EtOH solvents. The assembling of these extended chains into sheet-like aggregates takes place during the evaporation of solvent. The aggregation of some *rr*-P3OTchains in the solution probably causes the formation of

polymeric particles. When the samples are prepared from the PRD/EtOH system containing 50% v/v EtOH, the assembled domains in thin film mostly exhibit irregular shapes. Their thicknesses are also inhomogeneous. Since the polymer–solvent interactions are less favorable in the PRD/EtOH system, large polymer fraction at this state aggregates in solution, consistent with the absorption spectrum. At 90% v/v EtOH ratio, the drastic decrease of solvent quality forces the rr-P3OT chains to densely pack into nanoparticles in solution state. Interestingly, primary size of the rr-P3OT nanoparticles obtained from the CRB/EtOH system appears to be much smaller compared to that of the PRD/EtOH one. The high magnification AFM image reveals that the large domains detected in Figure 69c consists of small size nanoparticles. The large domains observed in the PRD/EtOH system, on the other hand, exhibit homogeneous surface and do not constitute any smaller internal structure. These discrepancies of rr-P3OT morphologies reflect the difference of segmental packing within the two systems, resulting in the variation of absorption pattern and PL spectra. Our recent study also detects the variation of rr-P3OT nanoparticle size and their photophysical properties, depending on type of the initial solvent. We note that the evaporation rate of solution increases upon increasing the EtOH ratio, which may affect the assembling behaviors of rr-P3OT in thin films. However, the boiling points of CRB and PRD are comparable and the polymer already forms dense aggregates at 90% v/v EtOH. Therefore, morphologies of the dried films should reflect the structure of aggregates in the CRB/EtOH and PRD/EtOH solutions.
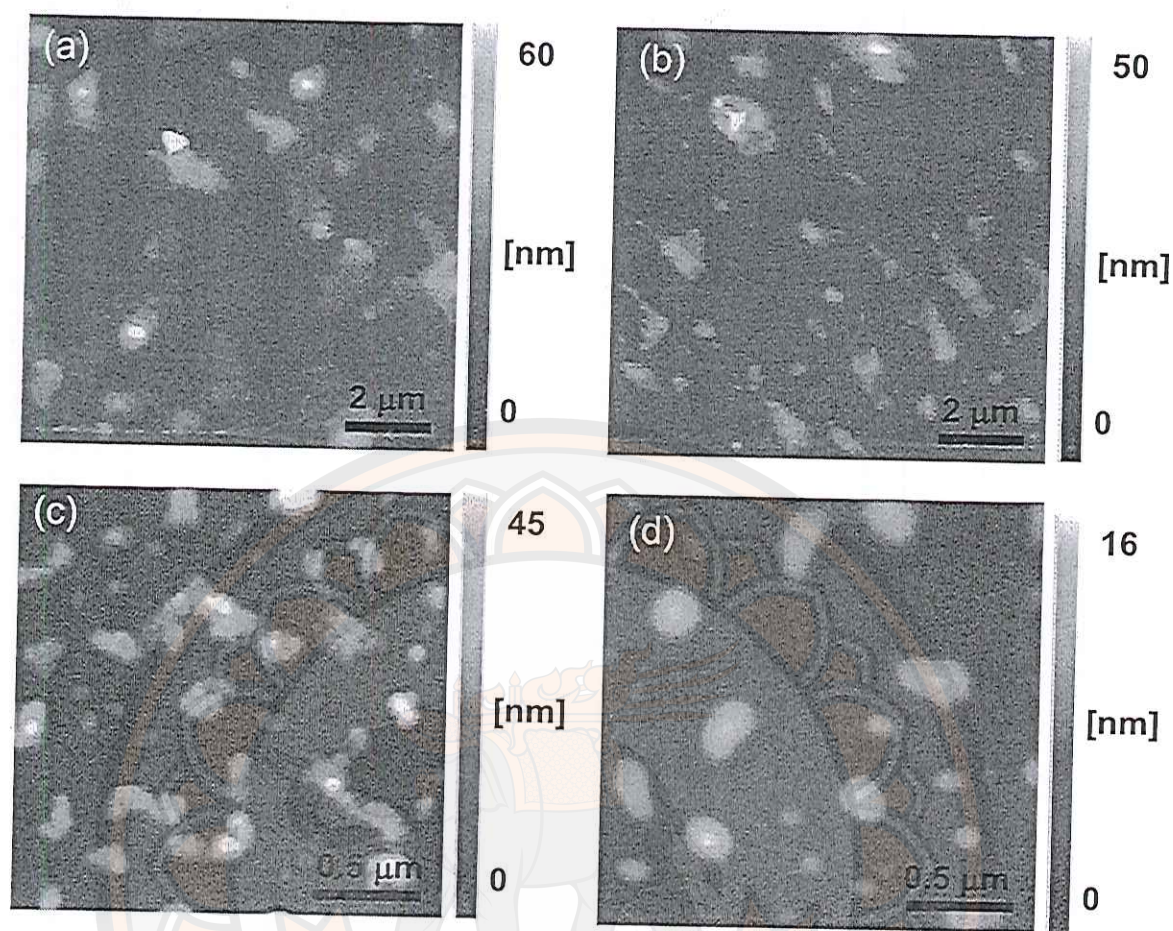
Figure 69 AFM topography images of *rr*-P3OT thin films on silicon wafer prepared by drop casting from 0.05 mg/mL in mixed solvents (a) chlorobenzene/ ethanol (50:50 v/v,%), (b) pyridine/ethanol (50:50 v/v, %), (c) chlorobenzene/ethanol (10:90 v/v, %) and (d) pyridine/ethanol (10:90 v/v, %).

The photophysical change of *rr*-P3OT in CRB/EtOH and PRD/EtOH is summarized in Figure 70 where λ_{max} of absorption and PL spectra are plotted as a function of EtOH ratio. In the CRB/EtOH system, an abrupt increase of absorption λ_{max} from 450 nm to 512 nm occurs when the aggregation takes place at about 60% v/v EtOH. Large aggregated fraction already exists in pure PRD solution. The increase of EtOH ratio to 20% v/v in the PRD/EtOH system causes the shift of absorption λ_{max} to 512 nm, corresponding to the increase of aggregated fraction. The λ_{max} of PL spectra, however, is still similar to that the isolated chain in pure CRB. The aggregates at this stage are loosely packed and do not emit light upon photoexcitation (i.e. non-emissive species). When the EtOH ratio is increased to 90% v/v, the absorption λ_{max} in both systems remains the same while the λ_{max} of PL spectra abruptly increases from 574 nm to 648 nm. At this condition, the decrease of solvent quality causes segmental rearrangement of some aggregated fraction, which in turn results in the formation of new emissive species. The further increase of EtOH ratio to 99% v/v causes segmental rearrangement of aggregates in PRD/EtOH system, indicated by the shift absorption λ_{max} to 625 nm. However, the PL spectra are not affected, indicating that these additional aggregates are the non-emissive species. We note that common X-ray diffraction method cannot be used to probe the packing parameters of *rr*-P3OT aggregates in different mixed solutions because the polymer concentration is extremely low (0.001 mg/mL). The preparation of *rr*-P3OT thin films by using different solvents usually results in the formation of emissive aggregates due to dense packing of polymer chains. In other words, we cannot control the extent of interchain interaction in the thin films.
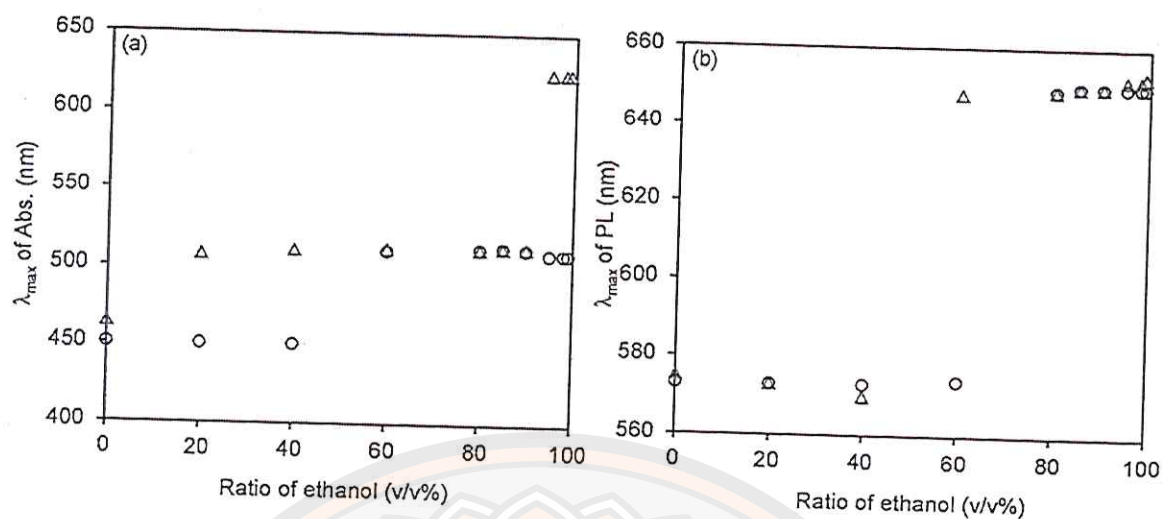
Figure 70 Variation of λ_{max} of (a) absorption and (b) PL spectra of *rr*-P3OT in mixed solutions upon increasing the ratio of ethanol. Initial solvents are (circle) chlorobenzene and (triangle) pyridine.

Relationship between the growth of redshift peaks in absorption and PL spectra is further investigated in Figure 71. The value of absorbance ratio at 605/450 nm reflects the amount of aggregates while the increase of PL intensity ratio at 650/575 nm indicates the formation of new emissive species. The absorbance and PL ratios are relatively small in mixed CRB/EtOH system containing 0, 20 and 40% v/v of EtOH, which corresponds to the presence of isolated chains. At 60% v/v EtOH, the absorbance ratio increases abruptly due to the aggregation of *rr*-P3OT chains. The amount of aggregates remains approximately the same at the higher EtOH ratios. The fraction of new emissive species (i.e. PL ratio at 650/575 nm), however, continuously increase upon increasing EtOH ratio to 85% v/v. The absorbance ratio is quite high in the PRD/EtOH system containing 0% and 20% v/v EtOH. The PL ratio, on the other hand, is still comparable to that of isolated chain in pure CRB. The absorbance ratio steadily increases upon increasing EtOH ratio to 80% v/v and then remains roughly constant. Further increase of the EtOH ratio to 95 and 99% v/v causes an abrupt increase of the absorbance ratio. The increase of PL ratio is similar to that of the CRB/EtOH system. These plots illustrate that there is no clear correlation between the growth of redshift peaks in absorption and PL spectra. The non-emissive aggregates form in the early stage of interchain association. The increase of EtOH ratio forces

dense segmental packing within these aggregates resulting in the formation of new emissive species. The formation of these emissive species hardly affects the absorption pattern.
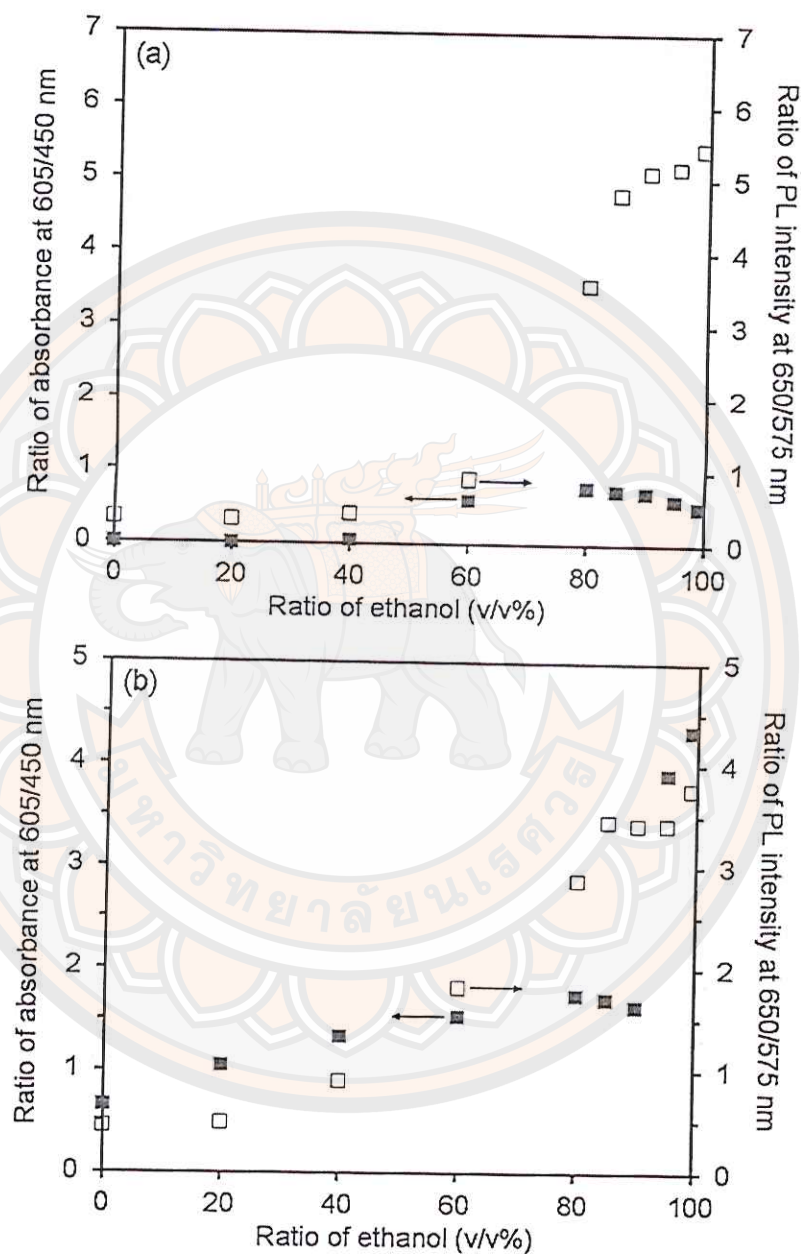
Figure 71 Ratio of (filled square) absorbance at 605/450 nm and (open square) PL intensity at 650/575 nm of 0.001 mg/mL *rr*-P3OT in mixtures of (a) chlorobenzene/ethanol and (b) pyridine/ethanol upon increasing the ratio of ethanol.

Emissive aggregates or excimer

As mentioned in previous section, the new emissive species may belong to aggregates or excimer. The formation of excimer takes place in the excited state. It dissociates during relaxation processes back to ground state. Therefore, absorption band of the excimer does not exist. To get more understanding about the nature of new emissive species, we measure PL and PLE spectra by varying excitation and emission wavelengths, respectively. The results obtained from CRB/EtOH and PRD/EtOH systems are illustrated in Figures 72 and 73. The PL pattern of isolated chain in pure CRB is independent of the excitation wavelength (see Figure 72a). The variation of excitation wavelength from 450 nm to 525 nm, exciting chromophores with different conjugation lengths, yields the same PL pattern. The result indicates the presence of only one type of emit-ting species. The measurements of PLE spectra detected at different emission wavelengths provide consistent results. The PLE spectra represent absorption band of emissive species within the system. In this case, the pattern of PLE spectra is similar to that of the corresponding absorption spectra. Studies have shown that conjugated chain consists of multiple chromophores with various conjugation lengths [47, 63]. However, the PL emission process usually takes place via the chromorphores with the lowest HOMO–LUMO energy gap (i.e. longest conjugation length) [47, 60, 63]. This is mainly due to the high efficiency of intrachain energy transfer process. In conjugated chain, the excited chromophores effectively transfer energy to the one with lowest energy before the PL emission process occurs. The PL spectra of *rr*-P3OT in pure PRD solution are also independent of the excitation wavelength as shown in Figure 73a. Although the absorption spectrum constitutes strong redshift peaks, the use of 450 nm and 525 nm excitation wavelength yields the same PL pattern, which is similar to that of the isolated chain in pure CRB. The PLE spectra obtained from both PRD and CRB solutions also exhibit similar pattern, indicating that both systems contain the same type of emitting species. The results from PL and PLE spectra confirm that the *rr*-P3OT aggregates in PRD solution is a non-emissive species. Only the non-aggregated segments contribute to the PL emission.
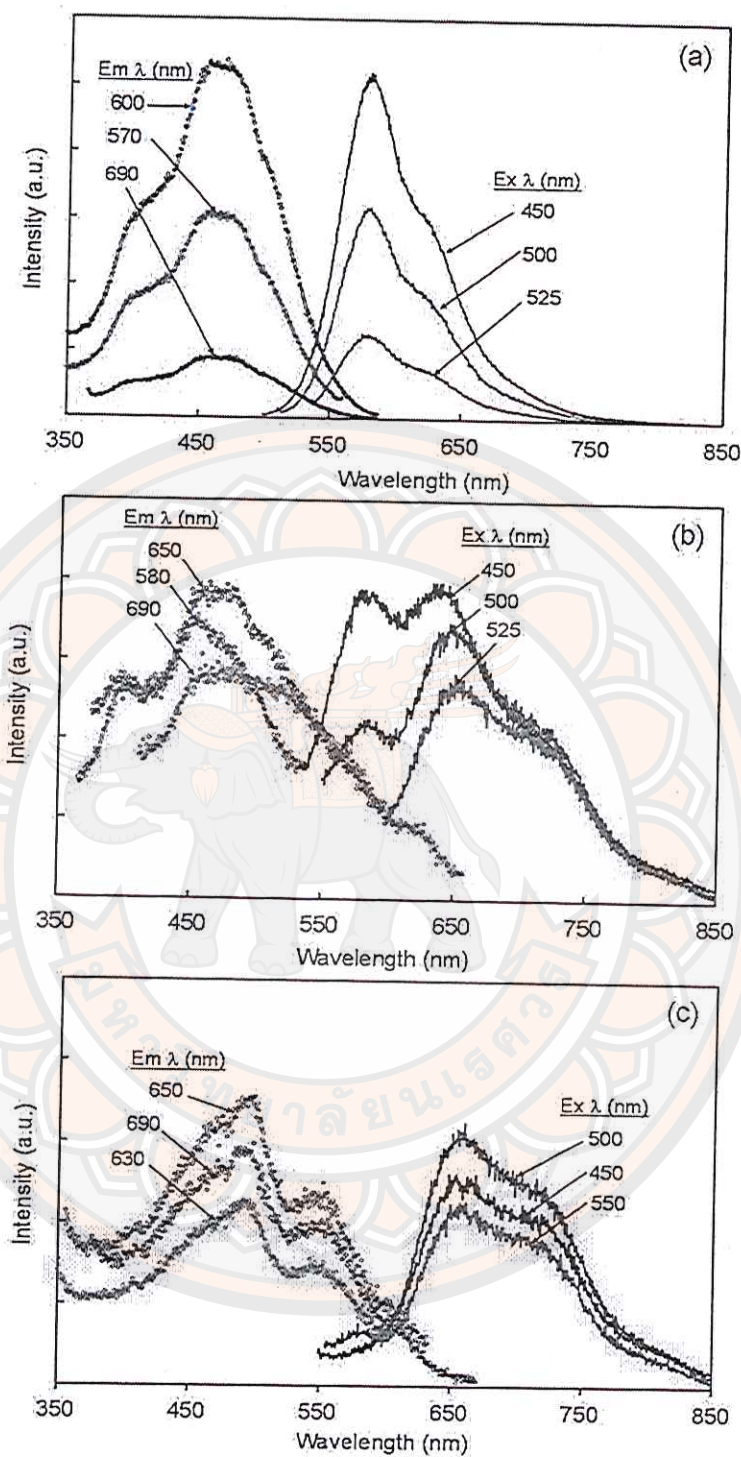
Figure 72 (left) PLE spectra and (right) PL spectra of 0.001 mg/mL *rr*-P3OT in mixtures of chlorobenzene and ethanol. The ratios of ethanol are (a) 0% v/v, (b) 60% v/v and (c) 99% v/v, respectively. The spectra were measured at different emission wavelengths (Em λ) and excitation wavelengths (Ex λ), respectively.
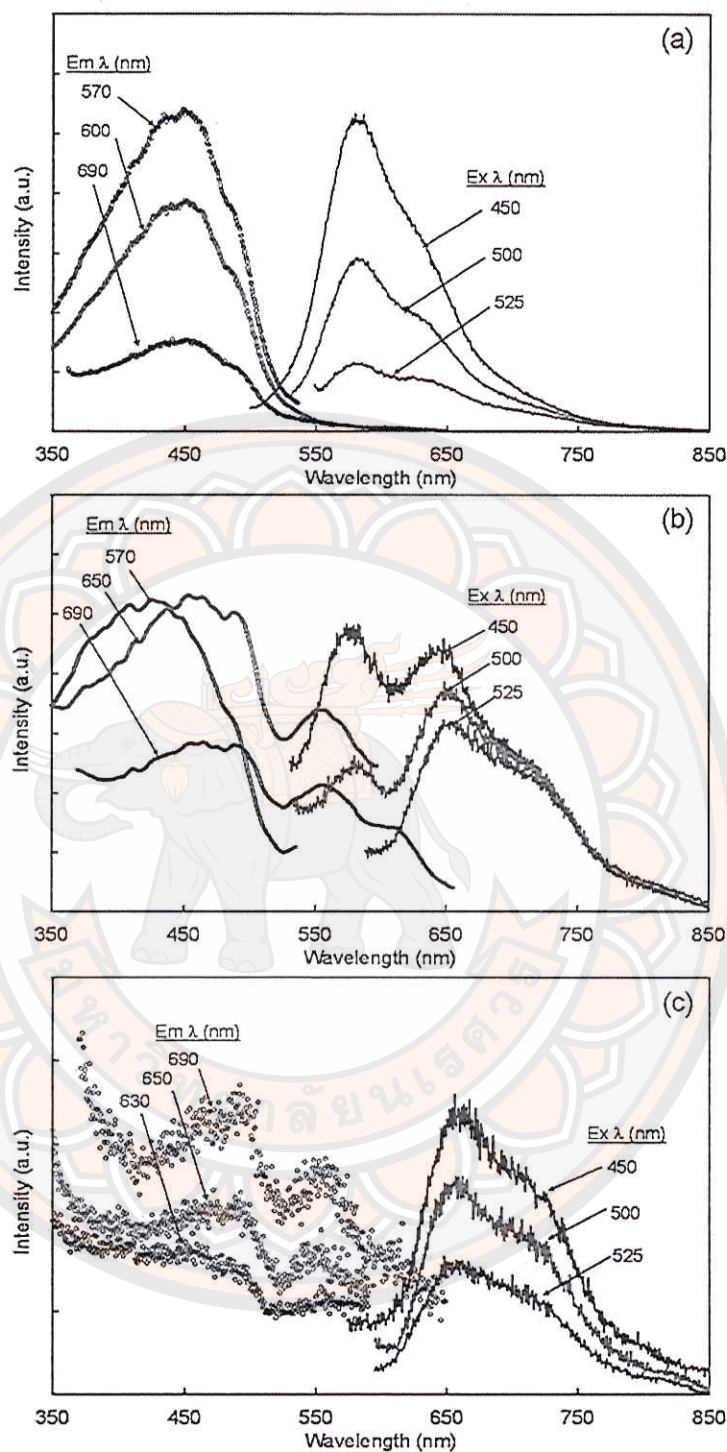
Figure 73 (left) PLE spectra and (right) PL spectra of 0.001 mg/mL *rr*-P3OT mixtures of pyridine and ethanol. The ratios of ethanol are (a) 0% v/v, (b) 40% v/v and (c) 99% v/v, respectively. The spectra were measured at different emission wavelengths (Em λ) and excitation wavelengths (Ex λ), respectively.

Significant change is detected in PLE and PL patterns when 60% v/v EtOH is added into the CRB solution. The PL pattern of *rr*-P3OT in this system varies upon increasing the excitation wavelength as shown in Figure 72b. Using excitation wavelength at 450 nm, which is at maximum absorption of the non-aggregated chains, yields PL spectra with two peaks at 575 nm and 625 nm. As discussed in previous section, the first peak relates to PL emission of non-aggregated segments while the second one arises from new emissive species. The increase of excitation wavelength to 500 nm results in the suppression of PL peak at 575 nm. Moving the excitation wavelength to 525 nm, which mostly excites the aggregated chromophores, provides PL spectrum with peak and shoulder at about 645 nm and 715 nm, respectively. This result indicates that two types of emitting species exist in the system. The PLE measurements also reveal that these emissive species absorb energy at different regions. When the emission wavelength is fixed at 580 nm, the PLE spectrum exhibits a peak at 450 nm, consistent with absorption λ_{max} of non-aggregated chains. The increase of emission wavelength to 650 nm and 690 nm causes systematic growth of redshift band in PLE spectra. The detection of the redshift band in PLE spectra indicates that the new emissive species belong to aggregates.

The measurements of PLE spectra in CRB/EtOH containing 99% v/v EtOH clearly reveal absorption band of the emissive aggregates (see Figure 72c). In this system, the PL spectrum is independent of excitation wavelength. The use of excitation wavelengths at 450 nm, 500 nm, and 550 nm, which excites both non-aggregated and aggregated segments, provides the same PL pattern. The PL spectra constitute a peak and shoulder at about 650 nm and 715 nm, respectively. The dense packing of chromophores in this unfavorable environment of nonsolvent promotes the efficiency of energy transfer processes. Therefore, the PL emission only occurs via aggregated chromophores with lowest HOMO–LUMO energy gap. The PLE spectra measured at different emission wavelengths show the same pattern, constituting three peaks at about 500 nm, 555 nm and 605 nm. The redshift peaks observed in absorption spectrum are at about 515 nm, 555 nm and 605 nm (see Figure 66a). This comparison shows that the absorption λ_{max} of emissive aggregates is slightly shorter than that of the non-emissive one. In other words, these aggregates possess different conjugation lengths. The measurements of PLE and PL of *rr*-P3OT in PRD/EtOH provide

consistent results (see Figure 73b and c). The variation of excitation wavelength causes the change of PL pattern, corresponding to the presence of two emitting species in the solution containing 40% v/v EtOH. At 99% v/v EtOH, three peaks are clearly observed in PLE spectra. The peak position is the same as that of the CRB/EtOH system, indicating that the same emitting species are presence in both systems.

The change of PLE and PL spectra upon increasing EtOH ratio is summarized in Figure 74. The PL spectra measured by using excitation wavelength at 450 nm show systematic growth of redshift peak upon increasing EtOH ratio to 60% v/v, corresponding to the formation of emissive aggregates. At 80% v/v EtOH, the emission of aggregates dominates the entire PL spectrum. The emission of aggregates is promoted when the excitation wavelength is increased to 525 nm (see Figure 74c). The measurements of PLE spectra by fixing emission wavelength at 600 nm reveal absorption band of non-aggregated segments. The PLE spectra obtained from the solutions containing 0, 40, 50 and 60% v/v EtOH show the same pattern (see Figure 74b). This is due to the presence of relatively large fraction of non-aggregated segments in these systems. At 80% v/v EtOH, PLE spectrum is not detectable because the emission processes only occurs via aggregated segments. When the emission wavelength is moved to 690 nm, systematic growth of redshift band in PLE is observed upon increasing EtOH ratio (see Figure 74d). This corresponds to the increase of emissive aggregates due to the dense packing of *rr*-P3OT segments.
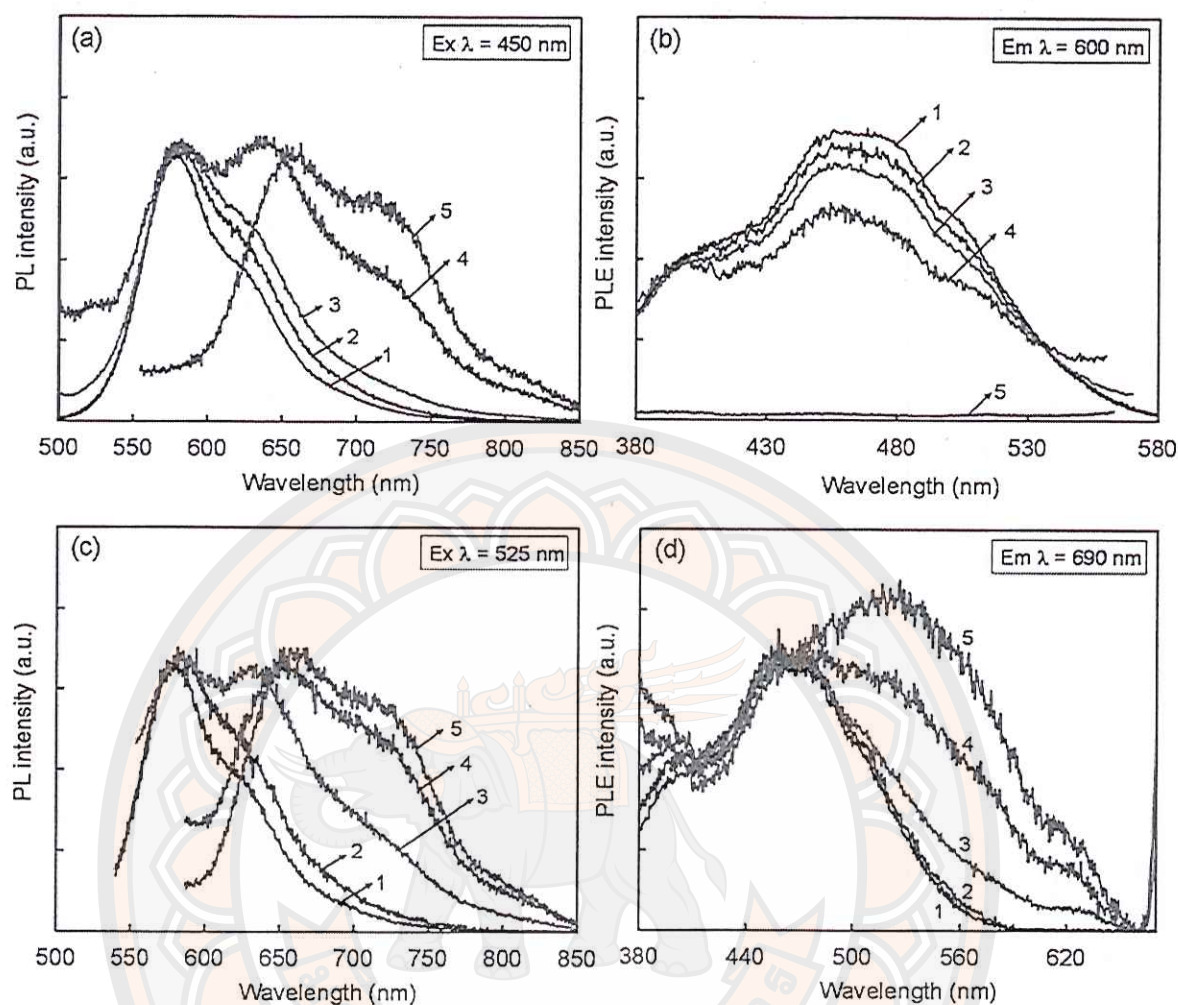
Figure 74 (a and c) PL spectra and (b and d) PLE spectra of 0.001 mg/mL *rr*-P3OT in mixtures of chlorobenzene and ethanol measured at excitation wavelengths (Ex λ), (a) 450 nm and (c) 525 nm and at emission wavelengths (Em λ), (b) 600 nm and (d) 690 nm. Ratios of ethanol are (1) 0% v/v, (2) 40% v/v, (3) 50% v/v, (4) 60% v/v and (5) 80% v/v.

Conclusion

Our study reveals different aggregation behaviors and photophysical properties of *rr*-P3OT in solvent–nonsolvent systems. Non-emissive aggregates form in an early stage of interchain association, resulting in the growth of three redshift peaks in absorption spectrum. The decrease of solvent quality forces dense packing of *rr*-P3OT segments within the aggregates, which in turn causes the formation of emissive aggregates. The PL emission of this type of aggregates occurs at lower energy region compared to that of the non-aggregated chains. The non-emissive and emissive aggregates exhibit slightly different absorption bands. We also observe that the photophysical properties of aggregates depend on the preparing conditions such as the initial solvent. The use of PRD and CRB as initial solvents provides aggregates with rather different absorption patterns. Our results provide fundamental understanding about aggregation behaviors of conjugated polymer in different states. This knowledge is important for controlling their properties in advanced technologies.

CHAPTER VII

CONTROL OVER THE PHOTOPHYSICAL PROPERTIES OF NANO-SIZE AGGREGATES OF *rr*-P3OT

Introduction

Regioregular poly(3-alkylthiophene) (*rr*-P3AT) is a very important semi-crystalline conjugated polymer which is intensively studied in the area of flexible organic electronic technologies such as polymer solar cells (PSCs) [1, 2, 3, 4], organic light-emitting diodes (OLEDs) [5, 6, 7], and organic field-effect transistors (OFETs) [10, 11, 12] for over few decades. Their environmental stability and large extent of π-orbital overlapping in their crystalline structure which promote high charge carrier mobility make them suitable for these advanced technologies [40, 41, 42, 43]. A key parameter in the optimization of the transport properties in devices is influenced by the existent of P3AT aggregate via the overlap of π-orbital stacks on top of each other. The π-π stacking distance and chain packing arrangement within the aggregated segments could affect a charge-hopping transport mechanism and their photophysical properties. For example, the OFETs technology require the edge-on orientation of polymer chain with the π-stacking in-plane for improving charge transport between source and drain electrodes. The face-on orientation is desired for PSCs to induce the charge transport along the film surface to evacuate photogenerated charges. For OLEDs, on the other hand, the polymer film should avoid from the aggregate to get high emission color [11, 51, 82].

The crystallinity of self-assembled polymer can be significantly modified by several parameters such as conjugated polymer solubility [39, 85, 107, 138, 141], solvent mixtures, and solution preparation method [86, 87, 88, 101, 140, 142]. For example, the use of different initial solvents, dichloromethane and tetrahydrofuran, for fabricating conjugated polymer nanoparticles presents the various chain packings which consequently show the emission color with green and red color, respectively [143]. The organization of *rr*-P3AT aggregation has been often studied in solvent-nonsolvent system by changing the composition of the solvent. The unfavorable

interactions between polymer chain and poor solvent can drive self-assembly and aggregation of polymer chain. The degree of crystallization should depend on the amount of poor solvent in the system. The kinetic and/or thermodynamic balance in the aggregation behavior of side chain and main chain upon changing the ratio of mixed solvent is also important factor for the formation of crystallinity [87]. The solvation properties of mixture of solvent-nonsolvent can affect not only the crystallinity of polymer but also the quality of the interfacial area between materials. Kiriy, et al. [74, 75] is pioneers group that report the solvation properties of different type of poor solvents on the formation of P3AT aggregation. The site selective interaction between poor solvent, hexane, and alkyl side chain of P3AT chain leads to the formation of the helical conformation which provides the one-dimensional aggregation in single-molecular level [73]. Our previous study, we have demonstrated the aggregation behavior of *rr*-P3OT in alkane system. The addition of less solubility solvent, hexane, into *rr*-P3OT in cyclohexane solution induces the formation of intrachain aggregation. The photoluminescent measurement indicates that the aggregate is a non-emissive species. The chain packing shows the nanorod structure with the formation of the intrachain packing upon increasing amount of hexane. Our following study shows that the photophysical properties of aggregates depend significantly on segmental packing. The loose aggregate packing provides the non-emissive species while the densely packed aggregate becomes emissive.

In this study, we seek a method to control photophysical nano-size aggregates of *rr*-P3OT. A series of linear alcohols is used as a poor solvent. These solvents allow fine tuning of the solubility parameter which in turn affects the segmental packing of *rr*-P3OT within the aggregates. The variation of polymer-solvent interactions induces different types of assembled states and subsequently affects their photophysical properties.

Results and discussions

Effect of hexane and hexanol on photophysical properties of aggregates

In this section, we investigate the effect of poor solvents on the aggregation behaviors and their photophysical properties of rr-P3OT in solvent-nonsolvent. Hexane and hexanol are used as poor solvents in this study. The structures of these two solvents are similar. However, the presence of hydroxyl group in hexanol causes drastic difference of the interactions with rr-P3OT segments. The rr-P3OT consists of the thiophene backbone and the octyl side chains with rather different solubility parameters. Therefore, the solubility of rr-P3OT depends on the specific interactions of each segment with surrounding solvents. The dielectric constant and solubility parameters in Table 6 show that hexane is a good solvent for octyl side chain. However, hexane is a poor solvent for thiophene backbone because their solubility parameters are quite difference. Hexanol is a poor solvent for both thiophene unit and octyl side chain. Although the solubility parameter of hexanol is close to that of the thiophene ring, its dielectric constant value is much higher. The differences of these polymer-solvent interactions are expected to affect local segmental packing, which in turn causes the variation of the photophysical properties of rr-P3OT aggregates.

The solubility parameters of the rr-P3OT and toluene (TOL) are equal, implying that the isolated chains are extended in this system. The absorption spectrum exhibits a single peak with λ_{max} at 453 nm (see Figure 75), assigned to the π-π^* transition within conjugated backbone. The PL spectrum (see Figure 76) exhibits a peak at about 574 nm with vibronic shoulder at about 615 nm corresponding to the relaxation of excited electrons to different vibrational energy levels at the electronic ground state. Addition of 0-60% v/v hexane hardly affects the change of absorption spectra (Figure 75a), implying the well-dissolved rr-P3OT chain in mixed solution. However, the absorption spectrum of rr-P3OT at 60% v/v of hexane slightly shows the blue shift of λ_{max} about 10 nm with respect to that of the rr-P3OT in TOL solution. This observation is attributed to the decrease of conjugation lengths because of the twisting of thiophene backbone to avoid the unfavorable interaction between thiophene unit and hexane. The increase of hexane ratio up to 80% v/v still causes the blue shift. In addition, the absorption spectrum exhibits the additional absorption bands at lower energies (λ = 558 and 607 nm), correlated to the main chain packing of

aggregates [83, 85, 86, 87, 88, 107, 138, 139, 140]. Therefore, at 80% v/v of hexane ratio, the *rr*-P3OT chains start to interact with each other, allowing intersegment delocalization of the π electrons. The further increase of the hexane ratio to 90% v/v causes the growth of the red-shift peaks while the absorption peak (λ_{max} at ~453 nm) representing the non-aggregated segments gradually decreases. Therefore, higher fraction of aggregates forms upon increasing concentration of hexane. Figure 75c shows the change of *rr*-P3OT solution color from yellow to purple upon increasing the hexane ratio.

The polymer-solvent interaction is changed by using hexanol as a poor solvent. Hexanol is a poor solvent for all *rr*-P3OT segments. The unfavorable interactions drive the polymer chains to form aggregates, possessing different photophysical properties. Addition of 20% v/v hexanol does not affect the absorption pattern. Addition of 40% v/v hexanol causes the appearance of red-shift peaks similar to the behavior of TOL/hexane system (Figure 75b). However, aggregation of *rr*-P3OT chains takes place at much lower concentration of hexanol. The increase of hexanol ratio to 60% v/v results in strong three red-shift peaks in absorption spectra at 515 nm, 552 nm and 603 nm. The increase the hexanol ratio to 99% v/v show systematically increases of the absorbance of these red-shift peaks, indicating the increase of aggregate fraction within the system. We also observe that absorption spectra of the aggregates obtained from two systems show rather different patterns. The absorbance peaks at about 515 nm and 552 nm in the system of TOL/hexanol are much higher than that of the system of TOL/hexane. The absorption peak at about 610 nm is comparable for both systems. The variation of these peaks can be attributed to the different type of chain packing. The H- and J- aggregates model has been reported by Spano, et al. [136, 137]. The H-type aggregate dominates a high degree of torsional disorder (i.e. shorter conjugation length) while J-type aggregate possess a high degree of planarity of the thiophene rings (i.e. longer conjugation length). The red shift of absorption pattern indicates that aggregates in our system belong to the J-type.

The chain packing of *rr*-P3AT has been proposed in two different characteristics, called From I and From II [77, 78, 79, 80, 81, 82]. The interdigation of alkyl side chain occurs in the structure of Form II, whereas the alkyl side chain in Form I is not interdigitated. The π-π stacking distance of thiophene ring in these two

forms is different. Form I structure usually provides the π-π stacking distance of about 0.38-0.39 nm, while Form II is about 0.47 nm [79, 82]. The optical properties are also rather different. Form II crystal usually exhibit the blue shift in the absorption spectra with respect to Form I. Qu and coworkers [80] have found the absorption peak of P3BT Form I crystal at about 610 nm and 560 nm while Form II show the blue shift to about 589 nm and 541 nm.
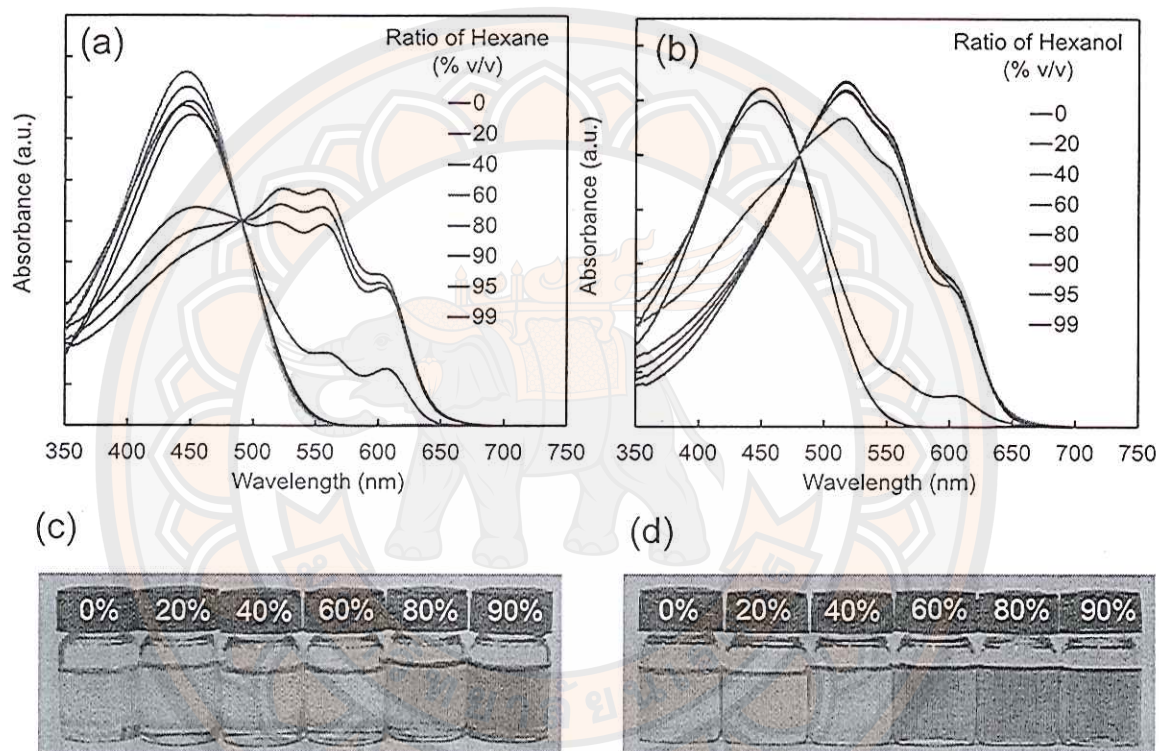
Figure 75 Absorption of 0.001 mg/mL *rr*-P3OT in mixture of (a) TOL/hexane and (b) TOL/hexanol. Photographs under ambient condition of *rr*-P3OT in mixture of (c) TOL/hexane and (b) TOL/hexanol.

The measurement of PL spectra of *rr*-P3OT aggregate shows the interesting photoluminescence properties. In TOL/hexane system, no change of PL spectra is observed (Figure 76a). Although the absorption spectra show the formation of aggregated segments when adding hexane, the PL spectra is still very similar to that of the isolated *rr*-P3OT chain in TOL solution. The emission species of *rr*-P3OT in mixed TOL/hexane is the similar to that of the *rr*-P3OT in TOL solution which arises from the non-aggregated segments. The emission efficiency also decreases upon increasing the amount of hexane as shown in Figure 76c. This behavior accords to the *rr*-P3OT in mixture of cyclohexane/hexane. Addition of hexane into *rr*-P3OT in cyclohexane solution forces the chain coiling to densely packing which causes the formation of intrachain aggregate. This aggregate type also shows the non-emissive properties. In addition, the non-emissive aggregates can be formed in the initial state of aggregation, where the conjugated segments weakly interact. The aggregates of poly(9,9-di(2-ethylhexyl)fluorene) in mixtures of chloroform/methanol also show the non-emissive species [129].

In TOL/hexanol system, the addition of 20-60% v/v hexanol does not affect the PL pattern. The PL spectra are still similar to that of *rr*-P3OT in TOL solution. The results indicate that the PL spectrum arise from the non-aggregate segment. Although the absorption spectra of *rr*-P3OT in TOL/hexanol at 40-60% v/v of hexanol ratio exhibit the red-shift peaks, the PL pattern remains unchanged. This result indicates that the aggregated segment at the early state cannot emit the light. This behavior is similar to the properties of *rr*-P3OT aggregates in mixed PRD/EtOH and CRB/EtOH. We have found significant change of PL spectra when increasing the hexanol ratio up to 80-99% v/v. The PL spectra show the red-shift peak at 650 nm following the shoulder at about 720 nm. This observation indicates that the aggregate is emissive species which have lower HOMO-LUMO energy gap. Our previous study has reported that the emissive aggregate results from the dense packing of *rr*-P3OT. The emission color of *rr*-P3OT in TOL/hexanol shows red-orange color. The emission efficiency also decreases due to the formation of aggregates when the hexanol ratio is increased (see Figure 76d).
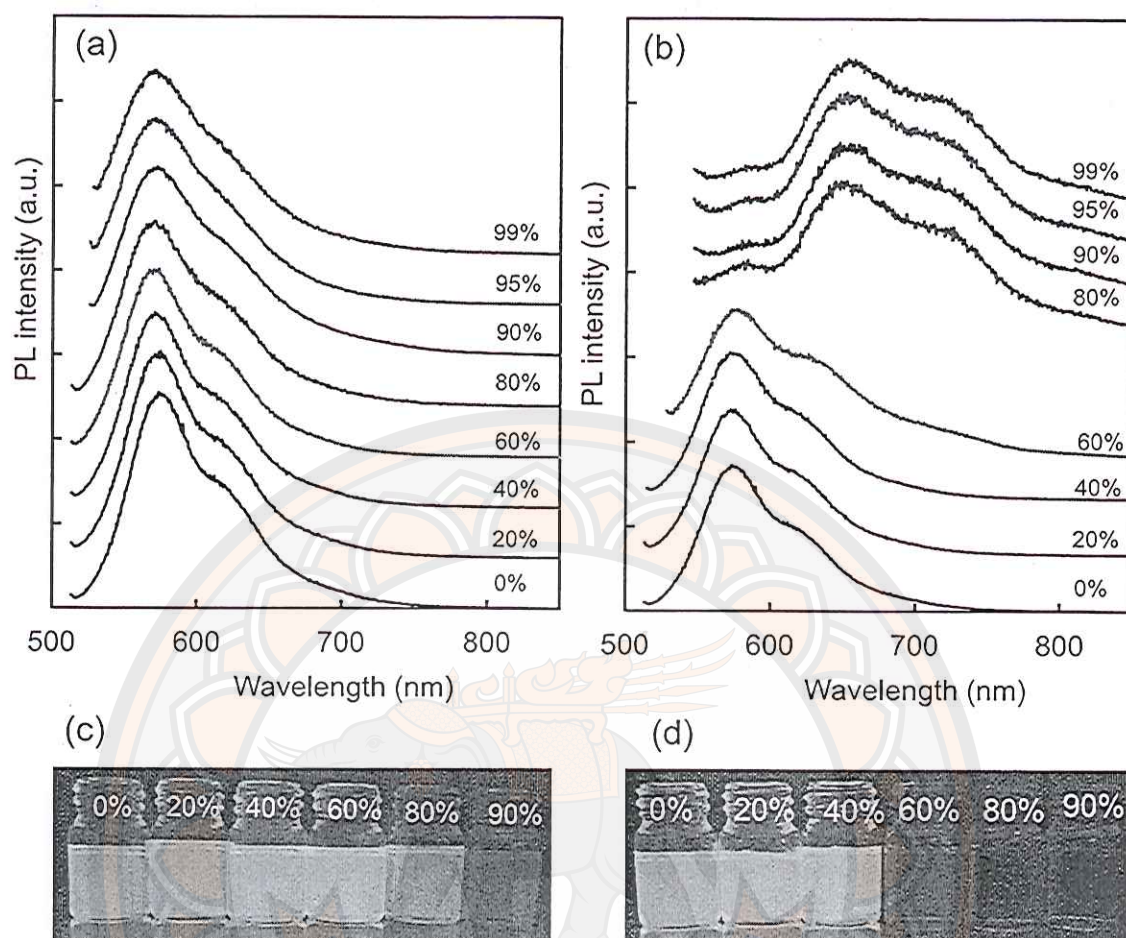
Figure 76 PL spectra of 0.001 mg/mL *rr*-P3OT in mixtures of (a) TOL/hexane and (b) TOL/hexanol. Ratios of poor solvents in %v/v are shown on the right hand side of each spectrum. Photographs under UV light irradiation of *rr*-P3OT in mixtures of (c) TOL/hexane and (d) TOL/hexanol. The spectra were recorded at excitation wavelength 500 nm.

The photophysical changes of *rr*-P3OT in mixed TOL/hexane and TOL/hexanol are summarized in Figure 77. The λ_{max} of absorption and PL spectra are plotted as a function of poor solvent ratio. In TOL/hexane system, the addition of 0-80% v/v of hexane slightly decreases λ_{max} about 10 nm, implying the decrease of conjugation length due to the twist of thiophene rings to avoid the unfavorable interaction between the thiophene unit and poor solvent. PL spectra show the consistent results with blue shift of PL spectra. Addition of hexane at 90% v/v slightly increases the λ_{max} of absorption spectra due to the existent of chromophores with long conjugation length. Increase of the hexane ratio up to 95 and 99% v/v show drastic red shift of λ_{max} of absorption spectra to about 553 nm indicating the increase of π-electron delocalization along the conjugation length. The delocalization of π-electron probably takes place within the intrachain aggregate in which the electrons can hop along the thiophene backbones. However, the PL spectra continuously show blue-shift of λ_{max} indicating that the aggregate from this system is the non-emissive type. In TOL/hexanol system, the λ_{max} of absorption spectra is hardly affected when adding the hexanol at 20-40% v/v. The PL spectra show the similar results. When hexanol ratio is increased up to 60-99% v/v, the absorption spectra show red-shift of λ_{max} to about 513 nm. The results indicate the formation of aggregate. The variation of PL spectra changes accordingly. In this system, the aggregate can emit the light.

We further investigate the relationship between the photophysical properties and aggregation of *rr*-P3OT by plotting of the absorbance ratio at 515/450 nm and PL intensity ratio at 650/575 nm as function of poor solvent ratio (see Figure 77c, d). The absorbance ratio indicates the degree of aggregate in the system while the PL intensity ratio points to the occurrence of emissive type of aggregate. The absorbance ratio shows that the aggregate fraction increases with the poor solvent ratio. The degree of aggregate obtained from TOL/hexanol system is larger than that of the TOL/hexane system indicated by the higher absorbance ratio. In TOL/hexanol system, the absorbance ratio is steady when increasing the hexanol ratio up to 90-99% v/v. This may result from the dense of polymer chain packing in solution due to the decrease of solubility. For the PL intensity ratio, the system of TOL/hexane does not show the increase of this ratio. The PL intensity ratio is still comparable to that of the isolated

rr-P3OT chain in TOL solution. This indicates that the aggregate type in this system cannot emit the light. This system consists of non-emissive type. In TOL/hexanol system, the PL intensity ratio at 0-60% v/v of hexanol is comparable to that of the rr-P3OT in TOL solution. This is indicated that the aggregates of rr-P3OT at this state are loosely aggregate and do not emit the light. The PL intensity ratio increases when the hexanol is added up to 80-99% v/v. The results indicate that the emissive species of aggregate increases with increasing amount of hexanol.
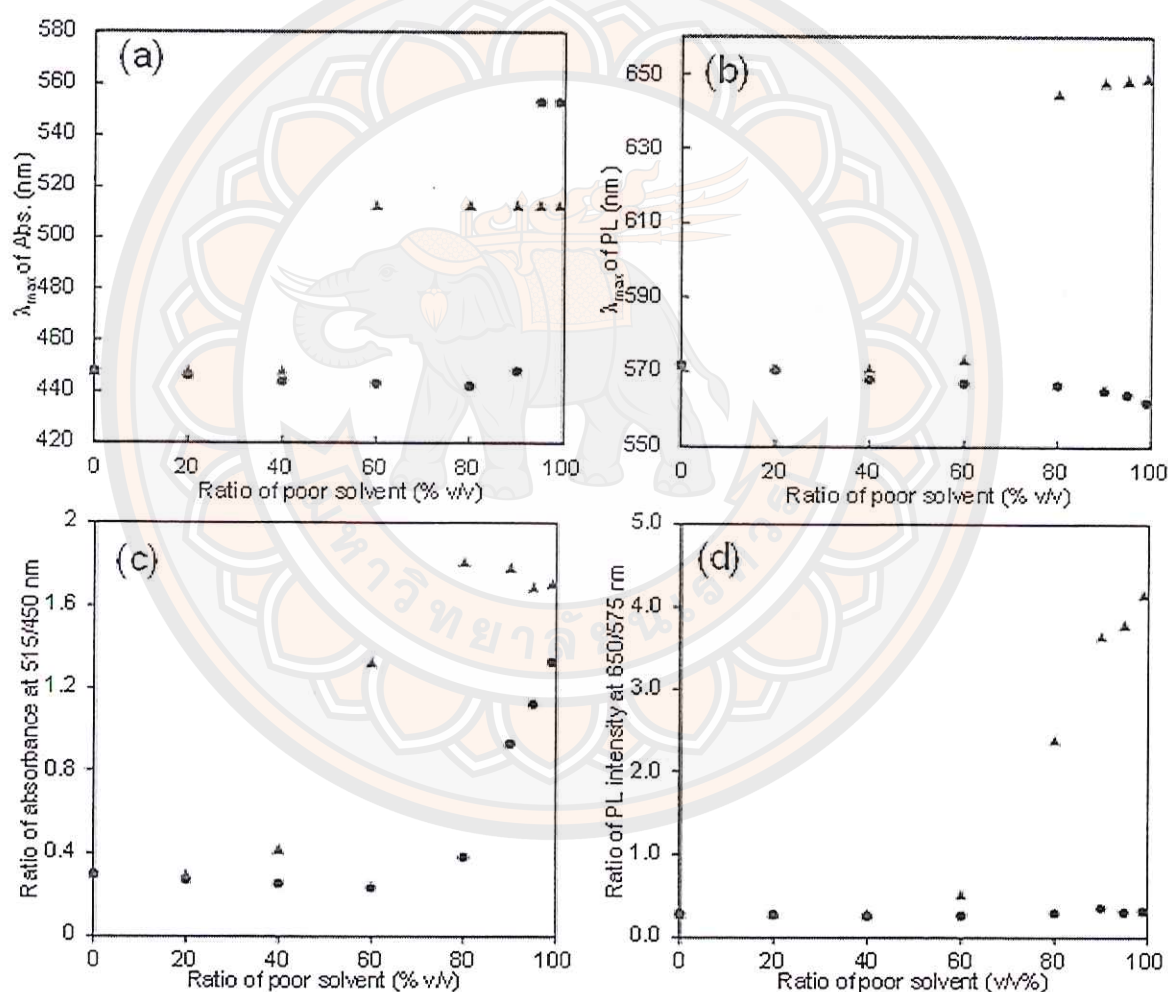
Figure 77 Variation of λ_{max} of (a) absorption and (b) PL spectra of 0.001 mg/mL rr-P3OT in TOL/hexane and TOL/hexanol and plots of (c) absorbance ratio at 515/450 nm and (d) PL intensity ratio at 650/575 nm of 0.001 mg/mL rr-P3OT in TOL/hexane and TOL/hexanol. The circle and triangle symbols represent for hexane and hexanol, respectively.

We have measured the PLE spectra to evaluate the types of emissive species in each system. The PLE spectra represent the absorption band of emissive species. Figure 78 illustrates the PLE spectra recorded at emission wavelength 650 nm which is the λ_{max} of emissive aggregate. In TOL/hexane system, the variation of hexane ratio does not affect the PLE pattern. The PLE spectra of rr-P3OT in TOL/hexane show the similar pattern to that of rr-P3OT isolated chain in TOL solution. The PLE spectra do not show any red shift peaks although the absorption spectrum of rr-P3OT in mixture of TOL and 99% v/v of hexane exhibit the drastic red-shift peaks. This result indicates that the emission properties of rr-P3OT arise from the non-aggregated chain. Therefore, it is confirmed that aggregates in TOL/hexane solution are the non-emissive type.

In TOL/hexanol system, on the other hand, the patterns of PLE spectra shift to the low-energy region upon increasing the ratio of hexanol. Addition of 60% v/v hexanol exhibits the λ_{max} of PLE spectrum at the same position to that of rr-P3OT in TOL. This indicates that the emission properties come from the non-aggregate. However, the PLE spectrum also constitutes of the low-energy tail in the range of 520-630 nm, indicating the absorption energy of emissive species. The significant change of PLE spectra is detected when the amount of hexanol is increased to 80-99% v/v. The PLE spectra clearly exhibit the growth of red-shift peaks at about 490, 550 and 600 nm which is also observed in absorption spectra. The results indicated that the dense packing of rr-P3OT in mixture of TOL and 80-99% v/v hexane is emissive type. The result is similar to our previous study of rr-P3OT in CRB/ethanol and PRD/ethanol. The dense packing of rr-P3OT shows the emissive specie when the ratio of ethanol is increased.
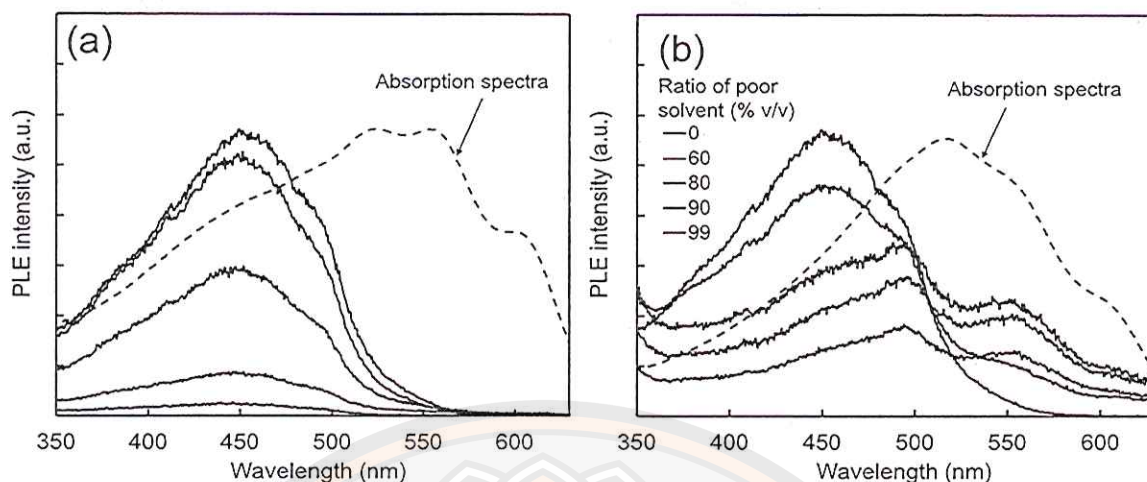
Figure 78   Comparison of PLE and absorption spectra of 0.001 mg/mL *rr*-P3OT
in mixture of (a) TOL/hexane and (b) TOL/hexanol. Absorption
spectra were measured from 99% v/v of poor solvents. The PLE
spectra were recorded at emission wavelength 650 nm.

To get more information about the photophysical properties of aggregates, we
have analyzed the PL and PLE spectra at different excitation wavelengths and
emission wavelengths, respectively. The PL patterns of *rr*-P3OT in TOL solution are
independent of excitation wavelength (see Figure 79a). The variation of excitation
wavelength from 450 nm to 525 nm, exciting chromophores with different conjugation
lengths, provides the same PL patterns. The result indicates the existence of only one
type of emitting species. The measurement of PLE spectra at different emission
wavelengths shows the consistent results. In this system, the PLE patterns are similar
to that of the corresponding absorption spectra of *rr*-P3OT in TOL. Previous studies
have shown that long chain length of conjugated polymer consists of multiple
chromophores with various conjugation lengths. The PL emission process can take
place via the chromophore with the lowest HOMO-LUMO energy gap. Therefore, the
energy can transfer from the shorter chromophore to the longer one before the
emission process take place. We have found the similar photophysical behavior of
rr-P3OT in mixture of TOL and 80% v/v of hexane. In this system, the measurement
of PL and PLE spectra also show the independent of recording wavelengths as shown
in Figure 79b. The measurement of PL spectra at different emission wavelengths from

450 to 525 nm, exciting the short chromophores to long chromophores, shows the similar PL patterns to that of *rr*-P3OT in TOL solution. Therefore, it is believed that the emission properties of *rr*-P3OT in mixture of TOL and 80% v/v of hexane originate from the species similar to that of *rr*-P3OT in TOL. This arises from non-aggregate chains. The PLE spectra show the consistent results. The PL and PLE measurement indicate that the aggregate type in mixture of TOL and 80% v/v of hexane is non-emissive type.

In system of hexanol, on the other hand, the PL pattern (Figure 79c) change with the variations of excitation wavelengths. The use of 450 nm excitation wavelength results in two emission peaks at about 575 nm and 655 nm. These two peaks correspond to the emission properties of non-aggregated and the new emissive aggregate, respectively. Moving the excitation wavelength to 500 nm, which excites the longer chromophore, causes the decrease of the emission peak of isolated chain. The PL spectra exhibit the red-shift of λ_{max} at 650 nm with the shoulder at about 720 nm. The use of excitation wavelength at 525 nm exhibits only the red-shift peak of PL spectra. This indicates that the emission properties arise from the aggregated species. The aggregate type in this system is emissive species. The PLE spectra also show the variation of the patterns with the emission wavelengths. The use of emission wavelength at 570 nm, normally detecting the isolated chain, shows the PLE pattern with a peak at about 450 nm. This peak corresponds to the absorption peak of isolated chain. Moving the emission wavelength to measure the longer chromophores or aggregate segments shows the red-shift peaks of the PLE spectra. Therefore, the aggregate segments in mixture of TOL and 80% v/v hexanol are emissive types.
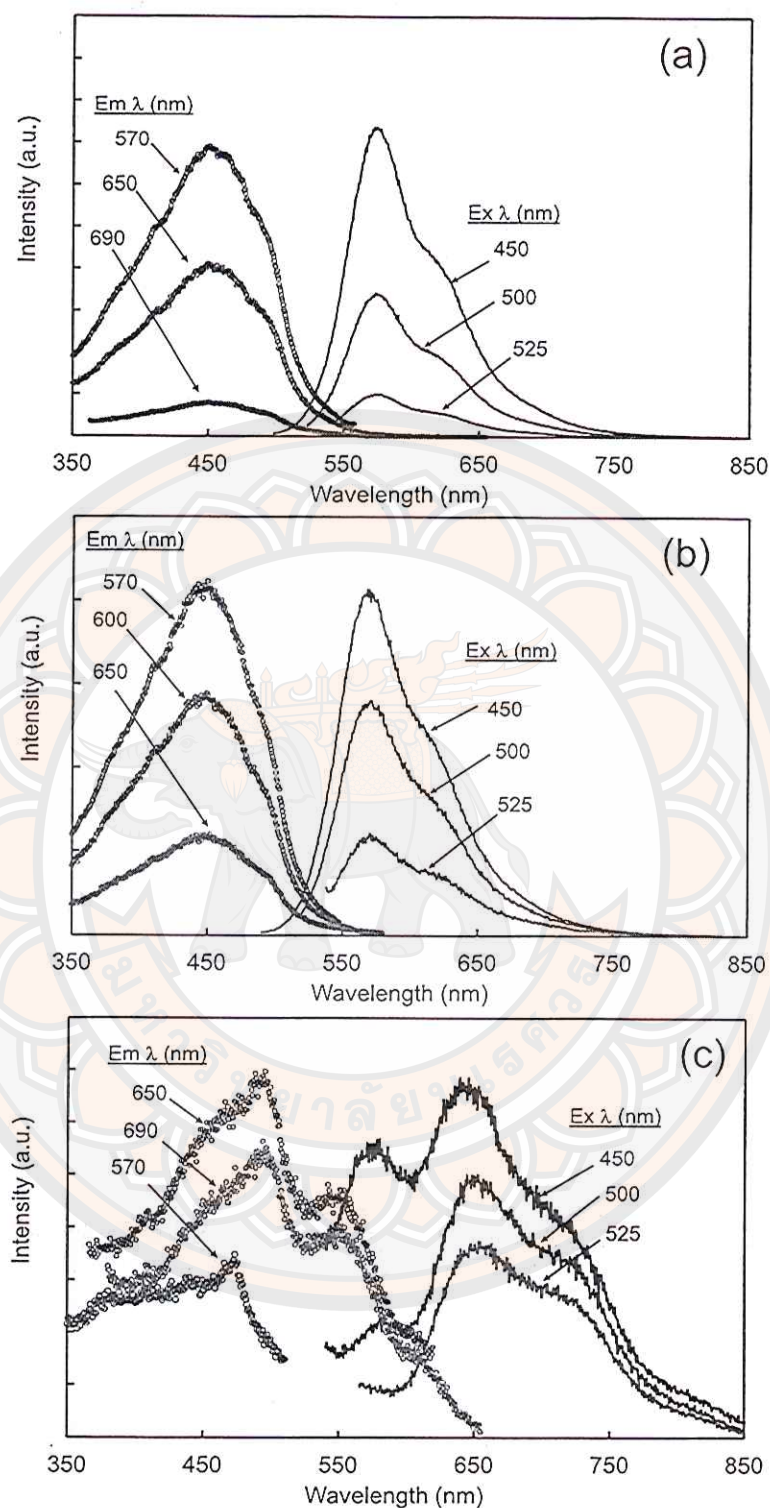
Figure 79 PLE spectra (symbol) and PL spectra (solid line) of 0.001 mg/mL *rr*-
P3OT in (a) TOL, (b) TOL/hexane (20:80% v/v) and (c) TOL/hexanol
(20:80% v/v). The spectra were measured at different emission
wavelengths (Em λ) and excitation wavelengths (Ex λ), respectively.

Effect of alcohols

In this section, a series of linear alcohol is used to control the photophysical properties of *rr*-P3OT aggregates. The long chain alcohol leads to the decrease of dielectric constant. The solubility parameter also decreases to the value of the thiophene ring. These factors increase the solubility of polymer in mixed solvents. Figure 80 shows the absorption and PL spectra of *rr*-P3OT in TOL/decanol. The solubility parameter of decanol is suitable for dissolving the thiophene ring but not for octyl side chain. Addition of 20-40% v/v decanol does not affect the patterns of absorption spectra, indicating the well-dissolved of *rr*-P3OT in mixed solvents. The absorption spectra show the λ_{max} at about 450 nm which is similar to that of the *rr*-P3OT in TOL solution. The PL spectra show the consistent result with the PL emission of non-aggregate chain. Increasing the amount of decanol to 60% v/v, the absorption spectra exhibit the red-shift peaks at 510 nm, 549 nm and 600 nm. These red shift peaks correspond to the aggregation of *rr*-P3OT chains via the overlap of π-orbital resulting in the increase of electron delocalization. However, the PL spectra show the pattern similar to that of the *rr*-P3OT isolated chain in TOL solution. This indicates that the aggregated chains in this system are loosely packing and cannot emit the light. The addition of decanol in the range of 0 to 60% v/v provides rather similar results to that of TOL/hexanol, which observes the non-emissive aggregates at the early state. We have found the interesting results in PL properties when the ratio of decanol is increased up to 80-99 %v/v. The absorption spectra of *rr*-P3OT in TOL/decanol at 80-99% v/v show continuous growth of the red-shift peaks. The measurement of PL spectra yields the interesting result that had never been reported. The PL spectra comprise with two emission peaks at about 575 nm and 640 nm, respectively. The first peak is the emission from the isolated chain. Other emission peak is at about 640 nm following with the shoulder at about 715 nm. This emission band arises from the aggregate segments. Although the site selective interaction between decanol and *rr*-P3OT chain is rather similar to that of the system of TOL/hexanol, the lower polarity of decanol as compared to hexanol could help the better solubility of *rr*-P3OT chain in mixed TOL/decanol. Therefore, the local environment of *rr*-P3OT in TOL/decanol has more favorable interaction than the system of TOL/hexanol.
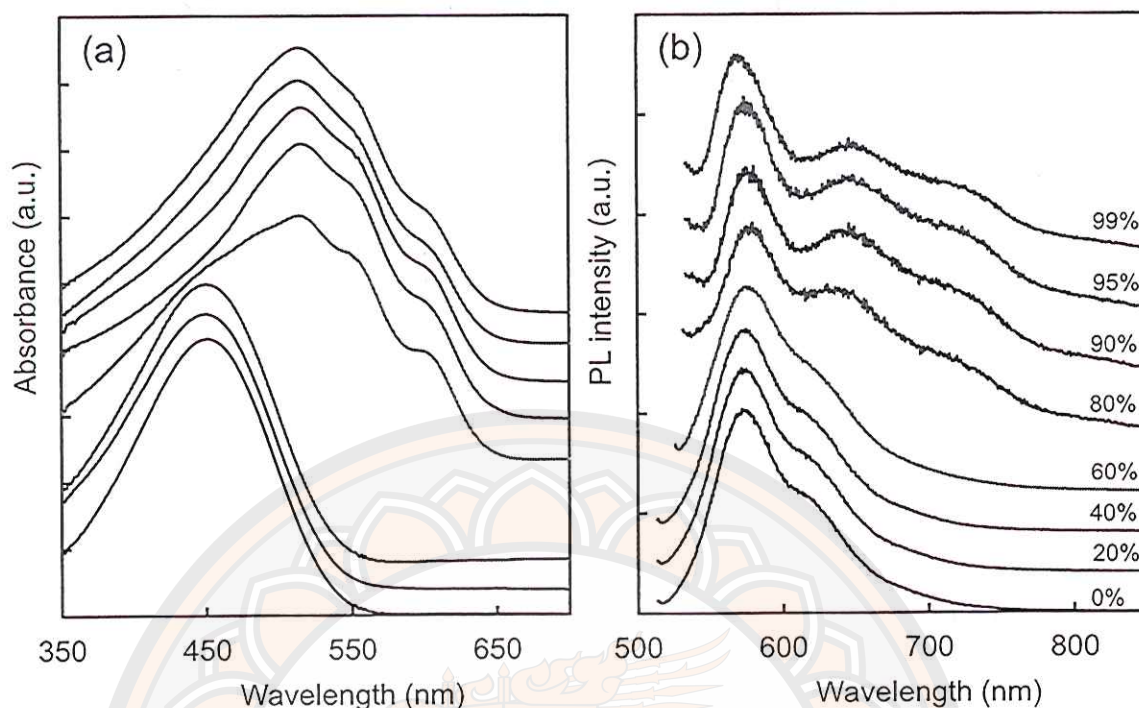
Figure 80 (a) Absorption and (b) PL spectra of 0.001 mg/mL *rr*-P3OT in mixed TOL/decanol. Ratios of decanol in %v/v are shown on the right hand side of each PL spectrum. The PL spectra were recorded at excitation wavelength 500 nm.

Figure 81 shows the absorption and PL spectra of *rr*-P3OT in mixed solutions with alcohols ranging from ethanol to decanol. The polarity of solvents gradually increases with decreasing length of alkyl group. The solubility parameters decrease when using longer linear alcohols. At 60 v/v% alcohols, the red-shift peaks in absorption spectra are observed. The absorption spectra of all alcohol systems show similar pattern. The PL spectra, however, depend significantly on the polarity of alcohols. When the ethanol is used as a poor solvent, the PL spectrum shows red-shit peak at 650 nm and shoulder at about 720 nm. This is because the high polarity of ethanol causes dense packing within the aggregates, forming emissive species. The increase of alcohol side chain results in the formation of non-emissive aggregates. The PL spectra exhibit the emission peaks similar to that of the non-aggregate chain (~575 nm). In the systems of butanol and hexanol, the PL spectra also consist of a small peak at about 720 nm. This feature indicates the formation of small amount of emissive

species. The use of octanol and decanol as poor solvents provides the PL spectra arising from non-aggregate of *rr*-P3OT. The observation demonstrates that the PL properties of aggregates are dictated by polarity of the alcohols.

The solvent quality drastically decreases upon increasing the amount of poor solvent to 90% v/v. The *rr*-P3OT chains are forced to densely pack within the aggregates. All systems exhibit similar growth of red-shift peaks in absorption spectra. However, the patterns of absorption spectra of *rr*-P3OT in mixed with alcohols are different from a mixture of TOL/hexane. This is attributed to the different types of aggregation behaviors between hexane system and alcohol system. The measurement of PL spectra of *rr*-P3OT in alcohol systems, ranging from ethanol to octanol, shows the red-shift peak at about 650 nm with the shoulder around 720 nm. The results indicate the formation of new emissive species with lower HOMO-LUMO energy gap. The difference of PL property is observed when using decanol as a poor solvent. The PL properties arise from both the non-aggregate (PL peak at 575 nm) and aggregate segment (PL peak at 640 nm) as described earlier.
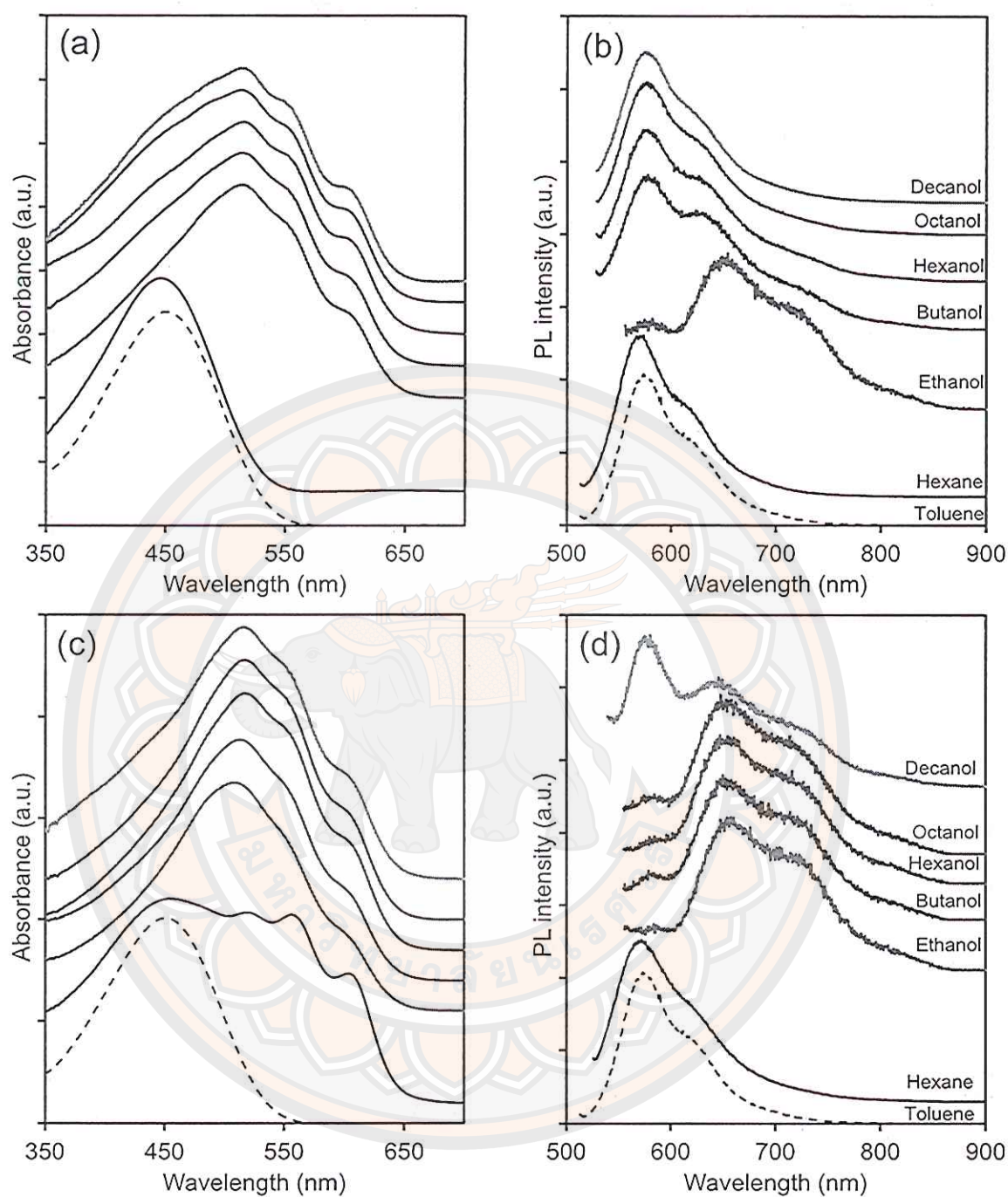
Figure 81 Absorption (left) and PL spectra (right) of 0.001 mg/mL *rr*-P3OT in TOL solution and mixed solutions. The types of poor solvents are shown on the right hand side of PL spectra. Ratios of poor solvents are (a, b) 60 v/v% and (c, d) 90 v/v%. The PL spectra are recorded at excitation wavelength 500 nm.

The photophysical properties of *rr*-P3OT in mixture of TOL and alcohols are summarized in Figure 82. Plots of absorbance ratio at 515/450 nm indicate the formation of aggregate fraction. The absorbance ratio increases with the alcohol ratio, corresponding to the increase of aggregates fraction. The ratio of PL intensity at 650/575 nm implies the formation of emissive species in the system. In all systems, the PL intensity ratio increases with increasing alcohol ratio. However, the fraction of emissive aggregates depends on polarity of alcohol. The magnitude of PL intensity ratio is smallest in the system of decanol with lowest polarity. This indicates that the emission intensity of *rr*-P3OT in TOL/decanol system mostly arises from the non-aggregated chains.
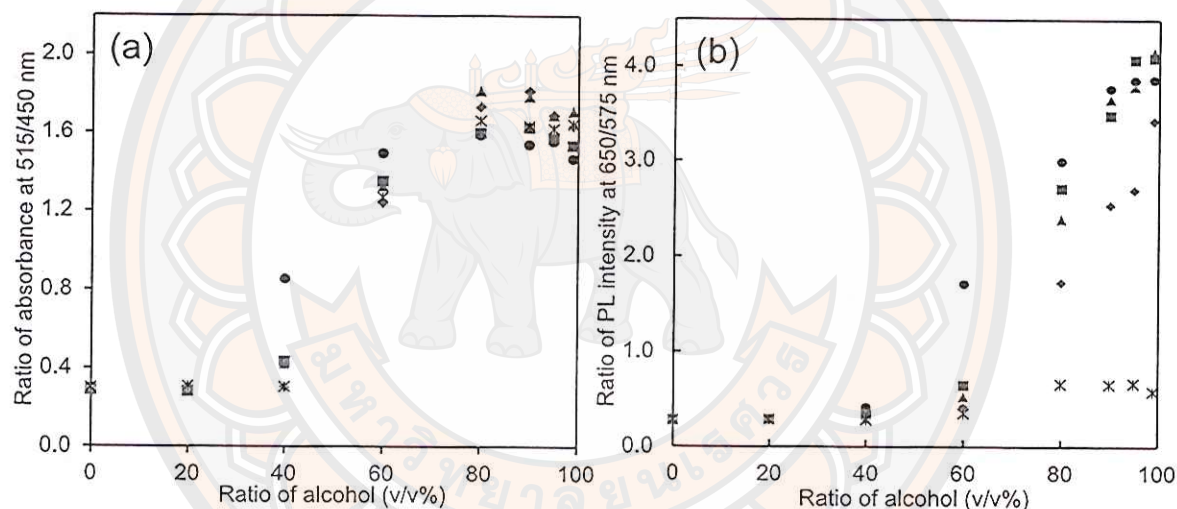
Figure 82 Plots of (a) absorbance ratio at 515/450 nm and (b) PL intensity ratio at 650/575 nm of 0.001 mg/mL *rr*-P3OT in mixture of TOL and series of alcohols. The alcohols are including (•) ethanol, (■) butanol, (▲) hexanol, (◆) octanol and (∗) decanol.

To further explore the nature of chromophore of *rr*-P3OT in TOL/decanol, we record the PL and PLE spectra at difference excitation wavelengths and emission wavelengths, respectively. Figure 83a illustrates the PL and PLE spectra of *rr*-P3OT in TOL/decanol at 80% v/v of decanol. The PL spectra change with the excitation wavelengths. The recorded PL spectrum at 450 nm excitation wavelength which is at maximum absorption of non-aggregate chains shows the PL spectra rather similar to

that of the *rr*-P3OT in TOL solution. The PL spectrum provides the broad pattern with the peak at 575 nm and shoulder at 640 nm. The small emission peak at about 470 nm is also observed. Moving the excitation wavelength to 500 nm and 525 nm which excite both non-aggregated and aggregated chain, the PL spectra show more define pattern as compared to that of the using excitation wavelength 450 nm. The emission peaks still appear at 575 nm and 640 nm, respectively. However, we have found that the intensity ratio at 640/575 nm increases. This result is attributed to the existence of the small amount of emissive species in the system. The measurement of PLE spectra also reveals the absorption energy at different regions. The use of emission wavelength at 570 nm which is close to the maximum emission intensity of non-aggregate chains show the PLE spectrum similar to the absorption spectra of non-aggregated *rr*-P3OT in TOL. The increase of emission wavelength to 650 nm and 690 nm which detects the emissive aggregates yields the growth of red-shift peak in PLE spectra. The red-shift peak indicates the formation of emissive species in aggregate.

The PL and PLE of *rr*-P3OT in TOL and 90% v/v decanol are further investigated (Figure 83b). The use of excitation wavelength at 450 nm exhibits the λ_{max} at 575 nm and shoulder at about 635 nm which correspond to the emission of non-aggregate chain. In addition, we observe the growth of high energy peak at the wavelength about 480 nm. We have suggested that this peak is the emission of some collapsed chain in the system. Moving the excitation wavelength to 500 nm and 525 nm for exciting both non-aggregate and aggregate segments, provide the same PL pattern with two emission peaks at 575 nm and 640 nm, respectively. The emission peak at 575 nm results from the non-aggregate segments which is similar to that of *rr*-P3OT in TOL solution. Another emission peak is at about 640 nm followed by shoulder at about 680 nm. This addition peak reflects the emission intensity of emissive species in the aggregated segments. The measurement of PLE spectra shows the pattern change with the emission wavelengths. The use of emission wavelength at 570 nm which detect the emission species arising from non-aggregate chain exhibits the pattern similar to that of the *rr*-P3OT in TOL solution. The red-shift peak, which indicates the absorption energy of emissive species within the aggregated segments, is observed when moving the emission wavelength to 650 and 690 nm. This red-shift peak is consistent with the red-shift peak in absorption spectra.
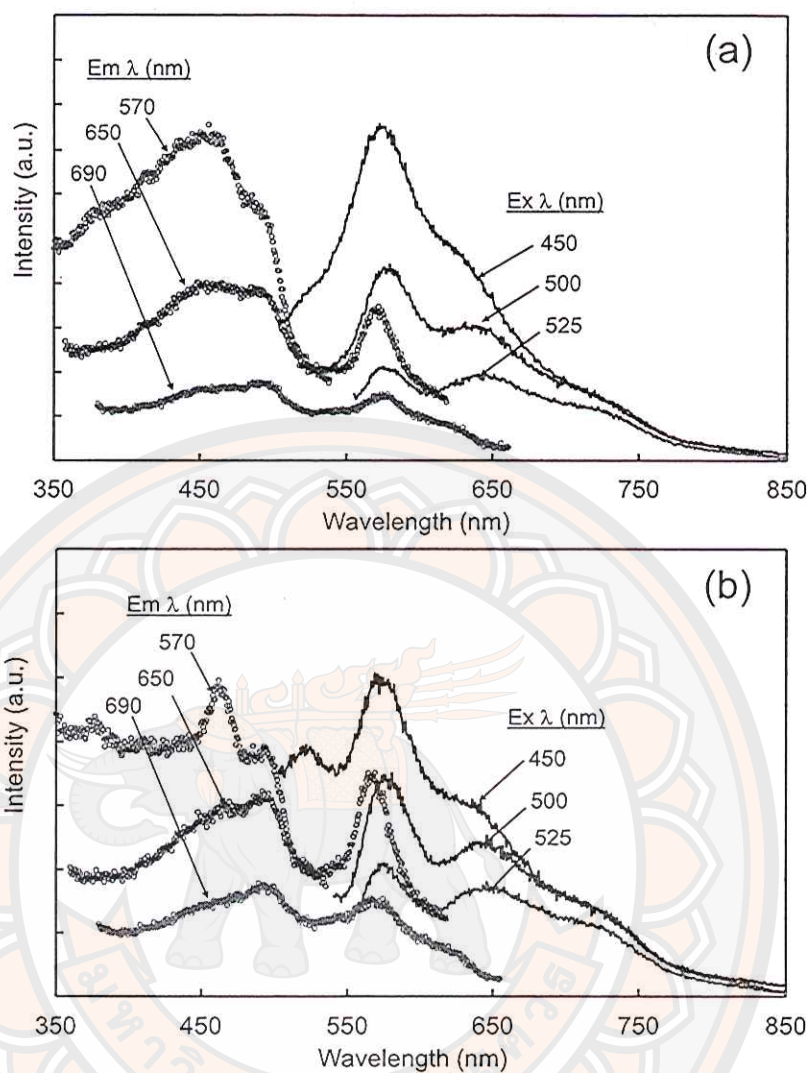
Figure 83 PLE spectra (symbol) and PL spectra (solid line) of 0.001 mg/mL
rr-P3OT in mixed TOL/decanol. The ratios of decanol are (a) 80% v/v
and (b) 90% v/v. The spectra were measured at different emission
wavelengths (Em λ) and excitation wavelengths (Ex λ).

We have explored the morphology of self-assembled *rr*-P3OT in TOL and alcohols by using SEM as shown in Figure 84. The SEM samples were prepared by drop casting of polymer solution containing 80% v/v of alcohols. The SEM images show the spherical particle of *rr*-P3OT nano-aggregate. The morphologies of *rr*-P3OT nano-aggregate vary with the type of alcohols. However, we have found the variation of assembled morphologies when the type of linear alcohols is changed. The use of ethanol as a poor solvent provides the dense dispersion of spherical shape with the average size in the range of 20-40 nm. The morphology shows the narrow size distribution. The higher magnitude of unfavorable interaction causes rapid self-assembling in this system resulting in the fine spherical shape of nano-aggregate. When the long alkyl chain alcohols (butanol, hexanol and octanol) are used, the morphology consists of small and large particles. The average size for small particles is about 23-27 nm and for large particles is about 45-55 nm. The average particle size of these nano-aggregates is summarized in Table 7.

Table 7 **Spectroscopic properties and particle sizes of assembled *rr*-P3OT in mixture of toluene and series of alcohols at 80% v/v**

Alcohols	Spectroscopic properties		particle size (nm)	
	$\lambda_{max(abs)}$ (nm)	$\lambda_{max(ems)}$ (nm)	Small particle	Large particle
Ethanol	508	653	20.94 ± 4.74	38.96 ± 5.63
Butanol	508	647.5	27.84 ± 5.20	56.85 ± 11.17
n-Hexanol	510	645	23.56 ± 4.63	53.06 ± 10.70
n-Octanol	510	647	27.83 ± 5.27	45.76 ± 7.79
n-Decanol	510	572.5	N/A	N/A
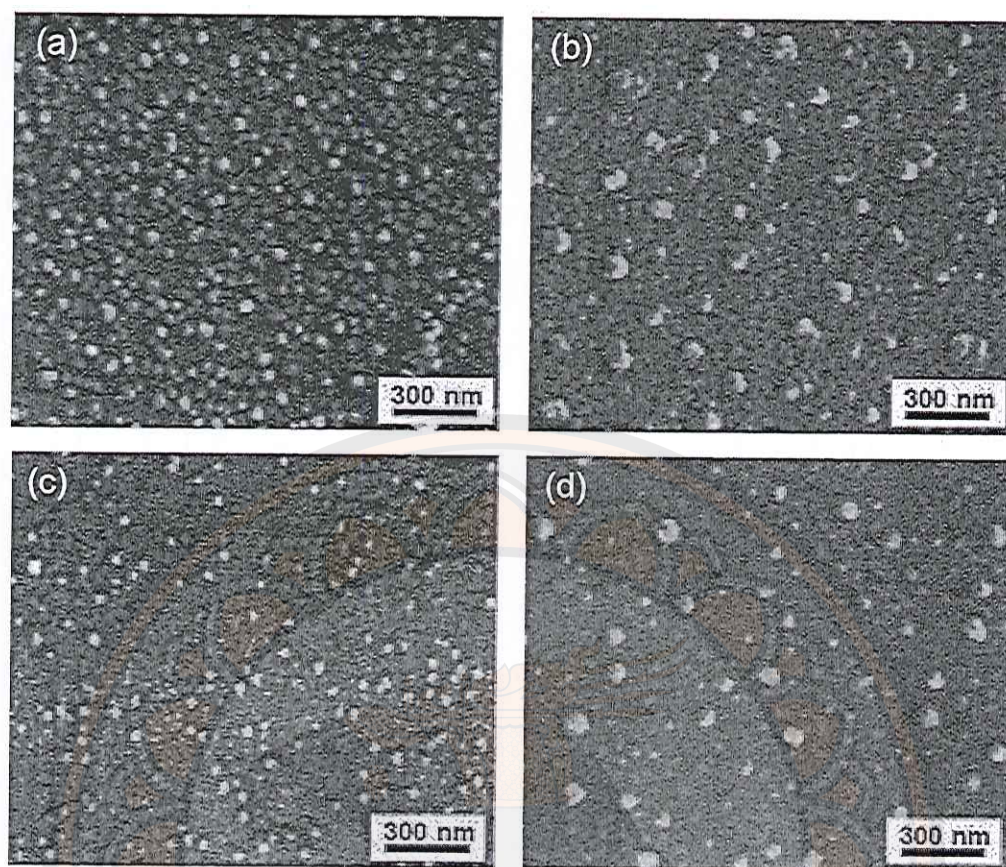
Figure 84 SEM images of *rr*-P3OT film drop-casting from 0.001 mg/mL *rr*-P3OT
in mixture of TOL and 80% v/v alcohols. The alcohols are (a) ethanol,
(b) butanol, (c) hexanol and (d) octanol, respectively.

Conclusion

In this study, we can control the photophysical properties of *rr*-P3OT aggregates by using different types of solvents. The aggregates and their photophysical properties are sensitive to the solubility parameter of the solvents. The use of poor solvent which has the site selective interaction with octyl side chain, for example hexane, leads to the formation of non-emissive aggregate. The system of alcohol induces the dense packing of polymer chains providing the emissive aggregate. The use of long alkyl chain alcohol which increases the solubility of polymer also provides both of non-emissive and emissive aggregates.

CHAPTER VIII

STUDY OF CONJUGATED POLYMER NANOPARTICLES

Introduction

Conjugated polymer is a class of material that has received tremendous attention from scientific community in the past few decades. Major applications of conjugated polymers, which exhibit electroluminescent and semiconducting properties, involve organic electronic technologies such as organic light emitting diode (OLED) [5, 6, 7], organic solar cell (OSC) [1, 2, 3], and organic field emission transistor [10, 11, 12]. Poly[2-methoxy-5-(2'-ethylhexyloxy)-1,4-phenylenevinylene] (MEH-PPV) and regio- regular poly (3-alkylthiophenes) (rr-P3ATs) are well-known conjugated polymers that have been extensively studied. The presence of branched side chains in MEH-PPV causes high fraction of amorphous region in thin film, which in turn enhances the fluorescent intensity [33]. The rr-P3ATs, on the other hand, are more crystalline materials with relatively high charge carrier mobility, while their fluorescent intensity in thin film is rather weak [44, 82]. Therefore, the MEH-PPV is more suitable for OLED application, while the rr-P3ATs are normally utilized as active materials in OSC [144, 145].

Conjugated polymer is also a potential material for being utilized in biotechnologies such as biological fluorescence imaging [19, 20, 21, 22], biological label [23, 24] and fluorescent sensor [25, 26]. To utilize conjugated polymers in these bio-technologies, the polymers are usually fabricated into nanoparticle form. Compared to other types of nanoparticles such as liposomes and micelles, conjugated polymer nanoparticles (CPNs) possess an increased colloidal stability and a better chemical resistance [17]. The fabrication process is usually easier as well. Moreover, the higher biocompatibility and less toxicity of CPNs compared to inorganic nanoparticles are desirable properties for using these materials in the biotechnologies [28, 90]. Because each CPN contains a number of chromophores, it normally exhibits higher brightness and better photostability compared to molecular dyes [19, 96]. Their

photoluminescent properties can also be tuned by varying particles size, composition, and types of conjugated polymers [28, 90].

CPNs can be prepared by using different methods such as oxidative polymerization, miniemulsion, and reprecipitation. The oxidative polymerization process requires catalyst/oxidant such as $FeCl_3/H_2O_2$ and appropriate surfactants [97, 98, 99, 146]. The polymerization of monomers is allowed to take place inside small droplets of the reaction medium stabilized by surfactant. The properties of CPNs can be optimized by varying the surfactant/oxidant/monomer ratio, polymer concentration, polymerization temperature, and reaction time [97, 147]. However, there are several problems involving this method such as poor water solubility of polymer, low oxidizing activity of catalysts, and extremely low conversion [99, 146]. For miniemulsion method, the conjugated polymer dissolved in organic solvent is injected into an aqueous medium containing surfactant molecules [27]. The process generates stable colloidal droplets of the polymer solution. The CPNs are obtained after evaporating the organic solvent. However, the surfactant molecules still remain in the system. The reprecipitation method can produce pure CNPs with controllable size [19, 28, 90]. The process requires the addition of small amount of dilute conjugated polymer solution into an excess volume of water. The sudden decrease in solubility drives the conjugated polymers to form nanoparticle. The reprecipitation method is a popular technique because it is quite simple, cheap and does not require any surfactant or template. The particle size can be simply controlled by adjusting the polymer concentration [19, 89, 90]. Moreover, this method can be applied to a wide variety of conjugated polymers that are soluble in organic solvents.

The preparation and photophysical properties of CPNs have been reported by several research groups. McNeill and co-workers have prepared various CPNs by using reprecipitation method. The injection of a dilute solution of MEH-PPV in tetrahydrofuran (THF) into aqueous medium provides CPNs with particle size ranging from 5 to 10 nm [93]. The use of other conjugated polymers such as polyfluorene, polyphenylene- ethynylene and their copolymers also yield the CPNs with similar size [19, 90]. They have demonstrated in these studies that the photoluminescent (PL) color of CPNs varies with types of the conjugated polymers. The size of CPNs also affects their PL properties. The CPNs of 2,7-poly(9,9-dialkylfluorene-co-fluorenone) exhibit

systematic shift of PL spectra to low-energy region when their size is increased from 5 to 500 nm [91]. The CPNs of polythiophene shows similar behavior. Their PL color changes from blue to red upon increasing the size from 12 to 51 nm [99].

In this work, we present a new and versatile method for controlling the photophysical properties of CPNs. Previous studies have shown that conjugated polymer such as MEH-PPV in solution adopts different conformations depending on the strength of local polymer–solvent interactions [14, 15, 56, 57, 61]. The MEH-PPV chain is extended in a good solvent, dichloromethane (DCM), while the chain forms collapsed coil in a poor solvent, THF [14, 15]. The decrease in solvent quality by addition of nonsolvent forces the MEH-PPV chains into aggregated state, which in turn causes the redshift of absorption and PL spectra [57, 61, 70]. In our recent study, we observe that the variation of initial solvents affects the degree of segmental aggregation in the solvent-nonsolvent system [57]. Since the preparation of CPNs via reprecipitation method also induces the assembling of polymer chains by decreasing solvent quality, the initial solvents are expected to play important role on their aggregation behavior. In this study, we use DCM and THF as initial solvents to prepare CPNs of MEH-PPV and regioregular poly(3-octylthiophene) (rr-P3OT) in aqueous medium. The difference of initial polymer conformations is expected to influence of chain packing within CPNs. In addition, the miscibility of DCM and THF with water is quite different [120, 148] (see Table 8), which may also play important role on the formation of CPNs. In fact, the CPNs obtained by using the DCM and THF exhibit quite different photophysical properties. Our approach provides a simple method for controlling photophysical properties of CPNs without modifying chemical structure and/or composition of the conjugated polymer.

Results and discussions

Nanoparticles of MEH-PPV

Morphologies and size distribution of MEH-PPV nanoparticles revealed by TEM are shown in Figure 85. The nanoparticles prepared from both THF and DCM solvents exhibit spherical shape. Their size, however, varies significantly with type of the solvents. The use of THF as an initial solvent provides the nanoparticles with smaller size. The majority of nanoparticles exhibit diameter of about 40 nm. When the

DCM is used as an initial solvent, average size of the nanoparticles significantly increases to about 120 nm. Their size distribution also becomes much broader. Furthermore, the packing of polymer chains within nanoparticles is affected by the variation of initial solvents. The nanoparticles prepared from DCM exhibit a rougher surface compared to that of the THF system. The interior density of each nanoparticle is also less homogeneous in the DCM system. These results indicate that mechanism for the nanoparticle formation strongly depends on type of the initial solvent. We note that the nanoparticles prepared from THF can be filtered through 200 nm pore size cellulose acetate membrane. Therefore, the agglomeration of nanoparticles in Figure 85a is likely to occur during the preparation process for TEM measurement. The SEM images also detect large fraction of isolated nanoparticles. The nanoparticles obtained in this study exhibit larger size compared to the previous reports [19, 28, 90, 93]. This is attributed to the difference in preparation conditions such as power of the ultrasonication and volume of the added solution in each step. The average particle size is summarized in Table 8.

Table 8 **Physical properties of solvents [120, 148] and size of conjugated polymer nanoparticles prepared by using different solvents**

Solvents	Boiling point (^{o}C)	Dielectric constant	Solubility in water (g/L, 25°C)	Average particle size (nm)	
				MEH-PPV	*rr*-P3OT
THF	66.0	7.52	Miscible	41.3 ± 10.3	49.4 ± 13.1
DCM	39.8	8.93	17.6	127.2 ± 29.8	99.6 ± 64.5
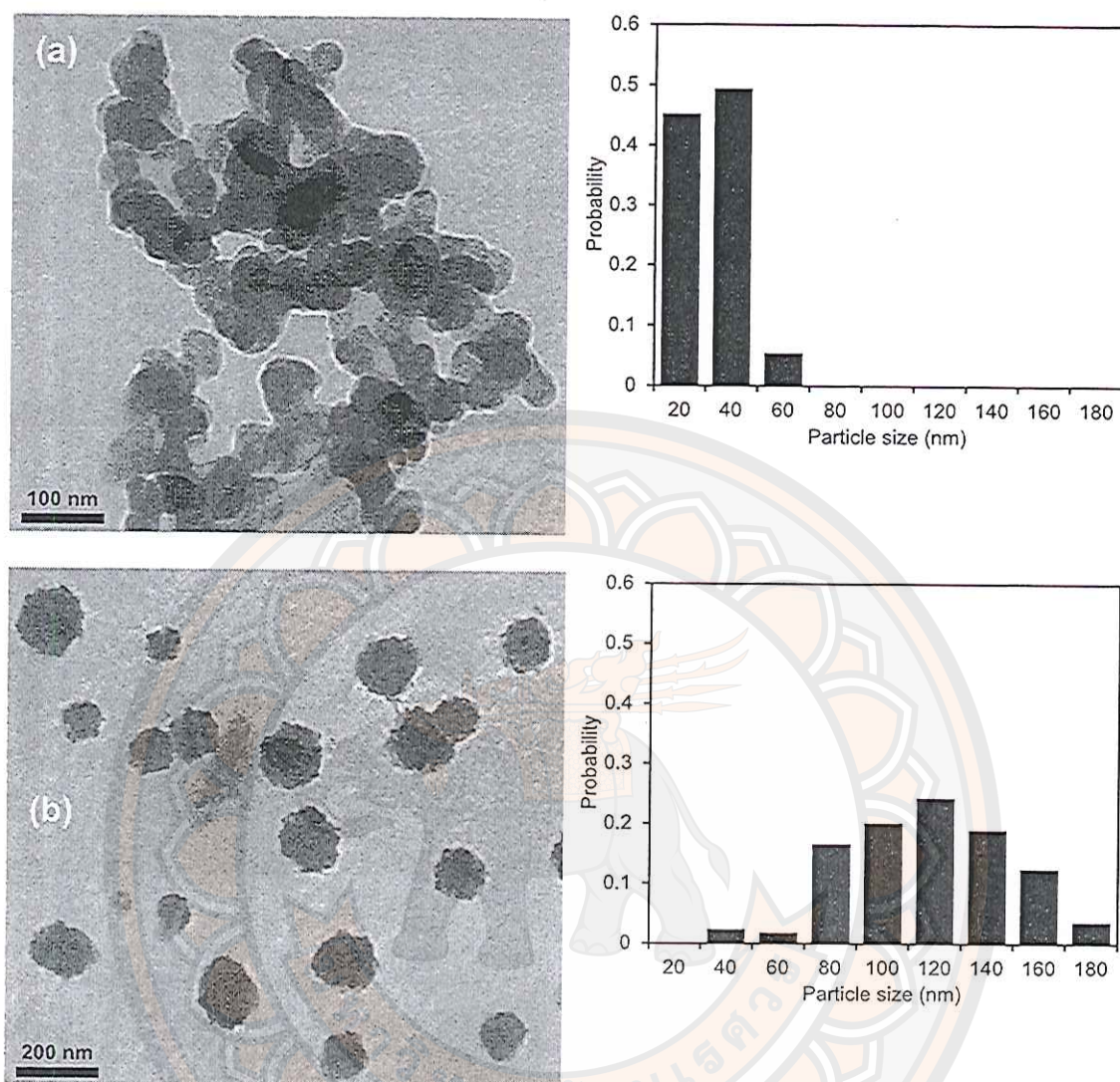
Figure 85 TEM images of MEH-PPV nanoparticle prepared from different solvents, (a) THF and (b) DCM. Their size distributions are presented at the right side.

Photophysical properties of the MEH-PPV nanoparticles vary significantly with type of the initial solvent. Figure 86 illustrates absorption and PL spectra of the MEH-PPV in different forms. The isolated chains in dilute THF solution exhibit a broad absorption spectrum with λ_{max} at about 504 nm. The broad pattern corresponds to electronic transition of various chromophores, possessing different conjugation lengths, within the conjugated chains. The photoemission process normally takes place via chromophores with the lowest HOMO–LUMO energy gap due to the high efficiency of energy transfer process [62, 63]. The PL spectrum showing a well-defined pattern with λ_{max} and vibronic shoulder at about 554 nm and 594 nm, respectively, reflects energy levels of the longest chromophore within the system. When the MEH-PPV chains are forced to densely pack into nanoparticles by injecting the solution into an excess amount of water, the absorption and PL patterns change drastically. The absorption spectrum of nanoparticles prepared from THF solution shifts to lower energy region where the λ_{max} is detected at 515 nm. New redshift peak is also observed at about 550 nm. The appearance of this redshift peak indicates the formation of inter- and/or intrachain aggregates where some conjugated segments or chromophores stack on top of each other. The appropriate overlapping of π-orbitals within the aggregates allows the formation of new electronic species with lower HOMO–LUMO energy gap. PL spectrum of the nanoparticles, reflecting electronic energy levels of the aggregates, exhibits λ_{max} and vibronic shoulder at about 594 nm and 640 nm, respectively. It is important to note that some conjugated segments do not form aggregates within the nanoparticles. The packing of these segments during the addition of water occurs in a random fashion, which does not allow the overlapping of π-orbitals. Absorption spectra of these segments remain unaltered. Therefore, fraction of the aggregates within the system is proportional to the ratio of absorbance at 550/500 nm. Detailed discussion of this topic is given in our previous reports [57, 61].

The MEH-PPV nanoparticles prepared by using DCM as an initial solvent exhibit quite different photophysical properties. Interestingly, the absorption spectrum shifts to higher energy region compared to that of the isolated chain. The absorbance at wavelength below 400 nm also rises significantly. Local λ_{max} is detected at about 420 nm. The significant blue shift of absorption spectrum indicates the collapse of MEH-PPV chains within the nanoparticles [14, 15, 56, 61]. The drastic shrinkage of

conjugated chains introduces kinks or physical defects within the backbone, which in turn limit local delocalization of π electrons. In other words, the conjugation length of chromophores in the collapsed chain is reduced. Our previous studies have shown that the location of absorption spectra depends on the extent of chain collapse [60]. The absorption spectrum of isolated MEH-PPV chain systematically shifts to high-energy region upon increasing the polarity of alcohol solvents (i.e., decreasing solvent quality). In methanol, the MEH-PPV exhibits λ_{max} at about 445 nm. In this study, λ_{max} of the nanoparticles in water is detected at about 420 nm. This indicates higher magnitude of the chain collapse, which is attributed to the higher polarity of water medium. However, we also detect a broad shoulder at wavelength above 550 nm, corresponding to the aggregation of some chromophores within the nanoparticles. The measurement of PL spectrum indicates the collapse of MEH-PPV chain as well. The PL spectrum shifts to high-energy region and exhibits a featureless pattern. The PL peak is detected at about 535 nm, while the vibronic shoulder is not observed. The absence of the vibronic shoulder suggests that the vibrational energy levels of this system are not well-defined. We also prepare the MEH-PPV nanoparticles by using polymer concentration at 1×10^{-2} mg/mL and 1×1^{-4} mg/mL. While quantity of the nanoparticles increases with concentration, their absorption and PL spectra are hardly affected. The size distribution also remains approximately the same. We believe that the filtration by using 0.45 μm pore size membrane allows only small-size nanoparticles to pass through.

It is important to note that the variation of CPN photophysical properties is not due to the difference of their size. It has been observed in other systems that an increase in CPN size causes a redshift of PL spectra [91, 99]. In our system, the CPN prepared from DCM exhibits much larger size compared to that of the THF system. Its PL spectrum, however, shifts to higher energy region. The conjugation length of chromophores within extended MEH-PPV backbone constitutes about 10–17 repeated units [149], which is shorter than the dimension of nanoparticles. The free volume required for segmental aggregation is also smaller. Therefore, the chain collapse and segmental aggregation causing the change of conjugation length can occur within the nanoparticles. In previous study where the size of MEH-PPV nanoparticles is about 5–10 nm, the aggregation is still detected [93].
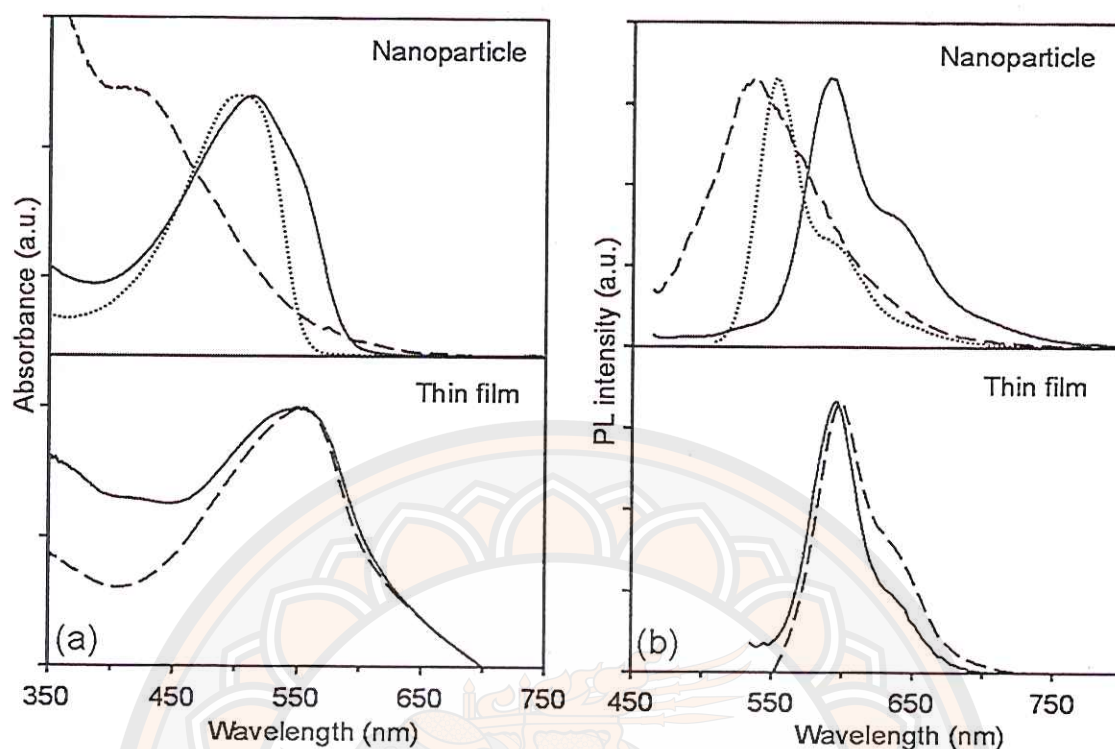
Figure 86 (a) Absorption and (b) PL spectra of MEH-PPV in different forms, (top) nanoparticles and (bottom) drop-cast films. The samples were prepared by using (solid lines) THF and (dashed lines) DCM as initial solvents. The spectra of MEH-PPV dilute solution in THF (dotted lines) are included for comparison.

Our results clearly show that the initial solvent plays a very important role on the formation and hence photophysical properties of the MEH-PPV nanoparticles. Table 9 summarizes the photophysical properties of MEH-PPV in different forms. The MEH-PPV nanoparticles prepared from DCM and THF exhibit green ($\lambda_{max} = 535$ nm) and red ($\lambda_{max} = 594$ nm) photoemission, respectively. To further explore the origin of our major finding, we prepare thin films of the conjugated polymer by drop-casting from 1 mg/mL THF and DCM solutions. This method allows self-assembling process of the conjugated polymer to take place without perturbing the individual chain conformation. The absorption patterns of resultant films are quite different from those of the nanoparticles. The change of solvents hardly affects their photophysical properties. The absorption spectra of both films exhibit λ_{max} at about 550 nm, accompanied with a broad low-energy tail extending above 600 nm. The significant

redshift of the whole spectra to 550 nm indicates the presence of high aggregate fraction within the thin films. The appearance of low-energy tail is attributed to electronic absorption of other types of aggregates with relatively low HOMU–LUMO energy gap [129]. It has been shown that aggregates can exist in different forms depending on the stacking configuration of chromophores [66, 136, 137]. The PL spectra of both films are also similar exhibiting λ_{max} at about 593 nm. The slight difference of their pattern is within error bar of the measurements. In our recent study where MEH-PPV chains in DCM and THF are forced to assemble into particles by addition of cyclohexane (nonsolvent), we observe different aggregation mechanisms [57]. At the very high fraction of cyclohexane, the use of DCM as initial solvent results in higher fraction of aggregates compared to that of the THF system. The tuning optical properties of ultrafine MEH-PPV fiber prepared by electro spinning method also show similar behavior [150, 151]. The preparation of the ultrafine MEH-PPV fiber provides the average diameters in the nanometer to submicrometer range. The measurement of photoluminescence properties of the electrospun fibers exhibit an emission maximum at about 578 nm and a shoulder at about 604 nm. The PL spectra of electrospun MEH-PPV fiber show the red-shift when compared to those of the corresponding solutions and the MEH-PPV nanoparticle in our study as well. The red-shift indicates the increase of longer conjugation length within MEH-PPV fiber. The researchers also report the color change of electrospun MEH-PPV fiber color by aging period after pyridinium formate addition and adjusting the pyridinium formate concentration. The emission colors of MEH-PPV fiber changes from orange to yellow and green.

Table 9 **Spectroscopic properties of conjugated polymers in different forms**

| Samples | Initial solvents | | | |
| | $\lambda_{max(abs)}$ of absorption spectra | | $\lambda_{max(abs)}$ of PL spectra | |
	THF	DCM	THF	DCM
MEH-PPV				
Solution	503	507	553 (585)	559 (600)
Nanoparticle	515 (550)	420	590 (630)	535[a]
Film	549	550	593 (632)	593 (631)
rr-P3OT				
Solution	448	450	566 (604)	572 (610)
Nanoparticle	512 (546, 593)	-	633 (686)	558[b]
Film	546 (610)	565 (615)	635 (663)	635 (662)

Note: The excitation wavelengths for PL measurements were [a]450 nm and [b]400 nm. Numbers in parentheses represent the location of shoulders in spectra.

An opposite result is obtained in this study where water is used as a poor solvent to drive the assembling of MEH-PPV chains into nanoparticles. Figure 87 compares the amount of aggregates in each system by plotting ratio of absorbance at 550/500 nm. The aggregate fractions in thin films prepared by using the two solvents are comparable. In nanoparticles, however, the use of THF as an initial solvent leads to much higher fraction of aggregates. The nanoparticles prepared from DCM also contain large fraction of collapsed coils. The discrepancies of segmental aggregation and chain conformation lead to drastic difference of their PL spectra. This fundamental knowledge can be utilized to control properties of the nanoparticles without changing the structure or composition of the constituent polymers. Our results clearly demonstrate that the nanoparticles with different sizes and properties can be fabricated by varying type of the initial solvent. We also note that the nanoparticles contain lesser amount of aggregates compared to the drop-cast films. This is attributed

to the confinement of polymer chains within a small volume that hinders the appropriate stacking of some chromophores. However, the intensity of low-energy peak (~630 nm) in PL spectra of the nanoparticle prepared from THF is higher than that of the thin film. Previous study shows that the photoemission of excimer contributes to the intensity of this peak [152]. Our observation suggests that the molecular packing within the nanoparticle favors the excimer formation.
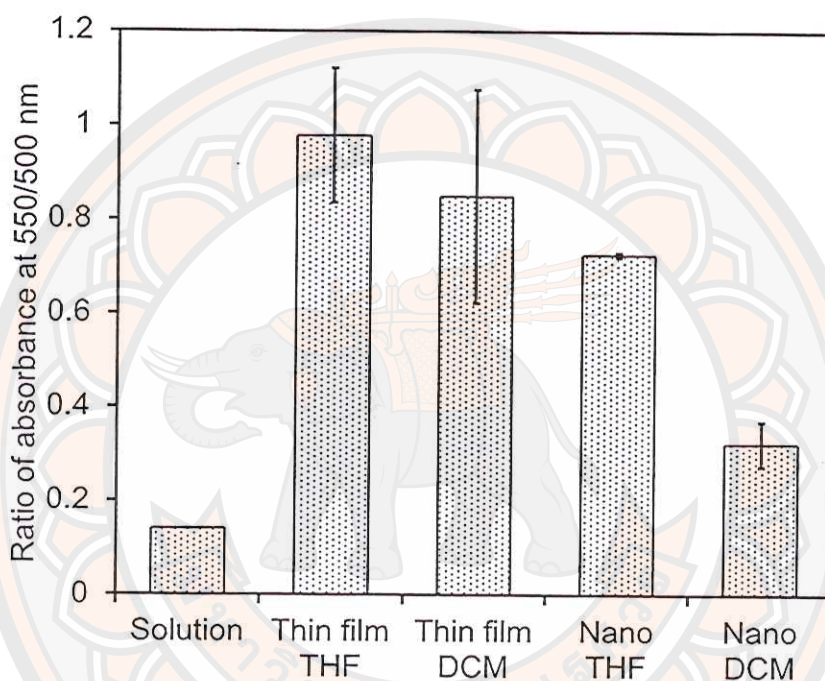
Figure 87 **Ratio of absorbance at 550/500 nm reflecting the aggregate fraction of MEH-PPV prepared in different forms**

Photophysical properties of the MEH-PPV nanoparticles are further explored by varying excitation wavelength as shown in Figure 88. The variation of excitation energy allows electronic transition of various chromophores with different conjugation lengths. However, the PL spectra of nanoparticles prepared by using THF as an initial solvent exhibit the same pattern (see Figure 88a). This result indicates that the photoemission process occurs via one type of chromophores. In this system, the fraction of aggregates, possessing the lowest HOMO–LUMO gap, is relatively high. The excited chromophores, therefore, can effectively transfer energy to aggregated sites before the photoemission process takes place. The PL pattern only reflects

electronic energy levels of aggregates. The measurements of photoluminescence excitation (PLE) spectra at different emission wavelengths provide consistent results. The PLE pattern is similar to the absorption spectrum and independent of the detecting emission wavelength as shown in Figure 88b. This behavior is similar to systems of thin films where aggregate fraction is also quite high. The result is quite different in the system of nanoparticles prepared by using DCM as an initial solvent. Figure 88c shows that the PL spectra systematically shift to low-energy region upon increasing excitation wavelength. Since the nanoparticles constitute collapsed chains and contain less amount of aggregates, the energy transfer process is less efficient compared to the system of THF. Therefore, this system allows photoemission of different chromophores upon varying the excitation energy. This observation is consistent with our previous studies where the multiple photoemissions are detected in the system of collapsed coils [60, 61]. The measurement of PLE spectrum by fixing emission wavelength at 500 nm detects the absorption at high-energy region with λ_{max} at about 395 nm (see Figure 88d). This corresponds to the excitation of relatively short chromophores within the system. When the detecting emission wavelength is increased to 590 nm, the excitation band at about 435 nm grows significantly.
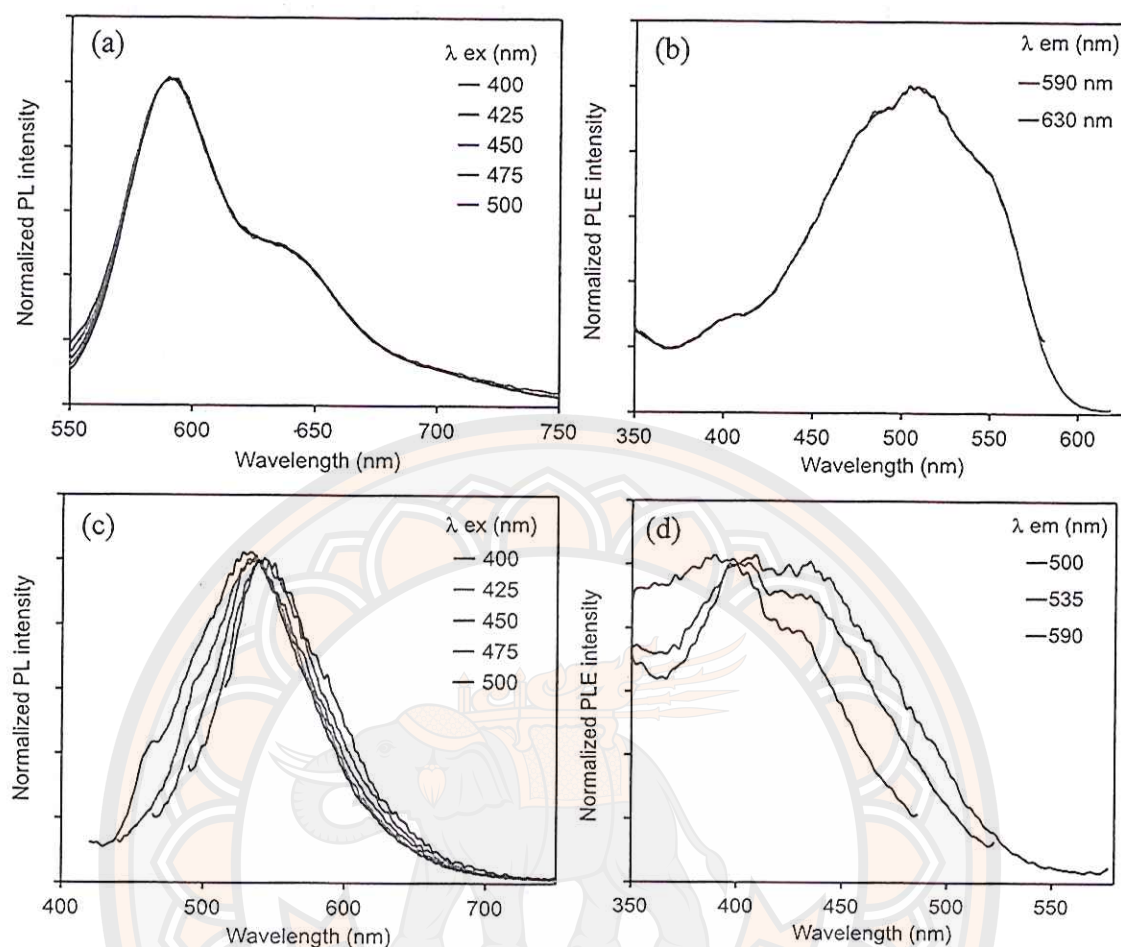
Figure 88 PL spectra (left) and PLE spectra (right) of MEH-PPV nanoparticles measured at different excitation wavelengths (Ex λ) and emission wavelengths (Em λ), respectively. The nanoparticles were prepared from (a,b) THF and (c,d) DCM initial solvents.

From the aforementioned results, we propose mechanism for the formation of MEH-PPV nanoparticles in Figure 89. Recent study by Cossiello, et al. [153] estimates solubility parameter (δ) of MEH-PPV and their components (δ_d (dispersion), δ_p (polar) and δ_h (hydrogen bonding)) as $\delta = 18.7$ $J^{1/2}$ $cm^{-3/2}$, $\delta_d = 18.0$ $J^{1/2}$ $cm^{-3/2}$, $\delta_p = 4.0$ $J^{1/2}$ $cm^{-3/2}$, and $\delta_h = 3.0$ $J^{1/2}$ $cm^{-3/2}$. They also observe that dispersion interaction between MEH-PPV and solvent is a major factor dictating the chain conformation and its photophysical properties. The absorption and PL spectra of MEH-PPV systematically blue shifts upon decreasing δ_d value of solvents, which corresponds to the decrease in conjugation length. Solubility parameters of solvents used in this study

are listed in Table 10 [36]. The δ_d value of DCM, 18.2 $J^{1/2}$ $cm^{-3/2}$, is very close to that of MEH-PPV, providing strong dispersion interaction. Therefore, the chain adopts extended conformation in this solvent. The dispersion interaction between MEH-PPV and THF (δ_d = 16.8 $J^{1/2}$ $cm^{-3/2}$) is weaker forcing the chain shrinkage, which leads to the decrease in conjugation length. Table 9 shows that λ_{max} of the absorption and PL spectra of MEHPPV in THF solvent are shorter than that of the DCM system.

When the polymer solutions in DCM or THF are injected into water medium, the interactions between the solvents play a crucial role on the formation of nanoparticles. Water is a nonsolvent for MEH-PPV. It has relatively high δ value (47.8 $J^{1/2}$ $cm^{-3/2}$). The THF is miscible with water, while the aqueous solubility of DCM is limited at 17.6 g/L. In the preparation process of nanoparticle, the initial droplets of THF or DCM solutions are disintegrated by continuous ultrasonication. Since the THF has favorable interactions with water, the solution is spontaneously broken into small droplets with narrow size distribution. The DCM, on the other hand, has weaker interactions with water, which in turn resist the breaking process. Therefore, the resultant DCM droplets exhibit larger size compared to that of the THF system. This hypothesis is supported by the size of obtained nanoparticles. The use of DCM as an initial solvent provides the nanoparticles with much larger size as shown in Table 8. This result is similar to the system of polymer blend where the size of polymer droplet increases with decreasing polymer–polymer interactions [154].

The mixing of THF with water is also relatively fast, which in turn drives the assembling of MEH-PPV molecules into nanoparticles with minimal change of individual chain conformation. The stacking of some conjugated segments occurs within the nanoparticles as indicated by the appearance of redshift peak in absorption spectrum (see Figure 86). The mixing of DCM with water probably takes place in a slower fashion, allowing the collapse of individual chains. When the mixing process is complete, the collapsed chains assemble into nanoparticles to minimize interaction with water medium. Since the collapsed chains constitute many kinks or physical defects, it is more difficult to form aggregates. Therefore, the photophysical properties of collapsed chains are dominant in this type of nanoparticles. The packing of collapsed chains may be responsible for the rough surface of nanoparticles as revealed by TEM in Figure 85b. It is worthwhile to point out that the aggregation of MEH-PPV

chains in DCM is very high when nonsolvent, cyclohexane, is added [35]. In this system, the high miscibility of DCM and cyclohexane does not allow the collapse of MEH-PPV prior to the assembling process.
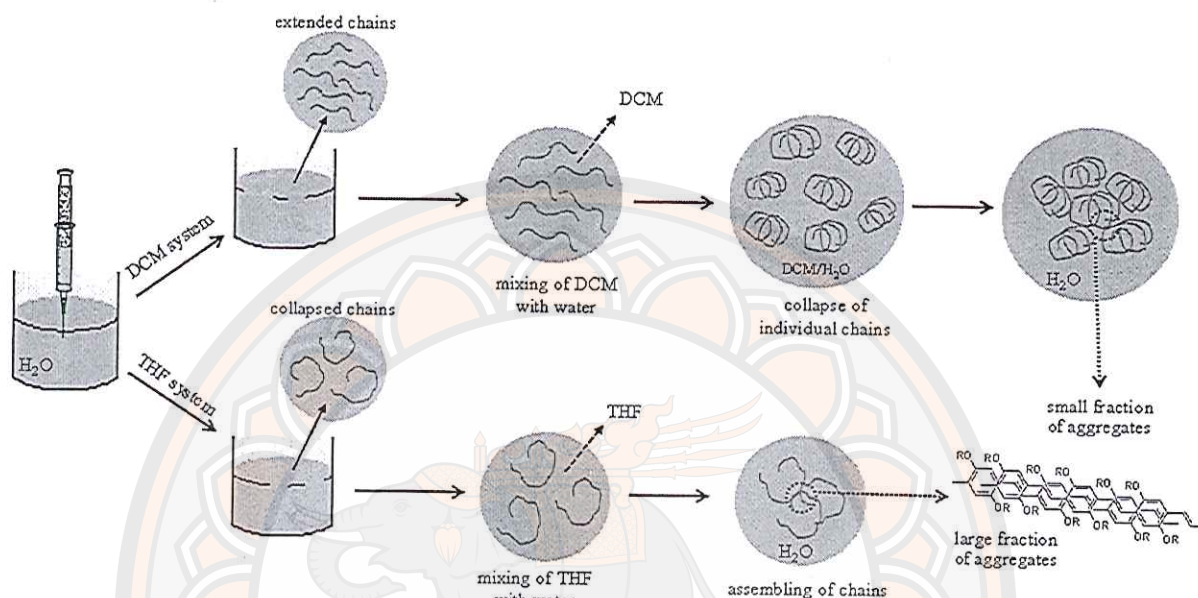
Figure 89 Proposed mechanisms for the formation of MEH-PPV nanoparticles prepared by using (top) DCM and (bottom) THF as initial solvents.

Table 10 Solubility parameter of solvents and conjugated polymers and their components [39, 66, 83, 136]

Sample	δ (J$^{1/2}$ cm$^{-3/2}$)	δ_d (J$^{1/2}$ cm$^{-3/2}$)	δ_p (J$^{1/2}$ cm$^{-3/2}$)	δ_h (J$^{1/2}$ cm$^{-3/2}$)
DCM	20.3	18.2	6.3	6.1
THF	19.4	16.8	5.7	8.0
Water	47.8	15.5	16.0	42.3
MEH-PPV	18.7	18.0	4.0	3.0
rr-P3OT	18.2	-	-	-

Nanoparticles of rr-P3OT

In this section, we further investigate the role of initial solvent on the formation of nanoparticles by using rr-P3OT. Our result from solvent-nonsolvent titration shows that the solubility of rr-P3OT in THF is higher compared to that of the DCM system. This result conforms to the solubility parameter (δ) of rr-P3OT and solvents. The solubility of polymer in solvent is promoted when the difference between their δ values is small [36, 39, 83]. The δ values of rr-P3OT, THF, and DCM are 18.2 $J^{1/2}$ $cm^{-3/2}$ [39], 19.4 $J^{1/2}$ $cm^{-3/2}$ and 20.3 $J^{1/2}$ $cm^{-3/2}$, respectively. Therefore, the THF is a better solvent for rr-P3OT, which is opposite to the MEH-PPV system. This discrepancy probably arises from the presence of S atoms in rr-P3OT backbone, which affects local interactions with the solvents. This result also indicates that the dispersion interaction between rr-P3OT and solvent is not a major factor that controls the solubility and conformation of rr-P3OT. We expect that rr-P3OT has very different solubility parameter components compared to those of the MEH-PPV. However, we still observe similar results. Figure 90 shows SEM and TEM images of rr-P3OT nanoparticles. The use of THF as an initial solvent provides spherical nanoparticles with average size of about 50 nm, which is comparable to that of the MEH-PPV nanoparticles (see Table 8). When the DCM is used, the average size increases significantly. This result supports our hypothesis that the size of nanoparticles is mainly dictated by the water solubility of initial solvent. However, the internal morphology of rr-P3OT nanoparticles is hardly affected. The high resolution TEM images show that the nanoparticles prepared from both solvents exhibit homogenous internal density and smooth surface.
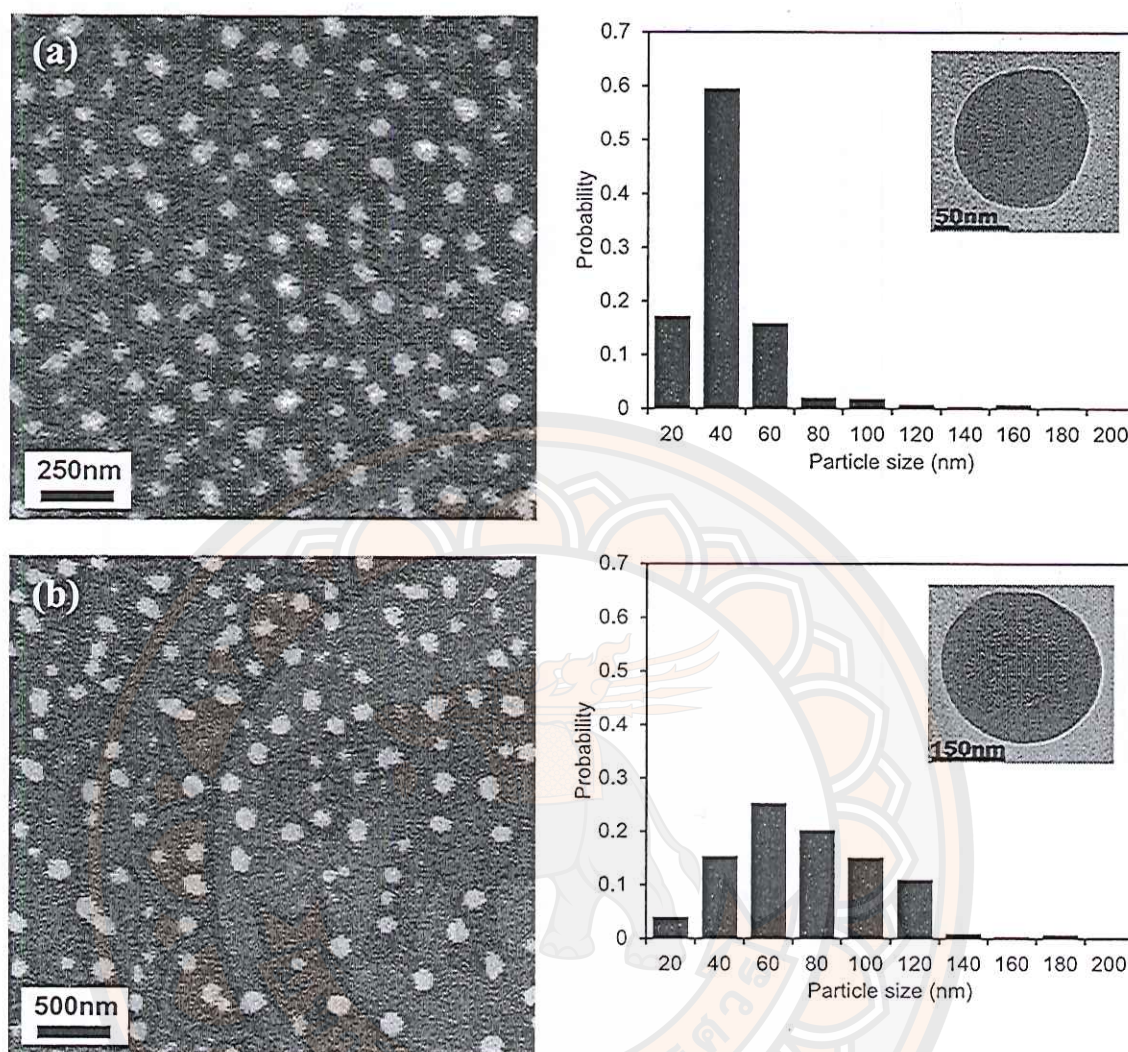
Figure 90 SEM images of *rr*-P3OT prepared from different initial solvents, (a) THF and (b) DCM. Their size distributions are presented in the right side. TEM images of these nanoparticles are shown in the insets.

The photophysical properties of *rr*-P3OT in different forms are shown in Figure 91. The isolated chain in THF solution exhibits a broad absorption pattern with λ_{max} at about 450 nm. Similar to MEH-PPV system, the PL spectrum constitutes peak and vibronic shoulder at 572 nm and 615 nm, respectively, reflecting electronic energy levels of the longest chromophore within the conjugated backbone [155].When the *rr*-P3OT forms nanoparticles by using THF as an initial solvent, the absorption spectrum drastically shifts to low-energy region. Three distinct redshift peaks are clearly observed at about 515 nm, 550 nm, and 605 nm. Previous studies have shown that the appearance of these peaks corresponds to the formation of aggregates within the nanoparticles [74, 88, 101]. These aggregates emit light at much lower energy region compared to the isolated chain. Their PL spectrum exhibits a well-defined pattern with λ_{max} and vibronic shoulder at about 638 nm and 695 nm, respectively.

In the system of DCM, absorption spectrum of the *rr*-P3OT nanoparticles still shifts to low-energy region. The three redshift peaks, however, are obscured. A rise of absorbance at high-energy region is also observed. These results indicate that the molecular packing and individual chain conformation of *rr*-P3OT within the nanoparticles are different from the THF system. Figure 92 compares the aggregate fraction in each system by plotting the ratio of absorbance at 550/440 nm. It is clear that the nanoparticles prepared from DCM solution contain lesser amount of aggregates. The measurement of PL spectrum provides a supportive result. PL spectrum of the nanoparticles shifts to relatively high-energy region, which is similar to the MEH-PPV system. It exhibits featureless pattern with λ_{max} at about 565 nm. The blue shift of PL spectrum indicates the collapse of conjugated chains within the nanoparticles [100]. Although relatively high amount of aggregates exists in this system, their PL peak at 638 nm is not observed. The photoemission of collapsed chains is still dominant. We suggest that the aggregate formed in the DCM system is a non-emissive species. We also note that the blue shift of PL spectrum of *rr*-P3OT is smaller than that of the MEH-PPV. This is attributed to the difference in chain rigidity of the two polymers.
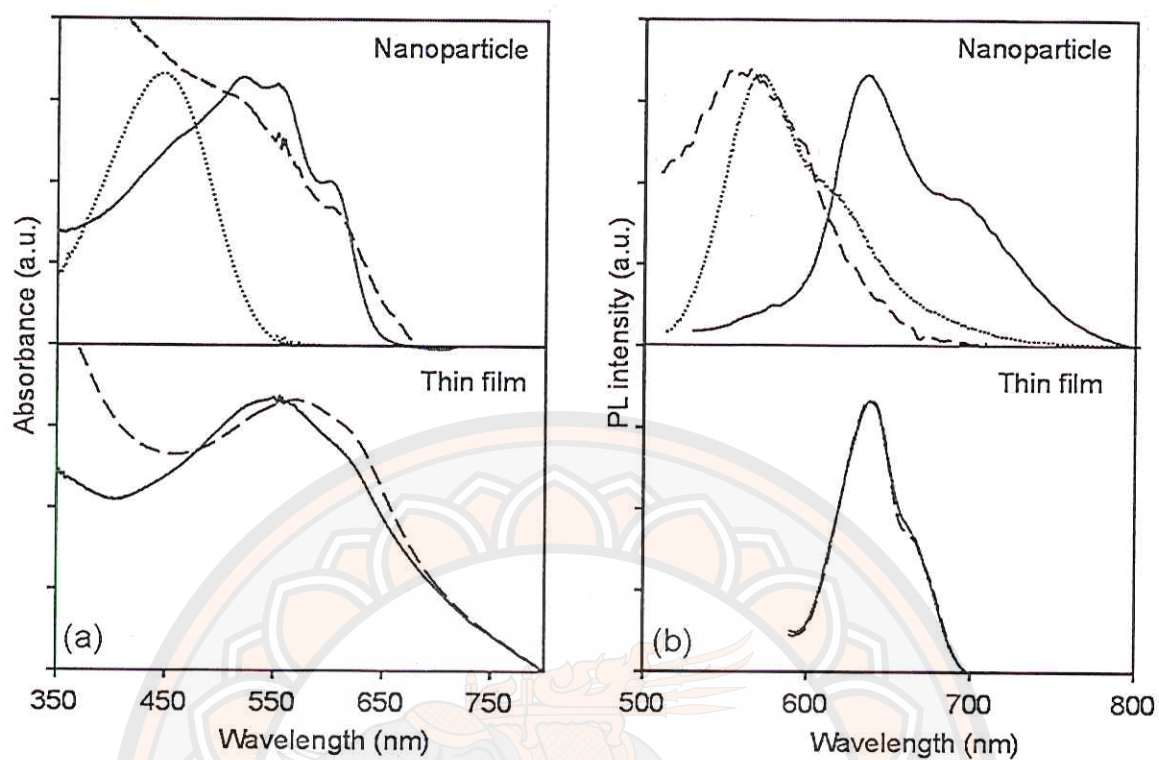
Figure 91 (a) Absorption and (b) PL spectra of *rr*-P3OT in different forms, (top)
nanoparticles and (bottom) thin films. The samples were prepared by
using (solid lines) THF and (dashed lines) DCM as initial solvents. The
spectra of *rr*-P3OT dilute solution in THF (dotted lines) are included
for comparison.
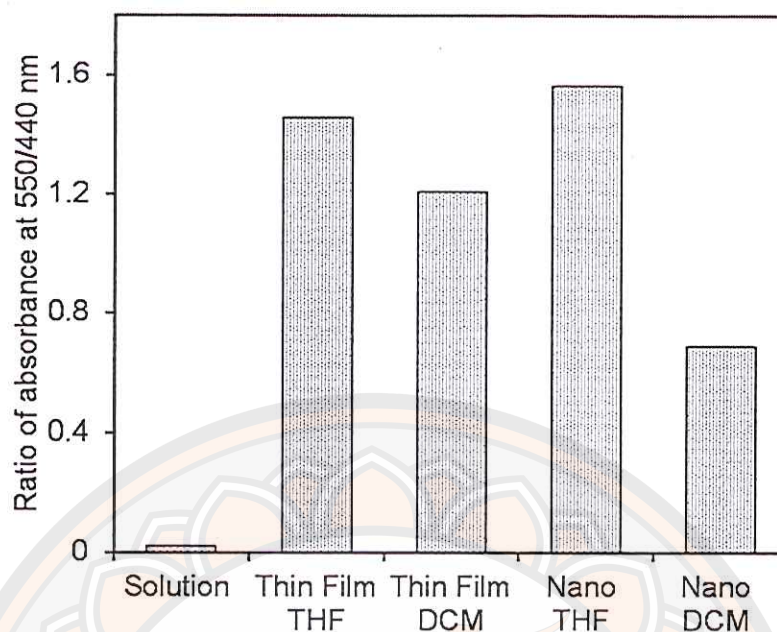
Figure 92 **Ratio of absorbance at 550/440 nm reflecting the aggregate fraction of**
_rr_-P3OT prepared in different forms

The absorption and PL spectra of drop-cast films prepared from THF and
DCM solutions exhibit similar pattern. The spectra significantly shift to lower energy
region compared to those of the isolated chain indicating the presence of high
aggregate fraction. Unlike the system of nanoparticles prepared from THF, we do not
detect the three distinct redshift peaks in the absorption spectra. This observation
suggests that local structures of aggregates formed in the nanoparticles and thin films
are different. The measurements of PL spectra also detect the discrepancy in pattern.
The λ_{max} values of PL spectra measured from the nanoparticles, and thin films are
comparable. Interestingly, the vibronic shoulder is detected at different wavelengths,
about 695 nm and 665 nm for the nanoparticles and thin films, respectively. This
indicates the variation of vibrational energy levels of aggregates in the two systems.
The separation between peak and vibronic shoulder, corresponding to vibrational
energy gap of the aggregates in ground state, increases from about 25 nm in thin films
to about 55 nm in the nanoparticles. The increase in vibrational energy gap is
attributed to the increase in confinement within the nanoparticles which may resist the

vibration of polymer segments. We note that the change of vibrational energy levels is also observed but less pronounced in the MEH-PPV system.

Conclusion

Our results in this study demonstrate that the mechanism of CPN formation in water is strongly influenced by properties of the initial solvents. We show that the solubility of initial solvent in water is a major factor dictating the conformational change and segmental aggregation of conjugated polymers within the CPNs. When the water solubility of initial solvent is relatively low, the collapse of conjugated chains occurs prior to the assembling process. The resultant CPNs contain large fraction of collapsed coils. Therefore, the photophysical properties of collapsed coils, which absorb and emit light at high-energy region, are dominant in this type of CPNs. When the initial solvent is miscible with water, the mixing process is relatively fast. The conjugated polymers are driven to assemble into CPNs with minimal change of individual chain conformation. This type of CPNs contains large fraction of aggregates and exhibits smaller size. Their absorption and PL spectra occur at low-energy region. The CPNs of MEH-PPV and rr-P3OT prepared in this study by using DCM and THF as initial solvents exhibit rather different photophysical properties. The difference in λ_{max} position of PL spectra is more than 50 nm. Our study shows that a careful choice of the solvent can be used to produce the CPNs with desired chain arrangement and photophysical properties, suitable for particular device application.

CHAPTER IX

CONCLUSIONS

This work mainly focuses on the solvent effects on the controlling over the aggregation behavior of conjugated polymers and their photophysical. The results can be summarized as follow.

Conformational change, intrachain aggregation and photophysical properties of *rr*-P3OT

In this study, the selective segmental solubility of *rr*-P3OT solution is major factor to induce the conformational change of *rr*-P3OT chain. In this system, the poor solvents, cyclohexane and hexane are good solvent for octyl side chain but poor solvent for thiophene backbone, the poor solvent for this system. Addition of cyclohexane into polymer solutions causes the polymer chain change into the coiled chain conformation which is indicated by the blue-shift in absorption and PL spectra. The fluorescence quantum yield decreases when the *rr*-P3OT chain transforms into coiled conformation upon increasing cyclohexane ratio. The conformation change of *rr*-P3OT is further induced by addition of hexane into the cyclohexane solution. The addition of hexane causes the reduction of *rr*-P3OT solubility. Therefore, the polymer chains trend to induce to dense packing which allow the formation of intrachain aggregation. The absorption spectra show the appearance of three redshift peaks. However, the fluorescence quanta yield drastic decreases. Therefore, the intrachain aggregates in this system are the non-emissive species.

Formation of non-emissive and emissive aggregates of *rr*-P3OT

The *rr*-P3OT chains are force into the aggregates by adding poor solvent ethanol. In this study, ethanol is poor solvent for both thiophene unit and octyl side chain. Addition of ethanol causes the growth of three redshift peaks in absorption spectra. However, the measurements of PL spectra have shown that ethanol can induces the formation of non-emissive aggregates in early state. This is due to the weakly packing. When the ethanol ratio is further increased to over 60% v/v, the aggregate segments can emit the light. The emissive aggregates show the red-shift of PL spectra at λ_{max} about 650 nm and shoulder about 720 nm. The non-emissive and emissive aggregates exhibit slightly different absorption bands. In addition, we have found that the use of different initial solvents, pyridine and chlorobenzene, provides aggregates with rather different absorption patterns.

Control over the photophysical properties of nano-size aggregates of *rr*-P3OT

In this part, *rr*-P3OT aggregates are controlled by varying types of poor solvents. The aggregates and their photophysical properties are sensitive to the solubility parameter of the solvents. The used of poor solvent, hexane, which is good solvent for octyl side chain, lead to the formation non-emissive aggregate. The use of series of alcohols as poor solvents leads to the formation of emissive aggregate due to the dense packing of polymer chains. The long alkyl chain alcohol which increases the solubility of polymer exhibits the formation of non-emissive and emissive aggregates.

Study of conjugated polymer nanoparticles

The conjugated polymer nanoparticles (CPNs) were prepared by using different initial polymer solutions. The types of initial solvents affect polymer chain packing within the nanoparticles and theirs photophysical properties. The solubility of initial solvent in water plays the important on the chain packing within the nanoparticle. The use of dichloromethane, which is low solubility in water, as initial solvent provide the collapse of conjugated chains in early state of the assembling process. The CPNs contain large fraction of collapsed coils. The photophysical properties of collapsed coils within CPNs absorb and emit light at high-energy region. When the initial solvent is tetrahydrofuran, which is miscible with water, the mixing

process is relatively fast. The conjugated polymer chains are driven to assemble into CPNs with minimal change of individual chain conformation. The CPNs in this system contains large fraction of aggregates and exhibits smaller size. Their absorption and PL spectra occur at low-energy region. Therefore, in this study, we can tune the photophysical properties of CPNs by choosing a careful choice of the solvents.

REFFERENCES

REFERENCES

[1] Spanggaard, H. and Krebs, F. C. (2004). A brief history of the development of organic and polymeric photovoltaics. **Solar Energy Materials & Solar Cells**, 83(2-3), 125-146.

[2] Brabec, C.J., Sariciftci, S.N. and Hummelen, J.C. (2001). Plastic solar cells. **Advanced Functional Materials**, 11(1), 15-26.

[3] Günes, S., Neugebauer, H. and Sariciftci, N.S. (2007). Conjugated polymer-based organic solar cells. **Chemical Reviews**, 107(4), 1324-1338.

[4] Cai, W., Gong, X. and Cao, Y. (2010). Polymer solar cells: Recent development and possible routes for improvement in the performance. **Solar Energy Materials & Solar Cells**, 94(2), 114-127.

[5] Facchetti, A. (2011). π-conjugated polymers for organic electronics and photovoltaic cell applications. **Chemistry of Materials**, 23(3), 733-758.

[6] Grimsdale, A.C., Chan, K.L., Martin, R.E., Jokisz, P.G. and Holmes, A.B. (2009). Synthesis of light-emitting conjugated polymers for applications in electroluminescent devices. **Chemical Reviews**, 109(3), 897-1091.

[7] Chen, Y. and Ma, D. (2012). Organic semiconductor heterojunctions as charge generation layers and their application in tandem organic light-emitting diodes for high power efficiency. **Journal of Materials Chemistry**, 22(36),18718–18734.

[8] Dini, D. (2005). Electrochemiluminescence from organic emitters. **Chemistry of materials**, 17(8), 1933-1945.

[9] Amelung, J. (April 21, 2008). Large-area organic light-emitting diode technology. **SPIE Newsroom**. Retrieved June 18, 2014, from http://spie.org/x23960.xml?highlight=x2408&ArticleID=x23960

[10] Horowitz, G. (1998). Organic field-effect transistors. **Advanced Materials**, 10(5), 365-377.

[11] Wang, C., Dong, H., Hu, W., Liu, Y. and Zhu, D. (2012). Semiconducting π-conjugated systems in field-effect transistors: A material odyssey of organic electronics. **Chemical Reviews**, 112(4), 2208–2267.

[12] Kola, S., Sinha, J. and Katz, H.E. (2012). Organic transistors in the new decade: toward n-channel, printed, and stabilized devices. **Journal of Polymer Science Part B: Polymer Physics**, 50(15), 1090-1120.

[13] Chochos, C. L. and Choulis, S. A. (2011). How the structural deviations on the backbone of conjugated polymers influence their optoelectronic properties and photovoltaic performance. **Progress in Polymer Science**, 36(10), 1326-1414.

[14] Sumpter, B. G., Kumar, P., Mehta, A., Barnes, M. D., Shelton, W. A. and Harrison, R. J. (2005). Computational study of the structure, dynamics, and photophysical properties of conjugated polymers and oligomers under nanoscale confinement. **The Journal of Physical Chemistry B**, 109(16), 7671-7685.

[15] Kumar, P., Mehta, A., Mahurin, S. M., Dai, S., Dadmun, M. D., Sumpter, B. G., et al. (2004). Formation of oriented nanostructures from single molecules of conjugated polymers in microdroplets of solution: The role of solvent. **Macromolecules**, 37(16), 6132-6140.

[16] Lei, T., Wang, J.-Y. and Pei, J. (2013). Roles of flexible chains in organic semiconducting materials. **Chemistry of Materials**, 26(1), 594-603.

[17] Mei, J. and Bao, Z. (2013). Side chain engineering in solution-processable conjugated polymers. **Chemistry of Materials**, 26(1), 604-615.

[18] Kerdcharoen, T. (2008). **Conductive plastics**. Retrieved June 18, 2014, from http://nanotech.sc.mahidol.ac.th/pe-thailand/condplastic.html

[19] Wu, C., Bull, B., Szymanski, C., Christensen, K. and McNeill, J. (2008). Multicolor conjugated polymer dots for biological fluorescence imaging. **ACS Nano**, 2(11), 2415-2423.

[20] Fernando, L.P., Kandel, P.K., Yu, J., McNeill, J., Ackroyd, P.C. and Christensen, K.A. (2010). Mechanism of cellular uptake of highly fluorescent conjugated polymer nanoparticles. **Biomacromolecules**, 11(10), 2675-2682.

[21] Li, K., Ding, D., Huo, D., Pu, K.-Y., Thao, N. N. P., Hu, Y., et al. (2012). Conjugated polymer based nanoparticles as dual-modal probes for targeted in vivo fluorescence and magnetic resonance imaging. **Advanced Functional Materials**, 22(15), 3107-3115.

[22] Pecher, J., Huber, J., Winterhalder, M., Zumbusch, A. and Mecking, S. (2010). Tailor-made conjugated polymer nanoparticles for multicolor and multiphoton cell imaging. **Biomacromolecules**, 11(10), 2776-2780.

[23] Bruchez, M., Moronne, M., Gin, P., Weiss, S. and Alivisatos, A.P. (1998). Semiconductor nanocrystals as fluorescent biological labels, **Science**, 281(5385), 2013-2016.

[24] Green, M., Howes, P., Berry, C., Argyros, O. and Thanou, M. (2009). Simple conjugated polymer nanoparticles as biological labels. **Proceedings of the Royal Society A: Mathematical, Physical and Engineering Science**, 465(2109), 2751-2759.

[25] Wu, C., Bull, B., Christensen, K. and McNeill, J. (2009). Ratiometric single-nanoparticle oxygen sensors for biological imaging. **Angewandte Chemie International Edition**, 48(15), 2741-2745.

[26] Moon, J.H., MacLean, P., McDaniel, W. and Hancock, L.F. (2007). Conjugated polymer nanoparticles for biochemical protein kinase assay. **Chemical Communications**, (46), 4910-4912.

[27] Landfester, K., Musyanovych, A. and Mailänder, V. (2010). From polymeric particles to multifunctional nanocapsules for biomedical applications using the miniemulsion process. **Journal of Polymer Science Part A: Polymer Chemistry**, 48(3), 493-515.

[28] Tuncel, D. and Demir, H.V. (2010). Conjugated polymer nanoparticles. **Nanoscale**, 2(4), 484-494.

[29] Varghese, S. and Das, S. (2011). Role of molecular packing in determining solid-state optical properties of π-conjugated materials. **The Journal of Physical Chemistry Letters**, 2(8), 863-873.

[30] Salleo, A., Kline, R. J., DeLongchamp, D. M. and Chabinyc, M. L. (2010). Microstructural characterization and charge transport in thin films of conjugated polymers. **Advanced Materials**, 22(34), 3812-3838.

[31] Wang, H., Xu, Y., Yu, X., Xing, R., Liu, J. and Han, Y. (2013). Structure and morphology control in thin films of conjugated polymers for an improved charge transport. **Polymers**, 5(4), 1272-1324.

[32] Rivnay, J., Mannsfeld, S. C. B., Miller, C. E., Salleo, A. and Toney, M. F. (2012). Quantitative determination of organic semiconductor microstructure from the molecular to device scale. **Chemical Reviews**, 112(10), 5488-5519.

[33] Schwartz, B.J. (2003). Conjugated polymers as molecular materials: How chain conformation and film morphology influence energy transfer and interchain interactions. **Annual Review of Physical Chemistry**, 54(1), 141-172.

[34] Gedde, U. W. (1995) **Polymer Physics**. London, England: Chapman & Hall.

[35] Hu, D., Yu, J., Wong, K., Bagchi, B., Rossky, P. J. and Barbara, P. F. (2000). Collapse of stiff conjugated polymers with chemical defects into ordered, cylindrical conformations. **Nature**, 405(6790), 1030-1033.

[36] Barton, A. F. M. (1975). Solubility parameters. **Chemical Reviews**, 75(6), 731-753.

[37] Burke, J. (1984). **Solubility parameters: theory and application**. Retrieved June 18, 2014, from http://cool.conservation-us.org/coolaic/sg/bpg/annual/v03/bp03-04.html

[38] Hansen, C. M. (1969). The universality of the solubility parameter. **Product R&D**, 8(1), 2-11.

[39] Zen, A., Saphiannikova, M., Neher, D., Asawapirom, U. and Scherf, U. (2005). Comparative study of the field-effect mobility of a copolymer and a binary blend based on poly(3-alkylthiophene)s. **Chemistry of Materials**, 17(4), 781-786.

[40] McCullough, R. D. (1998). The chemistry of conducting polythiophenes. **Advanced Materials**, 10(2), 93-116.

[41] Osaka, I. and McCullough, R. D. (2008). Advances in molecular design and synthesis of regioregular polythiophenes. **Accounts of Chemical Research**, 41(9), 1202-1214.

[42] Lim, J. A., Liu, F., Ferdous, S., Muthukumar, M. and Briseno, A. L. (2010). Polymer semiconductor crystals. **Materials Today**, 13(5), 14-24.

[43] Hoeben, F.J.M., Jonkheijm, P., Meijer, E.W. and Schenning, A.P.H.J. (2005). About supramolecular assemblies of π-conjugated systems. **Chemical Reviews**, 105(4), 1491-1546.

[44] Chen, J.-T. and Hsu, C.-S. (2011). Conjugated polymer nanostructures for organic solar cell applications. **Polymer Chemistry**, 2(12), 2707-2722.

[45] Xu, B. and Holdcroft, S. (1993). Molecular control of luminescence from poly(3-hexylthiophenes). **Macromolecules**, 26(17), 4457-4460.

[46] Adachi, T., Brazard, J., Ono, R.J., Hanson, B., Traub, M.C., Wu, Z.-Q., et al. (2011). Regioregularity and single polythiophene chain conformation. **The Journal of Physical Chemistry Letters**, 2(12), 1400-1404.

[47] Adachi, T., Lakhwani, G., Traub, M.C., Ono, R.J., Bielawski, C.W., Barbara, P.F., et al. (2012). Conformational effect on energy transfer in single polythiophene chains. **The Journal of Physical Chemistry B**, 116(32), 9866-9872.

[48] Chen, P.-Y., Rassamesard, A., Chen, H.-L. and Chen, S.-A. (2013). Conformation and fluorescence property of poly(3-hexylthiophene) isolated chains studied by single molecule spectroscopy: effects of solvent quality and regioregularity. **Macromolecules**, 46(14), 5657-5663.

[49] Kline, R.J., McGehee, M.D., Kadnikova, E.N., Liu,J., Fréchet, J.M.J. and Toney, M.F. (2005). Dependence of regioregular poly(3-hexylthiophene) film morphology and field-effect mobility on molecular weight. **Macromolecules**, 38(8), 3312-3319.

[50] Zen, A., Saphiannikova, M., Neher, D., Grenzer, J., Grigorian, S., Pietsch, U., et al. (2006). Effect of molecular weight on the structure and crystallinity of poly(3-hexylthiophene). **Macromolecules**, 39(6), 2162-2171.

[51] Brinkmann, M. and Rannou, P. (2009). Molecular weight dependence of chain packing and semicrystalline structure in oriented films of regioregular Poly(3-hexylthiophene) revealed by high-resolution transmission electron microscopy. **Macromolecules**, 42(4), 1125-1130.

[52] Chen, S.-A. and Lee, S.-J. (1995) Application of molecular dynamics in determination of conformation change with temperature of poly(3-dodecylthiophene) in crystalline cell. **Synthetic Metals**, 72(3), 253-260.

[53] Shibaev, P.V., Schaumburg, K., Bjornholm, T. and Norgaard, K. (1998). Conformation of polythiophene derivatives in solution. **Synthetic Metals**, 97(2), 97-104.

[54] Vukmirović, N. and Wang, L.-W. (2009). Electronic structure of disordered conjugated polymers: Polythiophenes. **The Journal of Physical Chemistry B**, 113(2), 409-415.

[55] Theander, M., Inganäs, O., Mammo, W., Olinga, T., Svensson, M. and Andersson, M. R. (1999). Photophysics of substituted polythiophenes. **The Journal of Physical Chemistry B**, 103(37), 7771-7780.

[56] Nguyen, T.-Q., Doan, V. and Schwartza, B. J. (1999). Conjugated polymer aggregates in solution: control of interchain interactions. **Journal of Chemical Physics**, 110, 4068-4078.

[57] Traiphol, R., Potai, R., Charoenthai, N., Srikhirin, T., Kerdcharoen, T. and Osotchan, T. (2010). Effects of chain conformation and chain length on degree of aggregation in assembled particles of conjugated polymer in solvents–nonsolvent: A spectroscopic study. **Journal of Polymer Science Part B: Polymer Physics**, 48(8), 894-904.

[58] Aimé, J. P., Bargain, F., Schott, M., Eckhardt, H., Miller, G.G. and Elsenbaumer, R.L. (1989). Structural study of doped and undoped polythiophene in solution by small-angle neutron scattering. **Physical Review Letters**, 62(1), 55-58.

[59] McCulloch, B., Ho, V., Hoarfrost, M., Stanley, C., Do, C., Heller, W.T., et al. (2013). Polymer chain shape of poly(3-alkylthiophenes) in solution using small-angle neutron scattering. **Macromolecules**, 46(5), 1899-1907.

[60] Traiphol, R., Sanguansat, P., Srikhirin, T., Kerdcharoen, T. and Osotchan, T. (2006). Spectroscopic study of photophysical change in collapsed coils of conjugated colymers: Effects of solvent and temperature. **Macromolecules**, 39(3), 1165-1172.

[61] Traiphol, R., Charoenthai, N., Srikhirin, T., Kerdcharoen, T., Osotchan, T. and Maturos, T. (2007). Chain organization and photophysics of conjugated polymer in poor solvents: Aggregates, agglomerates and collapsed coils. **Polymer**, 48(3), 813-826.

[62] Yu, Z. and Barbara, P. F. (2004). Low-temperature single-molecule spectroscopy of MEH-PPV conjugated polymer molecules. **The Journal of Physical Chemistry B**, 108(31), 11321-11326.

[63] Barbara, P.F., Gesquiere, A.J., Park, S.-J. and Lee, Y. J. (2005). Single-molecule spectroscopy of conjugated polymers. **Accounts of Chemical Research**, 38(7), 602-610.

[64] Bolinger, J.C., Traub, M.C., Brazard, J., Adachi, T., Barbara, P.F. and Vanden Bout, D.A. (2012). Conformation and energy transfer in single conjugated polymers. **Accounts of Chemical Research**, 45(11), 1992-2001.

[65] Conwell, E. M., Perlstein, J. and Shaik, S. (1996) Interchain photoluminescence in poly(phenylene vinylene) derivatives. **Physical Review B**, 54(4), R2308-R2310.

[66] Tretiak, S., Saxena, A., Martin, R. L. and Bishop, A. R. (2000) Interchain electronic excitations in poly(phenylenevinylene) (PPV) aggregates. **The Journal of Physical Chemistry B**, 104(30), 7029-7037.

[67] Noriega, R., Rivnay, J., Vandewal, K., Koch, F.P.V., Stingelin, N., Smith, P., et al. (2013). A general relationship between disorder, aggregation and charge transport in conjugated polymers. **Nat Mater**, 12(11), 1038-1044.

[68] Amrutha, S.R. and Jayakannan, M. (2008). Probing the π-stacking induced molecular aggregation in π-conjugated polymers, oligomers, and their blends of p-phenylenevinylenes. **The Journal of Physical Chemistry B**, 112(4), 1119-1129.

[69] Collison, C.J., Rothberg, L.J., Treemaneekarn, V. and Li, Y. (2001). Conformational effects on the photophysics of conjugated polymers: A two species model for MEH−PPV spectroscopy and dynamics. **Macromolecules**, 34(7), 2346-2352.

[70] Traiphol, R. and Charoenthai, N. (2008). Effects of conformational change and segmental aggregation on photoemission of illuminophores in conjugated polymer MEH-PPV: Blue shift versus red shift. **Synthetic Metals**, 158(3–4), 135-142.

[71] Rughooputh, S.D.D.V., Hotta, S., Heeger, A.J. and Wudl, F. (1987). Chromism of soluble polythienylenes. **Journal of Polymer Science Part B: Polymer Physics**, 25(5), 1071-1078.

[72] Rumbles, G., Samuel, I.D.W., Magnani, L., Murray, K.A., DeMello, A.J. Crystall, B., et al. (1996). Chromism and luminescence in regioregular poly(3-dodecylthiophene). **Synthetic Metals**, 76(1–3), 47-51.

[73] Magnani, L., Rumbles, G., Samuel, I.D.W., Murray, K., Moratti, S.C., Holmes, A.B., et al. (1997). Photoluminescence studies of chain interactions in electroluminescent polymers. **Synthetic Metals**, 84(1–3), 899-900.

[74] Kiriy, N., Jähne, E., Adler, H.-J., Schneider, M., Kiriy, A., Gorodyska, G., et al. (2003). One-dimensional aggregation of regioregular polyalkylthiophenes. **Nano Letters**, 3(6), 707-712.

[75] Kiriy, N., Jähne, E., Kiriy, A. and Adler, H.-J. (2004). Conformational transitions and aggregations of regioregular polyalkylthiophenes. **Macromolecular Symposia**, 210(1), 359-367.

[76] Lanzi, M., Bertinelli, F., Costa-Bizzarri, P., Paganin, L and Cesari, G. (2007). Tuning of the electronic properties of self-assembling and highly sensitive chromic polyalkylthiophenes. **European Polymer Journal**, 43(3), 835-846.

[77] Prosa, T. J., Winokur, M. J. and McCullough, R. D. (1996). Evidence of a novel side chain structure in regioregular poly(3-alkylthiophenes). **Macromolecules**, 29(10), 3654-3656.

[78] Arosio, P., Moreno, M., Famulari, A., Raos, G., Catellani, M. and Meille, S. V., (2009). Ordered stacking of regioregular head-to-tail polyalkylthiophenes: Insights from the crystal structure of form I′ poly(3-n-butylthiophene). **Chemistry of Materials**, 21(1), 78-87.

[79] Buono, A., Son, N. H., Raos, G., Gila, L., Cominetti, A., Catellani, M., et al. (2010). Form II poly(3-butylthiophene): Crystal structure and preferred orientation in spherulitic thin films. **Macromolecules**, 43(16), 6772-6781.

[80] Qu, Y., Su, Q., Li, S., Lu, G., Zhou, X., Zhang, J., et al. (2012). H-aggregated form II spherulite of poly(3-butylthiophene) grown from solution. **ACS Macro Letters**, 1(11), 1274-1278.

[81] Kayunkid, N., Uttiya, S. and Brinkmann, M. (2010). Structural model of regioregular poly(3-hexylthiophene) obtained by electron diffraction analysis. **Macromolecules**, 43(11), 4961-4967.

[82] Brinkmann, M. (2011). Structure and morphology control in thin films of regioregular poly(3-hexylthiophene). **Journal of Polymer Science Part B: Polymer Physics**, 49(17), 1218-1233.

[83] Samitsu, S., Shimomura, T., Heike, S., Hashizume, T. and Ito, K. (2008). Effective production of poly(3-alkylthiophene) nanofibers by means of whisker method using anisole solvent: Structural, optical, and electrical Properties. **Macromolecules**, 41(21), 8000-8010.

[84] Samitsu, S., Shimomura, T. and Ito, K. (2008). Nanofiber preparation by whisker method using solvent-soluble conducting polymers. **Thin Solid Films**, 516(9), 2478-2486.

[85] Park, Y. D., Lee, H. S., Choi, Y. J., Kwak, D., Cho, J. H., Lee, S., et al. (2009). Solubility-induced ordered polythiophene precursors for high-performance organic thin-film transistors. **Advanced Functional Materials**, 19(8), 1200-1206.

[86] Sun, S., Salim, T., Wong, L. H., Foo, Y. L., Boey, F. and Lam, Y. M. (2011). A new insight into controlling poly(3-hexylthiophene) nanofiber growth through a mixed-solvent approach for organic photovoltaics applications. **Journal of Materials Chemistry**, 21(2), 377-386.

[87] Xu, W., Li, L., Tang, H., Li, H., Zhao, X. and Yang, X. (2011). Solvent-induced crystallization of poly(3-dodecylthiophene): Morphology and kinetics. **The Journal of Physical Chemistry B**, 115(20), 6412-6420.

[88] Scharsich, C., Lohwasser, R. H., Sommer, M., Asawapirom, U., Scherf, U., Thelakkat, M., et al. (2012). Control of aggregate formation in poly(3-hexylthiophene) by solvent, molecular weight, and synthetic method. **Journal of Polymer Science Part B: Polymer Physics**, 50(6), 442-453.

[89] Park, E.-J., Erdem, T., Ibrahimova, V., Nizamoglu, S., Demir, H.V. and Tuncel, D. (2011). White-emitting conjugated polymer nanoparticles with cross-linked shell for mechanical stability and controllable photometric properties in color-conversion LED applications. **ACS Nano**, 5(4), 2483-2492.

[90] Wu, C. and Chiu, D. T. (2013). Highly fluorescent semiconducting polymer dots for biology and medicine. **Angewandte Chemie International Edition**, 52(11), 3086-3109.

[91] Pras, O., Chaussy, D., Stephan, O., Rharbi, Y., Piette, P. and Beneventi, D. (2010). Photoluminescence of 2,7-poly(9,9-dialkylfluorene-co-fluorenone) nanoparticles: Effect of particle size and inert polymer addition. **Langmuir**, 26(18), 14437-14442.

[92] Baier, M.C., Huber, J. and Mecking, S. (2009). Fluorescent conjugated polymer nanoparticles by polymerization in miniemulsion. **Journal of the American Chemical Society**, 131(40), 14267-14273.

[93] Szymanski, C., Wu, C., Hooper, J., Salazar, M.A., Perdomo, A., Dukes, A., et al. (2005). Single molecule nanoparticles of the conjugated polymer MEH-PPV, preparation and characterization by near-field scanning optical microscopy. **The Journal of Physical Chemistry B**, 109(18), 8543-8546.

[94] Wu, C., Szymanski, C., Cain, Z. and McNeill, J. (2007). Conjugated polymer dots for multiphoton fluorescence imaging. **Journal of the American Chemical Society**, 129(43), 12904-12905.

[95] Wu, C., Peng, H., Jiang, Y. and McNeill, J. (2006). Energy transfer mediated fluorescence from blended conjugated polymer nanoparticles. **The Journal of Physical Chemistry B**, 110(29), 14148-14154.

[96] Wu, C., Szymanski, C. and McNeill, J. (2006). Preparation and encapsulation of highly fluorescent conjugated polymer nanoparticles. **Langmuir**, 22(7), 2956-2960.

[97] Li, X.-G., Li, J. and Huang, M.-R. (2009). Facile optimal synthesis of inherently electroconductive polythiophene nanoparticles. **Chemistry-A European Journal**, 15(26), 6446-6455.

[98] Lee, S.J., Lee, J.M., Cheong, I.W., Lee, H. and Kim, J. H. (2008). A facile route of polythiophene nanoparticles via Fe^{3+}-catalyzed oxidative polymerization in aqueous medium. **Journal of Polymer Science Part A: Polymer Chemistry**, 46(6), 2097-2107.

[99] Lee, S.J., Lee, J.M., Cho, H.-Z., Koh, W.G., Cheong, I.W. and Kim, J. H. (2010). Poly(thiophene) nanoparticles prepared by Fe^{3+}-catalyzed oxidative polymerization: A size-dependent effect on photoluminescence property. **Macromolecules**, 43(5), 2484-2489.

[100] Ko, Y.-J., Mendez, E. and Moon, J. H. (2011). Controlled aggregation in conjugated polymer nanoparticles via organic acid treatments. **Macromolecules**, 44(13), 5527-5530.

[101] Nagarjuna, G., Baghgar, M., Labastide, J.A., Algaier, D.D., Barnes, M.D. and Venkataraman, D. (2012). Tuning aggregation of poly(3-hexylthiophene) within nanoparticles. **ACS Nano**, 6(12), 10750-10758.

[102] Yang, H., LeFevre, S.W., Ryu, C.Y. and Bao, Z. (2007). Solubility-driven thin film structures of regioregular poly(3-hexyl thiophene) using volatile solvents. **Applied Physics Letters**, 90(17), 172116.

[103] Koynov, K., Bahtiar, A., Ahn, T., Cordeiro, R.M., Hörhold, H.-H. and Bubeck, C. (2006). Molecular weight dependence of chain orientation and optical constants of thin films of the conjugated polymer MEH-PPV. **Macromolecules**, 39(25), 8692-8698.

[104] Kobashi, M. and Takeuchi, H. (1998). Inhomogeneity of spin-coated and cast non-regioregular poly(3-hexylthiophene) films. Structures and electrical and photophysical properties. **Macromolecules**, 31(21), 7273-7278.

[105] Yang, C., Orfino, F.P. and Holdcroft, S. (1996). A phenomenological model for predicting thermochromism of regioregular and nonregioregular poly(3-alkylthiophenes). **Macromolecules**, 29(20), 6510-6517.

[106] Friedel, B., McNeill, C.R. and Greenham, N. C. (2010). Influence of alkyl side-chain length on the performance of poly(3-alkylthiophene)/polyfluorene all-polymer solar cells. **Chemistry of Materials**, 22(11), 3389-3398.

[107] Xue, L., Yu, X. and Han, Y. (2011). Different structures and crystallinities of poly(3-hexylthiophene) films prepared from aged solutions. **Colloids and Surfaces A: Physicochemical and Engineering Aspects,** 380(1–3), 334-340.

[108] Owen, T. (2000). **Fundamentals of Modern UV-visible Spectroscopy: Primer.** Germany: Agilent Technologies.

[109] Valeur, B. (2001). **Molecular Fluorescence: Principles and Applications.** Weinheim, Germany: Wiley-VCH Verlag GmbH.

[110] Lakowicz, J. R. (2007). **Principles of Fluorescence Spectroscopy** (3rd ed). Singapore: Springer.

[111] Jobin Yvon Ltd . (n.d.). **A Guide to Recording Fluorescence Quantum Yields.** Retrieved June 18, 2014, from http://www.horiba.com/fileadmin/uploads/ Scientific/Documents/Fluorescence/quantumyieldstrad.pdf

[112] Yang Leng. (2008). **Materials Characterization Introduction to Microscopic and Spectroscopic Method.** Singapore: John Wiley & Sons (Asia) Pte Ltd.

[113] Wang, Z. L. (2000). Transmission electron microscopy and spectroscopy of nanoparticles, **Characterization of Nanophase Materials.** Weinheim, Germany: Wiley-VCH Verlag GmbH.

[114] Zhou, W., Apkarian, R., Wang, Z. and Joy, D. (2007). Fundamentals of scanning electron microscopy (SEM), **Scanning Microscopy for Nanotechnology.** New York: Springer.

[115] Bhushan, B., Marti, O. (2011). Scanning probe microscopy - principle of operation, instrumentation, and probes, **Nanotribology and Nanomechanics I.** Berlin Heidelberg, Germany: Springer.

[116] Liu, J., Loewe, R. S. and McCullough, R. D. (1999). Employing MALDI-MS on poly(alkylthiophenes): Analysis of molecular weights, molecular weight distributions, end-group structures, and end-group modifications. **Macromolecules,** 32(18), 5777-5785.

[117] Merlo, J. A. and Frisbie, C. D. (2004). Field effect transport and tapping in regioregular polythiophene nanofibers. **The Journal of Physical Chemistry B**, 108(50), 19169-19179.

[118] Yaws, C. L. and Li, K. Y. (2008). Solubility parameter and liquid volume - organic compounds, **Thermophysical Properties of Chemicals and Hydrocarbons**. Norwich, New York: William Andrew.

[119] Wohlfarth ,C. (2005). Permittivity (dielectric constant) of liquids, **CRC Handbook of Chemistry and Physics** [Internet Version 2005]. Retrieved June 18, 2014, from http://www.hbcpnetbase.com.

[120] Lide, D.R. (2005). Physical constants of organic compounds, **CRC Handbook of Chemistry and Physics**, [Internet Version 2005]. Retrieved June 18, 2014, from http://www.hbcpnetbase.com.

[121] Guśkova, O. A.; Khalatur, P. G.; Khokhlov, A. R. (2009). Self-assembled polythiophene-based nanostructures: Numerical studies. **Macromolecular Theory and Simulations**, 18(4-5), 219-246.

[122] Curcó, D. and Alemán, C. (2007). Computational tool to model the packing of polycyclic chains: Structural analysis of amorphous polythiophene. **Journal of Computational Chemistry**, 28(10), 1743-1749.

[123] Moreno, M., Casalegno, M., Raos, G., Meille, S. V. and Po, R. (2010). Molecular modeling of crystalline alkylthiophene oligomers and polymers. **The Journal of Physical Chemistry B**, 114(4), 1591-1602.

[124] Perahia, D., Jiao, X. and Traiphol, R. (2004). From the conformation of a single molecule to physical networks in highly interacting polymers: A small-angle neutron study. **Journal of Polymer Science Part B: Polymer Physics**, 42(17), 3165-3178.

[125] Bidan, G., De Nicola, A., Enée, V. and Guillerez, S. (1998). Synthesis and UV−visible properties of soluble regioregular oligo(3-octylthiophenes), monomer to hexamer. **Chemistry of Materials**, 10(4), 1052-1058.

[126] Wu, C.-G., Lai, C.-Y. and Hsiao, N.-L. (2009). Molecular engineering leading to better processability of conjugated chromophores: The optical properties of new soluble copolymers containing alternative oligo-octylthiophene and oligo-methylene blocks. **European Polymer Journal**, 45(3), 879-887.

[127] Meier, H. (2005). Conjugated oligomers with terminal donor–acceptor substitution. **Angewandte Chemie International Edition**, 44(17), 2482-2506.

[128] Zhang, L., Colella, N. S., Liu, F., Trahan, S., Baral, J. K., Winter, H. H., et al. (2012). Synthesis, electronic structure, molecular packing/morphology evolution, and carrier mobilities of pure oligo-/poly(alkylthiophenes). **Journal of the American Chemical Society**, 135(2), 844-854.

[129] Traiphol, R., Charoenthai, N., Manorat, P., Pattanatornchai, T., Srikhirin, T., Kerdcharoen, T., et al. (2009). Photophysical change of poly(9,9-di(2-ethylhexyl)fluorene) and its copolymer with anthracene in solvent–non-solvent: Roles of interchain interactions on the formation of non-emissive and emissive aggregates. **Synthetic Metals**, 159(12), 1224-1233.

[130] Traiphol, R.and Perahia, D. (2006). Growth of nanoscale aggregates of dialkyl-poly(p-phenyleneethynylene)s on mica: Roles of molecular architectures and interchain association in solution. **Thin Solid Films**, 515(4), 2123-2129.

[131] Dong, H., Jiang, S., Jiang, L., Liu, Y., Li, H., Hu, W., et al. (2009). Nanowire crystals of a rigid rod conjugated polymer. **Journal of the American Chemical Society**, 131(47), 17315-17320.

[132] Traiphol, R., Charoenthai, N., Srikhirin, T. and Perahia, D. (2010). Self-assembling into interconnected nanoribbons in thin films of hairy rod poly(9,9-di(2-ethylhexyl)fluorene): Effects of concentration, substrate and solvent. **Synthetic Metals**, 160(11–12), 1318-1324.

[133] Liu, J., Sun, Y., Gao, X., Xing, R., Zheng, L., Wu, S., et al. (2011). Oriented poly(3-hexylthiophene) nanofibril with the π–π stacking growth direction by solvent directional evaporation. **Langmuir**, 27(7), 4212-4219.

[134] Haraguchi, S., Tsuchiya, Y., Shiraki, T., Sugikawa, K., Sada, K. and Shinkai, S. (2009). On the helical motif of the complexes created by association of helix-forming schizophyllan (SPG) and helix-forming polythiophene derivatives. **Chemistry – A European Journal**, 15(42), 11221-11228.

[135] Ripoll, J. D., Serna, A., Guerra, D. and Restrepo, A. (2010). Electronic structure calculations on helical conducting pPolymers. **The Journal of Physical Chemistry A**, 114(41), 10917-10921.

[136] Siddiqui, S. and Spano, F. C. (1999). H- and J-aggregates of conjugated polymers and oligomers: A theoretical investigation. **Chemical Physics Letters**, 308(1–2), 99-105.

[137] Spano, F. C. (2010). The spectral signatures of frenkel polarons in H- and J-aggregates. **Accounts of Chemical Research**, 43(3), 429-439.

[138] Park, Y. D., Lee, S. G., Lee, H. S., Kwak, D., Lee, D. H. and Cho, K. (2011). Solubility-driven polythiophene nanowires and their electrical characteristics. **Journal of Materials Chemistry**, 21(7), 2338-2343.

[139] Liu, J., Arif, M., Zou, J., Khondaker, S. I. and Zhai, L. (2009). Controlling poly(3-hexylthiophene) crystal dimension: Nanowhiskers and nanoribbons. **Macromolecules**, 42(24), 9390-9393.

[140] Ihn, K. J., Moulton, J. and Smith, P. (1993). Whiskers of poly(3-alkylthiophene)s. **Journal of Polymer Science Part B: Polymer Physics**, 31(6), 735-742.

[141] Oh, J. Y., Shin, M., Lee, T. I., Jang, W. S., Min, Y., Myoung, J.-M., et al. (2012). Self-seeded growth of poly(3-hexylthiophene) (P3HT) nanofibrils by a cycle of cooling and heating in solutions. **Macromolecules**, 45(18), 7504-7513.

[142] Aiyar, A. R., Hong, J.-I., Izumi, J., Choi, D., Kleinhenz, N. and Reichmanis, E. (2013). Ultrasound-induced ordering in poly(3-hexylthiophene): Role of molecular and process parameters on morphology and charge transport. **ACS Applied Materials & Interfaces**, 5(7), 2368-2377.

[143] Potai, R. and Traiphol, R. (2013). Controlling chain organization and photophysical properties of conjugated polymer nanoparticles prepared by reprecipitation method: The effect of initial solvent. **Journal of Colloid and Interface Science**, 403, 58-66.

[144] Gong, X., Moses, D. and Heeger, A.J. (2006). In K. Müllen, U. Scherf (Eds.), **Polymer-Based Light-Emitting Diodes (PLEDs) and Displays Fabricated from Arrays of PLEDs**, Weinheim: Wiley-VCH.

[145] Saunders, B. R. and Turner, M. L. (2008). Nanoparticle–polymer photovoltaic cells. **Advances in Colloid and Interface Science**, 138(1), 1-23.

[146] Lee, J. M., Lee, S. J., Jung, Y. J. and Kim, J. H. (2008). Fabrication of nano-structured polythiophene nanoparticles in aqueous dispersion. **Current Applied Physics**, 8(6), 659-663.

[147] Wang, Z., Wang, Y., Xu, D., Kong, E. S.-W. and Zhang, Y. (2010). Facile synthesis of dispersible spherical polythiophene nanoparticles by copper(II) catalyzed oxidative polymerization in aqueous medium. **Synthetic Metals**, 160(9–10), 921-926.

[148] Lide, D.R. (2005). Aqueous solubility and Henry's law constants of organic compounds, **CRC Handbook of Chemistry and Physics** [Internet Version 2005]. Retrieved June 18, 2014, from http://www.hbcpnetbase.com.

[149] Woo, H.S., Lhost, O., Graham, S.C., Bradley, D.D.C., Friend, R.H., Quattrocchi, C., et al. (1993). Optical spectra and excitations in phenylene vinylene oligomers. **Synthetic Metals**, 59(1), 13-28.

[150] Wutticharoenmongkol, P., Supaphol, P., Srikhirin, T., Kerdcharoen, T. and Osotchan, T. (2005). Electrospinning of polystyrene/poly(2-methoxy-5-(2′-ethylhexyloxy)-1,4-phenylene vinylene) blends. **Journal of Polymer Science Part B: Polymer Physics**, 43(14), 1881-1891.

[151] Chuangchote, S., Srikhirin, T. and Supaphol, P. (2007). Color change of electrospun polystyrene/MEH-PPV fibers from orange to yellow through partial decomposition of MEH side groups. Macromolecular Rapid Communications, 28(5), 651-659.

[152] Jakubiak, R., Collison, C. J., Wan, W. C., Rothberg, L. J. and Hsieh, B. R. (1999). Aggregation quenching of luminescence in electroluminescent conjugated polymers. **The Journal of Physical Chemistry A**, 103(14), 2394-2398.

[153] Cossiello, R. F., Susman, M. D., Aramendía, P. F. and Atvars, T. D. Z. (2010). Study of solvent-conjugated polymer interactions by polarized spectroscopy: MEH–PPV and poly(9,9′-dioctylfluorene-2,7-diyl). **Journal of Luminescence**, 130(3), 415-423.

[154] Kamdar, A. R., Hu, Y. S., Ansems, P., Chum, S. P., Hiltner, A. and Baer, E.
       (2006). Miscibility of propylene-ethylene copolymer blends.
       Macromolecules, 39(4), 1496-1506.

[155] Palacios, R. and Barbara, P. (2007). Single molecule spectroscopy of poly 3-
       octyl-thiophene (P3OT). **J Fluoresc**, 17(6), 749-757.